



VYSOKÁ ŠKOLA CHEMICKO-TECHNOLOGICKÁ V PRAZE
Fakulta potravinářské a biochemické technologie
Ústav biochemie a mikrobiologie

Intracelulární interakce a transport retrovirových proteinů

HABILITAČNÍ PRÁCE

PRO OBOR

BIOCHEMIE

Praha 2019

Ing. Jan Lipov, Ph.D.

Poděkování

Mé poděkování patří v první řadě prof. Ing. Tomáši Rumlovi, CSc., pod jehož vedením již dvě desítky let pracuji a který mi umožnil podílet se na řešení mnoha zajímavých témat. Rád bych poděkoval i svým nejbližším spolupracovnícím, Ing. Petře Grznárové-Prokšové, Ph.D. a Ing. Evě Jablonské, Ph.D., dále všem kolegům z laboratorní skupiny i Ústavu biochemie a mikrobiologie. Děkuji i všem studentům, kteří v rámci řešení svých bakalářských a diplomových prací přispěli k řešení témat, zahrnutých v této habilitační práci. V neposlední řadě chci poděkovat své rodině za vytrvalou podporu v dobách dobrých i zlých.

Jan Lipov

OBSAH

1. Úvod
2. Retroviry a jejich životní cyklus
 - 2.1 Taxonomie retrovirů
 - 2.2 Retrovirová částice a její komponenty
 - 2.2.1 Organizace genomu
 - 2.2.2 Virové polyproteiny
 - 2.2.3 Morfologie
 - 2.3. Mason-Pfizerův opičí virus (M-PMV)
 - 2.3.1 Organizace genomu a jeho transkripce
 - 2.3.2 Strukturní a obalové proteiny
 - 2.3.3 Životní cyklus
3. Přehled řešené problematiky I - virologie
 - 3.1 Vyřešení struktury MA proteinu
 - 3.2 Interakce virových polyproteinů s buněčnými motory
 - 3.3 Myristoylovaný MA protein
 - 3.4 Role mikrotubulů v intracelulárním transportu prekursorů
 - 3.5 Inkorporace obalových glykoproteinů do virového obalu
4. Přehled řešené problematiky II – testování degradovatelných biomateriálů
 - 4.1 Hořčík a jeho slitiny
 - 4.2 Zinek a jeho slitiny
 - 4.3 Železo a jeho slitiny
 - 4.4 Normy pro preklinické testování implantátů
 - 4.5 Metody testování
 - 4.6 Testování biodegradovatelných slitin
5. Závěr
6. Seznam použité literatury
7. Přílohy

1. Úvod

Retroviry jsou již řadu let předmětem velmi intenzivního studia, a to nejen v souvislosti s pandemií AIDS a onkogenními účinky na některé organismy, včetně člověka. AIDS a jeho původce, HIV, jsou zřejmě nejkřiklavějším případem pandemie, způsobené zástupcem čeledi *Retroviridae*. Dle statistik světové zdravotnické organizace bylo celosvětově od začátku epidemie infikováno virem lidské imunodeficiencie 75 milionů lidí, z nichž zhruba 32 milionů zemřelo. Odhaduje se, že v současnosti je infikováno HIV přibližně 0,8 % dospělých obyvatel Země ve věku mezi 15 a 49 lety. Nelze zapomenout ani na lidské endogenní retroviry (HERV), tvořící jednu skupinu transponovatelných elementů, které reprezentují cca 8 % lidského genomu. Lze je rozdělit zhruba do 40 fylogeneticky nezávislých skupin. Jsou pozůstatky dávných retrovirových infekcí a kromě pozitivních dopadů (např. syncitin, nezbytný při vývoji placenty) mají i dopady negativní – rakovinné bujení, roztroušená skleróza a mnoho dalších. (Grabski et al., 2019)

Detailní studium životního cyklu, způsobu skládání virionu a mechanismu infekce přináší poznatky použitelné nejen v oblasti medicíny a farmakologie, ale pomáhá i v řešení odvěké otázky vztahu struktury a funkce biomakromolekul. Studium intracelulárního transportu proteinů retrovirů a jejich interakce je extrémně zajímavé nejen díky přesahu do oblasti hledání účinných antivirových léčiv, ale i použitými technikami (především pokročilou fluorescenční mikroskopií).

2. Retroviry a jejich životní cyklus

Retroviry jsou skupinou virů s diploidním genomem, který je tvořen dvěma identickými molekulami jednořetězcové RNA o délce 7 – 10 kbp. Replikace RNA genomu probíhá za účasti virem kódovaného enzymu RNA dependentní DNA polymerasy (reverzní transkriptasy, RT, EC 2.7.7.49), která vykazuje kromě polymerasové i aktivitu RNAsovou (EC 3.1.26.13), neboť degraduje genomovou RNA z hybridu RNA•DNA. Tento enzym je charakteristickým rysem této skupiny a byl i základem jejího pojmenování. Produkt transkripce - dvouřetězcová DNA - je začleněn do genomu hostitelské buňky prostřednictvím dalšího virového enzymu – integrasu (EC 2.7.7.B22) (Coffin et al., 1997).

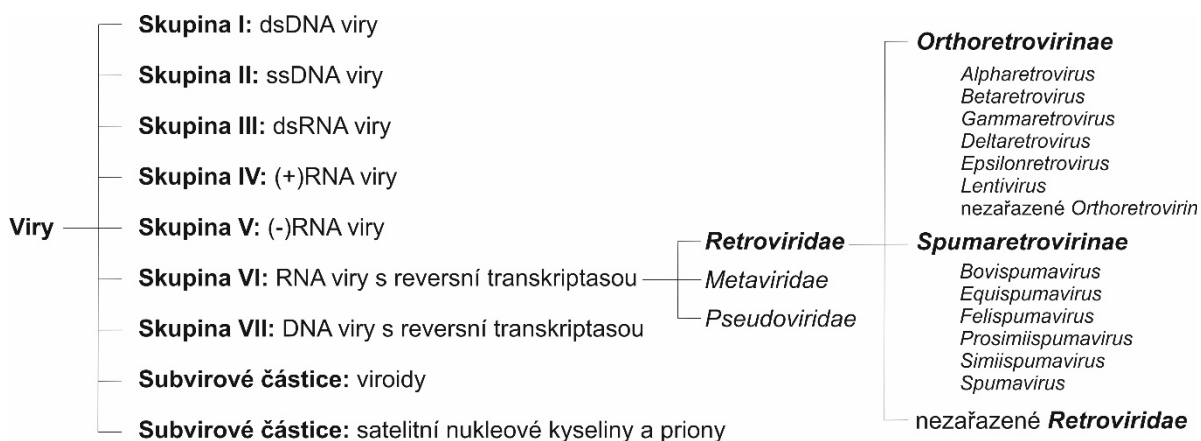
Dalším charakteristickým znakem retrovirů je jejich maturace mimo hostitelskou buňku. V průběhu tohoto procesu se nezralá neinfekční kapsida změní na zralý, infekční virion.

2.1 Taxonomie retrovirů

Dle Baltimorovy klasifikace spadají retroviry do VI skupiny, čeledi *Retroviridae*, čili RNA viry s reverzní transkriptasou (Fauquet C.M. et al., 2005).

Z hlediska struktury genomu dělíme retroviry na komplexní a jednoduché. Genom komplexních retrovirů kóduje oproti jednoduchým retrovirům řadu regulačních proteinů, které ovlivňují charakter retrovirové infekce jednotlivých zástupců. Typicky jsou dle exprese genů a morfologie (celková velikost virionu, tvar, velikost a frekvence glykoproteinových

povrchových jednotek a tvar jádra virionu (core) ve zralém virionu) klasifikovány do dvou podčeledí: *Orthoretrovirinae*, kam patří všechny onkogenní retroviry a *Spumaretrovirinae*, se specifickou morfologií (foamy virus). Existuje ovšem i mnoho zástupců, kteří nespádají ani do jedné podčeledi.



Obr. 1 Baltimorova klasifikace retrovirů, založená na genetické informaci a unikátním způsobu replikace

Jiným používaným způsobem dělení retrovirů je jejich klasifikace na základě způsobu tvorby kapsidy. Do první skupiny se společně řadí retroviry typu A, B a D:

- Částice typu A jsou endogenní a podobné virům. Dle lokalizace se dále dělí na intracytoplasmatické (ICAPs) a intracisternální (IAPs).
- Skupina retrovirů typu B je charakterizována tvorbou částic v cytoplasmě a excentrickým uložením core ve zralé partikuli. Zástupcem této skupiny virů je např. MMTV (Mouse Mammary Tumor Virus).
- U retrovirů typu D se kapsidy skládají na určitém místě uvnitř cytoplasmy, odkud jsou poté transportovány k cytoplasmatické membráně a dochází k pučení. Typickým zástupcem této skupiny je Mason-Pfizerův opičí virus (M-PMV).

Do druhé skupiny patří retroviry typu C:

- U těchto retrovirů se virová kapsida skládá současně s procesem pučení virionu cytoplasmatickou membránou hostitelské buňky a následně je uvolněna ve formě nezralé částice. Zástupcem této skupiny je např. HIV-1 (Human Immunodeficiency Virus).

2.2 Retrovirová částice a její komponenty

2.2.1 Organizace genomu

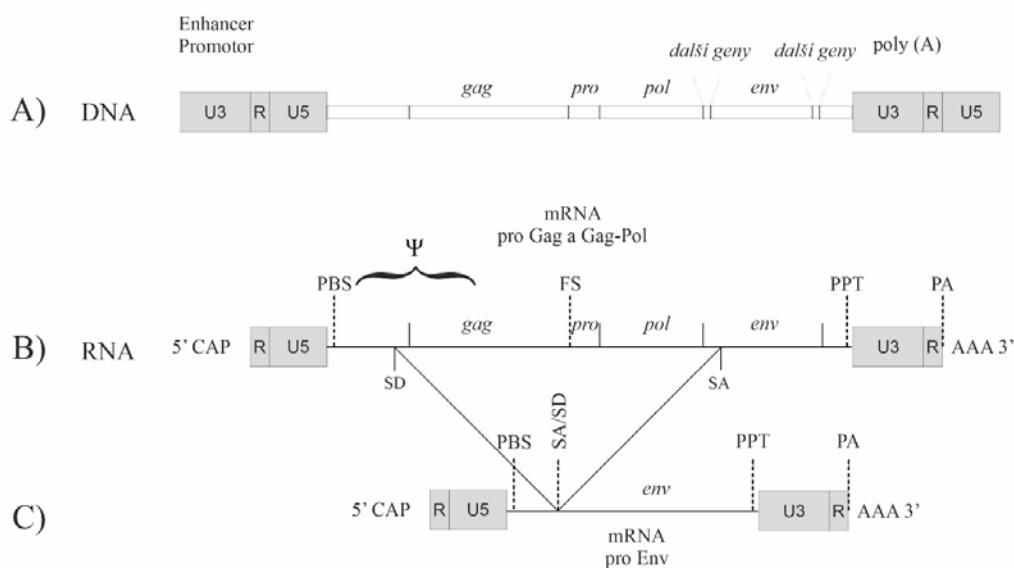
Ve zralé částici je genom tvořen dvěma shodnými kopiemi jednořetězcové (+)RNA. Po reverzní transkripci je genom retroviru začleněn ve formě DNA do genomu hostitelské buňky. Z provirové DNA je po aktivaci transkribována mRNA, které slouží pro syntézu virových proteinů. Část vzniklé RNA je také inkorporována do nově vznikajících virionů.

U jednotlivých retrovirů lze sledovat značnou podobnost ve formální struktuře genomu. U všech lze nalézt na 5' konci methylovanou čepičku, následuje regulační oblast označovaná jako "long terminal repeat" (LTR-sekvence), oblast kódující strukturní proteiny, případně regulační proteiny, opět LTR a poslední část tvoří polyadenylátový úsek na 3' konci (Obr. 2).

LTR sekvence hrají důležitou roli v regulaci transkripce retrovirových genů. Jsou to místa, na která se váží vlastní retrovirové proteiny a proteiny hostitelské buňky regulující transkripci retrovirové mRNA (Marcello, 2004)

Obecný retrovirový genom obsahuje geny *gag*, *pro* a *pol*, které kódují strukturní proteiny (Gag), enzymy proteasu (Pro), integrasu a reverzní transkriptasu (dohromady tvořící Pol). Tyto tři geny jsou přepisovány z jednoho společného čtecího rámce a podle příslušné mRNA jsou pak na volných ribosomech translatovány odpovídající polyproteiny. V genomu většiny retrovirů je v blízkosti 3' LTR přítomen gen *env*, který kóduje povrchové glykoproteiny. Na rozdíl od výše zmíněných genů vzniká mRNA kódující Env alternativním sestřihem.

Genomy retrovirů mohou kódovat i další proteiny jako např. regulační bílkoviny viru HIV, mRNA pro tyto proteiny vznikají alternativním sestřihem z jedné pre-mRNA.



Obr. 2 Genom generalizovaného proviru

A) provirová DNA tak, jak je integrována do hostitelské DNA;

B) mRNA (primární produkt transkripce) kódující strukturní polyproteiny Gag, Gag-Pro, Gag-Pro-Pol

C) mRNA (vzniklá sestřihem primární mRNA) kódující povrchový glykoprotein Env (zkratky z angl. PBS, primer binding site – vazebné místo primeru; Ψ, encapsidation sequence – vbalovací sekvence; SD, splice donor site – donorové místo sestřihu; FS, frameshift site – místo posunu čtecího rámce; SA, splice acceptor site – akceptorové místo sestřihu; PPT, polypurine tract – polypurinová oblast; PA, polyadenylation signal – polyadenylační signál; AAA, poly(A) tail – poly(A) oblast)

(Coffin et al., 1997), modifikováno

Genom retrovirů dále obsahuje oblasti, které hrají regulační roli v průběhu reverzní transkripce a sbalování viru. Mezi LTR a iniciačním kodonem Gag je lokalizováno místo pro RNA primer (PBS, z *angl.* Primer Binding Site), na které se váže tRNA, sloužící jako primer v průběhu reverzní transkripce (Hargittai et al., 2004; Yu and Morrow, 1999). Dále jsou v genomu lokalizovány sekvence nutné pro specifickou inkorporaci nesestřížené retrovirové RNA do nově vznikající částice (Schmidt et al., 2003) a tzv. CTE sekvence (z *angl.* Constitutive Transport Element), která je nutná pro transport retrovirové mRNA z jádra do cytoplasmy (Ernst et al., 1997).

2.2.2 Virové polyproteiny

Všechny retroviry obsahují proteiny Gag, Pro, Pol a Env a tyto mají ve všech retrovirech stejné základní funkce. Gag je hlavním strukturním proteinem, tvořícím nezralou kapsidu. Pro je proteasa, štěpící polyproteiny Gag, Gag-Pro a Gag-Pro-Pol na jednotlivé funkční proteiny, u některých virů rovněž zkracuje Env od C-konce. Pol je virová polymerasa – reverzní transkriptasa. Env je vazebným proteinem pro receptory, zprostředkovávajícím interakci mezi zralým virionem a buňkou a řídícím fúzi virové a buněčné membrány. Komplexní retroviry mají ještě řadu doplňkových proteinů, které zajišťují virově specifické úlohy. Při plnění základních úkolů virové replikace interagují retrovirové proteiny s mnoha buněčnými proteiny.

Produkty základních genů jsou translatovány ve formě polyproteinových prekursorů, které jsou dále štěpeny buď virovou (Gag prekursor), nebo buněčnou (Env prekursor) proteasou. Kromě výše zmíněných polyproteinových prekursorů (tj. Gag a Env) vznikají i polyproteiny Gag-Pol nebo Gag-Pro a Gag-Pro-Pol. Gen *pol* je umístěn v jiném čtecím rámci než *gag*, v průběhu translace dochází k posunu čtecího rámce o jeden nukleotid zpět vlivem vlásenkových struktur v blízkosti terminačních kodonů (Staple and Butcher, 2003), produktem je polyprotein Gag-Pol. V některých případech vyžaduje přečtení genu *pol* dvou změn čtecího rámce. Virová proteasa je zde kódována vlastním otevřeným čtecím rámcem na rozhraní genů *gag* a *pol*. Právě tehdy vznikají produkty Gag-Pro a Gag-Pro-Pol.

Gen *gag* kóduje strukturní proteiny. Jsou to obecně:

MA - matrixový protein, tvoří vnější obal virové kapsidy, v nezralé částici je jakožto N-terminální doména Gag nutný pro transport tohoto polyproteinu na místo skládání a pro interakci s membránou, z níž virus získává obal

CA - kapsidový protein, formuje ve zralém virionu core, uvnitř které je lokalizován nukleoproteinový komplex a virové enzymy, je také hlavní interakční doménou polyproteinu Gag při skládání nezralé částice

NC - nukleokapsidový protein, tvoří komplex s virovou RNA a je zodpovědný za specifickou inkorporaci virového genomu do vznikající částice

Gen *pro* kóduje virovou proteasu, v některých virech je gen *pro* součástí čtecího rámce

genu *pol*

PR - proteasa, zodpovědná za štěpení polyproteinových prekursorů na jednotlivé proteiny zralého virionu

Gen *pol* kóduje enzymy nezbytné pro životní cyklus retroviru:

RT - reverzní transkriptasa, přepisující genomovou RNA do DNA

IN - integrasa, včleňující výsledný transkript do genomu hostitele

Gen *env* kóduje obalové glykoproteiny:

SU – povrchový protein

TM - transmembránový protein

Ve zralém virionu lze nalézt několik základních struktur (Obr. 3). První z nich je vnitřní obal virové kapsidy, který je tvořen matrixovým proteinem (MA). Vrstva tvořená tímto proteinem leží těsně pod fosfolipidovou membránou a interaguje s ní prostřednictvím basické oblasti a kyseliny myristové, vázané kovalentně na matrixový protein..

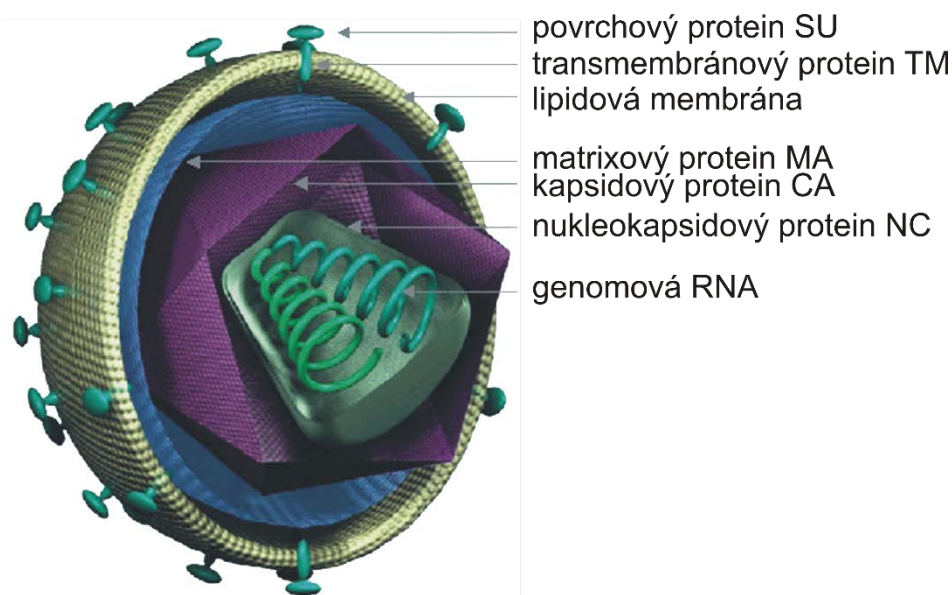
Kapsidový protein tvoří hlavní součást zralého virionu - core. Core je tvořeno kapsidovým proteinem (CA), obklopujícím ribonukleoproteinový komplex. NC je vysoce basický protein, který tvoří komplex s virovou RNA a ve zralém virionu je k ní pevně vázán. Vytvoření nukleoproteinového komplexu je nezbytné pro správné sbalení a dimerizaci genomové RNA. Core obsahuje také virové enzymy reverzní transkriptasu (RT), integrasu (IN) a proteasu (PR). Tvar core se u jednotlivých retrovirů liší. Může být kónický (HIV-1) (Briggs, J. A. a kol., 2003), sférický (RSV) (Kingston, R. L. a kol., 2001), nebo válcovitý (M-PMV) (Coffin, J. a kol., 1997).

2.2.3 Morfologie

Retroviry mají obecně sférický virion s průměrem 100 – 200 nm. Vnější obal je tvořen fosfolipidovou membránou, pocházející z hostitelské buňky. Tento lipidový obal má oproti průměrnému složení cytoplasmatické membrány vyšší obsah cholesterolu a sfingomyelinu (Rawat et al., 2003). Toto složení je připisováno pučení retrovirů v oblastech tzv. lipidových raftů, membránových mikrodomén obohacených o tyto sloučeniny. U většiny retrovirů jsou do vnější lipidové vrstvy zanořeny transmembránové glykoproteiny (TM), které jsou nekovalentně spojené s povrchovými glykoproteiny (SU). Povrchové proteiny SU jsou zodpovědné za rozpoznání receptorů cílové buňky, jejich velikost a tvar se u jednotlivých retrovirů liší. Povrchová doména transmembránového glykoproteinu zprostředkovává fúzi membrán při vstupu viru do buňky (Freed and Martin, 1995). Membránou procházející integrální protein TM slouží k ukotvení SU na povrchu viru. Interakce mezi těmito podjednotkami je nekovalentní a poměrně slabá. Nezralá částice je složena z virové membrány, polyproteinů Env, Gag/Gag-Pol/Gag-Pro-Pol a diploidního retrovirového genomu. Gag je organizován do vrstvy v těsném kontaktu s vnitřní stranou virové membrány. V souběhu s pučením jsou trimerní heterodimery Env inkorporovány do virové membrány

pomocí buněčných mechanismů. Nezralá částice má na elektronmikroskopických snímcích tvar dvou soustředných kruhů. MA doména Gag leží pod membránou viru na okraji vrstvy, NC směřuje do středu virionu. Kapsidový protein je složen ze dvou strukturně nezávislých domén propojených flexibilní spojkou. Jak N-terminální, tak C-terminální domény CA jsou hlavními interakčními motivy při tvorbě hexagonální sítě nezralé částice. Průměrný počet molekul Gag v retrovirových částicích byl odhadnut na 1500 - 5000.

V průběhu pučení, či bezprostředně po něm dochází k aktivaci proteasy, štěpení polyproteinu za uvolnění jednotlivých funkčních proteinů a k reorganizaci kapsidy; tento proces se nazývá maturace. Výsledkem je sférická částice, která obsahuje nekovalentně spojené molekuly TM a SU (vzniklé z Env). Vnitřní obal částice je tvořen matrixovým proteinem MA. Jádro virionu, tzv. core je tvořeno kapsidovým proteinem CA, který obaluje komplex virové RNA s nukleokapsidovým proteinem NC



Obr. 3 Morfologie zralé retrovirové částice.

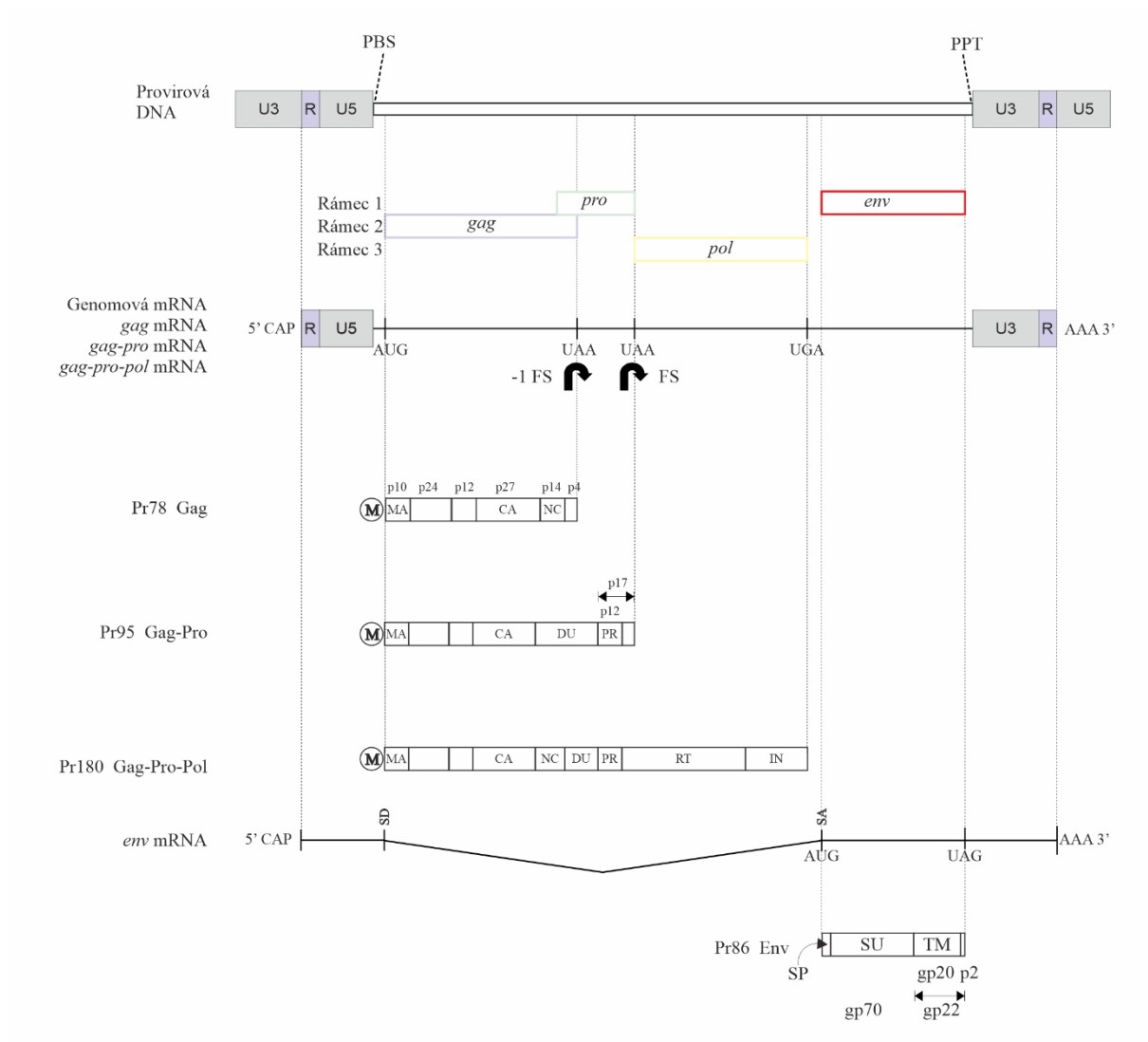
Na vnějším lipidovém obalu kapsidy jsou umístěny trimery povrchového proteinu SU. Vnitřní obal částice pod membránou je tvořen matrixovým proteinem MA. Jádro virionu, tzv. core je tvořeno kapsidovým proteinem CA, který chrání nukleoproteinový komplex dvou molekul virové genomové RNA pokrytých nukleokapsidovým proteinem NC.

2.3 Mason-Pfizerův opičí virus (M-PMV)

2.3.1 Organizace genomu a jeho transkripce

Přibližná velikost genomu M-PMV je 7900 nukleotidů. Hlavní částí je sekvence kódující stejné geny polyproteinů jako je tomu u jiných retrovirů: *gag*, *pro*, *pol* a *env*. Obě molekuly genomové RNA jsou využity pro reverzní transkripci, probíhající v několika fázích, kdy dochází postupně ke kopírování RNA do DNA, následované sekvenční degradací úseků RNA templátu. Retrovirový 5' LTR obsahuje vlastní promotor pro expresi genomové RNA. Primer

pro reverzní transkripci není v případě retrovirů syntetizovaný RNA polymerasou, ale jeho funkci iniciace syntézy (-) řetězce DNA nahrazuje savčí tRNA_{Lys}, která se váže na komplementární sekvenci nazývanou primer binding site (PBS), sousedící s 5' LTR (Coffin et al., 1997; Sonigo et al., 1986). Konstitutivní transportní element (CTE) je úsek na 3' konci genomu M-PMV, který slouží pro export mRNA z jádra. Je členem skupiny jaderných exportérů interagujících s TAP (tyrosine kinase-interacting protein), (Gruter et al., 1998). SD a SA jsou signály pro sestřih, rozeznávané buněčnými spliceosomy pro odstranění sekvence *gag*, *pro* a *pol*. Vzniklá subgenomová mRNA je využita pro translaci povrchových glykoproteinů Env. Retrovirová RNA obsahuje také Ψ signál rozpoznávaný nukleokapsidovým proteinem pro specifické a efektivní vbalování do vznikajících částic (Vile et al., 1992). Primární transkript M-PMV je terminálně modifikován podobně jako buněčná pre-mRNA, tj. připojením čepičky na 5' konci a polyadenylací na 3' konci (Obr. 4).

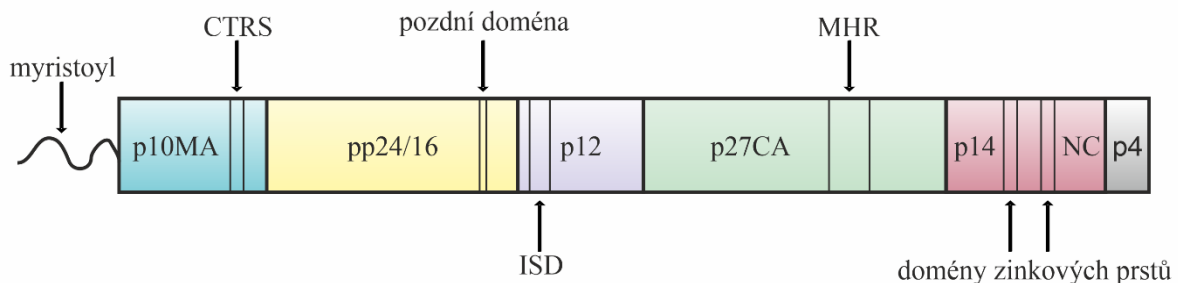


Obr. 4 Organizace genomu M-PMV s vyznačenými výslednými polyproteiny; (Coffin et al., 1997), modifikováno

2.3.2 Strukturní a obalové proteiny

Nezralá kapsida je v případě M-PMV tvořena třemi typy strukturních polyproteinových prekursů: Gag, Gag-Pro a Gag-Pro-Pol v poměru přibližně 100:10:1 (Kohoutova et al., 2009).

První popis šesti hlavních proteinů M-PMV pochází již z roku 1975. Tehdy byly pojmenovány dle odhadu molekulové hmotnosti zjištěné pomocí SDS-PAGE, tedy p10, p12, p27, p14, gp20 a gp68, přičemž „p“ znamená protein a „gp“ glykoprotein (Schochetman et al., 1975). Později byla studie reprodukována a byly nalezeny další proteiny s molekulovými hmotnostmi 24, 16–18 a 6 kDa. Byl nalezen polyproteinový precursor pro strukturní proteiny Pr78, pojmenovaný Gag („group antigen“ pro svou imunogenitu) a byla vyslovena hypotéza, že protein Pr95 může představovat precursor virové proteasy. Štěpení Pr78 vedlo ke vzniku pěti hlavních strukturních proteinů: p27 (kapsidový protein, CA), pp16 (fosfoprotein, PP), p14 (nukleokapsidový protein, NC), protein p12 a p10 (matrixový protein, MA) (Bradac and Hunter, 1984) (Obr. 5). Rovněž povrchové glykoproteiny vznikají nejprve ve formě precursoru, který je štěpen buněčnou proteasou, furinem na povrchovou a transmembránovou podjednotku. Existence precursoru pro povrchový glykoprotein byla odvozena právě z pozorování jeho štěpných produktů. Větší z nich (SU) z nich je tvořen 55kDa bílkovinnou částí, na kterou jsou navázány oligosacharidy o velikosti 15 kDa, tvořící dohromady gp70 (gp68 z originální studie). Druhý je tvořen 20kDa jednotkou s jedním oligosacharidovým řetězcem. Později bylo zjištěno, že tento protein gp20 je výsledkem maturace, ve které virová proteasa zkracuje Env podjednotku gp22 na gp20 (Sommerfelt et al., 1992).



Obr. 5 Schéma organizace strukturních proteinů v polyproteinu Gag ((Sakalian and Hunter, 1999), modifikováno)

Matrixový protein (MA, p10) je N-terminálním proteinem polyproteinu Gag. Bylo zjištěno, že po odstranění iniciačního methioninu je kotranslačně myristoylován na N-koncovém glycinu. Obsahuje doménu CTRS (cytoplasmic targeting/retention signal), která je zodpovědná za cílení Gag, Gag-Pro a Gag-Pro-Pol do pericentriální oblasti, ve které dochází ke skládání nezralé virové částice. Má se rovněž za to, že se účastní interakce Gag s molekulami Env, a to prostřednictvím vazby na 38 aminokyselin dlouhou cytoplasmatickou C-koncovou doménu transmembránového proteinu. Prostřednictvím zbytku kyseliny myristové a seskupení basických aminokyselin se rovněž účastní interakce s membránovými fosfolipidy. MA protein M-PMV je na lipidovém obalu pravděpodobně ve formě trimeru (Conte, M. R. a kol., 1997; Hill, C. P. a kol., 1996) a nekovalentně interaguje s TM proteinem (Song, C. a kol., 2003)

Fosfoprotein (PP, p24/16) p16 je C-terminálním štěpným produktem proteinu p24. Obsahuje tzv. pozdní domény PPPY a PSAP, nutné pro odškrcení virové částice od membrány hostitelské buňky v průběhu pučení a hraje roli ve vbalování virového genomu (Bohl et al., 2005).

Protein p12 (p12) se účastní tvorby nezralé částice, prvních 25 aminokyselin tvoří tzv. internal scaffold domain (ISD), nutnou pro efektivní skládání (Sakalian and Hunter, 1999), a to zejména prostřednictvím domény obsahující motiv leucinového zipu (Knejzlik et al., 2004).

Kapsidový protein (CA, p27) hraje důležitou roli ve skládání částic a tvoří tzv. core, čili obal nukleoproteinového komplexu ve zralé částici. Obsahuje oblast 20 aminokyselin tzv. major homology region (MHR), zapojenou ve skládání a časné fázi infekce (Strambio-de-Castillia and Hunter, 1992).

Nukleokapsidový protein (NC, p14) obsahuje dva motivy zinkových prstů a hraje roli v rozeznání a vbalení genomové RNA, se kterou poté tvoří nukleoproteinový komplex (Gao et al., 1998).

Protein p4 (p4) je spíše peptid (36 aminokyselin), hraje důležitou roli při skládání. Je bohatý na proliny a interaguje s podjednotkou buněčného chaperonu TRiC.

dUTPasa (DU) je deoxyuridin 5'-trifosfát nukleotidhydrolasa (EC 3.6.1.23) která brání inkorporaci deoxyuridinu do DNA. Vzniká po prvním posunu čtecího rámce ve formě fúzního proteinu NC-DU, který odolává proteolytickému štěpení virovou proteasou i buněčnými proteasami (Barabas et al., 2003).

Proteasa (PR) je virová aspartátová proteasa, EC 3.4.23.B6, která rovněž vzniká jako součást Gag-Pro prekursoru díky posunu čtecího rámce. Do částic je inkorporována v této neaktivní formě. Její aktivace a autokatalytické štěpení nastává v okamžiku uvolnění částice z infikované buňky. Spouští se tím proces maturace, kdy proteasa štěpí Gag i Pol na jednotlivé proteiny a zkracuje rovněž cytoplasmatickou C-terminální část TM.

Reverzní transkriptasa (RT) vzniká spolu s integrasou posunem čtecího rámce poblíž konce genu *pro*. Je inkorporována ve formě prekursoru Gag-Pro-Pol a vyštěpena během maturace virovou proteasou.

Integrasa (IN) zprostředkovává integraci virové DNA do hostitelského genomu. Je vyštěpována virovou proteasou rovněž z prekursoru Gag-Pro-Pol štěpením na C-konci RT.

Obalový glykoprotein (Env) je integrální membránový protein, který je syntetizován na drsném endoplasmatickém retikulu. Na N-konci má signální sekvenci 25 aminokyselin, která cílí vznikající protein do membrány ER a v lumen ER je ihned odštěpena. Syntetizovaný protein pokračuje v průchodu membránou ER až do okamžiku, kdy se do membrány integruje oblast hydrofobních aminokyselin, tzv. membrane-spanning domain. V ER je Env částečně glykosylován, což spustí správné sbalení proteinu a tvorbu trimerů. Po opuštění ER je Env transportován do Golgiho aparátu, kde je jednak dále glykosylován, jednak štěpen buněčnou proteasou (furin, EC 3.4.21.75) na dvě podjednotky **SU** a **TM**, které zůstávají asociovány (Bradac and Hunter, 1986; Sonigo et al., 1986).

Ve virionech byla nalezena také celá řada buněčných proteinů. U HIV-1 to jsou například ubikvitin, Tsg101, povrchové buněčné receptory, proteiny cytoskeletu a mnoho dalších (Ott, 2002). Ve virionech M-PMV byl zatím prokázán pouze Tsg101 (Gottwein et al., 2003), ale lze předpokládat, že budoucí práce odhalí další proteiny.

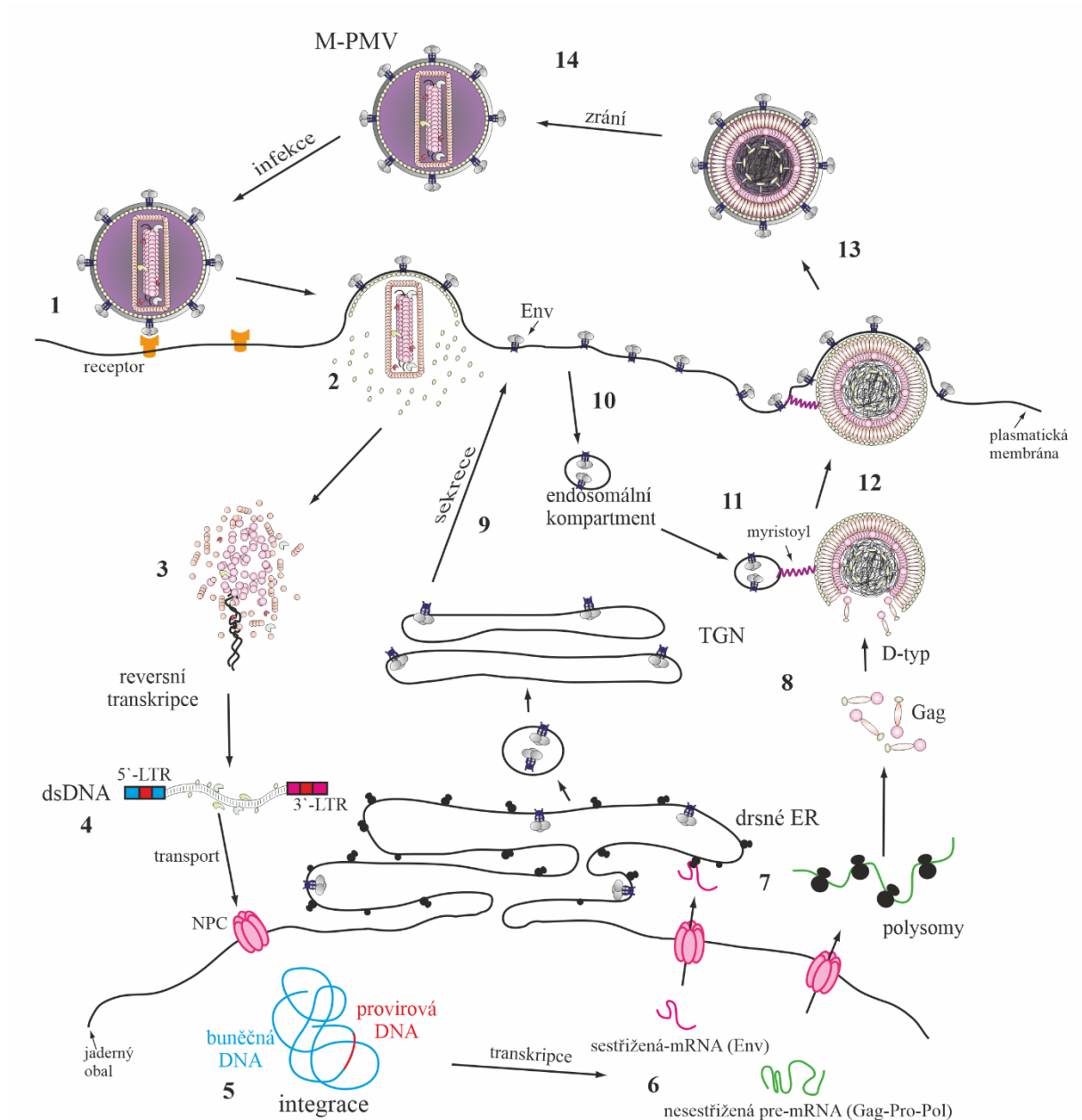
2.3.3 Životní cyklus

Časná fáze životního cyklu zahrnuje vstup viru do cílové buňky, transport virového core k jádru, reverzní transkripci a tvorbu preintegračního komplexu, jeho vstup do jádra a následně integraci virové DNA do hostitelského genomu ve formě proviru. Pozdní fáze životního cyklu poté zahrnuje aktivaci, transkripci a transport virové RNA, její vbalování nebo sestřih a syntézu všech prekursorů, složení nezralé virové částice, uvolnění této částice z hostitelské buňky a maturaci virionu (Obr. 6).

Pro infekci používá M-PMV, stejně jako ostatní betaretroviry, receptor SLC1A5, transportér neutrálních aminokyselin závislý na sodíku (známý též jako RD114) (Rasko et al., 1999). Pro interakci s tímto receptorem je esenciální SU. Po jejím navázání na receptor prochází Env konformační změnou v TM, která vede k fúzi virové membrány s cytoplasmatickou membránou buňky. Po fúzi membrán následuje uvolnění obsahu virionu do cytoplasmy. Reverzní transkripce nezačíná ihned, ale pravděpodobně současně s rozbalením (disociace CA z komplexu) a transportem do jádra v tzv. reverzně-transkripčním komplexu, který obsahuje NC, genomovou RNA, RT, IN a MA. Obecně je tato část životního cyklu velmi málo prozkoumána, takže nelze porovnávat, zda je u všech retrovirů zachováno stejné pořadí kroků. Je ale známo, že je to proces velmi neefektivní, protože jen velmi malá část vstupujících retrovirových částic vede až k reverzní transkripci. Je to rovněž způsobeno akcí antivirových obranných mechanismů buňky, jako je např. Trim5 α , který se váže na CA protein a svou ubikvitin ligasovou aktivitou může způsobit cílení celého komplexu do proteasomů pro degradaci (alespoň v případě HIV, (Lukic et al., 2011)). Reverzní transkripce začíná vazbou tRNA_{Lys} primeru na komplementární sekvenci PBS na 5'konci virového genomu. Vzniknou postupně obě vlákna, přičemž jsou duplikovány U3 a U5 oblasti virových LTR. Vznikne tak dvouřetězcová provirová DNA s tupými konci (Wilhelm and Wilhelm, 2001). Tohoto procesu se rovněž účastní dUTPasa, která zřejmě kompenzuje aktivitu buněčných deaminas z rodiny APOBEC. Ty jsou inkorporovány do virové částice a mohou způsobovat transici C na U během reverzní transkripce. Jakmile dorazí reverzně-transkripční komplex k jádru, je již reverzní transkripce téměř hotova a komplex se mění na preintegrační, obsahující RT, IN a dsDNA genom. Mechanismus vstupu do jádra je různý u různých retrovirů, translokace jadernými póry je ale vždy ATP dependentní proces (Bukrinsky, 2004). Integrasa zajistí vložení DNA proviru do genomu hostitele, tohoto procesu se pravděpodobně účastní i buněčné opravné mechanismy (Skalka and Katz, 2005). Místem integrace jsou oblasti s vysokou transkripční aktivitou bez další preference.

Prvním krokem pozdní fáze je transkripce virové RNA z integrované provirové DNA. Primární transkript slouží jednak jako genomová RNA pro nově vznikající virové částice, jednak jako informační molekula pro produkci virových proteinů. M-PMV obsahuje dvě sestřihová místa, rozeznávaná buněčným komplexem, vzniká tak RNA kódující Env. Většina buněčných pre-mRNA je sestřižena a polyadenylována před svým exportem z jádra. RNA M-PMV je z jádra exportována pomocí oblasti CTE (constitutive transport element), interagující s buněčným exportním faktorem NXF1 (Gruter et al., 1998). Po transportu virových mRNA do cytoplasmy je zahájena translace polyproteinů Gag, Gag-Pro, Gag-Pro-Pol a Env. První tři jsou

translatovány na volných polysomech v cytosolu a prostřednictvím interakce své CTRS domény s dyneinem jsou kotranslačně transportovány k mikrotubulárnímu organizačnímu centru, kde oligomerizují za vzniku nezralé částice. Svou roli zde hraje i vbalovaná RNA, která indukuje konformační změny vedoucí k multimerizaci a následnému skládání (Ulbrich et al., 2006). Signální sekvence Ψ se nachází v intronu mezi donorovým místem pro sestřih a iniciačním kodonem Gag, čímž je zajištěno, že se bude vbalovat pouze nesestřižená RNA. Ve zhruba sférické nezralé částici jsou molekuly Gag uspořádány radiálně, s N-terminální doménou (MA) orientovanou vně a C-terminální doménou (NC-p4) směřující do vnitřku částice. Nezralé částice jsou poté transportovány endosomální drahou a při transportu se setkají s molekulami Env. Pučení virových částí je závislé na buněčném komplexu ESCRT I - III (endosomal sorting complex required for transport), a to prostřednictvím interakce s pozdními doménami. M-PMV prokazatelně interaguje s BUL1, což je Nedd4-ubikvitin ligasa, přičemž tato interakce stačí pro indukci aktivity ESCRT (Freed, 2002). Maturace nastává poté, co nezralá částice opustí infikovanou buňku a je nezbytná pro infektivitu viru. Prvním krokem maturace je autoaktivace M-PMV proteasy, která začíná vyštěpením aktivní formy o velikosti 17 kDa. Ta je dále C-terminálně štěpena (opět vlastní aktivitou) na dvě aktivní formy; 13 a 12kDa. V částicích byly nalezeny dvě formy; jak proteasa o velikosti 17 kDa, tak 13 kDa (Zabransky et al., 1998). Gag je během maturace štěpen na jednotlivé proteiny a dochází k přeskupení částice. NC a virová RNA vytvoří v centru částice nukleoproteinový komplex, který je obalen CA, zatímco MA zůstává asociován s membránou. Rovněž dochází ke zkrácování TM o 16 aminokyselin, které jsou klíčové pro inkorporaci Env do virové částice.



Obr. 6 Životní cyklus M-PMV

1. částice interaguje s receptorem cílové buňky; 2 fúze membrán, uvolnění virového core do cytoplasmu; 3. transport core k jádru; 4. reverzní transkripce a tvorba preintegračního komplexu; 5. integrace proviru do genomu hostitele; 6. transkripce; 7. produkce virových prekursorů; 8. oligomerizace strukturálních polyproteinů; 9. transport povrchových glykoproteinů k membráně; 10. endocytosa povrchových glykoproteinů; 11. kotransport virové částice k membráně; 12/13. pučení a uvolnění z hostitelské buňky; 14. zrání částice (Grznárova, 2013) modifikováno

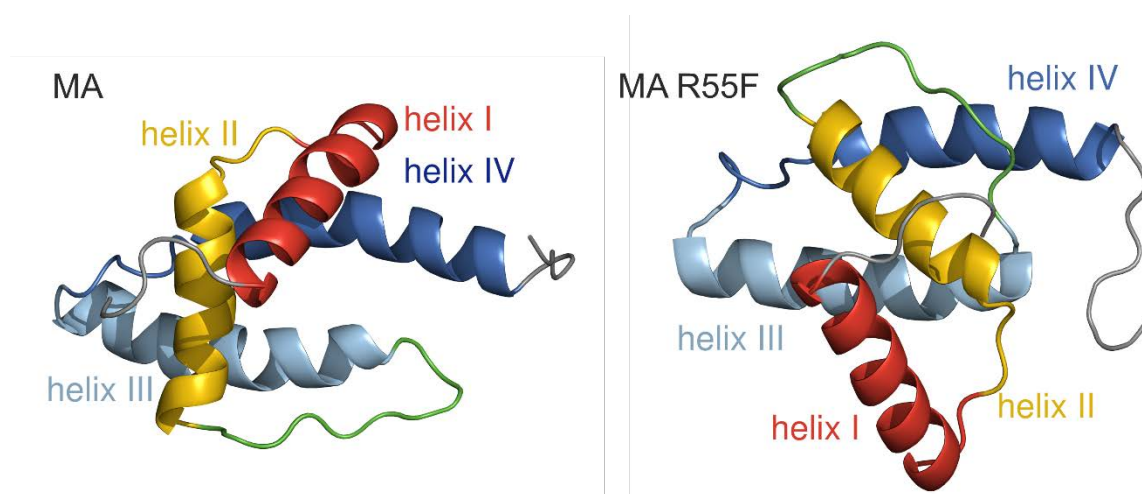
3. Přehled řešené problematiky I - virologie

3.1 Vyřešení struktury MA proteinu

Matrixový protein plní celou řadu funkcí v životním cyklu retroviru. Jakožto protein nacházející se ve zralém virionu nejbližší cytoplasmatické membráně hraje roli při interakci jak s membránovými fosfolipidy, tak s obalovými glykoproteiny. V časně fázi životního cyklu hraje roli v cílení preintegračního komplexu do jádra nově infikované buňky. Jako N-terminální doména strukturního polyproteinu Gag hraje také významnou úlohu v cílení molekul Gag do místa skládání. V MA proteinu M-PMV byla nalezena sekvence tzv. CTRS (z angl. Cytoplasmic Targeting Retention Signal), oblast 43-60. Byla připravena řada fyziologicky významných mutací fenotypově se projevujících změnou životního cyklu M-PMV – v tkáňových kulturách byly pozorovány změny množství, místa skládání a infekivity vznikajících virových částic. Pravděpodobně nejvýznamnější z nich byla mutace R55F, která zásadním způsobem mění morfogenetickou dráhu M-PMV z typu D na typ C (Rhee and Hunter, 1990). Vzhledem k tomu, že aminokyselina Arg55 je ve struktuře MA umístěna v prostorově přístupné smyčce, byla vyslovena hypotéza, že toto místo je interakčním partnerem pro složku buněčného transportního mechanismu, a že zavedenou mutací je tato interakce znemožněna. Pomocí zkoumání exprese mutantních prekursorů Gag v různých systémech bylo potvrzeno, že tato mutace nezpůsobuje defekt ve skládání virionů, nýbrž má vliv na transport jejich prekursorů. Tento fakt byl prokázán dalším experimentem, ve kterém byla CTRS matrixového proteinu M-PMV vložena do MA MuLV. Tento virus je představitelem C-typu s charakteristickým skládáním na membráně. Vložení CTRS vedlo ke vzniku intracytoplasmatických částic MuLV (Choi et al., 1999). Tím byla oblast CTRS definitivně identifikována jako transportní signál. Později bylo ještě prokázáno, že tato doména zprostředkovává interakci molekul Gag s dynein/dynaktinovým komplexem a zajišťuje tak kotranslační transport molekul Gag do pericentriolární oblasti buňky (Sfakianos et al., 2003). To je vhodné místo pro skládání virových kapsid, neboť obsahuje mnoho chaperonů (interakce molekul Gag s chaperonem TRiC byla dokonce prokázána (Hong et al., 2001)), navíc slouží v buňce jako centrum organizace mikrotubulů a může tudíž zprostředkovat interakci s cytoskeletem a vezikulárním transportním systémem buňky. Složené kapsidy jsou poté transportovány z pericentriolární oblasti k membráně pravděpodobně prostřednictvím složek systému recyklačních endosomů.

Přestože primární struktura MA proteinů nevykazuje vysokou vzájemnou homologii, jejich terciární struktura je až překvapivě podobná. Z vyřešených trojrozměrných struktur MA několika retrovirů lze usoudit, že základním strukturním rysem všech retrovirových MA je strukturní motiv několika α -helixů propojených krátkými flexibilními smyčkami. Kromě podobné vzájemné orientace helixů uvnitř molekuly je též zajímavé, že všechny MA vystavují většinu svých basických postranních řetězců na jedné straně molekuly. To souvisí s rolí oblasti basických aminokyselin při interakci s membránovými fosfolipidy. Struktura MA M-PMV byla publikována již v roce 1997, určeny však byly pouze polohy uhlíkových atomů, tvořících páteř molekuly (Conte et al., 1997). Jedním z prvních úkolů, na kterých jsem se v rámci své práce

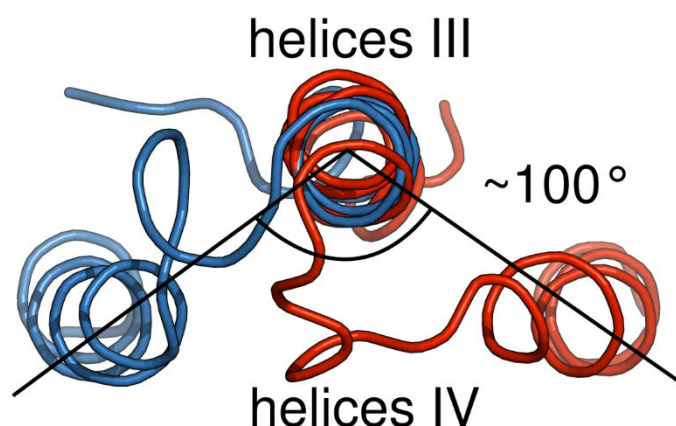
podílel, bylo vyřešení prostorové struktury mutantu R55F, ve snaze odhalit molekulární podstatu fenotypové změny skládání. Současně s tím byla *de novo* řešena struktura nemutované formy proteinu, neboť publikovaná data k detailnímu porovnání nestačila. V obou případech byla řešena struktura nemyristoylované verze proteinu. Již identifikace helikálních domén na základě indexů chemických posunů ukázala, že obě formy proteinu mají, stejně jako jiné retrovirové MA proteiny, čtyři helixy. Největším rozdílem je ovšem vzájemná orientace N- a C-koncových částí MA proteinu, tj. mezi dvojicemi helixů I, II a III, IV (Obr. 7). Vyjádříme-li tuto změnu jako změnu úhlu mezi podélnými osami helixu II a III, zjistíme, že zatímco u nemutované formy MA jsou tyto helixy k sobě téměř kolmé (úhel 98 stupňů), u mutantu R55F svírají úhel 322 stupňů. Úhly svírané podélnými osami helixů I a II, případně III a IV se přitom od sebe významně neliší (124 stupňů versus 120 stupňů a 172 stupňů versus 175 stupňů).



Obr 7. Grafická reprezentace vyřešené struktury MA a mutantní formy R55F. Struktury jsou zarovnané přes helix III a IV, aby byla zřejmá změna úhlu mezi helixem II a III

Druhým podstatným rozdílem mezi oběma molekulami je fakt, že helix IV a následně celý C-koncový zbytek molekuly R55F za helixem III je otočen kolem podélné osy helixu III cca o 100 stupňů oproti nemutované formě (Obr. 8).

Hnací silou obou těchto strukturních změn, tj. reorientace celé C-koncové části MA proteinu vzhledem k jeho N-koncové doméně a rotace helixu IV kolem osy helixu III, je zřejmě tendence hydrofobního a objemného zbytku aminokyseliny fenylalaninu schovat se před vodným prostředím. Původní hydrofilní aminokyselina arginin takovou tendenci neměla a postranní řetězec Arg55 trčí z proteinové globule nemutované formy MA ven. (Příloha 1)



Obr 8. Superpozice struktur obou proteinů přes oblast helixů III, dobře patrné je vzájemné otočení helixů IV

3.2 Interakce virových polyproteinů s buněčnými motory

Eukaryotické buňky organizují svou cytoplasmu přesunem organel a makromolekulárních komplexů podél mikrotubulů a aktinových vláken. Tyto pohyby jsou zprostředkovány řadou motorů, které musí specificky rozeznávat transportovanou molekulu. Jedním z takových motorů je i dynein, masivní molekulární motorové komplexy o velikosti 1 – 2 MDa. Pohybují se opačným směrem než kinesiny, tedy vždy k (-) konci mikrotubulů. Vazbu k mikrotubulům zprostředkovávají dva tzv. těžké řetězce (DHC) o molekulové hmotnosti cca 500 kDa, které tvoří homodimer a vykazují motorickou aktivitu při současné hydrolyze ATP. Tzv. středně těžké řetězce (DIC, cca 74 kDa) se podílejí na cílení transportu přepravovaných molekul. Středně lehké řetězce (52 - 61 kDa) regulují aktivitu dyneinového motoru. Poslední složkou komplexu jsou tzv. lehké řetězce (DLC, 8-22 kDa), rozeznávající transportované molekuly. Již dříve bylo prokázáno, že cílení Gag k místu skládání je závislé na neporušeném mikrotubulárním systému buňky. Naruší-li se organizace mikrotubulů např. účinkem nocodazolu či snížením teploty na 20 °C, Gag ztrácí perinukleární lokalizaci (Sfakianos et al., 2003). Z naší vyřešené struktury MA proteinu vyplývá, že dříve nalezená doména CTRS (zodpovědná za cílení prekursorů Gag do pericentriónální oblasti) tvoří svou částí ohebnou smyčku mezi helixy II a III a nachází se na povrchu molekuly MA proteinu. Nám se podařilo prokázat dříve navrženou hypotézu, že Tctex-1 (též nazýván DYNLT1), komponenta dyneinového motorového komplexu, je interakčním partnerem MA proteinu. Zjistili jsme to pomocí porovnání lokalizace polyproteinu Gag v buňkách bez a s potlačenou expresí fyziologické hladiny Tctex-1 pomocí siRNA. Současně jsme tím zjistili, že fenotypově zajímavý mutant R55F s Tctex-1 neinteraguje, a to ani *in vivo*, ani *in vitro* v interakčních studiích, využívajících imobilizovaného MA proteinu s GST kotvou. (Příloha 2)

3.3 Myristoylovaný matrixový protein

Většina retrovirových matrixových proteinů je N-terminálně myristoylována. Připojení nasycené C14 mastné kyseliny na N-terminální glycin je poměrně běžná posttranslační modifikace eukaryotických proteinů, odhaduje se, že zhruba 0,5 % všech kódovaných proteinů

může být substrátem pro N-myristoyltransferasu (myristoyl-CoA:glycylpeptid N-myristoyltransferasa, EC 2.3.1.97). Role této modifikace může být ve stabilizaci struktury proteinu kvůli snaze mastné kyseliny zanořit se do hydrofobní kapsy proteiny. Myristoylace je rovněž jedna ze tří acylací, které zprostředkovávají vazbu na membránu (Resh, 1999). Důležitost myristoylace byla prokázána při transportu molekul Gag do místa skládání. Myristát je rovněž spolu s oblastí basických aminokyselin esenciální pro asociaci Gag s plasmatickou membránou (Manrique et al., 2004). Vazba MA na plasmatickou membránu musí být dostatečně silná, ale zároveň reverzibilní, aby mohl být samotný MA zralého viru po infekci uvolněn. Proto existuje MA ve dvou konformacích – se zanořenou a exponovanou kyselinou myristovou. Přechodu mezi těmito stavy se říká myristový přepínač a byla prokázána i pro další myristoylované proteiny. V cytoplasmě je myristát zanořen do hydrofobní kapsy v MA a k jeho expozici dojde, až když se Gag přiblíží k plasmatické membráně. V případě HIV-1 MA bylo prokázáno, že myristový přepínač je spouštěn interakcí s fosfatidylinositol -4,5-bisfosfátem (Saad et al., 2006). Dále se ukázalo, že MA domény Gag proteinů trimerizují právě prostřednictvím exponovaných myristátů. Vzhledem k tomu, že trimery vznikají lokálním koncentrováním molekul Gag v oblastech lipidových mikrodomén plasmatické membrány, je právě trimerizace spouštěcím mechanismem pro myristový přepínač matrixového proteinu (Tang et al., 2004).

Pro studium přepínače jsme se pokusili připravit myristoylovaný matrixový protein M-PMV v dostatečném množství a kvalitě. Za tímto účelem jsme protein produkovali v bakteriích *E. coli*, nesoucích kvasinkovou N-myristoyltransferasu v médiu s přídavkem kyseliny myristové. Současnou produkcí obou těchto proteinů by mělo dojít ke kotranslační modifikaci vznikajícího MA. Princip purifikace MA byl totožný s předchozím experimentem, tj. protein byl produkován ve fúzi s 18 aminokyselinami fosfoproteinu (PP) nacházejícím se v molekule Gag bezprostředně za MA. C-konec tohoto fúzního proteinu byl tvořen hexahistidinovou kotvou pro purifikaci metaloafinitní chromatografií. V případě nemyristoylovaného proteinu byla s úspěchem použita rekombinantně připravená M-PMV proteasa, která uvolnila z purifikovaného imobilizovaného MA-PP-His proteinu čistý matrixový protein. Poněkud překvapivým zjištěním pro nás bylo, že rekombinantní myristoylovaný protein je proteasou štěpen výrazně méně než nemyristoylovaný. Tohoto jevu bylo nakonec využito pro odstranění části MA proteinu, který nebyl myristoylován, po expozici protease a promytí byl z NiNTA agarosy uvolněn vysokou koncentrací imidazolu prakticky čistý myristoylovaný MA. Porovnáním struktur nemyristoylovaných proteinů MA a MA-PP-His se rovněž ukázalo, že extenze na C konci nemá významný vliv na strukturu samotného MA. (Příloha 3)

3.4 Role mikrotubulů v intracelulárním transportu prekursorů

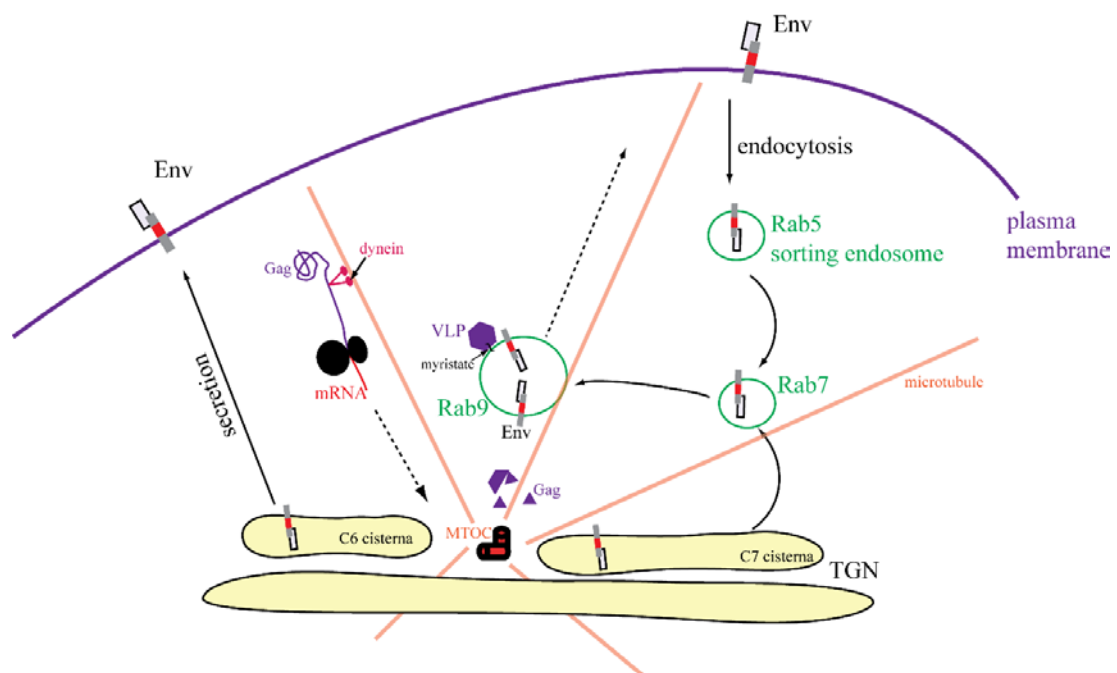
Jak již bylo řečeno, retroviry využívají buněčných mechanismů svého hostitele pro produkci vlastních virionů. Je tedy nevyhnutelné, aby se na produkci a transportu prekursorů virové kapsidy podílelo mnoho buněčných faktorů. Jednou z experimentálních výhod M-PMV např. v porovnání s HIV je to, že skládá částice uvnitř cytoplasmy. Procesy skládání a pučení jsou tak prostorově i časově odděleny, což z M-PMV dělá nenahraditelný model pro studium

těchto procesů. Vzhledem k tomu, že kromě mutace R55F byla nalezena i celá řada dalších, fenotypově zajímavých mutantů matrixového proteinu, začalo být zajímavé nalézt způsob, jak sledovat transport mutovaných forem MA v kontextu celého retroviru a porovnat s chováním nemutovaných forem. Dalším důležitým cílem bylo vyvinutí metodiky sledování kotransportu Gag a Env, neboť o jejich transportu a způsobu inkorporace Env do virové membrány se mnoho neví. Dosud používané metabolické značení proteinu neposkytovalo dostatečně detailní náhled na transport v živé buňce. Začali jsme tudíž pracovat na systému fluorescenčního značení s následnou mikroskopií v reálném čase. Za tímto účelem jsme se pokusili připravit Gag s vloženým zeleným fluorescenčním proteinem (GFP). Obdobné vložení GFP do MA proteinu Gag HIV bylo již publikováno (Muller et al., 2004). Byl tudíž připraven konstrukt pro vložení genu pro eGFP (enhanced green fluorescent protein) místo genů *pro* a *pol*. Současně s tím byl mutagenesí odstraněn interní iniciační kodón (M100A). Bylo nutno použít optimalizaci kodonu pro produkci Gag, což mělo za následek nefunkční sestřih. Tento fakt vedl k chybě v produkci Env, bylo proto nutno použít kotransfekcí s provirovou DNA. Tímto způsobem bylo dosaženo morfologie a efektivity uvolnění částic srovnatelné s M-PMV divokého typu. Následně byla intracelulární lokalizace značeného Gag porovnána s imunofluorescenčně značeným nativním Gag ve fixovaných buňkách a byla shledána ekvivalentní. Po potvrzení použitelnosti nového systému byly značené virové částice vizualizovány v živých buňkách a jak kolokalizace, tak kinetika prokázaly klíčovou roli mikrotubulů v intracelulárním transportu z pericentriální oblasti k plasmatické membráně infikované buňky. Analýzou trajektorií značených virových částic byly nalezeny tři populace – první vykazovala velmi malý laterální pohyb, zřejmě z důvodů ukotvení částic na buněčné struktury. Druhá populace vykazovala typický Brownův pohyb, pravděpodobně se jedná o kapsidy volně se pohybující v cytoplasmě. Třetí populace vykazovala oscilační pohyby relativně dalekého rozsahu s kinetikou konzistentní s pohybem po mikrotubulech. (Příloha 4).

3.5 Inkorporace obalových glykoproteinů do virového obalu

Fluorescenční mikroskopie živých buněk se ukázala jako nesmírně mocný nástroj. Rozhodli jsme se proto zkusit vyřešit otázku, kde se setkají obalové glykoproteiny s prekursory Gag nebo složenými částicemi. Bylo již uvedeno, že částice M-PMV se skládají ze strukturních polyproteinů Gag, GagPro a GagProPol v definovaném poměru. Tyto polyproteiny jsou syntetizovány na volných polysomech v cytoplasmě a následně jsou transportovány po mikrotubulech k mikrotubulárnímu centru pomocí interakce s dyneinem. V této oblasti se nachází rovněž mnoho chaperonů, které procesu skládání napomáhají, bylo např. prokázáno, že interakce s chaperonem TRiC stabilizuje M-PMV Gag a zprostředkovává jeho oligomerizaci (Hong et al., 2001). Bylo rovněž publikováno, že oligomerizace je indukována konformačními změnami Gag, indukovanými specifickými interakcemi s nesestřiženou virovou RNA (Ulbrich et al., 2006). Prekursor Env je translatován na endoplasmatickém retikulu a je následně transportován do lumen ER, kde tvoří trimery a je částečně glykosylován. V Golgiho aparátu je glykosylace dokončena a Env je rovněž rozštěpen na povrchovou jednotku SU a transmembránovou jednotku TM. Je známo, že prostá sekrece z Golgiho aparátu

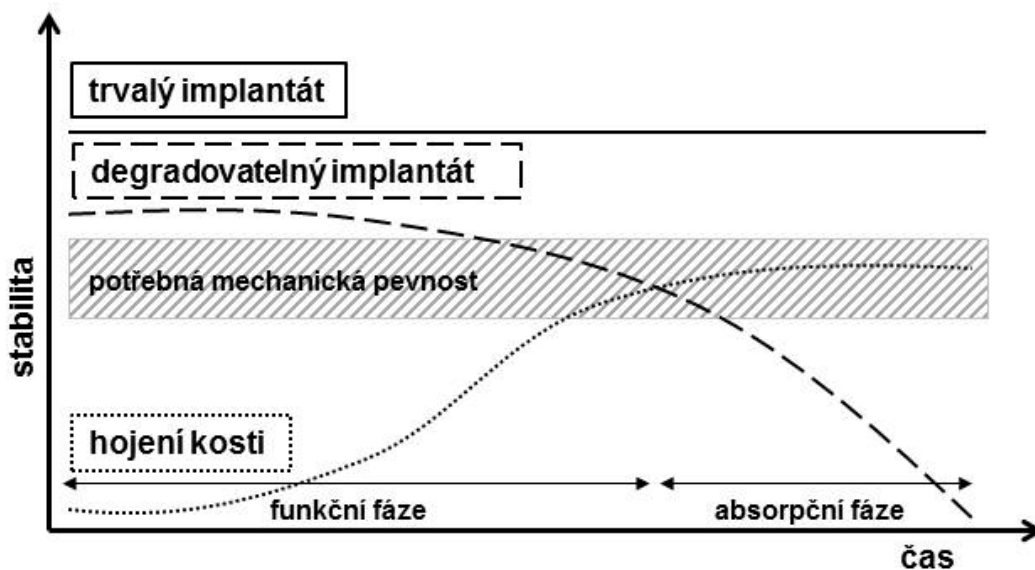
na plasmatickou membránu by nezajistila inkorporaci Env do membrány pučící částice, pro tento účel je třeba, aby byl Env z plasmatické membrány endocytován. Bylo totiž publikováno, že mutace blokující endocytosu Env zabránila jeho inkorporaci do viru (Song et al., 2003). Kam je tedy Env endocytován a kde se setká s nezralou částicí, bylo hlavním předmětem našeho zájmu. Použili jsme vektor s provirovou sekvencí, ve které byla do genu transmembránového proteinu Env vložena kódující sekvence pro červený fluorescenční protein mCherry. Experimenty na živých buňkách prokázaly lokalizaci mCherry v intracelulárních váčcích neznámého původu. Provedli jsme proto kolokalizační studie se sadou endosomálních markerů, založených na RabGTPasách, značených pomocí eGFP. Tímto způsobem se nám podařilo prokázat, že TM je v membráně Rab7a pozitivních endosomů a částečně i v Rab9a pozitivních endosomech. Rab7a se používá často jako marker pozdních endosomů, zatímco Rab9a představuje marker retrográdního transportu z pozdních endosomů do Golgiho aparátu (Barbero et al., 2002; Vanlandingham and Ceresa, 2009). Finálním krokem potom byla fluorescenční mikroskopie živých buněk, ve kterých byl sledován současně pohyb molekul Gag (značených eGFP) a molekul Env (značených mCherry). Získané výsledky nám umožnily navrhnout mechanismus, kterým virus pravděpodobně omezuje riziko imunitní odpovědi hostitele, a to endocytosou molekul Env, dopravených na povrch buňky bez přítomnosti molekul Gag. Je-li tedy molekula Env transportována z Golgiho aparátu na membránu a současně není endocytický signál blokován interakcí s nezralou částicí, je Env endocytován a endosomální drahou, zahrnující Rab5a, Rab7a a Rab9a pozitivní endosomy se vrací zpět do Golgiho aparátu, odkud může cyklovat opět do pozdních endosomů. Je-li poblíž mikrotubulárního organizačního centra přítomna složená nezralá částice, dojde k interakci s molekulami Env, navázanými na Rab9a pozitivní endosomy, což následně vede k kotransportu částice a obalových glykoproteinů k plasmatické membráně (Obr. 9) (Příloha 5)



Obr. 9 Model intracelulárního transportu a inkorporace Env

4. Přehled řešené problematiky II – testování degradovatelných biomateriálů

Jednou z významných spoluprací, kterou jsme navázali především s Ústavem kovových materiálu a korozního inženýrství a kterou nemohu opomenout, je práce na testování nových slitin pro využití v ortopedii. Některé ortopedické aplikace vyžadují dočasnou fixaci např. komplikovaných zlomenin, s čímž je spojena nutnost pozdější reoperace (vyjmutí fixátoru), která představuje další zátěž pro pacienta a riziko pooperačních komplikací. Proto existuje snaha vyvíjet takové materiály, které jsou v těle odbouratelné. Během hojení by se měl fixátor postupně vstřebávat/rozpouštět, ve výsledku by měl být plně nahrazen zhojenou kostí. Degradovatelné biomateriály pro tyto účely musí splňovat celou řadu kritérií – musí mít dostatečnou pevnost i modul pružnosti, jejich korozní rychlost musí odpovídat rychlosti vzniku nové kostní tkáně, degradační produkty nesmějí být pro tělo toxické a musí se z těla vyloučit (Obr. 10). Prvním krokem v testování biomateriálů je testování *in vitro* (lépe řečeno *ex vivo*, neboť se jedná o test na živých buňkách tkáňových kultur). Stanoví se nejprve korozní rychlost a poté se určuje cytotoxicita. Tento postup je finančně výhodný, neboť umožní případné vyřazení nevhodných slitin ještě před drahým a eticky komplikovaným testováním na zvířatech, které je ovšem zdravotnickou legislativou vyžadováno před povolením pro humánní medicínu.



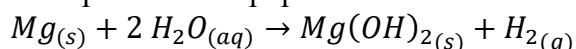
Obr. 10 Požadavky na stabilitu implantátu v závislosti na čase v souvislosti s dobou hojení kosti.

V současné době jsou komerčně dostupné zejména materiály polymerní (kyselina polymléčná) a kompozitní (polymery s přidavkem hydroxyapatitu), jejich mechanické vlastnosti však limitují možnosti aplikace. Existují proto snahy vyvinout degradovatelné biomateriály kovové, přičemž nadějnými kandidáty jsou zejména slitiny hořčíku, případně zinku a železa.

4.1 Hořčík a jeho slitiny

Hořčík je biogenní prvek s hojným výskytem v lidském těle, přebytek hořečnatých iontů je navíc snadno vyloučen močí. Historicky je jako biomateriál znám již dlouho, velkým problémem však je vznik podkožních kapes vodíku, vylučovaného příliš rychlou korozi. Samotný hořčík je málo pevný, používá se proto ve formě slitin s dalšími legujícími prvky. Slitiny hořčíku mají významně větší pevnost v tahu a vyšší lomovou houževnatost než degradabilní polymery. V porovnání s používanými kovovými materiály (ocel, titan) pro změnu vykazují významně lepší modul pružnosti, blíží se kostní tkáni. Použitím hořčíkových slitin se tudíž zmenšuje jev zvaný stress shielding, tedy převzetí zátěže implantátem, resultující v zeslabení okolní kostní tkáně.

Degradaci hořčíku ve vodném prostředí lze popsat rovnicí



Snaha je vyvinout slitiny se zpomalenou korozi, aby se vznikající vodík stihl difúzí dostat z místa implantátu a nebránil procesu hojení. Druhou komplikací je lokální nárůst pH v okolí hořčíkového implantátu.

V současnosti jsou studovány zejména slitiny, původně vyvinuté pro průmyslové aplikace, jako je např. AZ31 (96 % hořčík, 3 % hliník, 1 % zinek) nebo WE43 (93 % hořčík, 4 % yttrium, 3 % směs kovů vzácných zemin). Paralelně se vyvíjejí slitiny primárně určené pro biomedicínské použití, ve kterých je omezeno použití potenciálně nebezpečných prvků (hliník). Kromě vhodného složení slitiny lze korozní rychlost ovlivnit také dodatečným tepelným nebo mechanickým zpracováním (např. extruzí) či povrchovou úpravou slitin.

4.2 Zinek a jeho slitiny

Zinek je dalším slibným prvkem, korozní rychlost slitin zinku je totiž v porovnání s hořčíkem nižší. Při korozi zinku rovněž nevzniká plynný vodík ani nedochází k nárůstu pH. I zinek je biogenní prvek, jeho tolerovaný denní příjem je však významně nižší než u hořčíku. Samotný zinek je příliš křehký, v úvahu tudíž připadá pouze jeho použití ve formě slitin, nejčastěji s přidavkem vápníku a stroncia.

4.3 Železo a jeho slitiny

Železo je rovněž biogenní prvek, použitelný pro přípravu degradovatelných slitin. Jeho korozní rychlost je v tělním prostředí příliš pomalá a je tudíž potřeba jeho korozi urychlit. Je potřeba se rovněž vypořádat s feromagnetickými vlastnostmi železa, které by mohly interferovat s diagnostickými metodami (např. magnetická resonance). Metabolismus železa je složitější a přebytek nemůže být snadno vylučován močí, jako je tomu v případě hořčíku a zinku, hrozí jeho ukládání v orgánech a jejich poškození.

4.4 Normy pro preklinické testování implantátů

Implantáty jsou z legislativního pohledu zdravotnickými prostředky a před uvedením na trh musí být schváleny. V porovnání s léčivými je však jejich vývoj rychlejší a výrazně levnější. Při hodnocení rizik použití a schvalování je postupováno dle norem, což jsou však pouze soubory doporučení. Nejpoužívanější je řada norem ISO 10993 (Biologické hodnocení zdravotnických prostředků), flexibilita v jejich použití a možnosti úprav však způsobují neporovnatelnost výsledků získaných v různých laboratořích.

Normy řady 10933 doporučují nejprve provést odhad rizika, uvažuje se potenciální uvolnění škodlivých látek a provádí se porovnání s již schváleným materiálem podobného typu. Poté následují testy cytotoxicity, genotoxicity, mutagenicity a další.

4.5 Metody testování

Před zahájením biologických testů je nejprve určena korozní rychlost. Její znalost je nutná pro posouzení odhadu rizik. Technik určování je mnoho, ať již měření váhového úbytku, měření koncentrace iontů uvolněných do roztoku nebo elektrochemickou impedanční spektroskopií. U hořčíku lze rovněž použít metodu jímání plynného vodíku. Korozní rychlost se nejčastěji vyjadřuje v jednotkách $\text{mg}/\text{cm}^2/\text{den}$ nebo mm/rok . Je závislá na složení zvoleného média (obsah proteinů, použitý pufr), jeho pH, atmosféře, teplotě a na čase (nejedná se o lineární děj). I to je spolu s volně nastavenými parametry norem důvodem, proč nelze porovnávat korozní rychlosti mezi jednotlivými studiemi.

První biologickou zkouškou je test cytotoxicity *in vitro* (ISO 10993-5), což je test obecné toxicity při krátkodobé expozici bez snahy odhalení jejího mechanismu. Pokud v testu uspějí. Lze takové materiály považovat za cytocompatibilní. Norma opět umožňuje několik typů uspořádání, a to zkoušku extraktů, zkoušku přímým kontaktem nebo nepřímým kontaktem (difuzí). Vyhodnocení je pak kvalitativní nebo kvantitativní, hodnotí se ukazatele jako je morfologie, viabilita nebo proliferace. Doporučeny jsou buněčné linie, konkrétně myší fibroblasty L929, neboť jsou nenáročné na kultivaci a jsou zástupcem buněk, které přichází s prostředkem do styku. Nejčastěji se používá kvantitativní test na metabolickou aktivitu s použitím výluhů testovaných materiálů, a to přídatkem tetrazoliové soli (MTT, XTT, WST), která je v přítomnosti metabolicky aktivních buněk redukována na barevný formazan. Absorbance výsledného roztoku je porovnána s neovlivněnou kontrolou a je přímo úměrná metabolické aktivitě. Alternativou může být např. pozorování buněk po interakci s výluhem pomocí světelné mikroskopie v reálném čase. Poté je kvantitativně vyhodnocena rychlost buněčné adheze a doba zdvojení v porovnání s kontrolou. V kontaktním testu jsou buňky aplikovány přímo na povrch materiálu a po zvolené době expozice jsou hodnoceny podobné parametry jako u zkoušek s extrakty. Možnost normativního vyhodnocení zkoušek shrnuje tabulka 1.

Tabulka 1: Testy *in vitro* uvedené v normě ISO 10993-5, jejich vyhodnocení, výhody a nevýhody (Anderson et al., 2004; Houska, 2009; Wolf et al., 2013)

	Zkouška na extraktech	Zkouška přímým kontaktem	Zkouška nepřímým kontaktem
Kvalitativní vyhodnocení	- zhodnocení morfologie	- zóna inhibice	- zóna inhibice
Kvantitativní vyhodnocení	- příjem neutrální červeně - zkouška tvorbou kolonií - MTT (XTT)	- příjem neutrální červeně - MTT (XTT)	X
Výhody	- lze volit podmínky extrakce a média - sledování vztahu dávka-odezva	- není nutná extrakce - lepší napodobení podmínek	- není nutná extrakce - možnost testování pouze jedné strany materiálu
Nevýhody	- nutná extrakce	- riziko traumatizace buněk (zatížení, pohyb materiálu)	- pouze kvalitativní - riziko teplotního šoku (tvorba agarové vrstvy) - závislé na rozpustnosti látek v agaru - nutný rovný povrch materiálu

Mutagenní aktivita se nejčastěji měří pomocí Amesova testu. Používá se kmen bakterie *Salmonella typhimurium* s mutací v genu syntézy histidinu. Je-li pěstována na minimálním médiu bez histidinu, bakterie nepřežívají. Po expozici bakterií sledované látky je sledován růst na médiu bez histidinu. Jedná-li se o mutagenní látku, může nastat zpětná mutace, vedoucí k opravě původně defektního genu, čímž bakterie znovu získá schopnost syntetizovat histidin a přežít. Kmen má charakteristický počet spontánních revertantů, tj. buněk rostoucích na médiu bez ovlivnění mutagenem. Výsledný efekt je kvantifikován porovnáním počtu kolonií rostoucích na minimálním médiu po ovlivnění sledovanou látkou s počtem spontánně revertujících bakterií.

Genotoxicitu lze určit např. pomocí jednobuněčné gelové elektroforézy, známé též pod názvem kometový test. V alkalickém uspořádání se používá zejména pro detekci jednořetězcových zlomů, v neutrálním uspořádání poté pro stanovení zlomů dvouřetězcových. Buňky (lze použít dělicí se i nedělicí se buňky živočišné, rostlinné buňky nejsou vhodné kvůli své buněčné stěně) jsou po expozici extraktům zalaty do agarosy na mikroskopickém sklíčku a lyzovány. Zlomy v DNA jsou poté určeny elektroforézou při alkalickém pH. Komety jsou barveny fluorescenčním barvivem (ethidium bromid, propidium jodid, akridinová oranž a jiné) a mikroskopovány. Čím větší je množství zlomů, tím větší je „ohon“ za hlavou komety (tvořenou nepoškozenou DNA). Vyhodnocení probíhá buď softwarově, nebo vizuálně, rozdělením do kategorií dle míry poškození a stanovením počtu buněk v jednotlivých kategoriích po vyhodnocení statisticky významného souboru obrazů.

4.6 Testování biodegradovatelných slitin

Soubor výše zmíněných metod byl aplikován na řadu vzorků, připravených na Ústavu kovových materiálů a korozního inženýrství VŠCHT Praha či na Ústavy fyziky materiálů Univerzity Karlovy.

V případě slitin hořčíku s tzv. nízkotavitelnými kovy byl testován vliv různých koncentrací (1 - 7 % w/w) cínu, gallia a india na mechanické vlastnosti a byl ověřován vliv korozních produktů na viabilitu buněk. Používali jsme korozní ve fyziologickém roztoku (nejjednodušší typ tzv. simulované tělní tekutiny, SBF z angl. Simulated Body Fluid), buněčnou linií byla U-2 OS, osteosarkomatská linie blízká kostním buňkám těla. Zatímco přídavek cínu je dobře prostudován, výsledky slitin s indiem jsou zatím rozporuplné a gallium nebylo dosud studováno vůbec. Ukázalo se, že přídavek india má relativně malý příspěvek ke zvýšení pevnosti a tvrdosti slitiny, navíc mělo indium (resp. jeho korozní produkty) dramatické cytotoxické vlastnosti. Gallium zvyšovalo pevnost i tvrdost, navíc zvýšilo plasticitu slitiny. V případě legování tímto prvkem se navíc podařilo dosáhnout nejnižší korozní rychlosti (až 10x menší v porovnání s čistým hořčíkem) z testovaných prvků. Korozní produkty slitin Mg-Ga také vykazovaly nejnižší cytotoxicitu v nepřímém kontaktním testu (Příloha 6).

Slitiny železa jsou lepší pro některé typy implantátů, jako jsou kardiovaskulární stenty nebo porézní ortopedické implantáty. Jejich největší nevýhodou je pomalá korozní rychlost a feromagnetické vlastnosti, jak již bylo zmíněno. Antiferomagnetických vlastností lze dosáhnout ve slitinách s niklem nebo manganem, nikl je však silný alergen a potenciální karcinogen. Testovali jsme proto slitinu FeMn30 (w/w). Přídavkem manganu byla zvýšena korozní rychlost (zůstává však pořád dosti nízká a bude ji třeba zvýšit přídavkem dalších prvků) a byly zlepšeny mechanické vlastnosti v porovnání s čistým železem i s běžně používanou nerezovou ocelí 316L. Dlouhodobá korozní byla prováděna buď v simulované tělní tekutině dle Müllera (SBF - simulated body fluid) při 37°C, nebo v DMEM (Dulbeccem modifikované Eaglovo médium) v atmosféře 5% CO₂ při 37°C). Toxicita byla měřena pomocí WST-1 testu s použitím buněk myších fibroblastů L929. Ukázali jsme, že přídavek manganu vedl k lehce zvýšené toxicitě (90% kontroly), která je ale stále v bezpečném limitu a slitina je tak slibným meziproduktem při přípravě biokompatibilních slitin na bázi železa (Příloha 7).

Zinek se často používá jako legující prvek ve slitinách hořčíku, přičemž je možné dosáhnout až 50% obsahu zinku, takové slitiny však jsou obtížně připravitelné. Skupina prof. Vojtěcha na Ústavu kovových materiálů a korozního inženýrství jako první na světě připravila slitiny na bázi zinku s přídavkem hořčíku. Byly testovány slitiny Zn-Mg (0-1.6 % w/w) a systematicky sledovány jejich vlastnosti v porovnání s velmi slibnou, komerčně dostupnou slitinou WE43 (Mg-4Y-3RE-0.4Zr). Kromě mechanických vlastností byla intenzivně studována též korozní v různých simulovaných tělních tekutinách a kromě cytotoxicity byla prověřena rovněž mutagenní aktivita a genotoxicita. Výsledky prokázaly zvyšování pevnosti a síly slitiny se zvyšující se koncentrací hořčíku, při vyšších koncentracích Mg však dochází ke ztrátě plasticity. Slitina Zn-0.8 Mg se jeví jako velmi slibná, neboť přesahuje vlastnosti dosud používaných biodegradovatelných materiálů (jako např. kyselina polymléčná), dosahuje velmi

podobných mechanických vlastností jako WE43, má však významně nižší korozní rychlost, což je výhoda s ohledem na plánované použití v přípravě stentů a zejména šroubů a destiček v kostních implantátech (udržení 95 % zátěže po 6 týdnech po implantaci). Přestože zinek vykazuje vyšší cytotoxicitu než hořčík, je slitina stále v normativních mezích a nevykazuje žádnou genotoxicitu ani mutagenní aktivitu, byl proto doporučen její postup do fáze testování na zvířatech (Příloha 8).

Korozní zkoušky kovových biomateriálů jsou prováděny v různých typech simulovaných tělních tekutin. Těchto typů je celá řada, liší se zejména koncentrací chloridů a uhličitanů, stabilitou a schopností udržet pH. To dále komplikuje jak porovnání výsledků mezi laboratořemi, tak predikci chování slitiny v živém systému na základě korozních zkoušek *in vitro*. Výsledkem může být i několikanásobně nižší koroze *in vivo*, protože se na povrchu implantátu vytvoří protektivní korozní vrstvy. Tuto situaci jsme se pokusili simulovat preinkubací v SBF před vlastními korozními testy. Slitina Zn-1.5Mg byla dva týdny inkubována v SBF dle Müllera a následně byla analyzována vzniklá vrstva a měřena korozní rychlost a cytotoxicita uvolněných produktů při vlastní korozi. Zjistili jsme, že během předkoroze se slitina pokryje vrstvou s vysokým obsahem vápníku a fosforu. Fosforečnany mají vyšší odolnost (nižší součinn rozpustnosti) než např. hydroxidy a sloučeniny Ca/P (apatity) jsou také buňkami lépe snášeny v porovnání např. s oxidy. Preinkubace měla i pozitivní vliv ve smyslu nižšího uvolňování zinečnatých iontů, což vedlo k vyšší viabilitě buněk při nepřímém testu (Příloha 9).

Moderní technologie umožňují celou řadu mechanických úprav slitin, vedoucích ke změně jejich vlastností. Jednou z nich je metoda intenzivní plastické deformace (ECAP, z angl. equal-channel angular pressing), spočívající v protlačování odlitku pravoúhlým kanálem. Pomocí této metody lze dosáhnout homogenizace a tzv. ultrajemnozrného stavu. Na hořčíkové slitině LAE442 (Mg-4Li-4Al-2RE) jsme testovali vliv této úpravy na snížení korozní rychlosti v různých SBF (Kirklandovo biokorozní médium a MEM) v porovnání s neošetřenou (tedy pouze litou a extrudovanou) slitinou. Byl rovněž testován vliv přídavku fetálního séra. Úprava pomocí ECAP vedla ve všech případech ke snížení korozní rychlosti vzorků, nejnižší koroze byla zjištěna v KBM s 10% FBS, tedy v médiu s obsahem proteinů a fyziologickou koncentrací chloridů, přičemž metabolická aktivita buněk po inkubaci s extrakty byla ve všech případech srovnatelná s kontrolou (Příloha 10).

5. Závěr

Ve své vědecko-výzkumné činnosti jsem se zabýval zejména dvěma velkými, těžko slučitelnými okruhy. Prvním z nich, který považuji za svou „srdeční záležitost“, je výzkum Mason-Pfizerova opičího viru, kterým se skupina prof. Rumla zabývá již řadu let. V rámci tohoto výzkumu jsme vyřešili strukturu N-terminální domény strukturního polyproteinu Gag – matrixového proteinu, a to v nemyristoylované i myristoylované formě. Na základě těchto dat jsme byli, kombinací biochemických a molekulárně biologických metod ve spojení zejména s fluorescenční mikroskopií, schopni objasnit fenotypové odchylky u mutantních forem M-PMV. Potvrdili jsme zásadní změnu struktury MA po zavedení jednobodové mutace a prokázali účinek této změny na životní cyklus ve smyslu ztráty schopnosti interakce s dyneinovým komplexem. Zavedením fluorescenčního značení Gag a později i Env jsme vytvořili funkční model, který nám umožnil sledovat transport strukturních a obalových proteinů v reálném čase v živých buňkách. Díky tomu jsme následně ověřili hypotézu o místě setkání obalových glykoproteinů s molekulami Gag, resp. složenou nezralou částicí. Využili jsme ho rovněž pro testování dalších mutantů, tentokrát v cytoplasmatické doméně Env, která by měla interagovat s matrixovým proteinem, nacházejícím se těsně pod membránou virové částice.

Druhým okruhem je testování biokompatibility biodegradovatelných materiálů, hlavně kovových slitin na bázi hořčíku, železa a zinku. Zavedli jsme řadu metod, prověřili jsme vhodnost doporučených postupů pro korozní zkoušky jak ve smyslu použitých buněčných linií, tak zejména ve výběru vhodné simulované tělní tekutiny. Našli jsme podmínky vhodné pro testování a pomohli jsme tak našim kolegům materiálovým inženýrům při výběru vhodných legujících prvků. Pro testování hořčíkových slitin jsme rovněž sestavili seznam doporučení pro změnu normy za účelem přiblížení se podmínkám testování *in vivo* a možnosti lepší porovnatelnosti mezi jednotlivými laboratořemi. Metodika byla rovněž využita pro studium vlivu metody přípravy slitiny či úpravy povrchu vyrobené slitiny pro lepší adhezi cílových buněk a jejich přežití.

6. Seznam použité literatury

- Anderson, J.M., Bianco, R.W., Grehan, J., F., Grubbs, B.C., Hanson, S.R., Hauch, K.D., Lahi, M., Mrachek, J.P., Northup, S., J., 2004. Biological Testing of biomaterials, in: Ratner, B.D., Hoffman, A.S., Schoen, F.J., Lemons, J.E. (Eds.), *Biomaterials science: an introduction to materials in medicine*, 2 ed. Elsevier Amsterdam.
- Barabas, O., Rumlova, M., Erdei, A., Pongracz, V., Pichova, I., Vertessy, B.G., 2003. dUTPase and nucleocapsid polypeptides of the Mason-Pfizer monkey virus form a fusion protein in the virion with homotrimeric organization and low catalytic efficiency. *J Biol Chem* 278, 38803-38812.
- Barbero, P., Bittova, L., Pfeffer, S.R., 2002. Visualization of Rab9-mediated vesicle transport from endosomes to the trans-Golgi in living cells. *J Cell Biol* 156, 511-518.
- Bohl, C.R., Brown, S.M., Weldon, R.A., Jr., 2005. The pp24 phosphoprotein of Mason-Pfizer monkey virus contributes to viral genome packaging. *Retrovirology* 2, 68.
- Bradac, J., Hunter, E., 1984. Polypeptides of Mason-Pfizer monkey virus. I. Synthesis and processing of the gag-gene products. *Virology* 138, 260-275.
- Bradac, J., Hunter, E., 1986. Polypeptides of Mason-Pfizer monkey virus. II. Synthesis and processing of the env gene products. *Virology* 150, 491-502.
- Bukrinsky, M., 2004. A hard way to the nucleus. *Molecular medicine* 10, 1-5.
- Coffin, J.M., Hughes, S.H., Varmus, H.E., 1997. *Retroviruses*. Cold Spring Harbor Laboratory Press, New York, USA.
- Conte, M.R., Klikova, M., Hunter, E., Ruml, T., Matthews, S., 1997. The three-dimensional solution structure of the matrix protein from the type D retrovirus, the Mason-Pfizer monkey virus, and implications for the morphology of retroviral assembly. *EMBO J.* 16, 5819-5826.
- Ernst, R.K., Bray, M., Rekosh, D., Hammarskjold, M.L., 1997. Secondary structure and mutational analysis of the Mason-Pfizer monkey virus RNA constitutive transport element. *Rna* 3, 210-222.
- Fauquet C.M., Mayo M.A., Maniloff J., Desselberg U., L.A., B., 2005. *Virus Taxonomy: Eight Report of the International Committee on Taxonomy of Viruses*. Elsevier Academic Press, Londok UK.
- Freed, E.O., 2002. Viral Late Domains. *J Virol* 76, 4679-4687.
- Freed, E.O., Martin, M.A., 1995. The role of human immunodeficiency virus type 1 envelope glycoproteins in virus infection. *Journal of Biological Chemistry* 270, 23883-23886.
- Gao, Y., Kaluarachchi, K., Giedroc, D.P., 1998. Solution structure and backbone dynamics of Mason-Pfizer monkey virus (MPMV) nucleocapsid protein. *Protein Sci.* 7, 2265-2280.
- Gottwein, E., Bodem, J., Muller, B., Schmechel, A., Zentgraf, H., Krausslich, H.G., 2003. The Mason-Pfizer Monkey Virus PPPY and PSAP Motifs Both Contribute to Virus Release. *J Virol* 77, 9474-9485.
- Grabski, D.F., Hu, Y., Sharma, M., Rasmussen, S.K., 2019. Close to the Bedside: A Systematic Review of Endogenous Retroviruses and Their Impact in Oncology. *J Surg Res* 240, 145-155.
- Gruter, P., Taberero, C., von Kobbe, C., Schmitt, C., Saavedra, C., Bachi, A., Wilm, M., Felber, B.K., Izaurralde, E., 1998. TAP, the human homolog of Mex67p, mediates CTE-dependent RNA export from the nucleus. *Molecular cell* 1, 649-659.
- Grznárova, P., 2013. Intracellular transport of glycoprotein precursor of the Mason-Pfizer monkey virus.
- Hargittai, M.R., Gorelick, R.J., Rouzina, I., Musier-Forsyth, K., 2004. Mechanistic insights into the kinetics of HIV-1 nucleocapsid protein-facilitated tRNA annealing to the primer binding site. *J Mol Biol* 337, 951-968.
- Hong, S., Choi, G., Park, S., Chung, A.S., Hunter, E., Rhee, S.S., 2001. Type D retrovirus Gag polyprotein interacts with the cytosolic chaperonin TRiC. *J Virol* 75, 2526-2534.

- Houska, M., 2009. Biologické hodnocení zdravotnických prostředků - Část 5: zkoušky na cytotoxicitu in vitro, ČSN EN ISO 10993-5:2009. Úřad pro technickou normalizaci, metrologii a státní zkušebnictví
Praha.
- Choi, G., Park, S., Choi, B., Hong, S., Lee, J., Hunter, E., Rhee, S.S., 1999. Identification of a cytoplasmic targeting/retention signal in a retroviral Gag polyprotein. *J Virol* 73, 5431-5437.
- Knejzlik, Z., Strohalm, M., Sedlackova, L., Kodicek, M., Sakalian, M., Ruml, T., 2004. Isolation and characterization of the Mason-Pfizer monkey virus p12 protein. *Virology* 324, 204-212.
- Kohoutova, Z., Rumlova, M., Andreansky, M., Sakalian, M., Hunter, E., Pichova, I., Ruml, T., 2009. The impact of altered polyprotein ratios on the assembly and infectivity of Mason-Pfizer monkey virus. *Virology* 384, 59-68.
- Lukic, Z., Hausmann, S., Sebastian, S., Rucci, J., Sastri, J., Robia, S.L., Luban, J., Campbell, E.M., 2011. TRIM5alpha associates with proteasomal subunits in cells while in complex with HIV-1 virions. *Retrovirology* 8, 93.
- Manrique, M.L., Gonzalez, S.A., Affranchino, J.L., 2004. Functional relationship between the matrix proteins of feline and simian immunodeficiency viruses. *Virology* 329, 157-167.
- Marcello, A., 2004. Nuclear organization and the control of HIV-1 transcription. *Gene* 326, 1-11.
- Muller, B., Daecke, J., Fackler, O.T., Dittmar, M.T., Zentgraf, H., Krausslich, H.G., 2004. Construction and characterization of a fluorescently labeled infectious human immunodeficiency virus type 1 derivative. *Journal of virology* 78, 10803-10813.
- Ott, D.E., 2002. Potential roles of cellular proteins in HIV-1. *Rev Med Virol* 12, 359-374.
- Rasko, J.E., Battini, J.L., Gottschalk, R.J., Mazo, I., Miller, A.D., 1999. The RD114/simian type D retrovirus receptor is a neutral amino acid transporter. *Proc Natl Acad Sci U S A* 96, 2129-2134.
- Rawat, S.S., Viard, M., Gallo, S.A., Rein, A., Blumenthal, R., Puri, A., 2003. Modulation of entry of enveloped viruses by cholesterol and sphingolipids (Review). *Mol Membr Biol* 20, 243-254.
- Resh, M.D., 1999. Fatty acylation of proteins: new insights into membrane targeting of myristoylated and palmitoylated proteins. *Biochim.Biophys.Acta* 1451, 1-16.
- Rhee, S.S., Hunter, E., 1990. A single amino acid substitution within the matrix protein of a type D retrovirus converts its morphogenesis to that of a type C retrovirus. *Cell* 63, 77-86.
- Saad, J.S., Miller, J., Tai, J., Kim, A., Ghanam, R.H., Summers, M.F., 2006. Structural basis for targeting HIV-1 Gag proteins to the plasma membrane for virus assembly. *Proc Natl Acad Sci U S A* 103, 11364-11369.
- Sakalian, M., Hunter, E., 1999. Separate assembly and transport domains within the Gag precursor of Mason-Pfizer monkey virus. *J Virol* 73, 8073-8082.
- Sfakianos, J.N., LaCasse, R.A., Hunter, E., 2003. The M-PMV cytoplasmic targeting-retention signal directs nascent Gag polypeptides to a pericentriolar region of the cell. *Traffic*. 4, 660-670.
- Schmidt, R.D., Mustafa, F., Lew, K.A., Browning, M.T., Rizvi, T.A., 2003. Sequences within both the 5' untranslated region and the gag gene are important for efficient encapsidation of Mason-Pfizer monkey virus RNA. *Virology* 309.
- Schochetman, G., Kortright, K., Schlom, J., 1975. Mason-Pfizer monkey virus: analysis and localization of virion proteins and glycoproteins. *Journal of virology* 16, 1208-1219.
- Skalka, A.M., Katz, R.A., 2005. Retroviral DNA integration and the DNA damage response. *Cell Death Differ* 12 Suppl 1, 971-978.

Sommerfelt, M.A., Petteway, S.R., Jr., Dreyer, G.B., Hunter, E., 1992. Effect of retroviral proteinase inhibitors on Mason-Pfizer monkey virus maturation and transmembrane glycoprotein cleavage. *J Virol* 66, 4220-4227.

Song, C., Dubay, S.R., Hunter, E., 2003. A Tyrosine Motif in the Cytoplasmic Domain of Mason-Pfizer Monkey Virus Is Essential for the Incorporation of Glycoprotein into Virions. *J Virol* 77, 5192-5200.

Sonigo, P., Barker, C., Hunter, E., Wain-Hobson, S., 1986. Nucleotide sequence of Mason-Pfizer monkey virus: an immunosuppressive D-type retrovirus. *Cell* 45, 375-385.

Staple, D.W., Butcher, S.E., 2003. Solution structure of the HIV-1 frameshift inducing stem-loop RNA. *Nucleic acids research* 31, 4326-4331.

Strambio-de-Castillia, C., Hunter, E., 1992. Mutational analysis of the major homology region of Mason-Pfizer monkey virus by use of saturation mutagenesis. *Journal of virology* 66, 7021-7032.

Tang, C., Loeliger, E., Luncsford, P., Kinde, I., Beckett, D., Summers, M.F., 2004. Entropic switch regulates myristate exposure in the HIV-1 matrix protein. *Proc Natl Acad Sci U S A* 101, 517-522.

Ulbrich, P., Haubova, S., Nermut, M.V., Hunter, E., Rumlova, M., Ruml, T., 2006. Distinct roles for nucleic acid in in vitro assembly of purified Mason-Pfizer monkey virus CANC proteins. *J Virol* 80, 7089-7099.

Vanlandingham, P.A., Ceresa, B.P., 2009. Rab7 regulates late endocytic trafficking downstream of multivesicular body biogenesis and cargo sequestration. *J Biol Chem* 284, 12110-12124.

Vile, R.G., Ali, M., Hunter, E., McClure, M.O., 1992. Identification of a generalised packaging sequence for D-type retroviruses and generation of a D-type retroviral vector. *Virology* 189, 786-791.

Wilhelm, M., Wilhelm, F.X., 2001. Reverse transcription of retroviruses and LTR retrotransposons. *Cell Mol Life Sci* 58, 1246-1262.

Wolf, M.F., Coleman, K.P., Lewerenz, G.M., 2013. Chapter II.3.3 - In Vitro Assessment of Cell and Tissue Compatibility A2 - Ratner, Buddy D, in: Hoffman, A.S., Schoen, F.J., Lemons, J.E. (Eds.), *Biomaterials Science (Third Edition)*. Academic Press, pp. 593-608.

Yu, Q., Morrow, C.D., 1999. Complementarity between 3' terminal nucleotides of tRNA and primer binding site is a major determinant for selection of the tRNA primer used for initiation of HIV-1 reverse transcription. *Virology* 254, 160-168.

Zabransky, A., Andreansky, M., Hruskova-Heidingsfeldova, O., Havlicek, V., Hunter, E., Ruml, T., Pichova, I., 1998. Three active forms of aspartic proteinase from Mason-Pfizer monkey virus. *Virology* 245, 250-256.

Příloha 1

Letter to the Editor: Assignment of ^1H , ^{13}C , and ^{15}N resonances of WT matrix protein and its R55F mutant from Mason-Pfizer monkey virus

J. Vlach^{a,*}, J. Lipov^b, V. Veverka^a, M. Rumlová^c, T. Ruml^b & R. Hrabal^a

^a*NMR Laboratory, Institute of Chemical Technology Prague, Technická 5, CZ-166 28, Prague, Czech Republic;* ^b*Department of Biochemistry and Microbiology, Institute of Chemical Technology Prague, Technická 5, CZ-166 28, Prague, Czech Republic;* ^c*Department of Biochemistry, Academy of Sciences of the Czech Republic, Flemingovo náměstí 2, CZ-166 10, Prague, Czech Republic*

Received 24 January 2005; Accepted 9 February 2005

Key words: Mason-Pfizer monkey virus, NMR resonance assignment, matrix protein

Biological context

Matrix protein (MA) is the N-terminal domain of the Gag polyprotein in retroviruses. It plays an important role in the transport of retroviral proteins to the site of assembly of immature viral particles as well as in their association with the cell membrane and in budding (Wills et al., 1991). These so called late phases of the retroviral life cycle have been potential targets for intervention that might lead to the development of a new type of drugs against HIV or other retroviruses. Therefore, a better understanding of the mechanism of immature viral capsid assembly is an inevitable prerequisite for developing an efficient strategy for affecting this phase of the retroviral life cycle.

Mason-Pfizer monkey virus (M-PMV) belongs to the family of betaretroviruses (formerly called D-type retroviruses) which are characterized by a different mechanism of immature capsid assembly compared with a more extensively studied class of lentiviruses (formerly C-type), where HIV-1 is the best known member. While M-PMV forms immature virions within cytoplasm of infected cells and the virions are then transported to the plasma membrane, polyprotein precursors of lentiviruses are directly transported to the cell membrane where the process of assembly takes place (Rhee et al., 1990). It was demonstrated that a replacement of arginine in the position 55 in the sequence

of MA protein of M-PMV for a large hydrophobic amino acid residue, i.e. tryptophane or phenylalanine, results in a dramatically changed morphogenesis of M-PMV (Rhee et al., 1991). In this aspect the virus then behaves similarly as HIV-1, i.e. it assembles the immature virions at the plasma membrane. We have started a comparative structural study of WT MA and R55F mutant with the aim to reveal possible structural changes caused by the single point mutation. We present here the assignment of the backbone as well as side-chain resonances of both proteins.

Methods and experiments

For preparation of the proteins we used a bacterial expression vector pETMAPPHis containing the genes encoding the wild type M-PMV matrix protein or the R55F mutant in fusion with part of phosphoprotein and a histidine tag. The fusion protein was expressed in *E. coli* strain BL 21 (DE3) under the control of bacteriophage T7 promoter. The cells were grown either in a double labeled ($^{13}\text{C}/^{15}\text{N}$) rich growth medium (OD2, Silantes, GmbH, in case of R55F) or in a minimal growth medium (containing $^{13}\text{C}_6\text{-D-glucose}$ and ^{15}N ammonium chloride, Spectra Stable Isotopes, in case of WT) and induced by addition of IPTG. The cells were harvested 4 h after the induction and lysed using lysozyme, sodium deoxycholate and sonication. The fusion protein was purified using Ni-NTA agarose column and matrix protein

*To whom correspondence should be addressed. E-mail: vlachj@vscht.cz

was liberated from the fusion by the specific action of purified recombinant M-PMV protease (Zábranský et al., 1998; Rumlová et al., 2001). Released MA protein was further purified by gel permeation chromatography on Sephacryl 100 column (HR 16/26, Pharmacia), concentrated by ultrafiltration to the final concentration of 1 mM (measured by UV absorption using the recalculated extinction coefficient of $23590 \text{ mM}^{-1} \text{ cm}^{-1}$ at 280 nm for both MA proteins) in NMR buffer (50/100 mM phosphate buffer, 100/200 mM NaCl, 10 mM DTT, 5% D_2O , pH 6).

NMR experiments were performed on a Bruker DRX-500 Avance spectrometer equipped with a triple-resonance probe with three-axes actively shielded gradient coils at 25°C . Backbone and side-chain atom resonances were assigned using the following experiments: 2D ^1H - ^{15}N HSQC and ^1H - ^{13}C HSQC, 3D HNCA, HN(CO)CA, HNCACB, CBCA(CO)NH, HBHA(CBCACO)NH, CC-TOCSY(CO)NH and H(C)CH-COSY. NMR data were processed with the NMRPipe software (Delaglio et al., 1995) and analyzed in Sparky (Goddard T.D. and Kneller D.G., SPARKY 3, University of California, San Francisco).

Extent of assignments and data deposition

Complete assignment of the backbone resonances of both molecules has been obtained for most of the non-proline residues. H_N -N signals were not detected for several residues from the ends of the helical motifs, presumably due to the chemical exchange of H_N protons with water. The carbonyl carbons were not assigned for R55F MA. The resonances of side chain atoms were assigned to the extent of 65 % (WT) and 55 % (R55F), considering all assignable atoms (^1H , ^{13}C , ^{15}N).

A comparison of a part of ^1H - ^{15}N HSQC spectra of WT and R55F MA is shown in Figure 1. ^1H and ^{15}N chemical shifts are nearly identical for most residues. However, the chemical shifts differ substantially for the residues in the vicinity of the mutation point, probably due to large structural changes caused by the replacement of the hydrophilic side-chain of arginine 55 for a more hydrophobic phenylalanine.

The secondary structure of the proteins was predicted based on C_α , C_β , H_α and C' (for R55F without C') chemical shifts using the CSI program (Wishart and Sykes, 1994). The analysis revealed

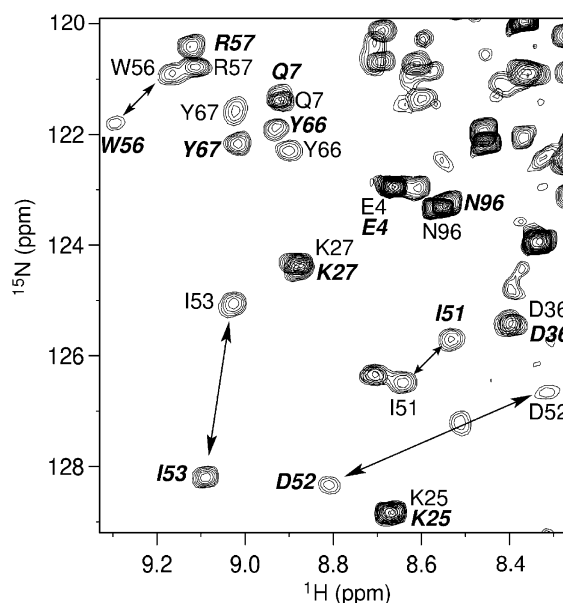


Figure 1. A part of overlaid 2D ^1H - ^{15}N HSQC spectra of WT and R55F MA proteins. The assignments of the WT MA resonances are in regular font, the assignments of the R55F MA resonances in bold oblique. The arrows indicate the largest differences in signal positions between WT and R55F MA.

four α -helical regions in both, WT and R55F MA, which is a typical feature of retroviral matrix proteins (Turner et al., 1999). The assignments of both proteins have been deposited in the BioMagResBank (<http://www.bmrb.wisc.edu>) under accession numbers 6400 (WT) and 6401 (R55F).

Acknowledgements

We thank Helena Bauerová, IOCB, for the generous gift of the purified recombinant M-PMV protease, as well as its inhibitor. The work was financially supported by the Grant Agency of the Czech Republic, Grant 203/00/0490 and by the Ministry of Education of the Czech Republic, Grant 1M6837805002.

References

- Delaglio, F. et al. (1995) *J. Biomol. NMR*, **6**, 277–293.
- Rhee, S.S. and Hunter, E. (1990) *Cell*, **5**, 77–86.
- Rhee, S.S. and Hunter, E. (1991) *EMBO J.*, **10**, 535–546.
- Rumlová, M. et al. (2001) *Prot. Expr. Purif.*, **23**, 75–83.
- Turner, B.G. and Summers, M.F. (1999) *J. Mol. Biol.*, **285**, 1–32.
- Wills, J.W. and Craven, R.C. (1991) *AIDS*, **5**, 639–654.
- Wishart, D.S. and Sykes, B.D. (1994) *J. Biomol. NMR*, **4**, 171–180.
- Zábranský, A. et al. (1998) *Virology*, **245**, 250–256.

Příloha 2

D-retrovirus morphogenetic switch driven by the targeting signal accessibility to Tctex-1 of dynein

Jiří Vlach*[†], Jan Lipov*[‡], Michaela Rumlová*[§], Václav Veverka*[¶], Jan Lang*^{||}, Pavel Srb*^{||}, Zdeněk Knejzlík*[‡], Iva Pichová*[§], Eric Hunter**^{††}, Richard Hrabal*^{††}, and Tomáš Ruml^{†§††}

*Laboratory of NMR Spectroscopy and [‡]Department of Biochemistry and Microbiology and Center of Applied Genomics, Institute of Chemical Technology, Prague, Technická 5, 16628 Prague, Czech Republic; [§]Institute of Organic Chemistry and Biochemistry, Academy of Sciences of the Czech Republic, Flemingovo nám. 2, 16610, Prague, Czech Republic; ^{||}Department of Low Temperature Physics, Faculty of Mathematics and Physics, Charles University, 18000 Prague, Czech Republic; and **Emory Vaccine Center, Yerkes National Primate Research Center, 954 Gatewood Road, Atlanta GA 30329

Edited by Peter K. Vogt, The Scripps Research Institute, La Jolla, CA, and approved May 23, 2008 (received for review February 22, 2008)

Despite extensive data demonstrating that immature retroviral particle assembly can take place either at the plasma membrane or at a distinct location within the cytoplasm, targeting of viral precursor proteins to either assembly site still remains poorly understood. Biochemical data presented here suggest that Tctex-1, a light chain of the molecular motor dynein, is involved in the intracellular targeting of Mason–Pfizer monkey virus (M-PMV) polyproteins to the cytoplasmic assembly site. Comparison of the three-dimensional structures of M-PMV wild-type matrix protein (wt MA) with a single amino acid mutant (R55F), which redirects assembly from a cytoplasmic site to the plasma membrane, revealed different mutual orientations of their C- and N-terminal domains. This conformational change buries a putative intracellular targeting motif located between both domains in the hydrophobic pocket of the MA molecule, thereby preventing the interaction with cellular transport mechanisms.

capsid assembly | dynein motor | matrix protein structure | retrovirus | transport

Gag polyproteins are major structural subunits of immature retroviral capsids and contain the determinants that mediate interactions with viral genomic RNA as well as particle assembly. The molecular mechanisms that control the accumulation of Gag molecules at the sites of assembly vary among retroviruses. Based on the assembly site, retroviruses have been shown to follow two major morphogenic pathways (1). While alpharetroviruses, gammaretroviruses, and lentiviruses (C-type retroviruses) assemble immature capsids at the inner side of the plasma membrane, the capsids of betaretroviruses (B/D-type) are formed in the cytoplasm. It has been shown that Mason–Pfizer monkey virus (M-PMV), which is the prototype of the D-type retroviruses, assembles at the pericentriolar region of an infected cell (2). Numerous studies have demonstrated that the matrix protein (MA), located at the N terminus of the Gag polyprotein, is responsible for targeting the polyprotein precursors to the site of assembly and for mediating transport of immature retroviral particles to the plasma membrane where budding occurs (3). A subtle difference in the regulation of the transport process has been suggested, as the results from several laboratories indicate that the destination of polyprotein precursors can be altered by mutations within MA. Amino acid substitutions in several domains of HIV-1 MA dramatically reduced the efficiency of particle production and redirected the majority of them to cytoplasmic vacuoles (4). Similarly, a substitution of basic for acidic residues in helix A of HIV-1 MA caused relocation of virus assembly to intracellular locations and produced normally budded noninfectious virions (5). Mutation of the N-terminal polybasic region of Moloney murine leukemia virus (Mo-MuLV) MA redirected virus assembly to the cytoplasm, suggesting a role of tryptophan residues in the intracellular transport (6).

The N terminus of MA from most retroviruses, including M-PMV, is myristoylated (7). This modification has several functions essential for the late phases of the viral life cycle. It serves as an anchor for binding Gag to the plasma membrane; provides the necessary conformation for the transport of assembled immature D-type retrovirus particles (8); and together with basic patches on the surface of MA, acts as a bipartite signal for the transport of Gag polyproteins of C-type retroviruses to the plasma membrane for assembly (9). Mutations that inhibit myristoylation or disrupt these basic patches also alter membrane binding and induce aberrant targeting of Gag to the cytoplasm or to intracellular membranes in both C- and D-type retroviruses (10). Molecular evidence for the interaction of HIV-1 Gag with membranes was provided by NMR measurements, which demonstrated that MA protein association promoted exposure of a myristate that was otherwise sequestered in the core of the molecule (10, 11). In M-PMV, the mutation blocking N-terminal Gag myristoylation does not prevent intracytoplasmic assembly; however, it totally blocks the transport of assembled viral capsids to the plasma membrane (8). Despite this evidence linking Gag myristoylation to targeting of preassembled intracytoplasmic immature particles to the site of budding and release, the role of the bipartite signal in targeting M-PMV Gag polyproteins to the assembly site is likely preempted by a dominant signal that mediates intracytoplasmic assembly.

In addition to the typical modification by myristate, MA proteins of retroviruses also share striking structural similarity despite low sequence homology (12–14). All of the MA structures solved to date are predominantly formed of four closely packed α -helices that are interconnected through loops and whose mutual orientations are similar within all structures. In addition to this conserved structural motif, lentiviral MAs (HIV-1, SIV, and EIAV) contain an additional α -helix at their C-termini.

Rather dramatic phenotypic changes induced by various point mutations also suggest that MA molecules are structurally

Author contributions: J. Lang, E.H., R.H., and T.R. designed research; J.V., J. Lipov, M.R., V.V., P.S., Z.K., and R.H. performed research; J.V., J. Lipov, M.R., V.V., J. Lang, P.S., I.P., R.H., and T.R. analyzed data; and J.V., J. Lipov, E.H., R.H., and T.R. wrote the paper.

The authors declare no conflict of interest.

This article is a PNAS Direct Submission.

Data deposition Assignments of NMR chemical shifts and restraints for structure calculation of the wild-type M-PMV MA and its R55F mutant were deposited in the BioMagResBank (www.bmr.b.wisc.edu) (accession nos. 6400 and 6401, respectively). Solution structures of the proteins were deposited in the Protein Data Bank, www.rcsb.org [PDB ID codes 2F76 (wt MA) and 2F77 (R55F mutant)].

[†]J.V. and J. Lipov contributed equally to this work.

[¶]Present address: Department of Biochemistry, University of Leicester, Leicester LE1 7RH, United Kingdom.

^{††}To whom correspondence should be addressed. E-mail: ruml@vscht.cz.

This article contains supporting information online at www.pnas.org/cgi/content/full/0801765105/DCSupplemental.

© 2008 by The National Academy of Sciences of the USA

adapted to mediate several fundamental and characteristic steps of the retroviral life cycle. Perhaps the most dramatic effect on morphogenesis was demonstrated by the replacement of arginine 55 of the M-PMV MA protein with a large hydrophobic amino acid residue (i.e., tryptophan or phenylalanine), which resulted in translocation of virus particle assembly to the plasma membrane (15, 16). In this respect, the virus behaves similarly to HIV-1 and other C-type retroviruses. The arginine 55 of M-PMV resides in the cytoplasmic targeting/retention signal (CTRS) spanning 18 aa residues from Pro-43 to Gly-60. The CTRS is conserved among D-type retroviruses and serves as a dominant translocation signal that directs M-PMV Gag precursors to an intracellular assembly site. More generally, the CTRS from M-PMV Gag is able to redirect the assembly site of C-type Mo-MuLV Gag precursors from the plasma membrane to the cytoplasm (17).

In this paper we demonstrate that a component of the dynein motor machinery, Tctex-1 (also known as DYNLT1), is the interaction partner of wild-type (wt) M-PMV MA and not R55F mutant, suggesting that this interaction is responsible for different phenotypes of M-PMV carrying either the wt MA protein or its R55F mutant. The comparison of their three-dimensional structures demonstrated substantial differences in the positions of the N- and C-terminal domains and rotation of helix III along its longitudinal axis. The driving force of this structural change is the tendency of the molecule to bury the hydrophobic side chain of phenylalanine into the core of the protein, thereby preventing interaction between the CTRS and the dynein motor machinery.

Results

Tctex-1 Is Required for Pericentriolar Targeting of M-PMV Gag. The cytoplasmic targeting of M-PMV Gag is controlled by a cytoplasmic targeting/retention signal within MA domain of Gag polyprotein (17), and point mutations within this sequence convert the type D to type C morphogenesis (15). Sfakianos *et al.* showed that the intracellular destination of wt M-PMV Gag polyproteins is the pericentriolar region of the cytoplasm and indicated the involvement of dynein-dynactin motor in this process (2). Another indication that the dynein motor can be responsible for Gag transport originates from a yeast two-hybrid screening that suggested Tctex-1 (t-complex testis-expressed-1) protein, a light chain of the dynein motor complex, to be a possible interacting partner (S. S. Rhee, personal communication).

To investigate the role of Tctex-1 in the transport of M-PMV Gag to the cytoplasmic assembly site, we compared the intracellular localization of wt Gag in 293T cells expressing physiological levels of Tctex-1 with that in the cells where the production of Tctex-1 was suppressed by specific siRNA. The effect of silencing was confirmed by Western blot analysis of the siRNA-treated cells, in which Tctex-1 levels were significantly reduced compared with the untreated control (Fig. 1A). In the Tctex-1 silenced cells, targeting of Gag to the pericentriolar region was blocked and most of the precursor was found accumulated at the plasma membrane (Fig. 1B Right). This contrasts to the noticeable intracytoplasmic accumulation of Gag in cells with wt levels of Tctex-1, where most of the Gag was either concentrated near the nucleus (Fig. 1B Left) or in the punctate sites beside the concentrated Gag in the vicinity of nucleus (white arrow in Fig. 1B Center). This effect of Tctex-1 depletion indicates the important role for this protein in the pericentriolar targeting of the wt M-PMV Gag.

M-PMV wt MA Protein, in Contrast to the R55F MA Mutant, Interacts with Tctex-1 *in Vitro*. To investigate this interaction and to elucidate the effect of the R55F mutation, we incubated equal aliquots of the same lysate of *E. coli* expressing human Tctex-1 (Fig. 2A and C, lane 1) overnight with GST-Bind resin loaded with identical amounts of purified and immobilized wt or R55F MA proteins C-terminally extended with GST. Although

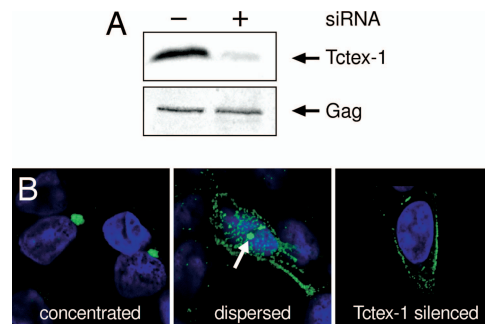


Fig. 1. The effect of Tctex-1 on localization of M-PMV wt Gag. 293T cells cotransfected by pSARM4Gag vector and Silencer siRNA for Tctex-1 (DYNLT1) were analyzed 24 h posttransfection. The cells were treated and stained with FITC conjugated antibody as described in *Materials and Methods*. Nuclei were stained by DAPI. (A) Western blot demonstrating the levels of Tctex-1 [detected by T1 mouse monoclonal antibody (Upper)] and Gag [detected by rabbit anti M-PMV MA antibodies (Lower)] in the control and Tctex-1-depleted cells, respectively. (B) Intracellular localization of M-PMV Gag in the control (Left and Center) and Tctex-1-depleted cells.

comparable amounts of wt and R55F MA were immobilized (Fig. 2A and B, lanes 2 and 3, respectively), Tctex-1 bound efficiently only to wt MA (Fig. 2C, lane 2). In contrast, no detectable amount of Tctex-1 bound to immobilized MA.R55F-GST (Fig. 2C, lane 3). No nonspecific binding of Tctex-1 to the GST-Bind resin was observed in the negative-control resin lacking immobilized MA (Fig. 2A and C, lane 4).

These results demonstrate that Tctex-1 can bind efficiently to M-PMV MA and that a point mutation in the CTRS sequence of this protein abrogates the ability of MA to bind to the Tctex-1 protein.

Replacement of Arginine 55 with Phenylalanine in the Matrix Domain Impairs the Interaction of M-PMV Gag with Tctex-1 in Mammalian Cells.

The intracellular interaction of M-PMV Gag polyprotein with Tctex-1 was investigated further by a coimmunoprecipitation experiment performed with lysates of COS-1 cells cotransfected

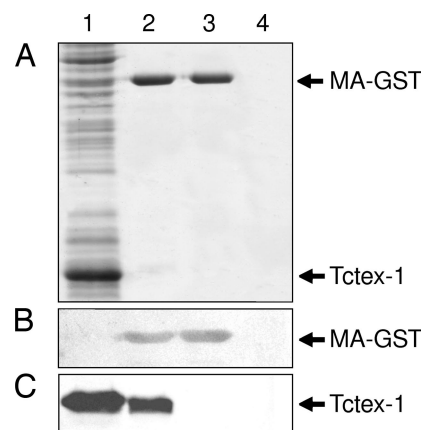


Fig. 2. The *in vitro* interaction of M-PMV wt and R55F MA with Tctex-1. The wt or R55F MA C-terminally extended with GST (MA-GST) were immobilized on GST-Bind resin (Novagen) and allowed to interact with lysates of *E. coli* BL21(DE3) cells expressing human Tctex-1. Proteins were resolved by SDS Tris-Tricine acrylamide gel electrophoresis. (A) Coomassie blue-stained gel. (B) Western blot; MA detected by rabbit anti-M-PMV MA antibody. (C) Western blot; Tctex-1, detected by rabbit anti-Tctex antibody. Lane 1, total lysate of *E. coli* BL21(DE3) after 4 h expression of Tctex-1; lane 2, binding of Tctex-1 to wt MA-GST immobilized on GST-Bind resin; lane 3, binding of Tctex-1 to MA.R55F-GST immobilized on GST-Bind resin; lane 4, Tctex-1 applied on GST-Bind resin (control of possible nonspecific Tctex-1 binding).

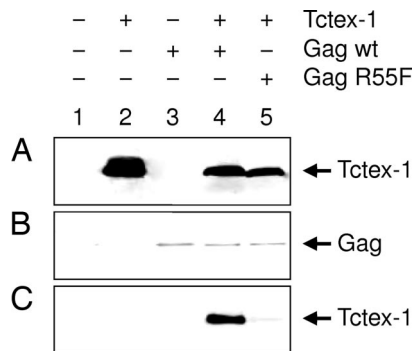


Fig. 3. The interaction of M-PMV wt and R55F Gag with human Tctex-1 in the COS-1 cells. The interaction of Gag with Tctex-1 was determined by coimmunoprecipitation from the lysate of COS-1 cells cotransfected with vectors carrying genes encoding human Tctex-1 tagged with a c-myc epitope (c-mycTctexCMV) and either wt Gag or R55F Gag as shown on top of the figure. Gag and Tctex-1 proteins were resolved by SDS/PAGE or SDS Tris-Tricine acrylamide gel electrophoresis, respectively. Rabbit anti-M-PMV CA and monoclonal anti-c-myc antibodies were used for Western blot detection of intracellular expression of Gag and Tctex-1 proteins, respectively. The complexes were immunoprecipitated with rabbit anti-CA antibody. Monoclonal anti-c-myc antibody was used for Western blot identification of immunoprecipitated Tctex-1. (A and B) Analysis of intracellular proteins. (C) Analysis of immunoprecipitated material.

with expression plasmids for production of human Tctex-1 tagged with the c-myc epitope and M-PMV wt or R55F Gag polyproteins. The molecular complexes were immunoprecipitated from the cell lysates by polyclonal antibody against capsid protein (a major immunogenic domain of Gag), and Tctex-1 interacting with the MA domain of Gag polyprotein was analyzed by Western blot using monoclonal anti-c-myc antibody. This experiment confirmed a strong interaction of Tctex-1 with the wt Gag (Fig. 3C, lane 4) compared to background levels of binding by the R55F mutant (Fig. 3C, lane 5). No detectable cross-reactivity of the antibodies was observed in the negative control (i.e., lysate from nontransfected cells; Fig. 3, lanes 1). Concentrations of the interacting partners in the samples subjected to immunoprecipitation were comparable, as indicated by Western blot analyses of Tctex-1 (Fig. 3A) and Gag proteins (Fig. 3B) of nonimmunoprecipitated samples.

The experiments described above demonstrate that the wt MA as an N-terminal domain of Gag interacts with Tctex-1, whereas the R55F MA mutant does not. The results suggest that either the amino acid motif *per se* or some structural change induced by the mutation alters the morphogenesis pathway due to the abrogation of the interaction between MA (or consequently Gag) and the dynein cargo recognition component Tctex-1.

Comparison of Structural Motifs of wt MA Protein and the R55F Mutant Reveals a Different Accessibility of the CTRS Sequence. We solved and compared the solution structures of wt and R55F MA to provide structural evidence for a CTRS-Tctex-1 interaction and to elucidate the mechanism of phenotype switching. Because the structure of the M-PMV MA previously published by Conte in 1997 (12) was deposited in the protein databank merely as a C α -trace (PDB accession code 1BAX), and no information regarding side chains was available, we solved an *ab initio* NMR structure of wt MA with a focus on a precise determination of the mutual positions of the helices, the structure of the CTRS region, and the definition of important side chains.

The secondary structure elements of both MA proteins follow the canonical structural motif described previously for matrix proteins of other retroviruses (10, 13, 14). The matrix proteins are composed of four α -helices whose positions were assessed

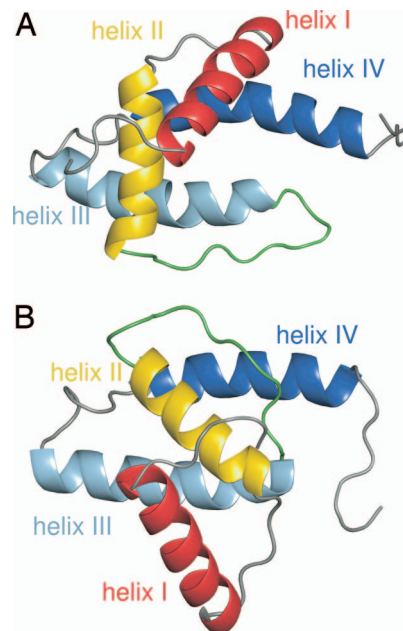


Fig. 4. Calculated structures of wt and R55F MA. Representative structures of wt MA (A) and R55F MA (B) are colored in red (helix I), yellow (helix II), light blue (helix III), and dark blue (helix IV), and the flexible loop between helices II and III is in green (residues 42–51). Structures are displayed with identical orientation of the C-terminal domain (helices III and IV). Images were created in Pymol (<http://www.pymol.org>).

from the calculated chemical shift index (18) and confirmed by complete calculation of structures [supporting information (SI) Table S1]. Helix I, spanning residues Gln-7–Thr-21, is joined to helix II through an extended loop formed by residues Arg-22–Lys-27 (Fig. 4). Helix II (residues Tyr-28–Asp-40) is terminated by a semistructured loop (Thr-41–Phe-45). Our results did not confirm the well defined 3_{10} helix in this region of the wt MA reported previously by Conte (12). The linker between helices II and III continues by a rather flexible hairpin (Phe-45–Asp-52). Numerous hydrophobic contacts have been found between helices III (residues Ile-53–Phe-70) and IV (residues Thr-78–Asp-91), which are connected by another semistructured loop formed by residues Gly-71–Val-77. Importantly, we found significant differences between the global folds of wt MA and the R55F mutant. The major difference relates to the mutual positions of their N- and C-terminal domains formed by helices I and II and helices III and IV, respectively. The reorientation of both domains can be expressed as a change of the angle between the longitudinal axes of helices II and III, which is 98° in the wt MA but increases to 322° in the R55F MA mutant. On the other hand, neither the angles between helices I and II nor those between helices III and IV differ substantially in the two molecules (124° vs 120° and 172° vs 175° , respectively). Another important structural difference between the molecules is a rotation of helix III of the R55F mutant along its longitudinal axis by $\approx 100^\circ$ compared to the helix III of the wt MA (see Fig. S1). These unexpected and relatively large changes in the global folds of both molecules are documented by comparison of ^1H and ^{15}N chemical shifts (Fig. S2) and confirmed by measurements of ^1H – ^{15}N residual dipolar couplings (RDCs) and validation of the calculated structures against them (Fig. S3).

The determinant of these structural changes is the replacement of the hydrophilic side chain of Arg-55 by a bulky and highly hydrophobic phenylalanine. The side chain of Arg-55 in the wt MA protrudes out from the protein globule while the aromatic side chain of Phe-55 in the mutant is buried in the core of the

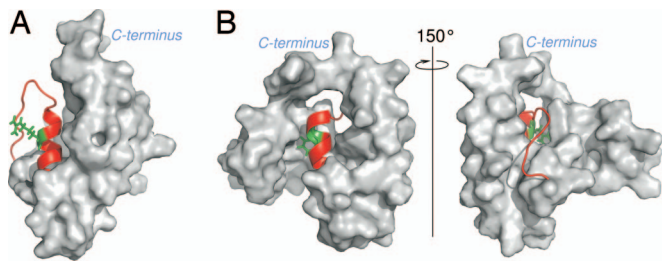


Fig. 5. Different accessibility of CTRS sequence in wt MA (A) and R55F MA (B). CTRS sequence (residues 43–60) is shown as a red ribbon and the rest of the proteins as a gray van der Waals surface; residues 55 (Arg in wt MA and Phe in R55F MA) are represented as green side-chain structures. C-terminal domains (helices III and IV) are oriented identically in both molecules.

protein as shown in Fig. 5. This is presumably driven by a need to prevent exposure of the hydrophobic side chain of Phe-55 to the solvent. This lowering of the free energy of the molecule through the hydrophobic effect results not only in the rotation of helix III but also in the reorientation of the whole C-terminal domain relative to the N-terminal domain. A result of these conformational changes is that the R55F MA CTRS is rendered inaccessible for its proposed interaction with its cellular partner.

The sets of superimposed structures of both molecules showed a large scatter in the region between residues Cys-42 and Ile-51, which is the linker between helices II and III (Fig. S4). This is also documented by comparison of positional pairwise RMSD values for the backbone heavy atoms between the well ordered parts (helices I, II, III, and IV), which were 0.69 Å for the wt or 0.85 Å for R55F, and values for the linker, which dropped to 2.38 Å or 1.36 Å, respectively. The results of a study of backbone dynamics by measurement of relaxation behavior of ^{15}N nuclei confirmed that this loop (residues 42–51) together with both termini represent the most flexible parts in the structures of both proteins. However, the flexibility of this region expressed as the order parameters S^2 of the individual peptide H-N bonds (order parameter equals 1 for absolutely rigid bond and 0 for totally flexible one, data shown in Fig. S5) is different for wt and R55F MA, especially in the Gln-47-Arg/Phe-55 region. Although the whole region (Phe-44 – Arg-55) is rather flexible in the wt structural motif (average $S^2 \approx 0.60$), the amino acid residues following Thr-50 in the R55F mutant are significantly more rigid ($S^2 \approx 0.85$). This finding supports the structural data demonstrating that residues Gln-47–Phe-55 of the CTRS sequence are buried into the core of the R55F molecule, which would limit their flexibility (Fig. 5).

Discussion

In this article we define an interaction partner of the M-PMV matrix protein that is likely responsible for intracellular trafficking of Gag polyproteins to the pericentriolar site of assembly. We also provide structural data for a functional link between the surface exposure of the CTRS and its role as a dominant targeting motif via interaction with dynein molecular motors. This provides a structural mechanism for the phenotypic switch between intracellular assembly of wt M-PMV Gag and membrane assembly for the R55F mutant.

Numerous mutagenesis studies have demonstrated the key role of the MA domain in the intracellular targeting and transport of the Gag polyproteins of various retroviruses. Despite the remarkable similarity of the retroviral MA structures solved to date, the destinations to which Gag molecules are targeted vary. The biochemical data presented here demonstrate that the wt M-PMV MA interacts with Tctex-1, a light chain of the multisubunit dynein molecular motor, which was shown to be responsible for recruiting cargos for retrograde protein transport (19). This finding supports the concept that the CTRS is recognized

by the dynein motor machinery for retrograde transport of Gag-synthesizing polysomes, as initially suggested by Sfakianos and Hunter (20). They reported that pericentriolar accumulation of Gag is dependent on intact microtubule-mediated transport and showed that both microtubule disruption by nocodazole, as well as over-expression of the dynein motor component dynamitin, blocked the pericentriolar accumulation of Gag. This finding is also consistent with the fact that Tctex-1 was a prominent M-PMV MA interacting partner in the yeast two-hybrid screening of a HeLa cDNA library (S. S. Rhee, personal communication).

We have verified that the ability of Gag to interact with Tctex-1 in the cell lysate depended on the presence of the basic arginine at position 55 in the matrix domain of M-PMV Gag and that the R55F mutation abrogated this interaction. The pull-down experiment demonstrated the interaction of purified wt MA-GST fusion protein with Tctex-1, and this interaction was confirmed in the context of the intact Gag polyprotein by coimmunoprecipitation experiments. The role of Tctex-1 in targeting of M-PMV Gag to the cytoplasmic assembly site was confirmed by a silencing experiment in which Tctex-1 was depleted by specific siRNA in the 293T cells. Targeting to the pericentriolar regions was efficiently blocked in the silenced cells and Gag was redirected to the plasma membrane (Fig. 1B Right). In contrast, we observed concentrated Gag localized near the nucleus and in some cases punctate staining in cells expressing normal levels of Tctex-1 (Fig. 1B Middle), reminiscent of data previously described by Sfakianos and Hunter for M-PMV wt Gag (2).

We also attempted to further characterize the MA–Tctex-1 interaction by mapping chemical shift changes of MA induced on Tctex-1 binding. However, the titration of isolated ^{15}N -labeled wt MA with isolated recombinant Tctex-1 did not yield expected shifts within the MA spectrum. Moreover, in contrast to the Tctex-1-containing cell lysate, the isolated Tctex-1 did not interact in the pull-down experiment (data not shown), suggesting that a conformational change of the Tctex-1 protein occurred during purification or that an additional cellular factor or posttranslational modification of MA might be involved in the interaction.

The solution structure of M-PMV wt MA shows that the CTRS consists of two structurally diverse moieties. The N-terminal region spanning residues Pro-43–Ile-51 forms a flexible linker between helices II and III, and due to its location at the periphery of the molecule, it is well tailored for the proposed interaction with a Tctex-1 dimer. The C-terminal half of the CTRS (residues Asp-52–Gly-60) is located at the beginning of helix III and contains an amino acid sequence Lys-54–Arg-55–Trp-56–Arg-57–Arg-58, corresponding to the motif K/R–K/R–X–X–K/R, which has been found within various proteins as a consensus motif for the interaction with Tctex-1 (21, 22).

A comparison of the structures of the wt MA and its R55F mutant shows a substantial difference in the accessibility of their respective CTRS sequences. Whereas the whole CTRS is fully displayed on the surface of the wt MA (thereby facilitating access to the dynein complex), the CTRS sequence of the R55F mutant is partially buried within the interior of the protein. Thus, in the mutant, the entire CTRS C terminus (residues Thr-50–Gly-60) would not be accessible for the interaction with Tctex-1 (Fig. 5B). Consequently, attachment to the dynein motor and transport of nascent R55F Gag proteins to their proper pericentriolar destination would be blocked. We suggest that it is the large reorientation of the whole MA domain and the limited access of the CTRS sequence that is responsible for the altered transport of Gag with the R55F mutation, rather than just the abrogation of the putative KR(55)WRR binding signal within the CTRS. This conclusion is supported by the finding that R55A mutation in M-PMV MA results in a mixture of both D- and C-type morphogenesis, in contrast to the predominantly C-type morphogenesis of the R55W or R55F mutants (C. Song and E. Hunter, unpublished results). Nevertheless, it remains possible that these

large conformational changes also interfere with the binding of other cellular components that are necessary for correct intracellular targeting of M-PMV Gag. However, the data described here and the fact that CTRS contains the Tctex-1 interaction motif (21, 22) strongly argue that it is the sequestration of the CTRS imposed by the R55F mutation that prevents the targeting of Gag, rather than other consequences of structural changes.

In summary, wt M-PMV MA, in contrast to the R55F MA, appears to interact with the dynein motor machinery through its Tctex-1 light chain. These results are consistent with the concept that the lack of interaction of the CTRS with this dynein component is responsible for the altered morphogenesis of M-PMV with a MA R55F mutation.

Comparison of the structures of wt MA and its R55F mutant demonstrated that this mutation caused not only local structural changes around the amino acid residue 55 but also global changes in protein structure, as evidenced by the reorientation of the mutual positions of the N- and C-terminal domains of the molecule and rotation of helix III by 100° along its longitudinal axis. Consequently, nascent Gag molecules bearing R55F mutation are not transported to the pericentriolar region of the cell, and an alternative transport mechanism results in the assembly of immature viral particles at the plasma membrane.

Materials and Methods

Construction of Expression Plasmids. The human Tctex-1 gene was obtained by reverse transcription of total RNA from HeLa cells and cloned into pET22b (Novagen) and pCMV-c-myc (Clontech). M-PMV gag wt and gag R55F were subcloned into pCMV (Clontech), and pSARM4 Gag was prepared by a deletion of *pro-pol-env* from the proviral vector (23). The constructs encoding GST fused to the C terminus of the MA wt and R55F were prepared in pET41a (Novagen). Bacterial plasmids for expression of pETMAPPHis and pETMAR55FPPHis, used for NMR studies, were prepared as described previously (18).

GST Pull-Down. Human Tctex-1-pET22b was expressed in *Escherichia coli* BL21 cells. The cleared lysate of the cells, lysed 4 h postinduction by lysozyme in the presence of SDS, was used for binding studies.

M-PMV MA.wt-GST and MA.R55F-GST were expressed in *E. coli* BL21 as described above. The proteins were extracted into wash/bind buffer (Novagen) and applied on GST-Bind resin. The resin was washed with three bed volumes of wash/bind buffer and then with three bed volumes of binding buffer B (25 mM Hepes, pH 7.5; 25 mM NaCl; 1% Triton X-100; 2.5 mM CaCl₂; 1 mM MgCl₂). The resin with immobilized MA wt or MA R55F protein was then incubated overnight at 4°C with the cleared lysate of *E. coli* expressing Tctex-1. The resin was then thoroughly washed with binding buffer B, resuspended in 2xSDS sample buffer, and boiled for 5 min. The bound proteins were resolved by Tris-Tricine electrophoresis and stained by Coomassie blue G-250 or blotted and detected immunochemically, by rabbit anti-M-PMV MA (RbxMPPMV MA) or rabbit anti-human Tctex-1 (RbxTctex, kindly provided by S. King).

Coimmunoprecipitation. COS-1 cells were cotransfected with c-mycTctex.pCMV and wtGag.pCMV or R55FGag.pCMV by using FuGENE 6 Reagent (Roche Applied Science). Two days post transfection, the cells were washed once with PBS and lysed in Co-IP buffer [20 mM Tris-HCl, pH 7.5; 150 mM NaCl; 1 mM EDTA; 1 mM DTT; 0.1 mM MgCl₂; 0.5% Nonidet P-40; protease inhibitor mix (Sigma)] for 15 min on ice. The cell lysate was cleared by centrifugation. One fifth of the cleared lysate for each sample was mixed with 2xSDS sample buffer and used for Western blot, with monoclonal anti-c-myc and rabbit anti-M-PMV CA antibodies. The rest of the samples of the cleared cell lysates were incubated with rabbit anti-M-PMV CA antibody overnight at 4°C, and the bound complex was precipitated by protein A for 2 h at 4°C. The pellets were washed three times with Co-IP buffer and then

once with PBS. Proteins were resolved by SDS/PAGE and electroblotted, and bound c-myc-tagged Tctex was detected using anti-c-myc antibody. Western blots were developed by using SuperSignalWest Femto (Pierce).

Tctex-1 Silencing and Immunofluorescence Microscopy. 293T cells grown on coverslips were co-transfected by pSARM4Gag vector and predesigned Silencer siRNA (#s13947, Ambion) for Tctex-1 (DYNLT1). The silencing effect was determined 24 h post transfection by SDS/PAGE and immunoblotting with T1 mouse monoclonal antibody (gift of Dr. Kevin Pfister) (24). For immunofluorescence, the cells were washed twice by preheated PBS and then fixed for 2 min with -20°C acetone. Cells were re-hydrated in PBS containing 0.1% TX-100, blocked (2% BSA in PBS) and incubated with rabbit anti-MA polyclonal antibody (prepared in our laboratory 1:100) for 1 h. Cells were washed by PBS containing 0.1% TX-100 and incubated with FITC-conjugated anti-rabbit antibody (1:300, Sigma-Aldrich) for 1 h. Nuclei were stained by DAPI.

NMR Spectroscopy. NMR data were acquired on a Bruker Avance DRX 500 spectrometer (500.13 MHz for ¹H) at 25°C, processed using NMRPipe software (25) and analyzed in Sparky. Distance restraints for structure calculations were obtained from edited (¹³C/¹⁵N) 3D NOESY spectra. ¹H chemical shifts were referenced directly to the internal standard (DSS) and ¹³C and ¹⁵N chemical shifts were referenced indirectly using ratios of NMR frequencies. ¹⁵N relaxation data (longitudinal relaxation time *T*₁, transverse relaxation time *T*₂ and heteronuclear {¹H}-¹⁵N NOE) were measured on uniformly ¹⁵N labeled samples of both proteins using a conventional set of experiments. Dynamic parameters of the backbone were derived from the experiments using the Lipari-Szabo motional model (26).

Structure Calculation of wt MA and R55F MA Proteins. The calculation of wt and R55F MA protein structures was based on interproton distance restraints derived from NOESY spectra, dihedral angles φ and ψ , and a regular hydrogen bond network. An estimate of backbone dihedral angles φ and ψ was performed in TALOS program based on ¹H α , ¹³C α , ¹³C β , ¹³C', and ¹⁵N chemical shifts. Hydrogen bond restraints were used for α -helical segments identified in later stages of computation. The Aria software package (version 2.0alpha) was initially used to calibrate NOE restraints, to assign NOESY cross peaks, and to calculate preliminary structures. Distance restraints, together with dihedral angles and hydrogen bond restraints, were then used as an input for Xplor-NIH (27), where the final sets of 100 (wt) or 50 (R55F) MA structures were calculated using standard protocol for torsion angle dynamics and simulated annealing. Distribution of φ and ψ dihedral angles in the Ramachandran core, additional allowed, generously allowed, and disallowed regions for the 20 best WT structures is (%) 88.6 ± 2.1, 9.8 ± 1.9, 1.2 ± 0.9 and 0.3 ± 0.5, respectively; and for 18 best R55F structures, 91.2 ± 1.5, 7.7 ± 1.7, 1.1 ± 1.0 and 0.1 ± 0.3.

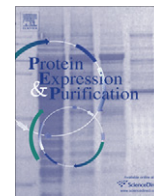
The accuracy of calculated structures was validated by comparison of measured and back-calculated RDCs. The signal splittings of isotropic and partially aligned wt or R55F MA in 5.5% or 4.5% polyacrylamide gel, respectively, were measured by using the D5SE-¹H,¹⁵N-HSQC experiment (28), yielding one-bond ¹H-¹⁵N RDCs. The synthetic RDCs were back-calculated by singular value decomposition method from a set of eight (wt MA) or six (R55F MA) structures recalculated with RDC constraints, and correlated with the measured values (Fig. S3). The back-calculations and analyses were performed in the iDC module (29) of Igor Pro 6.0 software (<http://www.wavemetrics.com>).

ACKNOWLEDGMENTS. We thank Sung S. Rhee (U.S. Food and Drug Administration, Rockville, MD) for providing unpublished results and discussions on the role of Tctex-1 in M-PMV replication and Dr. K. Pfister (University of Virginia, Charlottesville, VA) and Dr. S. M. King (McMaster University, Hamilton, ON, Canada) for kind gifts of anti Tctex-1 monoclonal and rabbit antibody, respectively. This work was supported by Czech Ministry of Education Grants 1M6837805002, MSM 6046137305, 0021620835, and ME 904, Z 40550506; Czech Science Foundation Grants 2003/02/P098, 2003/03/0490, and SCO/06/E001; the Grant Agency of the Academy of Sciences of the Czech Republic KAN200100801; the Grant Agency of Charles University 38707; and National Institutes of Health Grant CA 27834.

- Hunter E (1994) Macromolecular Interactions in the assembly of HIV and other retroviruses. *Sem Virol* 5:71–83.
- Sfakianos JN, LaCasse RA, Hunter E (2003) The M-PMV cytoplasmic targeting-retention signal directs nascent Gag polypeptides to a pericentriolar region of the cell. *Traffic* 4:660–670.
- Freed EO (2002) Viral late domains. *J Virol* 76:4679–4687.
- Freed EO, Orenstein JM, Bucklerwhite AJ, Martin MA (1994) Single amino-acid changes in the human-immunodeficiency-virus type-1 matrix protein block virus particle-production. *J Virol* 68:5311–5320.
- Cannon PM, et al. (1997) Structure-function studies of the human immunodeficiency virus type 1 matrix protein, p17. *J Virol* 71:3474–3483.
- Soneoka Y, Kingsman SM, Kingsman AJ (1997) Mutagenesis analysis of the murine leukemia virus matrix protein: Identification of regions important for membrane localization and intracellular transport. *J Virol* 71:5549–5559.
- Bryant M, Ratner L (1990) Myristoylation-dependent replication and assembly of human immunodeficiency virus-1. *Proc Natl Acad Sci USA* 87:523–527.
- Rhee SS, Hunter E (1987) Myristylation is required for intracellular-transport but not for assembly of D-type retrovirus capsids. *J Virol* 61:1045–1053.

9. Zhou W, Parent LJ, Wills JW, Resh MD (1994) Identification of a membrane-binding domain within the amino-terminal region of human immunodeficiency virus type 1 Gag protein which interacts with acidic phospholipids. *J Virol* 68:2556–2569.
10. Tang C, et al. (2004) Entropic switch regulates myristate exposure in the HIV-1 matrix protein. *Proc Natl Acad Sci USA* 101:517–522.
11. Saad JS, et al. (2006) Structural basis for targeting HIV-1 Gag proteins to the plasma membrane for virus assembly. *Proc Natl Acad Sci USA* 103:11364–11369.
12. Conte MR, Klikova M, Hunter E, Ruml T, Matthews S (1997) The three-dimensional solution structure of the matrix protein from the type D retrovirus, the Mason-Pfizer monkey virus, and implications for the morphology of retroviral assembly. *EMBO J* 16:5819–5826.
13. Hatanaka H, et al. (2002) Structure of equine infectious anemia virus matrix protein. *J Virol* 76:1876–1883.
14. Riffel N, et al. (2002) Atomic resolution structure of Moloney murine leukemia virus matrix protein and its relationship to other retroviral matrix proteins. *Structure* 10:1627–1636.
15. Rhee SS, Hunter E (1990) A single amino acid substitution within the matrix protein of a type D retrovirus converts its morphogenesis to that of a type C retrovirus. *Cell* 63:77–86.
16. Yasuda J, Hunter E (2000) Role of matrix protein in the type D retrovirus replication cycle: Importance of the arginine residue at position 55. *Virology* 268:533–538.
17. Choi G, et al. (1999) Identification of a cytoplasmic targeting retention signal in a retroviral Gag polyprotein. *J Virol* 73:5431–5437.
18. Vlach J, et al. (2005) Letter to the editor: Assignment of H-1, C-13, and N-15 resonances of WT matrix protein and its R55F mutant from Mason-Pfizer monkey virus. *J Biomol NMR* 31:381–382.
19. Karcher RL, Deacon SW, Gelfand VI (2002) Motor-cargo interactions: The key to transport specificity. *Trends Cell Biol* 12:21–27.
20. Sfakianos JN, Hunter E (2003) M-PMV capsid transport is mediated by Env/Gag interactions at the pericentriolar recycling endosome. *Traffic* 4:671–680.
21. Mok YK, Lo KWH, Zhang MJ (2001) Structure of Tctex-1 and its interaction with cytoplasmic dynein intermediate chain. *J Biol Chem* 276:14067–14074.
22. Sugai M et al. (2003) PTH/PTH-related protein receptor interacts directly with Tctex-1 through its COOH terminus. *Biochem Biophys Res Commun* 311:24–31.
23. Song C, Hunter E (2003) Variable sensitivity to substitutions in the N-terminal heptad repeat of Mason-Pfizer monkey virus transmembrane protein. *J Virol* 77:7779–7785.
24. Lo KW, et al. (2007) Interaction of the DYNLT (TCTEX1/RP3) light chains and the intermediate chains reveals novel intersubunit regulation during assembly of the dynein complex. *J Biol Chem* 282:36871–36878.
25. Delaglio F, et al. (1995) NMRPipe: A multidimensional spectral processing system based on UNIX pipes. *J Biomol NMR* 6:277–293.
26. Lipari G, Szabo A (1982) Model-free approach to the interpretation of nuclear magnetic resonance relaxation in macromolecules. 2. Analysis of experimental results. *J Am Chem Soc* 104:4559–4570.
27. Schwieters CD, Kuszewski JJ, Tjandra N, Clore GM (2003) The Xplor-NIH NMR molecular structure determination package. *J Magn Reson* 160:65–73.
28. Cordier F, Dingley AJ, Grzesiek S (1999) A doublet-separated sensitivity-enhanced HSQC for the determination of scalar and dipolar one-bond J-couplings. *J Biomol NMR* 13:175–180.
29. Wei YF, Werner MH (2006) iDC: A comprehensive toolkit for the analysis of residual dipolar couplings for macromolecular structure determination. *J Biomol NMR* 35:17–25.

Příloha 3



Expression and purification of myristoylated matrix protein of Mason-Pfizer monkey virus for NMR and MS measurements

Jan Prchal^{a,b}, Petra Junkova^b, Miroslava Strmiskova^a, Jan Lipov^b, Radovan Hynek^b, Tomas Ruml^b, Richard Hrabal^{a,*}

^aLaboratory of NMR Spectroscopy, Institute of Chemical Technology, Prague, Technická 5, 166 28 Prague 6, Czech Republic

^bDepartment of Biochemistry and Microbiology, Institute of Chemical Technology, Prague, Technická 5, 166 28 Prague 6, Czech Republic

ARTICLE INFO

Article history:

Received 8 March 2011
and in revised form 12 May 2011
Available online 24 May 2011

Keywords:

M-PMV
Matrix protein
Myristoylation
Retrovirus
N-myristoyl transferase

ABSTRACT

Matrix proteins play multiple roles both in early and late stages of the viral replication cycle. Their N-terminal myristoylation is important for interaction with the host cell membrane during virus budding. We used *Escherichia coli*, carrying N-myristoyltransferase gene, for the expression of the myristoylated His-tagged matrix protein of Mason-Pfizer monkey virus. An efficient, single-step purification procedure eliminating all contaminating proteins including, importantly, the non-myristoylated matrix protein was designed. The comparison of NMR spectra of matrix protein with its myristoylated form revealed substantial structural changes induced by this fatty acid modification.

© 2011 Elsevier Inc. All rights reserved.

Introduction

Mason-Pfizer monkey virus (M-PMV)¹ belongs to the family of betaretroviruses which form immature virus-like particles (VLP) within the cytoplasm of infected cells. VLPs are then transported to the plasma membrane for budding. In contrast, the immature particles of lentiviruses (e.g. HIV-1) are assembled directly on the inner leaflet of the cell membrane instantly before budding [1]. Temporal and spatial separation of assembly and budding in M-PMV enables to study these processes independently.

Matrix protein (MA) is the N-terminal domain of the structural polyprotein precursor Gag of all retroviruses. During the late phase of virus life cycle it is involved in the transport of Gag protein to the site of assembly of VLPs and afterwards in the association of VLP with the plasma membrane (PM) prior to budding [2]. In betaretroviruses the MA domain controls also the transport of VLPs from the pericentriolar region to the plasma membrane [3].

Most retroviral MAs are N-terminally myristoylated. The attachment of C₁₄ fatty acid to the N-terminal glycine is a common

posttranslational modification of eukaryotic proteins and it is one of three already described N-terminal fatty acylation motifs which confer binding to the membrane [4]. In contrast to numerous structures of non-myristoylated retroviral MAs, only two of myristoylated retroviral MAs have been published up to date [5,6].

Significant role of the myristoylation has been proved in the transport of Gag to the assembly site. Myristate and surface patch of basic residues of the MA molecule are essential for the association of Gag with PM [7–9]. On one side, the binding of MA to the plasma membrane must be tight, but on the other side it has to be reversible to allow a release of the MA protein from the membrane upon infection [10]. To fulfill such requirement, the MA protein exists in two states, i.e. myr-exposed [myr(e)] and myr-sequestered [myr(s)] as it was demonstrated by Tang et al. [5]. Such change of the state is called “myristoyl switch”, which has been described also for other N-terminally myristoylated proteins like recoverin or ADB ribosylation factor [11,12]. While in cytoplasm, the myristic moiety is buried inside a hydrophobic cavity of MA in the myr(s) state and it becomes exposed when Gag (soluble or assembled in VLP) approaches the plasma membrane to mediate the protein-membrane interaction. Saad et al. reported that phosphatidylinositol-4,5-bisphosphate triggers the myristoyl switch in HIV MA [13]. Furthermore, Tang et al. also discovered that the MA domain forms trimers through the interaction of the exposed myristates [5]. Trimers are readily formed due to an increased concentration of Gag proteins in lipid raft domains which are part of the PM [10,14]. Therefore, it is the formation of trimers that triggers the myristoyl switch. When the concentration of MA

* Corresponding author.

E-mail address: hrabal@vscht.cz (R. Hrabal).

¹ Abbreviations used: HSQC, heteronuclear single quantum coherence; IPTG, isopropyl β-D-1-thiogalactopyranoside; LB, Luria–Bertani medium; MA, matrix protein; myrMA, myristoylated matrix protein; MAPPHis, matrix protein with 18 N-terminal amino acid residues from M-PMV phosphoprotein and 6 histidines attached to its C-terminus; M-PMV, Mason-Pfizer monkey virus; Ni-NTA, nickel-nitrilotriacetic acid; NMT, N-myristoyltransferase; PE, pellet; PM, plasma membrane; SU, supernatant; VLP, virus-like particle.

drops upon infection of a new cell the trimers disintegrate, the myristate is buried and MA is released from the membrane.

Recently, we have reported that in contrast to the HIV-1 MA, the non-myristoylated M-PMV MA protein readily forms trimers upon increasing its concentration in solution [15]. The increased oligomerization capacity of M-PMV MA is probably related to the necessity to stabilize Gag within the capsid shell [15].

Here we report the production and isolation of N-terminally myristoylated matrix protein of M-PMV for structural and functional study by nuclear magnetic resonance spectroscopy (NMR) and mass spectrometry (MS). NMR spectroscopy requires highly concentrated protein sample uniformly labeled with ^{13}C and ^{15}N isotopes. Labeled proteins are usually produced in bacterial cells, because they can grow on relatively cheap minimal media and produce high yields of proteins.

Materials and methods

Microorganism strains and media

Escherichia coli strain DH5 α was used as a host for vector amplification while *E. coli* strain BL21 (DE3) was used for the production of the recombinant proteins. Cells were grown in Luria–Bertani medium (LB, 1% Tryptone, 1% NaCl, 0.5% yeast extract (w/w)) containing ampicillin (100 mg/l) and when using two-plasmid system also kanamycin (50 mg/l). For the production of isotopically labeled proteins the cells were grown in the M9 minimal medium [16] containing the same amount of the antibiotics.

Construction of production vectors

The sequence encoding the matrix protein and downstream 18 amino acids of phosphoprotein (PP) was introduced to the pET22b vector (Novagen) using the NdeI and XhoI restriction sites. PCR product was generated using primers MA_Nde_fwd (GTCACTCA TATGGGCAAGAATTAAGCCAG) and MA_Xho_bwd (AGTGACCTC GAGGTCTGTTTGAGAATTAC) and proviral vector pSARM4 [17] as a template. The product was cleaved by the appropriate restriction enzymes (New England Biolabs) and then ligated to the pET22b vector cleaved by the same enzymes to join the sequence encoding the His-tag (Fig. 1A). The resulting vector pEMAPPHis was verified by restriction cleavage and by sequencing.

The vector pETyNMT for the production of yeast N-myristoyltransferase was constructed by inserting the gene encoding the enzyme to the pET29b vector (Novagen) using the NdeI and XhoI restriction sites (Fig. 1B). The stop codon was introduced to the end of the gene.

The expression vector carrying both genes was constructed by inserting the gene encoding the matrix protein and 18 amino acids from phosphoprotein together with the His-tag (MAPPHis) in a plasmid containing a gene encoding the yeast N-myristoyltransferase.

PCR product, containing a gene for MAPPHis was generated using primers MAyNMT_NcoI_fwd (AACGTACCATGGGCAAGAA TTAAGCCAGC) and MAPPHisyNMT_PstI_bwd (TCTTAGCTGCAGT TAGTGGTGGTGGTGGTGC) and above described plasmid pEMAPPHis as a template. The acceptor vector was a kind gift of Prof. Michael Summers (Howard Hughes Medical Institute). This vector, based on the pET19b and pET11b vectors already harbors the gene encoding the yeast N-myristoyltransferase. The resulting PCR product was cleaved by restriction enzyme NcoI, the acceptor vector was cleaved by NcoI and XhoI enzymes (all from New England Biolabs). The XhoI site was then removed by the action of Mung Bean Nuclease (New England Biolabs). Semiblunt ligation was performed and the resulting vector pEMAPPHisyNMT was verified by sequencing (Fig. 1C).

In order to introduce both plasmids pEMAPPHis and pETyNMT, competent *E. coli* cells transformed by the pETyNMT vector were prepared by a standard protocol [16]. The plasmid pEMAPPHis was then introduced in bacteria and the positive transformants were selected on the LB agar containing ampicillin and kanamycin.

Production of recombinant myrMAPPHis

Transformed *E. coli* BL21(DE3) cells, containing the expression vector, were grown to OD₅₉₀ 0.5, then sodium myristate dissolved in water was added to the final concentration of 0.06 mM. Protein expression was induced 30 min later by adding isopropyl- β -D-thiogalactopyranoside (IPTG) to the concentration of 0.4 mM and the cells were then cultivated for 4 h at 37 °C. The cells were pelleted by centrifugation at 12,000 \times RCF for 10 min. Supernatants were discarded and pellets were resuspended in 30 ml of lysis buffer (50 mM phosphate, 300 mM NaCl, 10 mM imidazole, pH 8) and frozen at –20 °C.

Disruption of cells containing the recombinant protein

The cell suspension was thawed and combined with complete inhibitor mix (Roche) and 30 mg of lysozyme. The mixture was shaken and incubated at room temperature for 30 min, followed by sonication with 50 W for 1.5 min. To remove proteins bound on the cell membrane 0.1% (w/w) sodium deoxycholate was added and the lysate was incubated for 30 min at 4 °C. To decrease the viscosity of the cell lysate it was incubated for 30 min at 37 °C with DNase and RNase (10 $\mu\text{g}/\text{ml}$). Insoluble parts of the cells were pelleted by centrifugation at 30,000 \times RCF for 15 min. Pellets were resuspended in 30 ml lysis buffer (PE) and supernatant containing soluble myrMAPPHis (SU) was used for protein purification.

Purification of myrMAPPHis by metal-affinity chromatography

Following the centrifugation, 4 ml of Ni–NTA agarose (Qiagen) were added to SU and the mixture was incubated for 1 h at 4 °C. The agarose was washed with 20 ml of lysis buffer and 20 ml of

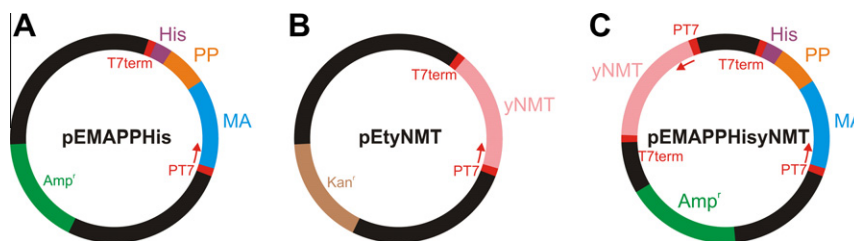


Fig. 1. Schematic representation of vectors for expression of MAPPHis and NMT. (A) The plasmid based on the pET22b vector coding gene for MAPPHis used in the two-plasmid expression system. (B) The plasmid based on the pET29b vector coding gene for NMT used in the two-plasmid expression system. (C) The plasmid carrying both MAPPHis and NMT genes constructed on the basis of the pET19b and pET11b vectors used in the single-plasmid system.

protease buffer (100 mM phosphate, 900 mM NaCl, pH 6.25). Following the washing step, the agarose was resuspended in 4 ml of protease buffer containing 0.2 mg of recombinant M-PMV protease (Pr13) prepared in our laboratory as described by Zabransky et al. [18]. MyrMAPPHis was cleaved for 1 h at room temperature with shaking. The cleaved protein was separated and the intact myrMAPPHis was then eluted using imidazole buffer (1 h, 50 mM phosphate, 200 mM imidazole, pH 7, 4 °C). Samples from purification and cell disruption were analyzed by Tris-Tricine SDS–PAGE stained by Coomassie blue.

Preparation of protein sample for MALDI–TOF measurements

Purified myrMAPPHis was exchanged to MS buffer (100 mM phosphate, 100 mM NaCl, 5 mM dithiothreitol, pH 6) using PD-10 desalting column (GE Healthcare). For peptide mapping experiments the protein sample was additionally purified using gel permeation chromatography on HiLoad 26/60 Superdex 75PG column (Amersham) with isocratic elution (100 mM phosphate, 100 mM NaCl, 0.01 % mercaptoethanol (v/v), pH 6). The flow rate was 2.3 ml/min. and 4 ml fractions were collected. Chromatography was monitored by UV spectroscopy at 280 nm and the largest peak at 213 ml was collected.

Peptide mapping method

MyrMAPPHis was digested by trypsin and chymotrypsin in MS buffer at 37 °C for two hours. Enzyme to substrate ratio used for both enzymes was 1:20 (w/w). Protein cleavage was stopped by adding TFA to the final concentration of 0.5% (v/v). Solution of peptides was purified and concentrated by ZipTip C18 pipette tips (Millipore).

Mass spectrometry

Peptide and intact protein spectra were obtained using Biflex IV MALDI–TOF mass spectrometer (Bruker Daltonics, Germany), equipped with a UV nitrogen laser (337 nm) and a dual microchannel microplate detector. The spectra of intact proteins were acquired in positive linear mode within a mass range of 2000–20,000 Da. The samples were prepared by mixing 1 µl of protein solution with 4 µl of freshly prepared matrix solution (10 mg/ml of 3,5-dimethoxy-4-hydroxycinnamic acid in 1:2 acetonitrile:0.1% TFA). Bruker protein calibration standard I (Bruker) was used for the calibration. The spectra of peptides were acquired in the positive reflector mode within a mass range of 500–4000 Da. Samples of peptides were prepared by mixing 1 µl of peptide solution and 1 µl of freshly prepared matrix solution (20 mg/ml of 2,5-dihydroxybenzoic acid in 1:2 acetonitrile:0.1% TFA). Bruker peptide calibration standard I (Bruker) was used for the calibration. In both cases a total of 1 µl of mixture was placed on a stainless steel probe plate and allowed to dry at room temperature. To reduce spot to spot signal variation at least 300 of individual spectra were collected and averaged. Spectra were analyzed using mMass software [19].

Preparation of protein sample for NMR measurements

Purified myrMAPPHis was exchanged to NMR buffer (100 mM phosphate, 300 mM NaCl, 5 mM dithiothreitol, 5% D₂O, pH 6) using PD-10 desalting column. The protein sample was then concentrated using Amicon Ultra–15 Ultracel 5 k (Millipore) to the final concentration of 0.5 mM. The concentration of the protein was determined by UV–spectroscopy at 280 nm using extinction coefficient 23590 M⁻¹cm⁻¹ determined by ProtParam [20].

NMR measurements

All NMR spectra were measured at 25 °C on a Bruker Avance III 600 spectrometer equipped with a triple-resonance cryoprobe (Bruker BioSpin GmbH). The ¹H–¹⁵N HSQC were acquired with a spectral width of 7003 Hz and 2048 complex points in the ¹H dimension and with 1521 Hz and 180 complex points in the ¹⁵N dimension. The ¹H–¹³C HSQC were acquired with a spectral width of 9615 Hz and 2048 complex points in ¹H dimension and width 13,582 Hz and 256 complex point in ¹³C dimension and all spectra were processed using TopSpin software (Bruker BioSpin GmbH, version 2.1) and NMRPipe [21] and analyzed using Sparky software [22].

Results and discussion

Protein expression and purification

Both single- and two-plasmid vectors showed a strong expression of the recombinant protein as demonstrated in Fig. 2 (lanes 4 and 5). However, the overall yield of the myristoylated protein was about 65% of the production of the non-myristoylated MA in both cases. Following the cell disruption and centrifugation most of the MA protein was soluble and could be found in supernatant (Fig. 2, lanes 6 and 7). Only a small amount of myrMAPPHis remained in the pellet (Fig. 2, lanes 8 and 9). The purification process of myrMAPPHis is illustrated on Fig. 3 (single-plasmid system) and 4 (two-plasmid system). Initially we sought to prepare the myrMA without the His-tag and the N-terminal part of phosphoprotein by cleaving the myrMAPPHis product by recombinant M-PMV protease (Pr13) using similar protocol as for the non-myristoylated protein [23]. However, Pr13 cleaved myristoylated MAPPHis very poorly when compared to the non-myristoylated protein. This phenomenon was utilized in a new purification procedure when the non-myristoylated MA was proteolytically released from the immobilized PPHis, while the myristoylated MAPPHis remained attached to the Ni–NTA resin from where it was subsequently eluted by imidazole. To illustrate the efficiency of the process, the myrMAPPHis bound on the Ni–NTA resin was split into two aliquots that were loaded on the column and washed. The first one was then directly eluted with imidazole and analyzed (Figs. 3 and 4, lane 3). The second aliquot was incubated with Pr13 for

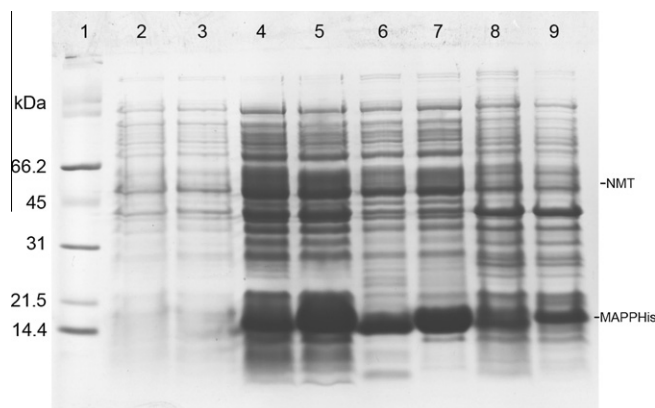


Fig. 2. Coomassie stained SDS–PAGE gel illustrating the production of myrMAPPHis and cell lysis. Odd lanes show proteins produced from the two-plasmid system, even lanes show proteins produced in the single-plasmid system. Lanes: (1) broad range SDS–PAGE standard (Bio-Rad), (2, 3) cells before induction, (4, 5) cells 4 h after induction, (6, 7) supernatant after cell lysis, (8, 9) pellet after cell lysis. MAPPHis is the large band with Mw 14.5 kDa, lanes 6–9 also contain lysozyme, which has similar mobility as MAPPHis. NMT has molecular weight of 55 kDa, but it can not be distinguished from other bacterial proteins.

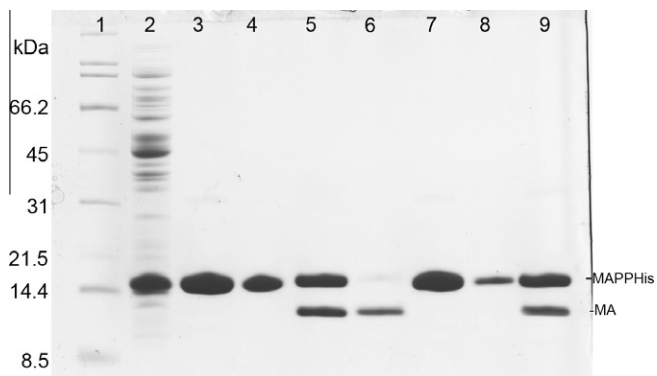


Fig. 3. Coomassie stained SDS-PAGE gel illustrating purification of myrMAPPHis produced using the single-plasmid system. Lanes 3–5 show purification of the first aliquot directly eluted by imidazole buffer and lanes 6–9 show purification of the second aliquot which was cleaved on Ni–NTA and then eluted by imidazole. Lanes: (1) broad range SDS-PAGE standard (Bio-Rad), (2) flow-through after binding (14 kDa band is lysozyme), (3) protein eluted from column using imidazole buffer, (4) sample of Ni–NTA agarose after elution, (5) eluate (the same as in lane 3) cleaved by Pr13 for 1 h, (6) protein cleaved from Ni–NTA by Pr13, (7) protein eluted from column using imidazole buffer after cleavage, (8) sample of Ni–NTA agarose after elution, (9) eluate (the same as in lane 7) cleaved by Pr13 for 1 h.

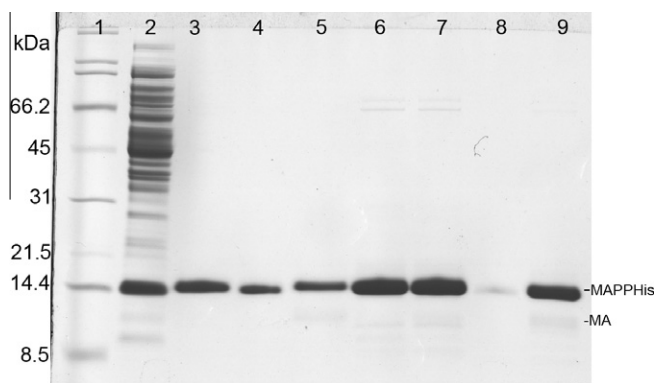


Fig. 4. Coomassie stained SDS-PAGE gel illustrating Ni–NTA purification of myrMAPPHis produced using the two-plasmid system. Lanes 3–5: purification of the first aliquot directly eluted by imidazole buffer and lanes 6–9: purification of the second aliquot, which was cleaved on Ni–NTA and then eluted by imidazole. Lanes: (1) broad range SDS-PAGE standard (Bio-Rad), (2) flow-through after binding (14 kDa band is lysozyme), (3) proteins eluted by imidazole buffer, (4) sample of Ni–NTA agarose after elution, (5) eluate (the same as in lane 3) cleaved by Pr13 for 1 h, (6) protein cleaved from Ni–NTA by Pr13, (7) protein eluted from column using imidazole buffer after cleaving, (8) sample of Ni–NTA agarose after elution, (9) eluate (the same as in lane 7) cleaved by Pr13 for 1 h.

one hour at room temperature. The cleaved non-myristoylated MA was collected (Figs. 3 and 4, lane 6) and the intact myrMAPPHis bound on the Ni–NTA was eluted by imidazole (Figs. 3 and 4, lane 7). To test whether the binding of myrMAPPHis to the Ni–NTA did not prevent the proteolytic cleavage, a small sample of the myrMAPPHis eluted from the column was exchanged to the protease buffer and incubated with Pr13 for one hour. From the comparison of lanes 5 and 9 on Figs. 3 and 4, respectively, it is obvious that the proteolysis efficiency is comparable and therefore, it is not the binding of myrMAPPHis on the Ni–NTA column that prevents the cleavage.

The single-plasmid system yielded insufficiently myristoylated protein (less than 25%) (Fig. 5). The content of the myristoylated MA in the sample was partially increased by removing the non-myristoylated MAPPHis by its cleavage on the Ni–NTA column. However, the complete cleavage of the non-myristoylated MAP-

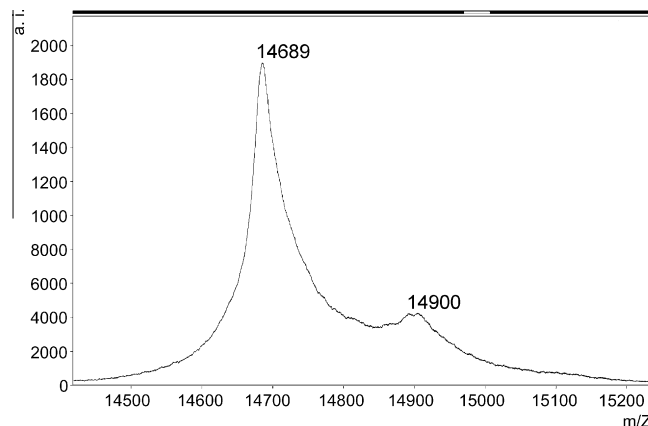


Fig. 5. MALDI–TOF MS spectrum of purified myrMAPPHis obtained from the single-plasmid system (same sample as in Fig. 3 lane 7). The m/z ratio of larger peak corresponds to Mw of non-myristoylated MAPPHis.

PHis would require a higher amount of Pr13 and the yield of myrMAPPHis would still remain lower than 33%. Therefore, we focused our attention to the two-plasmid system. The degree of myristoylation increased to over 90% (Fig. 6) and after removing the non-myristoylated MAPPHis (some myrMAPPHis was eluted during the cleavage) we obtained a product containing over 95% of the required myristoylated protein (Fig. 7). The yield of the product (especially of the isotopically labeled MA) was increased by elution of residual traces of myrMAPPHis from the Ni–NTA resin during repeated washing with imidazole (at least twice).

Preparation of myrMAPPHis for NMR and MALDI–TOF measurements

NMR spectroscopy requires a higher concentration of protein samples compared to other spectroscopic methods. We found that higher ionic strength (300 mM NaCl) increased the solubility of the myrMAPPHis. This allowed concentrating the myrMAPPHis sample to the final concentration of 0.5 mM. After several days, a minor precipitation appeared but most of the protein remained in solution (the final concentration was approximately 0.4 mM) and the sample was stable for several months (verified by repeated ^1H – ^{15}N HSQC experiments).

Although MALDI–TOF analysis does not require such a high concentration of protein as NMR spectroscopy, the protein was dissolved in a buffer containing 100 mM NaCl to increase its

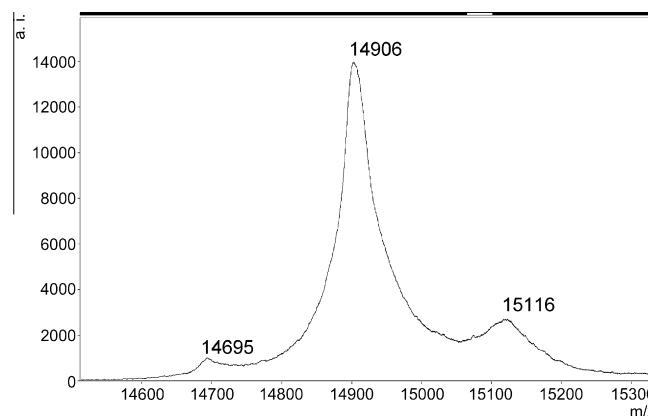


Fig. 6. MALDI–TOF MS spectrum of myrMAPPHis obtained from the two-plasmid system without cleavage by Pr13 on Ni–NTA (same sample as in Fig. 4 lane 3). Mw The m/z ratio of larger peak corresponds to Mw of myristoylated MAPPHis. Peak with m/z ratio of 15116 is an adduct of myrMAPPHis and MS matrix.

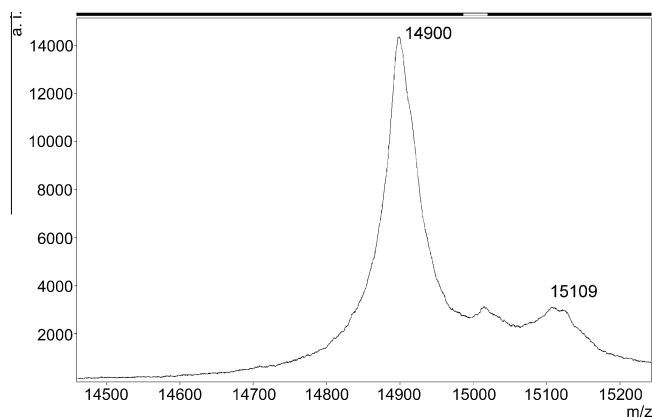


Fig. 7. MALDI-TOF MS spectrum of purified myrMAPPHis obtained from the two-plasmid system (the same sample as in Fig. 4 lane 7). The m/z ratio of larger peak corresponds to Mw of myristoylated MAPPHis. Peak with m/z ratio of 15109 is again an adduct of myrMAPPHis and MS matrix.

stability in solution. However, such a high concentration of salt would deteriorate the quality of MS spectra. The sample was therefore, mixed with the mass spectrometry matrix in ratio 1:4 immediately before the measurement to lower its ionic strength. ZipTip C18 pipette tips were not used as they would remove a significant portion of the myristoylated MAPPHis.

MALDI-TOF measurement

The major signal of $m/z = 14,900$ which represents the myrMAPPHis was present in the mass spectrum. We also detected a signal of the non-myristoylated MAPPHis ($m/z = 14,686$), but its intensity was quite low when compared to the myrMAPPHis (Fig. 6). This signal disappeared completely after the final purification step. Mixtures of the myrMAPPHis with the non-myristoylated MAPPHis ranging from ratio 10:1 to 1:10 (w/w) were prepared to quantify the content of the myristoylated protein in the sample. The intensity ratios of measured signals corresponded well to myr-/non-myristoylated MAPPHis ratios which allowed determination of the amount of the myristoylated MAPPHis. In isotopically labeled ($^{13}\text{C}/^{15}\text{N}$) samples this ratio was easily determined by NMR spectroscopy (*vide infra*). All samples used for MS or NMR studies contained less than 5% of the non-myristoylated MAPPHis. Peptide mapping method confirmed the identity of N-terminal peptides with the bound myristic acid. In the case of trypsin digestion 98% sequence coverage was achieved and by using chymotrypsin the sequence coverage was 92%. The results confirmed the quality of the myrMAPPHis.

NMR experiments

^{13}C -filtered ^1H spectra and 2D ^1H - ^{13}C HSQC were acquired to verify the content of the myrMAPPHis in the sample. Due to the binding of the myristic acid in the hydrophobic cavity it was possible to discriminate the signals of methyl groups of Val 38 and 59 and Ile 86 and 90 from the myristoylated and non-myristoylated proteins (Fig. 8, 1D spectra not shown). The ratio of their signal volumes corresponded directly to the ratio of their contents in the sample.

The ^1H - ^{15}N HSQC spectra of the non-myristoylated MA and MAPPHis were measured and compared to prove that the PPHis tail does not affect the structure of the MA domain (Fig. 9). Both spectra differed substantially only in chemical shifts of the cross peaks of the last five amino acid residues, which form the originally unstructured C-terminus of the MA domain, when omitting the signals of the PPHis part. The changes may be caused by a partial

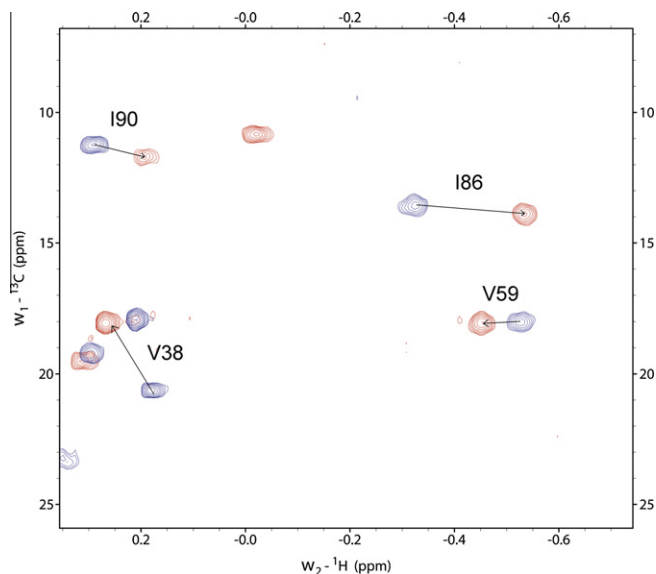


Fig. 8. Overlay of region of ^1H - ^{13}C HSQC spectra, measured on myrMAPPHis (red) and MAPPHis (blue), showing signals of gamma methyl groups of isoleucines 86 and 90 and valines 38 and 59, respectively. (For interpretation of the references to color in this figure legend, the reader is referred to the web version of this article.)

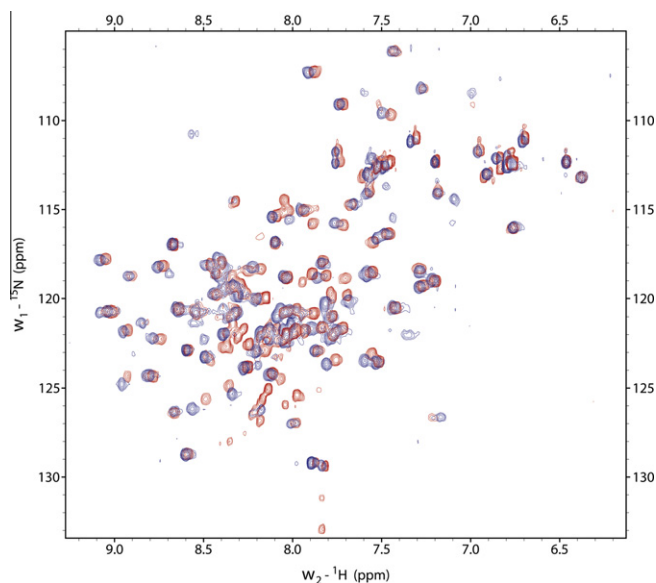


Fig. 9. Overlay of ^1H - ^{15}N HSQC spectra measured on MAPPHis (red) and MA (blue). Signals with different chemical shifts are located at the C-terminus of MA.

immobilization of this amino acid stretch working as a linker between the MA and PPHis domains in the MAPPHis molecule. The remaining signals of the MA protein core corresponded well for both MA and MAPPHis, which means that the PPHis tail does not have any significant impact on the structure of MA.

On the other hand, comparison of ^1H - ^{15}N HSQC and ^1H - ^{13}C HSQC spectra of the myristoylated and non-myristoylated MAPPHis showed large changes of chemical shifts of the corresponding signals (Fig. 8). Although we do not expect significant changes in the global MA structure caused by the presence of the myristic acid inside the protein core, a slightly different mutual arrangement of all four α -helices might be found. Similar phenomenon occurred when the myristoylated and non-myristoylated HIV-1 Nef protein were compared [24]. Therefore, to determine structural changes triggered by the buried myristic acid, the structure of the whole myrMAPPHis will be determined *ab initio*.

Conclusion

We have demonstrated that a large quantity of pure myristoylated M-PMV myrMA can be prepared as a fusion protein myrMAP-PPHis produced together with the yeast N-myristoyltransferase using the two-plasmid system. Due to a weak processing of the myristoylated fusion protein myrMAP-PPHis by 13 kDa form of M-PMV protease, it was advantageous to leave it intact, i.e. in the form of the matrix protein which is C-terminally flanked with a stretch of the first 18 amino acid residues from the phosphoprotein followed by His-tag purification anchor. We have proved that the C-terminal extension (PPHis) does not affect the tertiary structure of the MA domain. The contamination with the non-myristoylated M-PMV MA was less than 5% as evidenced from MS and/or NMR spectra. The protein is suitable for structural studies by a combination of isotopically aided NMR spectroscopy and computational methods. For the MS studies the protein was additionally purified using gel filtration chromatography. We also evaluated the production of the myristoylated M-PMV MA in the single-plasmid system, which had been successfully used for the production of the myristoylated HIV-1 MA. However, the degree of myristoylation was very low. A plausible explanation for the higher myristoylation efficiency of the two-plasmid system might be a higher amount of the produced NMT. However, the direct comparison of the amount of NMT expressed by both systems is prevented due to the presence of much higher amounts of numerous cellular proteins of comparable size (55 kDa). The availability of large quantities of the myristoylated M-PMV MA of sufficient purity will allow further characterization of its structural and functional features. Preliminary data indicate that the myristoylation caused large changes of chemical shifts of signals of backbone NH groups of the MA domain. The changes are much larger when compared with HIV-1 myrMA and spread over the whole molecule. Therefore, we hypothesize that either the myristate is buried deeper in the hydrophobic pocket than in HIV-1 MA or the myristoylation caused larger structural changes in the mutual positions of the helices.

Acknowledgments

We thank Prof. Michael Summers for the plasmid carrying the NMT gene. This research was supported financially by the Czech Science Foundation grant 203/07/0872, projects 1M6837805002, ME 904 and MSM 6046137305 from the Czech Ministry of Education, National Institutes of Health grant CA 27834 and by EU funds, project Operational Program Prague–Competitiveness (OP PC) CZ.2.16/3.100/22197.

References

- [1] S.S. Rhee, E. Hunter, Structural role of the matrix protein of type D retroviruses in gag polyprotein stability and capsid assembly, *J. Virol.* 64 (1990) 4383–4389.

- [2] E.O. Freed, J.M. Orenstein, A.J. Buckler-White, M.A. Martin, Single amino acid changes in the human immunodeficiency virus type 1 matrix protein block virus particle production, *J. Virol.* 68 (1994) 5311–5320.
- [3] E. Hunter, Macromolecular interactions in the assembly of HIV and other retroviruses, *Seminars in Virology* 5 (1994) 71–83.
- [4] M.D. Resh, Fatty acylation of proteins: new insights into membrane targeting of myristoylated and palmitoylated proteins, *Biochim. Biophys. Acta* 1451 (1999) 1–16.
- [5] C. Tang, E. Loeliger, P. Luncsford, I. Kinde, D. Beckett, M.F. Summers, Entropic switch regulates myristate exposure in the HIV-1 matrix protein, *Proc. Natl. Acad. Sci. U. S. A.* 101 (2004) 517–522.
- [6] J.S. Saad, S.D. Ablan, R.H. Ghanam, A. Kim, K. Andrews, K. Nagashima, F. Soheilian, E.O. Freed, M.F. Summers, Structure of the myristylated human immunodeficiency virus type 2 matrix protein and the role of phosphatidylinositol-(4, 5)-bisphosphate in membrane targeting, *J. Mol. Biol.* 382 (2008) 434–447.
- [7] H.G. Krausslich, R. Welker, Intracellular transport of retroviral capsid components, *Curr. Top. Microbiol. Immunol.* 214 (1996) 25–63.
- [8] Y. Soneoka, S.M. Kingsman, A.J. Kingsman, Mutagenesis analysis of the murine leukemia virus matrix protein: identification of regions important for membrane localization and intracellular transport, *J. Virol.* 71 (1997) 5549–5559.
- [9] M.L. Manrique, S.A. Gonzalez, J.L. Affranchino, Functional relationship between the matrix proteins of feline and simian immunodeficiency viruses, *Virology* 329 (2004) 157–167.
- [10] M.D. Resh, A myristoyl switch regulates membrane binding of HIV-1 Gag, *Proc. Natl. Acad. Sci. U. S. A.* 101 (2004) 417–418.
- [11] J.B. Ames, R. Ishima, T. Tanaka, J.I. Gordon, L. Stryer, M. Ikura, Molecular mechanics of calcium-myristoyl switches, *Nature* 389 (1997) 198–202.
- [12] J. Goldberg, Structural basis for activation of ARF GTPase: mechanisms of guanine nucleotide exchange and GTP-myristoyl switching, *Cell* 95 (1998) 237–248.
- [13] J.S. Saad, J. Miller, J. Tai, A. Kim, R.H. Ghanam, M.F. Summers, Structural basis for targeting HIV-1 Gag proteins to the plasma membrane for virus assembly, *Proc. Natl. Acad. Sci. U. S. A.* 103 (2006) 11364–11369.
- [14] P. Spearman, R. Horton, L. Ratner, I. Kuli-Zade, Membrane binding of human immunodeficiency virus type 1 matrix protein in vivo supports a conformational myristyl switch mechanism, *J. Virol.* 71 (1997) 6582–6592.
- [15] J. Vlach, P. Srb, J. Prchal, M. Grocky, J. Lang, T. Ruml, R. Hrabal, Nonmyristoylated matrix protein from the Mason-Pfizer monkey virus forms oligomers, *J. Mol. Biol.* 390 (2009) 967–980.
- [16] J. Sambrook, R. Russell, *Molecular Cloning A Laboratory Manual* (2001) pp. 1.112–1.115.
- [17] C. Song, S.R. Dubay, E. Hunter, A tyrosine motif in the cytoplasmic domain of mason-pfizer monkey virus is essential for the incorporation of glycoprotein into virions, *J. Virol.* 77 (2003) 5192–5200.
- [18] A. Zabransky, M. Andreansky, O. Hruskova-Heidingsfeldova, V. Havlicek, E. Hunter, T. Ruml, I. Pichova, Three active forms of aspartic proteinase from Mason-Pfizer monkey virus, *Virology* 245 (1998) 250–256.
- [19] M. Strohal, D. Kavan, P. Novak, M. Volny, V. Havlicek, MMass 3: a cross-platform software environment for precise analysis of mass spectrometric data, *Anal. Chem.* 82 (2010) 4648–4651.
- [20] E. Gasteiger, C. Hoogland, A. Gattiker, S. Duvaud, M.R. Wilkins, R.D. Appel, A. Bairoch, *Protein Identification and Analysis Tools on the ExPASy Server*, 2005, pp. 571–607.
- [21] F. Delaglio, S. Grzesiek, G.W. Vuister, G. Zhu, NMRPipe: a multidimensional spectra processing system based on UNIX pipes, *J. Biomol. NMR* 6 (1995) 277–293.
- [22] T.D. Goddard, D.G. Kneller, Sparky 3, University of California, San Francisco, 2006.
- [23] J. Vlach, J. Lipov, V. Veverka, M. Rumlova, T. Ruml, R. Hrabal, Letter to the editor: Assignment of H-1, C-13, and N-15 resonances of WT matrix protein and its R55F mutant from Mason-Pfizer monkey virus, *J. Biomol. NMR* 31 (2005) 381–382.
- [24] M. Geyer, C.E. Munte, J. Schorr, R. Kellner, H.R. Kalbitzer, Structure of the anchor-domain of myristoylated and non-myristoylated HIV-1 Nef protein, *J. Mol. Biol.* 289 (1999) 123–138.

Příloha 4

A Mason-Pfizer Monkey Virus Gag-GFP Fusion Vector Allows Visualization of Capsid Transport in Live Cells and Demonstrates a Role for Microtubules

Jasmine Clark¹, Petra Grznarova², Elizabeth Stansell^{1#a}, William Diehl^{1#b}, Jan Lipov², Paul Spearman³, Tomas Ruml², Eric Hunter^{1,4*}

1 Emory Vaccine Center at the Yerkes National Primate Research Center, Emory University, Atlanta, Georgia, United States of America, **2** Department of Biochemistry and Microbiology, Institute of Chemical Technology, Prague, Czech Republic, **3** Department of Pediatrics, Emory University School of Medicine, Atlanta, Georgia, United States of America, **4** Department of Pathology, Emory University, Atlanta, Georgia, United States of America

Abstract

Immature capsids of the Betaretrovirus, Mason-Pfizer Monkey virus (M-PMV), are assembled in the pericentriolar region of the cell, and are then transported to the plasma membrane for budding. Although several studies, utilizing mutagenesis, biochemistry, and immunofluorescence, have defined the role of some viral and host cell factors involved in these processes, they have the disadvantage of population analysis, rather than analyzing individual capsid movement in real time. In this study, we created an M-PMV vector in which the enhanced green fluorescent protein, eGFP, was fused to the carboxyl-terminus of the M-PMV Gag polyprotein, to create a Gag-GFP fusion that could be visualized in live cells. In order to express this fusion protein in the context of an M-PMV proviral backbone, it was necessary to codon-optimize *gag*, optimize the Kozak sequence preceding the initiating methionine, and mutate an internal methionine codon to one for alanine (M100A) to prevent internal initiation of translation. Co-expression of this pSARM-Gag-GFP-M100A vector with a WT M-PMV provirus resulted in efficient assembly and release of capsids. Results from fixed-cell immunofluorescence and pulse-chase analyses of wild type and mutant Gag-GFP constructs demonstrated comparable intracellular localization and release of capsids to untagged counterparts. Real-time, live-cell visualization and analysis of the GFP-tagged capsids provided strong evidence for a role for microtubules in the intracellular transport of M-PMV capsids. Thus, this M-PMV Gag-GFP vector is a useful tool for identifying novel virus-cell interactions involved in intracellular M-PMV capsid transport in a dynamic, real-time system.

Citation: Clark J, Grznarova P, Stansell E, Diehl W, Lipov J, et al. (2013) A Mason-Pfizer Monkey Virus Gag-GFP Fusion Vector Allows Visualization of Capsid Transport in Live Cells and Demonstrates a Role for Microtubules. PLoS ONE 8(12): e83863. doi:10.1371/journal.pone.0083863

Editor: Alexander Wlodawer, NCI-Frederick, United States of America

Received: June 30, 2013; **Accepted:** November 10, 2013; **Published:** December 26, 2013

Copyright: © 2013 Clark et al. This is an open-access article distributed under the terms of the Creative Commons Attribution License, which permits unrestricted use, distribution, and reproduction in any medium, provided the original author and source are credited.

Funding: This work was financially supported by NIH grant R01-CA-27834 from the National Cancer Institute, and by a Czech Science Foundation grant P302/12/1895. International travel for Petra Grznarova was supported by the Czech and Ministry of Education grant LH12011. Jasmine Clark was also the recipient of the American Society for Microbiology Robert D. Watkins fellowship. The funders had no role in study design, data collection and analysis, decision to publish, or preparation of the manuscript.

Competing interests: The authors have declared that no competing interest exist.

* E-mail: ehunte4@emory.edu

#a Current address: National Institute of Allergy and Infectious Diseases, Bethesda, Maryland, United States of America

#b Current addresses: Boston College, Chestnut Hill, Massachusetts, United States of America

Introduction

In studying the role of viral and host cell factors involved in retroviral assembly, trafficking, and budding, the mechanism by which capsids are transported through the cytoplasm is still an poorly understood process. It has been shown previously that for Mason-Pfizer Monkey Virus (M-PMV), capsids are assembled intracellularly at the pericentriolar region by way of a cytoplasmic targeting-retention signal (CTRS), and are subsequently trafficked to the plasma membrane for budding [1,2]. This process is unique when compared to a virus such as

HIV, which exhibits C-type retrovirus morphogenesis, in that assembly and budding are spatially and temporally separated. This separation thus allows for studying these processes individually in order to elucidate the role of viral and cellular factors necessary for assembly and intracellular transport.

Like most simple retroviruses, M-PMV encodes a Gag polyprotein, Pr78, that assembles to form the immature capsid and expression of this gene alone results in the assembly and release of immature virus particles [3]. Pr78 is modified by an N-terminal myristic acid residue that is mostly buried within the folded protein [4]. Following interaction of Gag with the plasma

membrane the exposure of this myristic acid moiety appears to be critical for envelopment and budding of the virus [5]. These previous studies with M-PMV have employed the use of genetic, biochemical and fixed-cell immunofluorescent methodologies for elucidating the role of viral and cellular components in viral assembly, transport, and budding [2,6-9]. Prior data has shown that blocking vesicular trafficking by shifting the temperature of the cell to 20°C causes a significant delay in M-PMV Gag release kinetics and maturation, indicating a role for the cellular vesicular transport system in capsid transport [10,11]. It has also been shown that Env glycoprotein expression is necessary for efficient capsid release and maturation [7,10,12]. Several capsid mutations have provided key insights into the processes involved in M-PMV assembly and transport. Specifically, a single amino acid change from arginine to tryptophan (R55W) in the CTRS causes a switch from B/D type capsid assembly to C-type assembly [3] by preventing nascent Gag molecules from interacting with the dynein light chain Tc-tex and their subsequent transport on microtubules to the pericentriolar region of the cell. Another mutation in the matrix (MA) protein of Gag, R22A, displays a transport defect in which assembled immature capsids are unable to reach the plasma membrane resulting in their aggregation under the cortical actin layer. This dominant negative mutation, which appears to block transit through the actin layer, causes a complete block in viral release from the cell [5]. Further, a double mutation, K16A/K20A, in a basic region of MA, results in the budding of immature capsids into intracellular vesicles, suggesting that these residues play an important role in regulating myristic acid exposure. These data and mutants, while providing insights into the dynamics of Gag assembly, intracellular trafficking, and interactions with cellular membranes, have not allowed studies of individual capsid movement within the cell.

Recent advances in molecular virology have allowed for the use of fluorescently tagged proteins for studying intracellular viral processes. In these studies, a fluorescent protein, usually enhanced green fluorescent protein (eGFP), is fused to the viral protein of interest followed by utilization of real-time live cell imaging techniques for visualizing its behavior. In fusing GFP to the protein of interest, however, several controls are required in order to make sure that the fusion does not disrupt the normal biological processes of the protein. For HIV, Muller et al., were able to successfully tag HIV Gag by inserting GFP near the C-terminus of the matrix (MA) domain of Gag, which had previously been shown to accept short epitope tags without disrupting replication [13]. Successful fusion of GFP to viral capsid proteins, has been used for the study of virus intracellular localization, assembly, and trafficking for other viruses such as herpes simplex virus (HSV) and adeno-associated virus (AAV) [14,15]. Therefore, construction of a GFP-tagged protein that functions similarly to the wild-type counterpart, can be an integral tool in studying viral-host cell interactions in a dynamic system.

In this study, we set out to create an M-PMV Gag-GFP fusion construct that could be used to investigate capsid assembly and the role of the cytoskeleton in intracellular trafficking in a dynamic system. In order to achieve this, it was

necessary to codon-optimize the M-PMV *gag*, strengthen the Kozak consensus sequence for the initiating methionine of Gag, mutate an internal initiating methionine codon of *gag* and replace the M-PMV *pro* and *pol* genes with the gene for eGFP. Cotransfection of this Gag-GFP vector with a helper provirus resulted in capsid assembly and release with an efficiency similar to WT M-PMV. The intracellular localization of eGFP-tagged WT and mutant constructs was compared to untagged proteins labeled by immunofluorescent staining in fixed cells and shown to be equivalent. Fluorescently-labeled, mobile capsids were visualized in live cells, and both the kinetics and co-localization of capsids show a key role for microtubules in their intracellular transport from the pericentriolar region to the plasma membrane.

Materials and Methods

Cell Lines

Infectious M-PMV-producing CMMT cells, were originally derived by co-culturing rhesus mammary tumor cells with rhesus monkey embryo cells [16-18]. COS-1 cells, derived from the African green monkey kidney cell line, CV-1, by transformation with an origin-defective mutant of SV40 [19] and 293T cells, derivatives of the 293 cell line containing an insertion of the temperature sensitive gene for the SV40 T-antigen [20], were obtained from the American Type Culture Collection. All cells were cultured in Dulbecco's modified Eagle's medium (DMEM) supplemented with 10% fetal bovine serum (Gibco). Cell lines were maintained at 37°C with 5% CO₂.

Plasmids

The plasmids used in this study are depicted in Figure 1. The plasmid pSARM-X is an M-PMV proviral vector that expresses the M-PMV genome under the control of the viral LTRs (Figure 1A). The plasmid pSARM-GagGFP was constructed by inserting a codon-optimized *gag* gene and linked *egfp* gene between the *EagI* and *XhoI* sites of pSARM-X, replacing the *gag*, *pro*, and *pol* genes. Briefly, the codon-optimized *gag* gene was amplified with primers containing an *EagI* site in the forward primer and an *AgeI* site in the reverse primer. The eGFP was amplified from a pEGFP-N1 vector using primers with an *AgeI* site in the forward primer and a *PspXI* site and putative splice acceptor site in the reverse primer. The amplified *gag* was digested with *EagI* and *AgeI*; the amplified eGFP was digested with *AgeI* and *XhoI* (and isoschizomer of *PspXI*); and the pSARM-X provirus was digested with *EagI* and *XhoI*. Fragments were ligated by three-way ligation to create pSARM-GagGFP (Figure 1B). The vector was confirmed using both diagnostic digestion with *BlnI* and sequencing of the complete insert.

To enhance the Kozak consensus sequence of the Gag-GFP construct and to prevent internal ribosomal initiation, the plasmid was mutated using four overlapping ultramers spanning from the *EagI* site to the *SbfI* site of codon-optimized *gag*. The ultramers contained a strengthened Kozak consensus sequence at the initiating methionine as well as a methionine to alanine substitution at the second methionine (M100A) (Figure

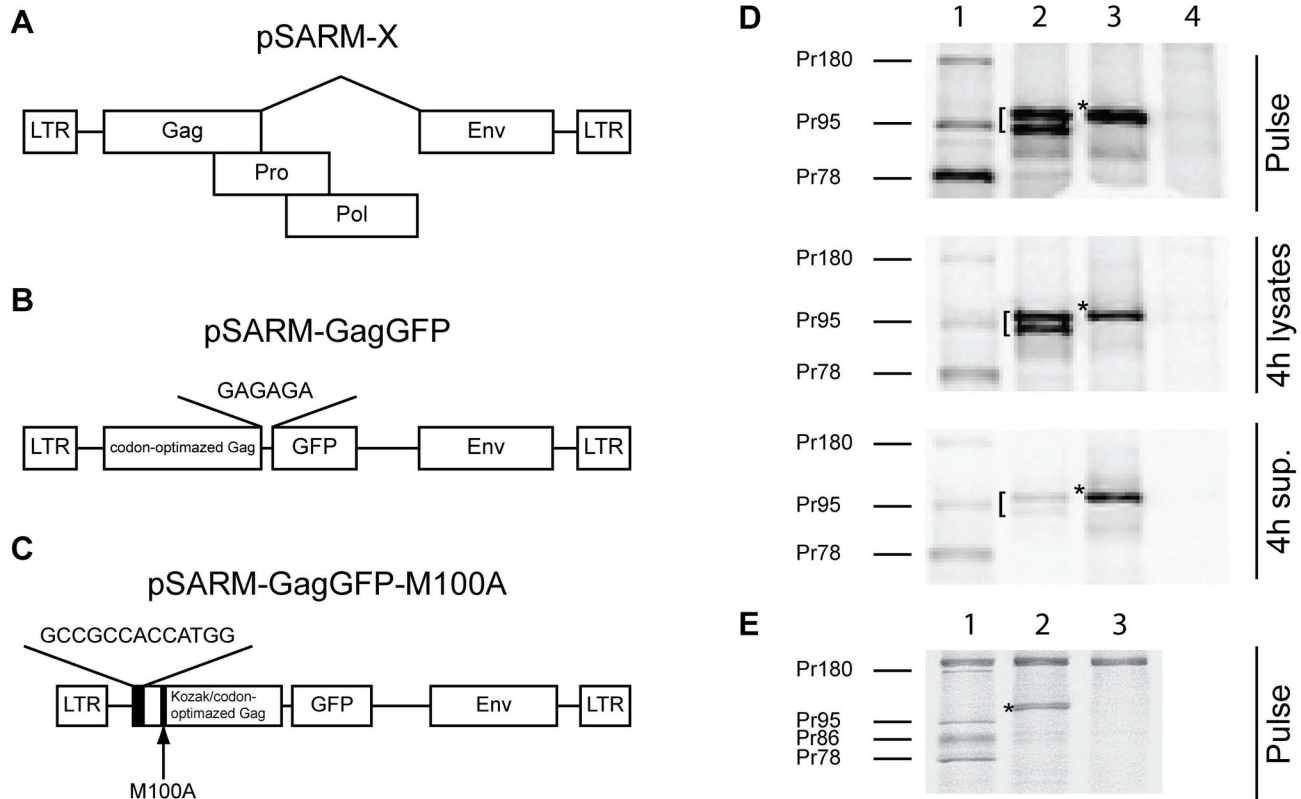


Figure 1. Construction of GagGFP pSARM-X. Genetic organization of construct pSARM-X (A), pSARM-GagGFP (B), pSARM-GagGFP-M100A (C). (D) 293T cells (untransfected, Lane 4) were transfected with pSARM-D26N (Lane 1), pSARM-GagGFP (lane 2) and pSARM-GagGFP-M100A (Lane 3). Viral proteins were metabolically labeled with [³⁵S]-methionine followed by a 4-hour chase in unlabeled media. Lysates from the pulse and chase (4h lysates) as well as culture medium from the chase (4h sup.) were then immunoprecipitated with rabbit anti-p27^{CA} antibody and resolved on SDS-PAGE. (E) 293T cells were transfected with pSARM-D26N (Lane 1) and pSARM-GagGFP-M100A (Lane 2). Viral proteins were metabolically labeled with [³⁵S]-methionine and lysates were then immunoprecipitated with goat anti-MPMV antibody and resolved on SDS-PAGE. Positions of the viral precursor proteins Pr180 (Gag-Pro-Pol), Pr95 (Gag-Pro), Pr86 (Envelope) and Pr78 (Gag) are shown. Products of pSARM-GagGFP ([]) and pSARM-GagGFP-M100A (*) are shown.

doi: 10.1371/journal.pone.0083863.g001

1C). All four ultramers were annealed using temperature-gradient PCR (50–65 °C) with Taq polymerase. The subsequent 500 bp fragment was digested with EagI and SbfI and inserted back into pSARM-GagGFP to create pSARM-GagGFP-M100A.

The M-PMV proviruses encoding the R55W, -R22A, -K16A/K20A mutations have been described previously [3,5]. The GagGFP-M100A-R55W, -R22A, -K16A/K20A mutants were derived using the QuikChange Lightning Site-directed Mutagenesis Kit (Agilent Technologies, La Jolla, CA), using pSARM-GagGFP-M100A as the template and respective mutagenic primers (Table 1). Mutants were confirmed by sequencing.

Metabolic Labeling and Immunoprecipitation

A total of 4 µg of the various pSARM-derived constructs were transfected into COS-1 or 293T cells using Lipofectamine 2000 (Invitrogen, Carlsbad, CA). At 18–24 hours after transfection,

cells were starved in DMEM lacking methionine and cysteine (Gibco) for 15 minutes. Cells were subsequently labeled with 100 µCi ³⁵S-methionine (Perkin-Elmer NEN, Boston, MA) per well for 30 minutes. Following labeling (Pulse), the labeling media was replaced with complete DMEM (Gibco) and cultured for the indicated times (Chase). Cell-associated and cell-free viral proteins were then analyzed. Cell supernatants were collected from each well and cellular debris was removed by low-speed centrifugation and virus particles lysed by the addition of Triton X-100 to 1%. Cells in each well were subsequently gently lysed with 1% Triton X-100 lysis buffer [1% Triton X-100, 50mM NaCl, 25mM Tris, pH 8.0]. Cell lysates were pre-cleared with fixed *Staphylococcus aureus* (*Staph. A.*) overnight at 4°C, then M-PMV proteins were immunoprecipitated using either polyclonal goat-anti-M-PMV or rabbit-anti-Pr78 anti-sera. Immune complexes were isolated by addition of fixed *Staph. A.* and washed with lysis buffer containing 0.1% SDS (0.1% SDS, 1% Triton X-100, 50mM

Table 1. List of primers.

Plasmid	Primer Name	Primer Sequence
pSARIM-GagGFP	GagGFP F-EagI	5'-TGCCTCTCAACCTCGGCCG
	GagGFP R-AgeI	5'-CGACCGTCCCGCACCTTCATACTGTGTTGGAGG
	GFP F-AgeI	5'-TGCCTCTCCAAACACAGTATTGAGTGGGACCCGGT
	GFP R-PspXI + SA	5'-ACTCTCTCGAGGAGAGAAATCACTTGTACAGCTCGTC CATGCCGA
PSARIM-GagGFP-M100A	Kozak F-EagI ultramer	5'-CAACCTCGGCCGGGATTAAGTGAAGTAAACTCTTTGGCCCGCGGGAAACCTGCCGCGTTGGACCTGAAAGT AAGTGTGGCCGCCACCATGGACAGAGCTGTACAGCATGAGAGGTATGTGGAGCAGCTGAAGCAG
	Kozak R ultramer	5'-GAAAGCAATCTCCCACTCTTCCAGCGCTTAATGTCGATGGTTCCCTCTTGGGAAACCAAGGACAGGTGTCTTTT ACGAAATCAAAAAATTTCAAGAGTCCGCGTATTTGACCTTCACTCCCTGGTTTAAAGGGCTGCTTCAAGTCCACATA
	M100A F ultramer	5'-GCTGGAGAGAGTGGGAGATTGCTTTCAGGACTACTATAACACATTTGGCCCCGAAAAAGTTCCCGTTACTGCAATTT AGTACTGGAATCTCATTAAAGAGCTGATTGATAAAAGGAAGTGAACCCACAGTCCGCTGCCGAGTCGCCGACAGACTGAG
	M100A R-SbfI ultramer	5'-CTTTGTCCTGCAGGGAAGACTTGGCTCCTTCGTGTCACTATCCAGAGAAATTAAGGTCCAAAGTCCGGATTCTGT GATGTCITCGTCAGGTCCTGACTATTGCTTTAAGAAATTTCCCTCAGTCTGGCCGACTGGCG
pSARIM-GagGFP-R55W	R55W F	5'-GGAACCATCGACATTAAGTGGTGGAGAAAGTGGGAGA
	R55W R	5'-TCTCCACTCTTCCACCACCTTAATGTGATGGTTTC
pSARIM-GagGFP-K16A/K20A	K16A/K20A F	5'-CATGAGAGGTATGTGGACAGCTGGCGAGGCCCTTGCAGACAGGGGAGTGAAGGTCAAATAC
	K16A/K20A R	5'-GATTTTGAACCTTCACTCCCTGGTGGCAAGGGCCCTGCCCCAGCTGCCACATACCTCTCATG
pSARIM-GagGFP-R22A	R22A F	5'-GCCCTTAAAAACCGGGGAGTGAAGGT
	R22A R	5'-GACCTTCACTCCCGCGGTTTAAAGGCG

doi: 10.1371/journal.pone.0083863.t001

NaCl, 25mM Tris, pH 8.0; lysis buffer B) [21]. The immunoprecipitated proteins were resolved by electrophoresis on 12% SDS-polyacrylamide gels (SDS-PAGE) (BioRad).

Quantifying Gag Release

SDS-PAGE gels were fixed in Coomassie Blue solution [0.05% Coomassie Brilliant Blue, 10% glacial acetic acid, 50% methanol, 40% H₂O], dried and then exposed to phosphor screens and the radiolabeled protein bands were digitally acquired using the Packard Cyclone™ system. Optiquant imaging analysis software (Perkin Elmer, Shelton, CT) was used to quantify the amount of viral proteins based on the number of digitized light units (DLU) for each band. To measure the percentage of M-PMV GagGFP released, the ratio of GagGFP in the supernatant versus total cell-associated and released GagGFP was determined. Conversely, to measure the percentage of cell-associated M-PMV Gag, the ratio of total cell-associated Gag versus total cell-associated and released Gag was determined. For the positive control, the total cell-associated and released Gag (Pr78, Pr95, and Pr180) was measured.

Electron Microscopy

COS-1 cells were transfected with the indicated plasmids using Fugene 6 (Promega) transfection reagent. At 24 hours post-transfection, cells were fixed in a 2.5% glutaraldehyde fixative (10%- 25% EM grade glutaraldehyde, 50% 0.2M cacodylate buffer, 40% distilled H₂O) for at least two hours at 4°C. The cells were washed and subsequently fixed in 1% osmium fixative (2 parts 0.2M cacodylate buffer, 1 part 6% potassium ferrocyanide, 1 part 4% osmium tetroxide). The cells were then dehydrated with ethanol, followed by infiltration with a 1:1 ratio of 100% ethanol and Epon resin for at least one hour. Cells were embedded in fresh Epon resin at 60°C for 48 hours, and then cut into ultrathin sections and picked up on a copper grid. Virus particles were viewed using a JEOL-JEM 1210 transmission electron microscope.

Virus Purification

293T cells seeded onto a 10 cm culture plate were transfected with 15 µg of total DNA with Lipofectamine 2000. For co-transfected cells, a ratio of approximately 4:1 (11.5 µg and 3.5 µg of pSARM-GagGFP-M100A and pSARM-D26N, respectively) was used. Proteins in transfected cells were radiolabeled with ³⁵S for 48 hours by incubating cells in 90% Met-/Cys- DMEM (Gibco) in complete DMEM complemented with 100 µCi/mL ³⁵S. Cellular supernatants were filtered through a 0.45 µm filter (Thermo-Scientific, Waltman, MA) then overlaid on a 20%-50% sucrose (w/w), with 10% steps, discontinuous gradient. Samples were spun at 35,000 rpm at 4°C for 3 hours in the Beckman-Coulter Optima L-80 XP Ultracentrifuge using the SW41-Ti swinging bucket rotor. Using upward displacement, 1 mL fractions were isolated. 200 µl of Lysis Buffer A and 6 µl of 20% SDS were added to each fraction, and virions were immunoprecipitated with a polyclonal goat-anti-M-PMV antisera. Immune complexes were isolated by addition of fixed *Staph. A.* and washed with lysis buffer B. Immunoprecipitated proteins were resolved on 12% SDS-

PAGE gels. The density of each fraction was calculated using refractive indices.

Western Blot

Supernatants from 10cm culture dishes of 293T cells transfected with 4µg of pSARM-GagGFP-M100A or 1.6 µg and 3.2 µg pSARM-GagGFP-M100A and pSARM-X, respectively, were collected 48h post transfection. Virions were isolated by ultracentrifugation through a 25% sucrose cushion and the pellet was resuspended in 100 µl protein loading buffer. 25 µl of each sample was resolved in a 12% SDS-PAGE gel. Samples were transferred to a nitrocellulose membrane, blocked with 5% non-fat dry milk, and blotted with a mixture of two monoclonal mouse-anti-GFP antibodies (Roche, Germany). Immune complexes were subsequently bound by a horseradish peroxidase (HRP)-conjugated donkey-anti-mouse IgG antibody (Santa Cruz Biotechnology, Dallas, Texas). Pierce SuperSignal West Femto Chemiluminescent HRP substrate (ThermoScientific, Rockford, IL) was applied to blot followed by exposure to film.

Fixed Cell Microscopy

For imaging GFP-tagged as well as untagged Gag, COS-1 cells were plated at 80-90% confluency on coverslips (Fisher Scientific). Cells were co-transfected at a ratio of 4:1 with 3.2 µg WT or mutant M-PMV provirus and 0.8 µg WT or mutant pSARM-GagGFP-M100A, or were transfected with the untagged WT or mutant provirus only. 24 hours post transfection, cells were fixed with cold methanol:acetone (1:1). Coverslips containing cells transfected with GFP-tagged virus were then placed on glass slides with Prolong Antifade Gold (Invitrogen). Coverslips containing the fixed cells transfected with untagged provirus were reacted with polyclonal rabbit-anti-p27 antisera (1:500 dilution), and after washing 3X in PBS, bound antibodies were tagged with 1:10,000 diluted Alexa-488-conjugated Goat-anti-Rabbit IgG (Invitrogen) and subsequently placed on glass slides with Prolong Antifade Gold. Cells were then imaged on the Deltavision Core Imaging System (Applied Precision, Issaquah, Washington) with a CoolSnap camera at 60X magnification.

Live Cell Microscopy

CMMT cells, which constitutively produce WT M-PMV proteins, were plated to 70-80% confluency on 35-mm coverslip-bottom dishes (Matek, Ashland, MA), then transfected with 4 µg pSARM-GagGFP-M100A construct using the Lipofectamine 2000 transfection reagent. For co-localization studies with microtubules, cells were co-transfected with pSARM-GagGFP-M100A and p-mCherry-tubulin (A gift from Roger Tsien to Paul Spearman). Images were acquired using the Deltavision Core Imaging System with a CoolSnap camera. All experiments were done in a 37°C chamber with CO₂ infusion at 60X magnification.

Time-lapse Image Analysis

Deltavision (.dv) files were imported into FIJI, an NIH open-source image analysis software distribution, using the Bio-

Formats Importer (LOCI) plugin [22,23]. Particles were detected and tracked in two- and three dimensions using the Particle Tracker (MOSAIC) plugin. This plugin allowed for automated tracking of single particles based on an algorithm described by Sbalzarini et al. [24]. To calculate maximum instantaneous velocity, the instantaneous velocity at each time point was calculated using the x- and y- position of a 2D image and the following formula:

$$v_n = \frac{\sqrt{(x_{n+1} - x_n)^2 + (y_{n+1} - y_n)^2}}{t} \times \text{pixel_size}$$

v_n - instantaneous velocity at time n
 x_n - x-position at time n
 y_n - y position at time n
 t - time lapse between successive frames

pixel size - representative size/pixel

To calculate the total displacement of a trajectory, the distance between the beginning and end of a trajectory was calculated using the x- and y- position of the 2D image and the following formula:

$$d_{\text{total}} = \sqrt{(x_{\text{last}} - x_{\text{first}})^2 + (y_{\text{last}} - y_{\text{first}})^2}$$

d_{total} - total displacement
 x_{first} - x-position at beginning of trajectory
 x_{last} - x-position at end of trajectory
 y_{first} - y-position at beginning of trajectory
 y_{last} - y-position at end of trajectory

For tracking along microtubules, single particles were manually tracked by following the particle in successive frames until the particle was no longer visible or no longer able to be discriminated by eye. To define trajectory types, trajectories were categorized by visual examination of the trajectories made using the ImageJ Particle Tracker (MOSAIC) plugin. Trajectories with less than (<) 10 frames were filtered out. For quality control, the total displacement of the trajectories was calculated.

Results

Construction of an M-PMV provirus expressing a Gag-eGFP fusion protein

Initial experiments to construct a GFP-tagged M-PMV Gag protein, in which the *pro-pol* region of the genome was replaced with the gene for eGFP, resulted in the synthesis of a ~70kD protein consistent with the product of aberrant splicing (Data not shown). We therefore codon-optimized the *gag* gene and created a *gag-eGFP* gene fusion as described in Methods. In order to express the codon-optimized Gag-GFP fusion protein from an M-PMV provirus, the chimeric gene was inserted into pSARM-X to replace the *gag*, *pro* and *pol* genes as described in Methods (Figure 1A, B). Since the *pro* and *pol* genes were removed from this construct and cleavage could not occur upon release, a pSARM-X construct containing a mutation in the active site of *pro*, D26N, was used as the positive control in the experiments described below.

In order to investigate whether the Gag-GFP construct was synthesized, assembled, and transported with similar kinetics

to WT Gag, pulse-chase experiments were carried out. Immunoprecipitation of pulse-labeled cells transfected 24 hours previously with the pSARM-D26N plasmid showed major bands at 78, 95, and 180 kD (Figure 1D, Lane 1 Pulse), consistent with the Gag, Gag-Pro, and Gag-Pro-Pol precursors. Pulse-chase analysis of the new construct, pSARM-GagGFP showed two major bands at approximately 95 and 105 kD (Figure 1D, Lane 2 Pulse). Both of the bands were inefficiently released into the supernatant after a 4h chase in complete medium (Figure 1D, Lane 2 4h Sup).

An analysis of the sequence of the codon-optimized *gag* gene showed a weak Kozak-consensus sequence preceding the initiating methionine, as well as a second in-frame methionine at amino acid 100 (M100), raising the possibility that ribosomes, were traversing the primary initiating methionine of *gag* and initiating translation at M100. We therefore optimized the Kozak consensus sequence at the initiating methionine, and substituted an alanine codon for that of M100 (M100A) (Figure 1C and Figure S1). M-PMV M100A had previously been shown to have no effect on Gag processing or release kinetics [9]. The Kozak-optimization and the M100A mutation in this pSARM-GagGFP-M100A construct resulted in efficient initiation from the first methionine, eliminated expression of the truncated protein, and showed Gag-GFP expression at comparable levels to D26N (Figure 1D, Lane 3 Pulse). Moreover, these modifications resulted in more efficient transport and release of the Gag-GFP fusion protein (Figure 1D, Lane 3 4h sup.).

A pulse-chase analysis also revealed that the Env glycoprotein was inefficiently expressed in the Gag-GFP fusion construct even though the *env* gene was present. In wild-type M-PMV Env is expressed from a spliced mRNA, and all putative *env* splice acceptor sites (Figure S1) are present in the region flanking the 3' end of GFP in the pSARM-GagGFP-M100A fusion, but this construct still yielded background levels of Env expression (Figure 1E). Analysis of the nucleotide sequence of non-codon-optimized versus codon-optimized M-PMV Gag showed that a majority of the potential splice branch points were removed during codon-optimization (data not shown). The possibility that the branch point for Env splicing was in the *pro* or *pol* genes, which have been completely removed from this construct, also cannot be ruled out.

Expression of eGFP-fused Gag alone causes aberrant capsid formation

To determine if the fusion of a 27 kD eGFP protein to the carboxyl terminus of Gag impacted the shape and size of the resulting immature capsids, capsid structure was visualized using transmission electron microscopy (TEM). 293T cells were transfected with pSARM-GagGFP-M100A or pSARM-X, and prepared for TEM. The results from analysis of thin section electron-micrographs showed that capsids from cells transfected with pSARM-GagGFP-M100A were aberrantly shaped in comparison to capsids from cells transfected with the WT provirus (Figure 2B), although they were distributed similarly throughout the cytoplasm (Figure S2A and B). The immature capsids in cells transfected with pSARM-GagGFP-M100A were larger in diameter, were not uniform in shape, and

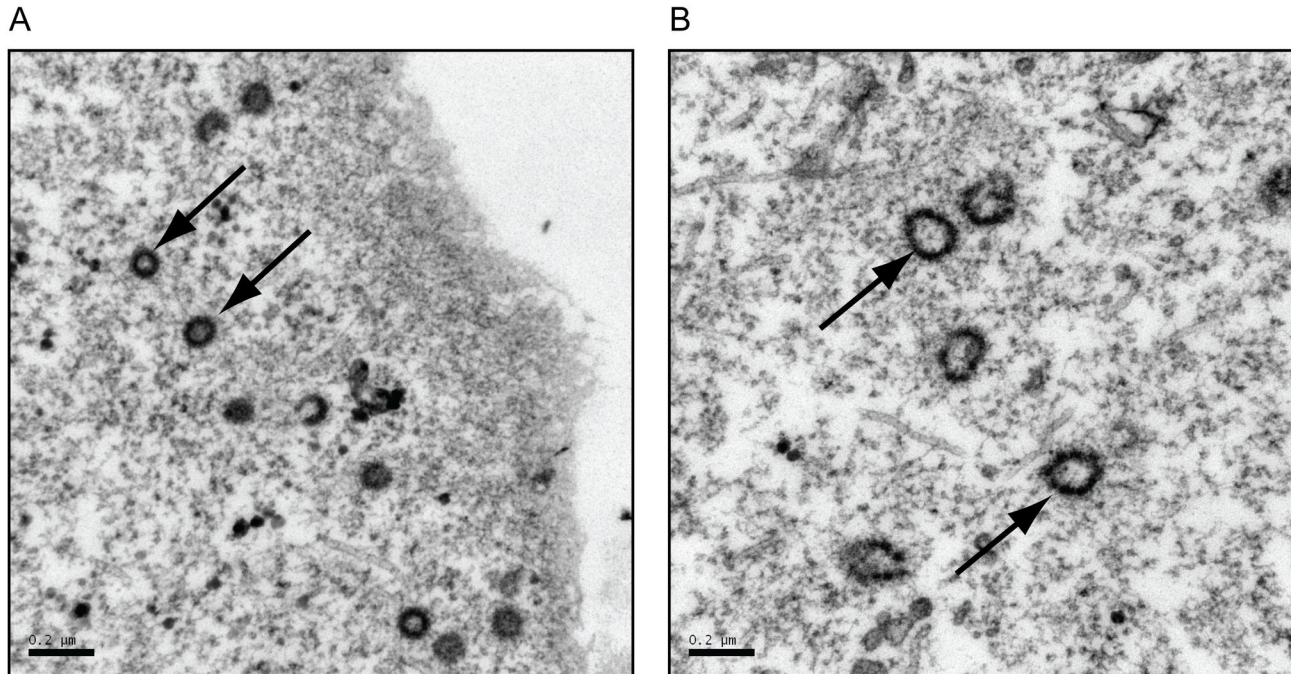


Figure 2. Verification of viral particles shapes by transmission electron microscopy. COS-1 cells were transfected with pSARM-X wild type provirus (A) or pSARM-GagGFP-M100A (B). 24 hours after transfection were cells fixed in a 2.5% glutaraldehyde fixative for 2 hours at 4 °C. The cells were washed and subsequently fixed in 1% osmium fixative. The cells were then dehydrated with ethanol, followed by infiltration with 100% ethanol and Epon resin for at least one hour. Cells were then embedded in fresh Epon resin at 60°C for 48 hours then cut into ultrathin sections and picked up on a copper grid. The arrows in (A) point to WT intracellular capsids of homogenous shape, with a diameter of approximately 100 nm. The arrows in (B) point to GagGFP-containing intracellular capsids having a beads-on-a-string shape and varying diameters greater than 100 nm. Bar = 200 nm.

doi: 10.1371/journal.pone.0083863.g002

had a “beads-on-a-string” morphology compared to the more compact, homogenously-shaped immature capsids of the WT (Figure 2B versus 2A).

Release kinetics of capsid is delayed in the absence of WT virus and rescued during cotransfection with WT

Since previous reports have shown that Env expression is necessary for efficient virion release and capsid maturation [2,7,10,12], and the TEM data showed improper capsid morphology when cells were transfected with pSARM-GagGFP-M100A alone, a pulse-chase experiment was carried out to determine whether cotransfection with WT pSARM-X changed the kinetics and efficiency of Gag-GFP release from cells. Proteins were pulse-labeled with ³⁵S methionine for 30min and chased with unlabeled media for 2 or 4 hours. Cell lysates from the pulse and each chase time-point, as well as cell culture medium (supernatants) from the chase plates were immunoprecipitated with rabbit anti-p27^{CA} antibody (Figure 3A). The mutant pSARM-D26N was used as the positive control (Lane 1). Radioactivity corresponding to the immunoprecipitated proteins were quantitated as described in Methods. Consistent with previous reports, approximately 2 hours after the pulse, 50% of the cell-associated precursors

(Pr78, Pr95, and Pr180) had been released into the culture medium (Figure 3B, Figure S3). Cells transfected with pSARM-GagGFP-M100A alone showed a large delay in release kinetics, and even after a 4 hour chase, only 45% had been released. For cells cotransfected at a ratio of 4:1 D26N to pSARM-GagGFP-M100A, which mimics WT protein expression, in which Pr95 and Pr180 are translated 15% and 5% of the time respectively through ribosomal slippage [25,26], there was an increase kinetics of Gag-GFP release, with 50% of Gag released approximately 3 hours after the pulse (Figure 3A, lane 3; Figure 3B). TEM microscopy of these cotransfected cells revealed capsids with WT morphology (Figure S2C)

In order to confirm that co-assembly of Gag-GFP and untagged Gag was occurring in co-transfected cells, two different experiments were performed. In the first cells were either singly transfected with pSARM-GagGFP-M100A, or co-transfected with this vector and WT pSARM-X, which expresses a functional viral protease. A Western blot analysis, using a mouse anti-GFP antibody, of virions pelleted through a 25% sucrose cushion showed that, in contrast to the 110 kD Gag-GFP released from singly transfected cells, the Gag-GFP

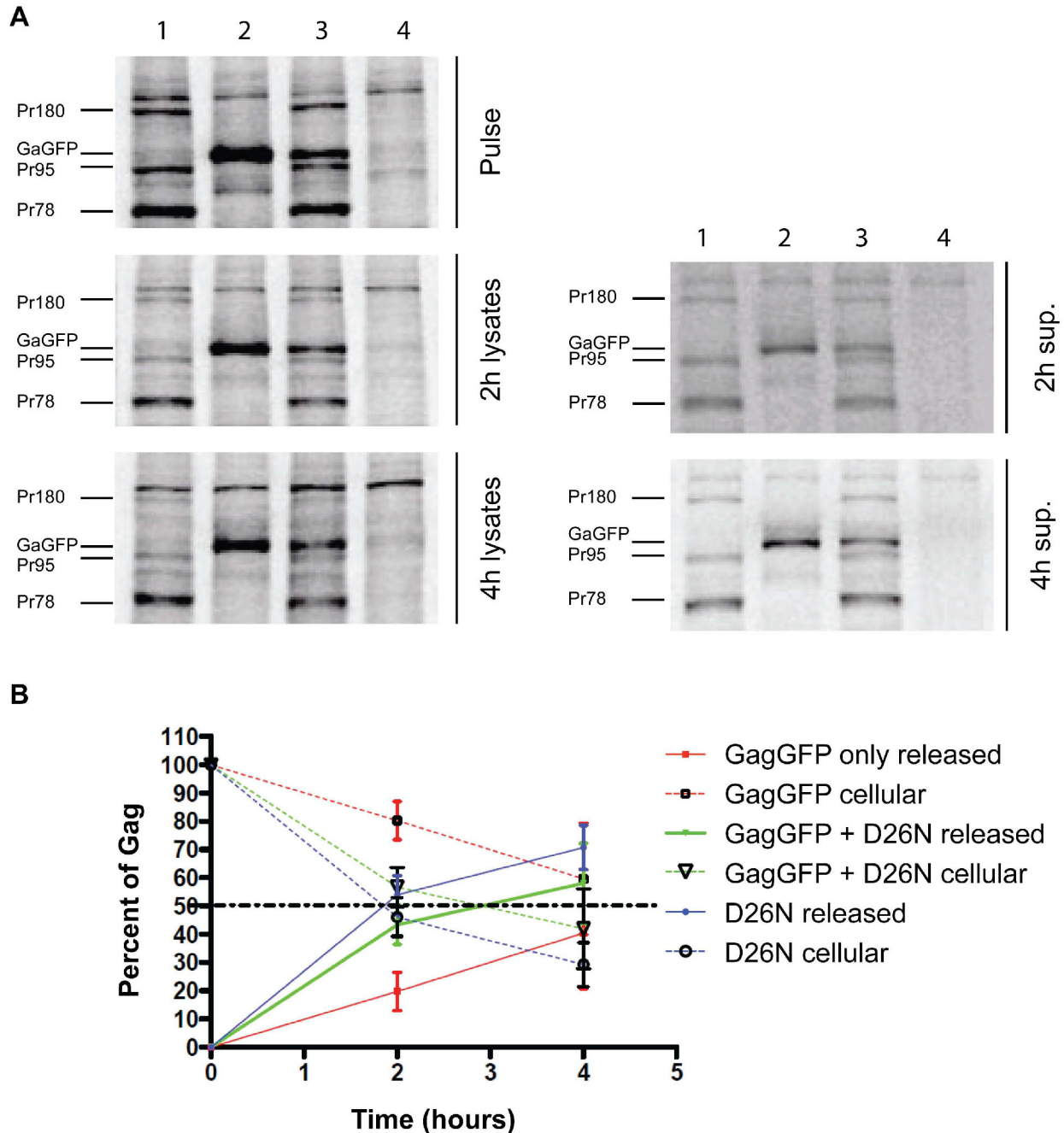


Figure 3. Analysis of release kinetics of the GagGFP fusion protein. (A) 293T cells (untransfected, Lane 4) were transfected with pSARM-D26N (Lane 1), pSARM-GagGFP-M100A (Lane 2) and co-transfected (Lane 3) with pSARM-D26N and pSARM-GagGFP-M100A at a 4:1 ratio. Viral proteins were metabolically labeled with ^{35}S methionine and then immunoprecipitated with rabbit anti-p27^{CA} antibody from lysates of pulse-labeled cells (pulse), pulse-labeled and 2h and 4h chased cells (2h lysates and 4h lysates) and from the culture media collected after 2h or 4h chase respectively (2h and 4h sup.). Positions of the viral precursor proteins Pr180 (Gag-Pro-Pol), Pr95 (Gag-Pro) and Pr78 (Gag) and product of pSARM-GagGFP-M100A are shown. (B) The percentage of cell associated viral protein was measured by calculating the ratio of protein from the lysates versus the total protein (lysates and sup.). Conversely, the percentage of released viral protein was measured by calculating the ratio of protein from the supernatants versus the total protein. For D26N, the total amount of cell-associated and released Gag is calculated by adding the amounts of each of the precursors (Pr180, Pr95, and Pr78). For GG and GG co-transfections, the amount of Gag cellular and released Gag corresponds to the amount of Gag-GFP.

doi: 10.1371/journal.pone.0083863.g003

in virions from co-transfected cells was efficiently cleaved to the expected p4-GFP (Figure S4, pSARM-GagGFP + WT).

In the second approach, supernatants from cells transfected with pSARM-GagGFP-M100A or co-transfected with pSARM-D26N, and radiolabeled with ^{35}S methionine, were analyzed on discontinuous sucrose gradients. As can be observed in Figure S5, Pr78 and Gag-GFP from co-transfected cells were observed primarily in fractions 4 and 5 (density 1.12 g/mL and 1.17 g/mL). Similar results were obtained for virus released from cells singly transfected by pSARM-D26N (Pr78) and pSARM-X (p27 and gp70). In contrast, virions released from pSARM-GagGFP-M100A transfected cells exhibited a more heterogeneous density and were observed in fractions 3-6 (density 1.08 g/mL - 1.20 g/mL).

Because of these results, further experiments with the pSARM-Gag-GFP-M100A vector included co-transfection with WT pSARM-X at a ratio of 4:1 (WT: GagGFP), or transfection into CMMT cells, a rhesus macaque mammary tumor fibroblast cell line that constitutively expresses WT M-PMV.

M-PMV GagGFP subcellular localization is similar to untagged M-PMV provirus

To verify that the GFP fusion was not affecting cellular localization of Gag, COS-1 cells were transfected with untagged forms of wild type provirus or previously described M-PMV Gag mutants (R55W, R22A, K16A/K20A) and following fixation were stained with a rabbit anti-Gag antibody. The staining pattern was compared to COS-1 cells co-transfected with pSARM-GagGFP-M100A or the same vector into which the R55W, R22A, or K16A/K20A mutations were introduced, along with the respective pSARM provirus at a 1:4 ratio.

The COS-1 cells producing untagged forms of Gag were fixed 24 h after transfection and immunostained; the cells producing GFP fused forms of Gag were fixed 24h after transfection.

Previous work with immunostained wild-type Gag reported a dispersed distribution of Gag in the cytoplasm, with a higher concentration of signal in pericentriolar region, which is the site of particle assembly and Env recruitment [2,10,19]. Similar subcellular localization was observed here in COS-1 cells expressing both untagged (Figure 4A, WT untagged) and WT GagGFP (Figure 4A, WT GFP-tagged). However, the WT GagGFP displayed a somewhat denser staining pattern, likely owing to enhanced protein production resulting from the codon optimization of gag.

Stansell et al. showed that a double mutation in the matrix domain, K16A/K20A results accumulation of capsids on and efficient budding into intracellular vesicles, with a concomitant 50 to 70% reduction in the efficiency of viral particle release [5]. In both the native and GFP-tagged systems, this mutation resulted in fewer discrete fluorescent capsids in the cytoplasm and the presence of large brightly fluorescent bodies, consistent with the previously described phenotype of budding into intracellular vesicles (Figure 4A, K16A/K20A Untagged and GFP-tagged). Co-staining with the red membrane dye, Dil, supports the conclusion of budding into vesicles (data not shown).

The R55W mutation within the matrix domain of M-PMV Gag, is known to significantly reduce intracellular assembly and redirect it to the plasma membrane of the cell [3]. In the immunostained cells, the dispersed intracytoplasmic staining of capsids was drastically reduced and was replaced by an intense fluorescent signal along the plasma membrane (Figure 4A, R55W Untagged). A similar, but more intense staining pattern was observed in the Gag-GFP expressing cells (Figure 4A, R55W, GFP-tagged).

Stansell et al also showed that an R22A mutation in the matrix protein of Gag results in a complete block to virus particle release from infected cells [5]. The particle release defect of the GFP-tagged and untagged form of R22A Gag was verified in a pulse-chase experiment. The cells were pulsed for 30min with ^{35}S - methionine and then chased for 4h. M-PMV proteins were immunoprecipitated, using a goat anti-MPMV antibody, then analyzed on an SDS-PAGE gel, from both the pulse (Figure 4B, Pulse gels) and pulse-chase cell lysates (Figure 4B, 4h lysates), as well as from the cell culture medium of the 4h chased cells (Figure 4B, 4h sup). Control wells were transfected with WT-D26N (Figure 4B, lane 2), pSARM-GagGFP-M100A (Figure 4B, lane 3), and pSARM-X (Figure 4B, lane 4), and detectable amounts of Pr78, Gag-GFP, and p27 respectively were observed in the 4h supernatants. In contrast, while pSARM-R22A (Figure 4B, lane 5) and pSARM-GagGFP-M100A-R22A (Figure 4B, lane 6) transfected cells exhibited similar precursor protein patterns in the pulse and pulse-chase cell lysates to their WT counterparts, no released proteins (p27 or Gag-GFP) were detectable in the 4h-supernatants.

Real-time imaging of the Gag-GFP fusion construct shows lateral movement throughout the cell

M-PMV-expressing CMMT cells were transfected with pSARM-GagGFP-M100A and visualized in real-time with exposures every 5 seconds for 2 minutes. Using the Particle Tracker plugin on the FIJI software package, particles were detected and then automatically tracked [24]. Trajectory data showed three different populations of fluorescent particles (Figure 5A, Movie S1, Figure S6). Population 1 showed trajectories with restricted movement and little to no displacement from the beginning to the end of the trajectory path (Figure 5B.1). The median displacement for trajectories that are seen in this population is 1.6 pixels, and occurred approximately 15% of the time for trajectories containing at least 10 time points (Figure S6A and B). Population 2 showed particles moving in an erratic, Brownian manner, with very little displacement (Figure 5B.2). The trajectories in this population appear larger than those of the first population, although there is very little long-range movement within the trajectory. The median total displacement of particles in this population is significantly higher (6.9 pixels) than in Population 1. Tracks in this population made up approximately 41% of the trajectories that had at least 10 times points (Figure S6A and B). Population 3, occurring 44% of the time, displayed long, linear tracks with, in most cases, significant displacement from the beginning of the track to the end (Figure 5B.3). The median displacement in this population was 15.5 pixels (Figure S6B).

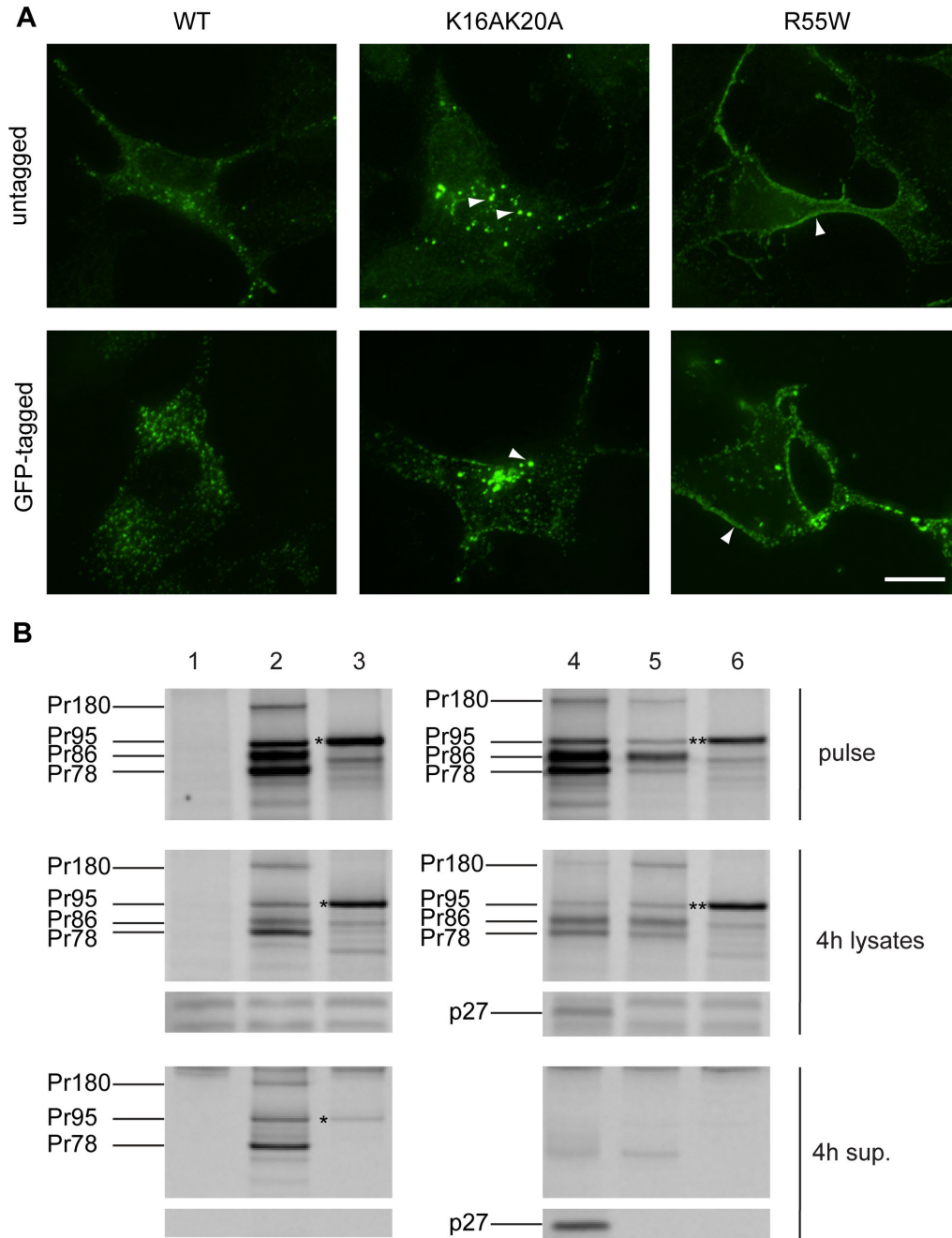


Figure 4. Comparison of untagged and GFP-tagged M-PMV Gag wild-type and mutants in COS-1 cells. (A) COS-1 cells were cotransfected at the ratio of 4:1 with pSARM-WT and pSARM-GagGFP-M100A, pSARM-R55W and pSARM-GagGFP-M100A-R55W, or pSARM-K16A/K20A and pSARM-GagGFP-M100A-K16A/K20A (tagged) or transfected with the untagged pSARM-WT, pSARM-R55W or pSARM-K16A/K20A mutants (untagged). Cells were fixed 24 h post-transfection with cold methanol:acetone (1:1). Cells transfected with untagged provirus were stained by primary rabbit antibody against M-PMV p27 and secondary FITC-conjugated anti-rabbit antibody. Localization of K16A/K20A mutant into intracellular vesicles and localization of R55W on plasma membrane is shown. Scale bar, 20 μ m. (B) COS-1 cells (untransfected, Lane 1) were transfected with pSARM-D26N (Lane 2), pSARM-GagGFP-M100A (Lane 3), pSARM-X (Lane 4), pSARM-R22A (Lane 5) and pSARM-GagGFP-M100A-R22A (Lane 6). Viral proteins were metabolically labeled with [35 S] and then immunoprecipitated with goat anti-MPMV antibody from lysates of pulse-labeled cells (pulse), pulse-labeled and 4h chased cells (4h lysates) and from the culture medium collected after the 4h chase (4h sup.). Positions of the viral precursor proteins Pr180 (Gag-Pro-Pol), Pr95 (Gag-Pro), Pr86 (Envelope) and Pr78 (Gag) are shown. Products of pSARM-GagGFP-M100A (*) and pSARM-GagGFP-M100A-R22A (**) are shown.

doi: 10.1371/journal.pone.0083863.g004

This lateral movement across the cell was bidirectional in nature at times, and the instantaneous velocities oscillated between periods of complete cessation of movement followed by periods of long-range movement. The median, maximum instantaneous velocity of tracks in Population 3 was approximately 700nm/s (Figure 5C).

Fluorescently-labeled capsids associate and transport along microtubules

The results from the live cell imaging of capsid transport suggested a possible role for microtubules in their intracellular transport. Specifically, the bidirectional movement and the oscillating velocities of capsid movement have been previously described for endosomal movement as well as viral movement along microtubules [27-30]. To test whether the capsids were associated with and were transported along microtubules, CMMT cells were co-transfected with pSARM-GagGFP-M100A and mCherry-labeled tubulin and then imaged 24 hours post-transfection. Images were captured every second for one minute in one z-stack. Time-lapse data of these cells shows a majority of the capsids are not moving, but nevertheless colocalize with a tubule (Movie S2). When a smaller section of the cell is examined at higher effective magnification, capsids that display rapid, lateral movement with significant displacement appear to traffic along the path of the microtubules (Figure 6). Examples of retrograde and anterograde movement along tubules can be seen, as well as examples of capsid that appear to switch from one tubule to another (data not shown).

Discussion

To date, the host cell factors involved in the assembly and intracellular trafficking of retroviral proteins remain poorly understood. For M-PMV, much work has been done to elucidate the cellular factors involved in assembly of premature capsids in the pericentriolar region of the cell. Factors such as the microtubule organizing center and dynein motors have previously been described to interact with the Gag assembling on polysomes through an interaction with the cytoplasmic targeting and retention signal in the matrix domain of Gag. It has also been shown that the cellular vesicular trafficking system has a role in intracellular capsid transport, since a temperature block of 20°C, which reversibly inhibits vesicle trafficking, causes an accumulation of capsid particles at the pericentriolar site of assembly [2,7,10,12]. In addition, several mutations in the cytoplasmic domain of the Env glycoproteins [2,7,10,12], and others in the Gag polyprotein has suggested that endocytic recycling pathways are critical for Env's involvement in efficient capsid intracellular transport [7,10]. However, most of these studies utilized population-based pulse-chase experiments and fixed cell immunofluorescence. The availability of fluorescently labeled M-PMV proteins that can be visualized in a living cellular system clearly has the potential to provide more insight into the roles of cellular factors in the intracellular transport of M-PMV capsids from their site of assembly to the plasma membrane site of egress.

Constructing and optimizing an M-PMV Gag-GFP fusion

The goal of this study was to construct an M-PMV Gag-GFP fusion protein that could be visualized in live cells and to use this construct to investigate intracellular trafficking of M-PMV capsids. First, the *gag*-gene of M-PMV was codon optimized to prevent aberrant splicing observed with the native coding region. Despite this, fusion of *gfp* to the 3' end of the codon-optimized *gag* resulted in the production of a truncated GFP-tagged protein, in addition to the full-length product. This shorter product was shown to result from ribosomal initiation from an internal, in-frame methionine 100 amino acids from the primary initiation codon for *gag*. Although this methionine is present in the WT M-PMV *gag*, only background levels of protein are initiated from this methionine. However, previous work had shown that even single nucleotide changes to the second codon of Gag could result in ribosomes skipping the initiating methionine (M1) and initiating translation of a truncated Gag more than 50% of the time [31]. It is therefore probable that initiation from this second methionine in the GFP fusion construct was due to codon optimization, which allowed the ribosome to recognize this second methionine at a higher rate than it would in the non-codon optimized *gag*. Introduction of the M100A mutation, previously shown to have no effect on virus infectivity, and optimization of the Kozak sequence before M1, resulted primarily in full-length translation products.

Another caveat to constructing a Gag-GFP fusion protein that is biologically relevant is the fact that fusion of a 27-kD GFP protein to the carboxyl-terminus of Gag could interfere with capsid morphogenesis. Indeed in a previous study, only incomplete and aberrant particles were assembled when the frame-shifting signal at the end of *gag* was mutated to generate only Gag-Pro and Gag-Pro-Pol precursors [32]. When 293T cells were transfected with the pSARM-Gag-GFP-M100A construct alone, transmission electron microscopy showed the assembly of larger, non-spherical capsids that had an unusual "beads-on-a-string" external surface. Additionally, when virus was subjected to density centrifugation through a 20%-50% sucrose gradient, GagGFP-containing virions appear in fractions 3-6, while WT virions and virions from co-transfected cells were primarily present in the 4th and 5th fractions, confirming that virions from cells transfected with pSARM-GagGFP-M100A alone have a more diverse and in some cases lower density than WT virions. Moreover, pulse-chase analyses showed that the kinetics of release for these aberrant capsids was also greatly reduced. In order to assemble a GFP-tagged capsid that is transported with kinetics similar to a WT capsid, co-assembly of Gag and Gag-GFP proteins in ratios resembling Gag and Gag-Pro must occur. Because of this, all experiments involving the Gag-GFP fusion protein were performed in the context of WT virus, either by cotransfection or by transfection of Gag-GFP into the CMMT cell line that constitutively expresses WT M-PMV.

To confirm further that the Gag-GFP fusion protein behaved similarly to untagged, WT Gag, a comparison was made of the subcellular localization of both WT and several well-characterized Gag mutants. Immunofluorescent staining showed that GFP-tagged Gag localized similarly to the untagged Gag. WT forms of both exhibited a dispersed

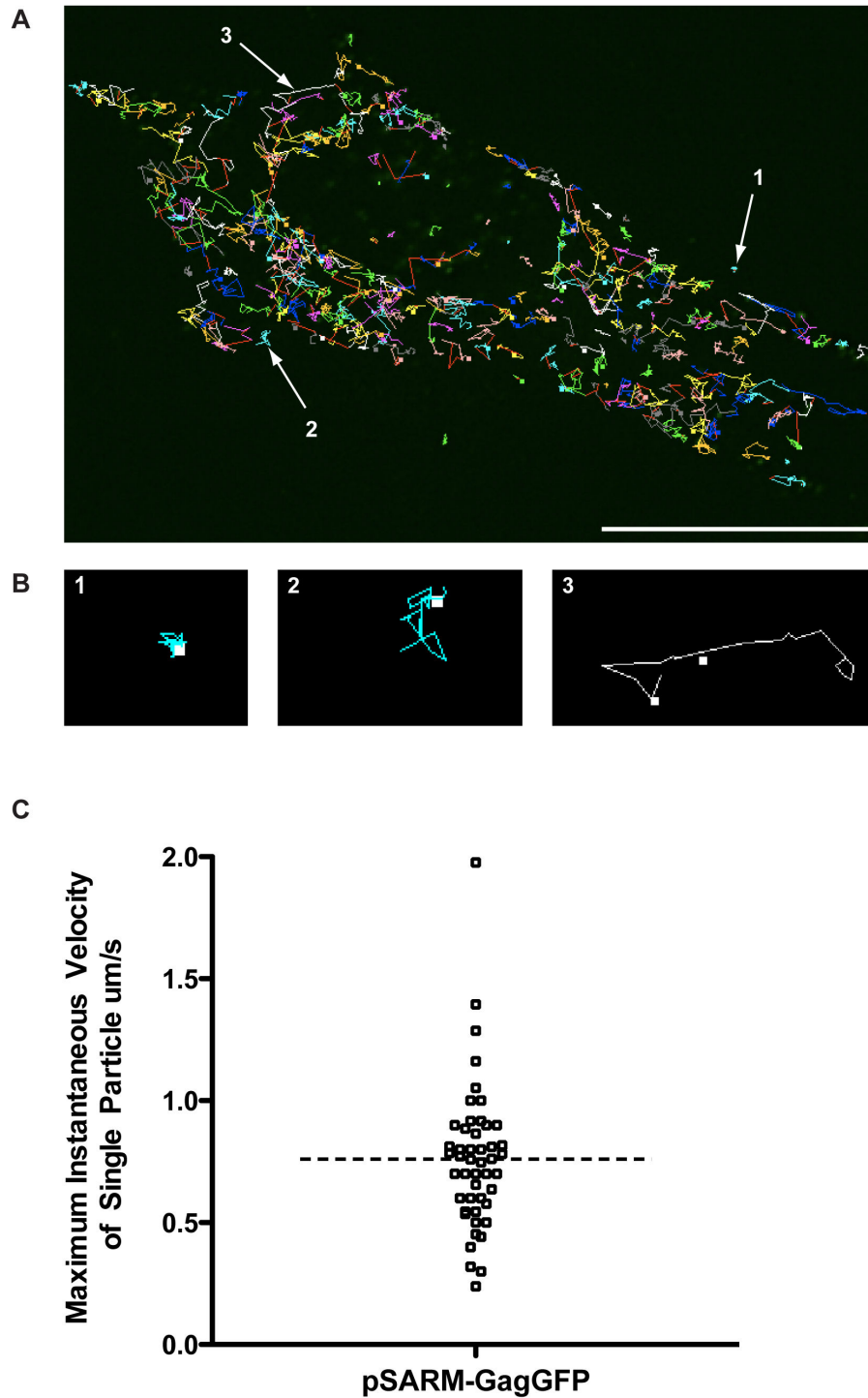


Figure 5. Real-time imaging of GagGFP fusion protein in live cells. (A) M-PMV expressing CMMT cells were transfected with pSARM-GagGFP-M100A and visualized 24 hours later in real-time every 5 seconds for 2 minutes. Using the Particle Tracker plug-in on FIJI, particles were detected and then tracked. Scale bar = 20 μm . Real time imaging of these frames is shown in movie S1. (B) Trajectory data showed trajectories with restricted movement and little to no displacement from the beginning to the end of the trajectory path (1), trajectories where the particle moved in an erratic, Brownian manner, and displayed very little displacement (2) and long tracks with significant displacement from the beginning of the track to the end (3). (C) To calculate the instantaneous velocity for a trajectory in population 3, the distance traveled between each time point was calculated and divided by the time interval (5s). Maximum instantaneous velocity refers to the maximum instantaneous velocity for an individual trajectory.

doi: 10.1371/journal.pone.0083863.g005

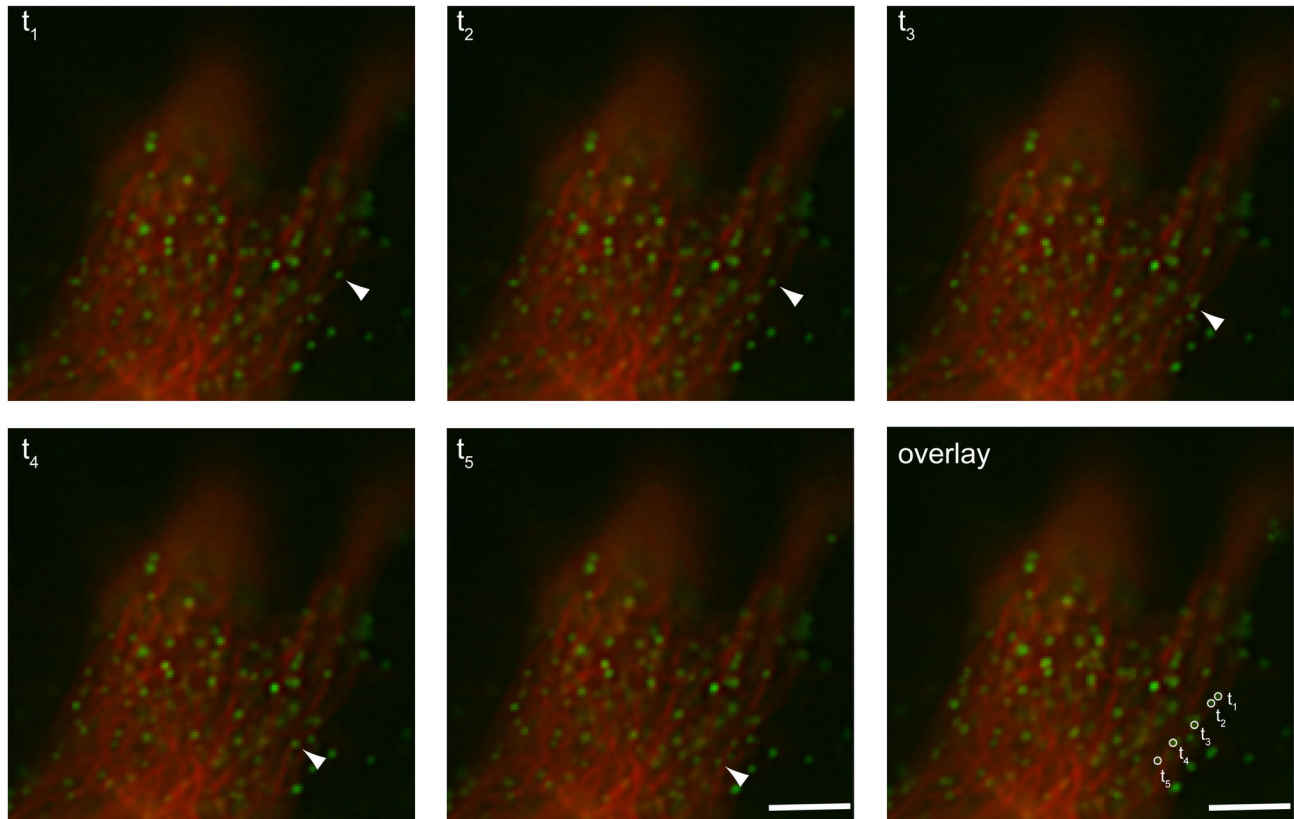


Figure 6. Real-time imaging of GFP labeled virus-like particles along the microtubule. M-PMV expressing CMMT cells were cotransfected with pSARM-GagGFP-M100A and mCherry-tubulin and imaged 24 hours later in real-time. Images were captured at consecutive intervals of 1 second for one minute in one focal plane. Scale bar= 1 μ m. Real time imaging of these frames is shown in movie S2.

doi: 10.1371/journal.pone.0083863.g006

distribution of fluorescent puncta, with a concentration in the pericentriolar region. This pattern was dramatically altered in pSARM-GFP-M100 vectors encoding the R55W and K16A/K20A mutants. In the former, Gag staining outlined the periphery of the cells with predominantly diffuse staining in the cytoplasm, consistent with capsid assembly now occurring on the plasma-membrane [3]. And for the latter, brightly staining vesicular structures were observed, consistent with budding into a variety of intracellular vesicles [5]. Along with this visual evidence that the Gag-GFP fusion protein behaves similarly to untagged Gag, a pulse-chase analysis of the tagged and untagged R22A mutant showed that, like the untagged mutant, pSARM-GagGFP-M100A-R22A also failed to be released from cells. This provides compelling evidence that the Gag-GFP fusion protein utilizes virus-cell interactions comparable to the untagged Gag, and can be used for characterizing the nature of M-PMV Gag intracellular transport in dynamic, real time applications.

Evidence for M-PMV capsid use of the cellular cytoskeleton for transport

Particle tracking of GFP-tagged capsids in transfected CMMT cells and COS-1 cells provided evidence for three types of capsid movement. In the first, the particles exhibited very little lateral movement, consistent with them being anchored to a subcellular structure. In the second, capsid movement was consistent with Brownian movement – presumably representing capsids free in the cytoplasm. Finally, a subset of capsids exhibited long-range oscillatory movement, with kinetics that are consistent with movement on microtubules. Characterization of endosomal intracellular transport, as well as the interaction of several different viruses with the microtubular network of the cell, shows that microtubular cargo have instantaneous velocities that are oscillatory in nature and movement is bidirectional [27-30,33]. The microtubule motors involved in anterograde transport toward the plasma membrane, kinesins, have been shown to propel cargo as fast as 4 μ m/s, as well as to stall cargo during “pauses” [27-29,33,34]. Microtubule-dependent transport of viruses has been extensively studied in Vaccinia virus [30,35]. In these studies, intracellular enveloped viruses (IEV) have been shown

to require the use of microtubule motor, kinesin-1, for saltatory transport from their intracellular site of replication and assembly to the cortical actin layer. These studies have shown a wide range of instantaneous velocities, with an average of approximately 8 $\mu\text{m/s}$. Live cell imaging analysis from these studies also describe bidirectional movement of IEVs and movement consistent with switching of IEVs from one microtubule to another.

In this current study, a subset of capsids was observed to be associated with microtubules, but not moving. Since these kinetic studies capture only a very small fraction of time (1-2 minutes), it is possible that the microtubule-associated capsids are stalled along the microtubule at this time. The capsids that appear to be transporting along the microtubules have instantaneous maximum velocities up to 2 $\mu\text{m/s}$ with a median of 700 nm/s, when images were captured every 5 seconds. The capsid movement observed in our system also displays bidirectional transport, and evidence of jumping from one microtubule to another microtubule can also be seen. These observations provide strong support for the hypothesis that the capsids are utilizing microtubules for intracellular transport.

A major caveat to this study is that the real-time imaging only captures approximately 4% of the time necessary for 50% of capsids to be released from the cell. This means the imaging is limited to characterizing localized movement of individual capsids in a small window of time. Further experimentation must be performed to characterize the collective nature of capsid movement over longer periods of time.

Conclusion

The current study shows that employing the use of a fluorescently-tagged M-PMV Gag protein can be useful in characterizing the nature of M-PMV Gag assembly and transport in a real-time imaging system. In order to utilize this system, however, it is necessary to use a codon-optimized Gag with an M100A mutation in the MA protein to prevent internal initiation. Codon-optimization results in a dysfunction in splicing necessary for Env expression, and Env expression has been shown to be critical in efficient capsid release kinetics. TEM results also show that transfection of 293T cells with the Gag-GFP fusion protein results in aberrantly shaped capsids. Both of these phenotypes amplify the importance of co-expression of the Gag-GFP fusion protein with the WT or D26N Gag from a proviral vector, which both express Env at WT levels and allows for co-assembly for tag and untagged Gag proteins. Following optimization of these conditions, Gag-GFP expressing cells display intracellular movement of assembled capsids that is consistent with transport along microtubules.

Supporting Information

Figure S1. Annotated nucleotide and amino acid sequence of pSARM-GagGFP-M100A.

The nucleotide sequence for pSARM-GagGFP-M100A was imported into the bioinformatics software Geneious™ version 5.5.5 (Biomatters, www.geneious.com). With this software, the nucleotide sequence was translated in the correct frame. The

position of the optimized Kozak consensus sequence, the initiating methionine (M1), the methionine to alanine substitution (M100A), GA-linker used to separate Gag and eGFP, and two putative splice acceptor sites for Env were annotated.

(PDF)

Figure S2. Transmission electron microscopic imaging of the intracellular localization of immature capsids.

(TIFF)

Figure S3. Percent GagGFP released from cells.

Quantitation of the % GagGFP released from the cell at each time point from pulse-chase analysis of 293T cells transfected with pSARM-GagGFP-M100A only (red), a 4:1 ratio of pSARM-D26N and pSARM-GagGFP-M100A as compared to the total amount of Gag released from cells transfected with pSARM-D26N (blue).

(TIFF)

Figure S4. Western blot analysis of virus released from cotransfected cells.

(A) Western blot of supernatants from 293T cells, untransfected (lane 1), or transfected with pSARM-GagGFP-M100A only (lane 2) or a 4:1 ratio of pSARM-X and pSARM-GagGFP-M100A (lane 3). Supernatants were resolved on 12% SDS-PAGE, and blotted with antibody against GFP. (B) Quantitation of band intensity of western blot. Black bars represent the band corresponding to the uncleaved Gag-GFP fusion and white bars represent the cleaved p4-GFP found in 293T cells transfected with pSARM-GagGFP-M100A, or cotransfected with pSARM-GagGFP-M100A and pSARM-X.

(TIFF)

Figure S5. Density fractionation of virions released into the cell supernatant.

(A) Sucrose gradient density fractionation of supernatants from 293T cells cotransfected with pSARM-D26N and pSARM-GagGFP, pSARM-GagGFP alone, pSARM-X, pSARM-D26N, or untransfected (mock). Culture supernatants were collected 48 hours after transfection and overlaid on a 20%-50% (w/w) sucrose gradient, followed by ultra-centrifugation in at 35,000 rpm for 3 hours in a SWTi-41 rotor. Fractions were collected by upward displacement and immunoprecipitated with an antibody against whole M-PMV. Samples were resolved on 12% SDS-PAGE gel. (*) represents the band corresponding to Gag-GFP fusion protein. (B) The refractive index of each fraction was measured using a refractometer. The density was determined by comparing the refractive indices to a standard conversion table for the density and refractive index in sucrose.

(TIF)

Figure S6. (A) Percentage of each type of trajectory found in Figure 5A.

Analysis is based on categorizing 20 different

trajectories from 4 subsections of the cell (left of nucleus, above nucleus, below nucleus, and right of nucleus). (B) The total displacement of 10 separate trajectories from each population type was calculated. The line represents the median for each population. Statistical analysis was based on the non-parametric Mann-Whitney t-test.

(TIFF)

Movie S1. Real-time imaging of GagGFP fusion in CMMT cells. M-PMV expressing CMMT cells were transfected with pSARM-GagGFP-M100A and visualized on the Deltavision Core Imaging System 24 hours later. 3D images (with 10 z-sections spaced 200 nm apart) were captured every 5 seconds for a total of 2 minutes. The video is a projection of all z-sections in one plane.

(AVI)

Movie S2. Real-time imaging of GFP labeled virus-like particles along the microtubule. M-PMV expressing CMMT cells were cotransfected with pSARM-GagGFP-M100A and mCherry-tubulin and imaged 24 hours later in real-time. Images were captured at consecutive intervals of 1s for one minute in one focal plane.

References

- Choi G, Park S, Choi B, Hong S, Lee J et al. (1999) Identification of a cytoplasmic targeting/retention signal in a retroviral Gag polyprotein. *J Virol* 73: 5431-5437. PubMed: 10364290.
- Sfakianos JN, LaCasse RA, Hunter E (2003) The M-PMV cytoplasmic targeting-retention signal directs nascent Gag polypeptides to a pericentriolar region of the cell. *Traffic* 4: 660-670. doi:10.1034/j.1600-0854.2003.00125.x. PubMed: 12956869.
- Rhee SS, Hunter E (1990) A single amino acid substitution within the matrix protein of a type D retrovirus converts its morphogenesis to that of a type C retrovirus. *Cell* 63: 77-86. doi: 10.1016/0092-8674(90)90289-Q. PubMed: 2170021.
- Prchal J, Junkova P, Strmiskova M, Lipov J, Hynek R et al. (2011) Expression and purification of myristoylated matrix protein of Mason-Pfizer monkey virus for NMR and MS measurements. *Protein Expr Purif* 79: 122-127. doi:10.1016/j.pep.2011.05.010. PubMed: 21640189.
- Stansell E, Apkarian R, Haubova S, Diehl WE, Tytler EM et al. (2007) Basic residues in the Mason-Pfizer monkey virus gag matrix domain regulate intracellular trafficking and capsid-membrane interactions. *J Virol* 81: 8977-8988. doi:10.1128/JVI.00657-07. PubMed: 17596311.
- Stansell E, Tytler E, Walter MR, Hunter E (2004) An early stage of Mason-Pfizer monkey virus budding is regulated by the hydrophobicity of the Gag matrix domain core. *J Virol* 78: 5023-5031. doi:10.1128/JVI.78.10.5023-5031.2004. PubMed: 15113883.
- Song C, Dubay SR, Hunter E (2003) A tyrosine motif in the cytoplasmic domain of mason-pfizer monkey virus is essential for the incorporation of glycoprotein into virions. *J Virol* 77: 5192-5200. doi:10.1128/JVI.77.9.5192-5200.2003. PubMed: 12692221.
- Chung HY, Morita E, von Schwedler U, Müller B, Kräusslich HG et al. (2008) NEDD4L overexpression rescues the release and infectivity of human immunodeficiency virus type 1 constructs lacking PTAP and YPXL late domains. *J Virol* 82: 4884-4897. doi:10.1128/JVI.02667-07. PubMed: 18321968.
- Sakalian M, Hunter E (1999) Separate assembly and transport domains within the Gag precursor of Mason-Pfizer monkey virus. *J Virol* 73: 8073-8082. PubMed: 10482556.
- Sfakianos JN, Hunter E (2003) M-PMV capsid transport is mediated by EnvGag interactions at the pericentriolar recycling endosome. *Traffic* 4: 671-680. doi:10.1034/j.1600-0854.2003.00126.x. PubMed: 12956870.
- Punnonen EL, Ryhänen K, Marjomäki VS (1998) At reduced temperature, endocytic membrane traffic is blocked in multivesicular carrier endosomes in rat cardiac myocytes. *Eur J Cell Biol* 75: 344-352. doi:10.1016/S0171-9335(98)80067-8. PubMed: 9628320.
- Song C, Micoli K, Bauerova H, Pichova I, Hunter E (2005) Amino acid residues in the cytoplasmic domain of the Mason-Pfizer monkey virus glycoprotein critical for its incorporation into virions. *J Virol* 79: 11559-11568. doi:10.1128/JVI.79.18.11559-11568.2005. PubMed: 16140733.
- Müller B, Daecke J, Fackler OT, Dittmar MT, Zentgraf H et al. (2004) Construction and characterization of a fluorescently labeled infectious human immunodeficiency virus type 1 derivative. *J Virol* 78: 10803-10813. doi:10.1128/JVI.78.19.10803-10813.2004. PubMed: 15367647.
- Lux K, Goerlitz N, Schlemminger S, Perabo L, Goldnau D et al. (2005) Green fluorescent protein-tagged adeno-associated virus particles allow the study of cytosolic and nuclear trafficking. *J Virol* 79: 11776-11787. doi:10.1128/JVI.79.18.11776-11787.2005. PubMed: 16140755.
- Desai P, Person S (1998) Incorporation of the green fluorescent protein into the herpes simplex virus type 1 capsid. *J Virol* 72: 7563-7568. PubMed: 9696854.
- Müller B, Mason MM (1970) A new virus in a spontaneous mammary tumor of a rhesus monkey. *Cancer Res* 30: 2081-2086. PubMed: 4195910.
- Jensen EM, Zelljadt I, Chopra HC, Mason MM (1970) Isolation and propagation of a virus from a spontaneous mammary carcinoma of a rhesus monkey. *Cancer Res* 30: 2388-2393. PubMed: 4990901.
- Mason MM, Bogden AE, Ilievski V, Esber HJ, Baker JR et al. (1972) History of a rhesus monkey adenocarcinoma containing virus particles resembling oncogenic RNA viruses. *J Natl Cancer Inst* 48: 1323-1331. PubMed: 4624149.
- Gluzman Y (1981) SV40-transformed simian cells support the replication of early SV40 mutants. *Cell* 23: 175-182. doi: 10.1016/0092-8674(81)90282-8. PubMed: 6260373.
- Graham FL, Smiley J, Russell WC, Nairn R (1977) Characteristics of a human cell line transformed by DNA from human adenovirus type 5. *J Gen Virol* 36: 59-74. doi:10.1099/0022-1317-36-1-59. PubMed: 886304.
- Kessler SW (1975) Rapid isolation of antigens from cells with a staphylococcal protein A-antibody adsorbent: parameters of the interaction of antibody-antigen complexes with protein A. *J Immunol* 115: 1617-1624. PubMed: 1102604.

22. Linkert M, Rueden CT, Allan C, Burel JM, Moore W et al. (2010) Metadata matters: access to image data in the real world. *J Cell Biol* 189: 777-782. doi:10.1083/jcb.201004104. PubMed: 20513764.
23. Schindelin J, Arganda-Carreras I, Frise E, Kaynig V, Longair M et al. (2012) Fiji: an open-source platform for biological-image analysis. *Nat Methods* 9: 676-682. doi:10.1038/nmeth.2019. PubMed: 22743772.
24. Sbalzarini IF, Koumoutsakos P (2005) Feature point tracking and trajectory analysis for video imaging in cell biology. *J Struct Biol* 151: 182-195. doi:10.1016/j.jsb.2005.06.002. PubMed: 16043363.
25. Bradac J, Hunter E (1984) Polypeptides of Mason-Pfizer monkey virus. I. Synthesis and processing of the gag-gene products. *Virology* 138: 260-275. doi:10.1016/0042-6822(84)90350-7. PubMed: 6333757.
26. Chatterjee S, Bradac J, Hunter E (1985) A rapid screening procedure for the isolation of nonconditional replication mutants of Mason-Pfizer monkey virus: identification of a mutant defective in pol. *Virology* 141: 65-76. doi:10.1016/0042-6822(85)90183-7. PubMed: 2579506.
27. Amorim MJ, Bruce EA, Read EK, Foeglein A, Mahen R et al. (2011) A Rab11- and microtubule-dependent mechanism for cytoplasmic transport of influenza A virus viral. *RNA - J Virol* 85: 4143-4156. doi:10.1128/JVI.02606-10.
28. Chambers R, Takimoto T (2010) Trafficking of Sendai virus nucleocapsids is mediated by intracellular vesicles. *PLOS ONE* 5: e10994. doi:10.1371/journal.pone.0010994. PubMed: 20543880.
29. Döhner K, Nagel CH, Sodeik B (2005) Viral stop-and-go along microtubules: taking a ride with dynein and kinesins. *Trends Microbiol* 13: 320-327. doi:10.1016/j.tim.2005.05.010. PubMed: 15950476.
30. Hollinshead M, Rodger G, Van Eijl H, Law M, Hollinshead R et al. (2001) Vaccinia virus utilizes microtubules for movement to the cell surface. *J Cell Biol* 154: 389-402. doi:10.1083/jcb.200104124. PubMed: 11470826.
31. Rhee SS, Hunter E (1987) Myristylation is required for intracellular transport but not for assembly of D-type retrovirus capsids. *J Virol* 61: 1045-1053. PubMed: 3493352.
32. Kohoutová Z, Rumlová M, Andreánský M, Sakalian M, Hunter E et al. (2009) The impact of altered polyprotein ratios on the assembly and infectivity of Mason-Pfizer monkey virus. *Virology* 384: 59-68. doi:10.1016/j.virol.2008.10.048. PubMed: 19062065.
33. Murray JW, Bananis E, Wolkoff AW (2000) Reconstitution of ATP-dependent movement of endocytic vesicles along microtubules in vitro: an oscillatory bidirectional process. *Mol Biol Cell* 11: 419-433. doi:10.1091/mbc.11.2.419. PubMed: 10679004.
34. Penfold ME, Armati P, Cunningham AL (1994) Axonal transport of herpes simplex virions to epidermal cells: evidence for a specialized mode of virus transport and assembly. *Proc Natl Acad Sci U S A* 91: 6529-6533. doi:10.1073/pnas.91.14.6529. PubMed: 7517552.
35. Rietdorf J, Ploubidou A, Reckmann I, Holmström A, Frischknecht F et al. (2001) Kinesin-dependent movement on microtubules precedes actin-based motility of vaccinia virus. *Nat Cell Biol* 3: 992-1000. doi:10.1038/ncb1101-992. PubMed: 11715020.

Příloha 5

Article

Mason-Pfizer Monkey Virus Envelope Glycoprotein Cycling and Its Vesicular Co-Transport with Immature Particles

Petra Grznárová Prokšová ^{1,2}, Jan Lipov ¹, Jaroslav Zelenka ¹, Eric Hunter ³,
Hana Langerová ⁴, Michaela Rumlová ⁴ and Tomáš Ruml ^{1,*}

¹ Department of Biochemistry and Microbiology, University of Chemistry and Technology, 166 28 Prague, Czech Republic; petra.grznarova@natur.cuni.cz (P.G.P.); jan.lipov@vscht.cz (J.L.); jaroslav.zelenka@vscht.cz (J.Z.)

² Imaging methods core facility at BIOCEV, Faculty of Science, Charles University, 252 50 Prague, Czech Republic

³ Emory Vaccine Center at the Yerkes National Primate Research Center, Emory University, Atlanta, GA 30329, USA; ehunte4@emory.edu

⁴ Department of Biotechnology, University of Chemistry and Technology, 166 28 Prague, Czech Republic; langeroh@vscht.cz (H.L.); michaela.rumlova@vscht.cz (M.R.)

* Correspondence: tomas.ruml@vscht.cz; Tel.: +420-220-443-022

Received: 1 July 2018; Accepted: 18 October 2018; Published: 20 October 2018



Abstract: The envelope glycoprotein (Env) plays a crucial role in the retroviral life cycle by mediating primary interactions with the host cell. As described previously and expanded on in this paper, Env mediates the trafficking of immature Mason-Pfizer monkey virus (M-PMV) particles to the plasma membrane (PM). Using a panel of labeled RabGTPases as endosomal markers, we identified Env mostly in Rab7a- and Rab9a-positive endosomes. Based on an analysis of the transport of recombinant fluorescently labeled M-PMV Gag and Env proteins, we propose a putative mechanism of the intracellular trafficking of M-PMV Env and immature particles. According to this model, a portion of Env is targeted from the trans-Golgi network (TGN) to Rab7a-positive endosomes. It is then transported to Rab9a-positive endosomes and back to the TGN. It is at the Rab9a vesicles where the immature particles may anchor to the membranes of the Env-containing vesicles, preventing Env recycling to the TGN. These Gag-associated vesicles are then transported to the plasma membrane.

Keywords: Mason-Pfizer monkey virus; envelope; intracellular trafficking; endosomes; virus-like particles; transport

1. Introduction

Mason-Pfizer monkey virus (M-PMV) is a D-type retrovirus that preassembles its immature particles in the cytoplasm of infected cells [1,2]. Due to both temporally and spatially separate steps of assembly and budding, M-PMV has been utilized as a model to study the retroviral life cycle with potential extrapolation to more complex viruses, e.g., human immunodeficiency virus (HIV).

As in other retroviruses, immature M-PMV particles assemble from the polyprotein precursors of structural proteins and enzymes: Gag, GagPro, GagProPol in defined ratios [3]. All three polyproteins initiate synthesis on free polysomes in the cytoplasm, but are co-translationally transported to the microtubule organizing center (MTOC) by the cellular molecular motor dynein. This requires the interaction of a cytoplasmic targeting/retention signal (CTRS) in the matrix domain of Gag and a light chain of dynein (Tctex-1) [4–6]. The MTOC region seems to be an ideal place for this intracellular assembly as it anchors many organelles and factors, including chaperonins, which may facilitate this

process. It was shown that interaction with the chaperonin TRiC stabilizes Gag and facilitates its multimerization [7]. The multimerization seems to be initiated by conformational changes of Gag induced by its specific interactions with unspliced viral mRNA [8]. The precursor of the envelope glycoprotein (Env) is translated from spliced mRNA on the rough endoplasmic reticulum (ER) and it is co-translationally transported to the lumen of the ER where it trimerizes and is partially glycosylated. The glycosylation is completed in the Golgi apparatus, which is also the site where the cellular protease furin cleaves Env into two subunits, gp70 (surface subunit) and gp22 (transmembrane subunit), which remain associated. A detailed explanation of the molecular mechanism of intracellular transport of M-PMV Env has been hindered by the lack of specific anti-Env antibody. Therefore, the detection of physiological levels of Env in M-PMV infected cells is limited to the use of polyclonal antibodies recognizing all M-PMV proteins.

In general, Env, as an integral type-I membrane protein, would be expected to be targeted from the TGN via the secretory pathway to the plasma membrane (PM). The incorporation of Env into budding particles does not appear to take place at the PM, but requires recycling since the mutation that blocks endocytosis also inhibits Env incorporation [9]. After Env is endocytosed from the PM, it is trafficked to recycling endosomes, which were suggested to be the location of initial Env/Gag interactions [10]. This interaction would then mediate the trafficking of Env and immature capsids-associated vesicles back to the PM where budding is initiated.

Here we present a follow-up study focused on the Env/Gag trafficking pathway. The intracellular transport of Env was monitored using a construct encoding the whole M-PMV genome where the transmembrane domain (TM) of Env is tagged with the mCherry fluorescent protein (mCherryTM). Live-cell imaging experiments showed that a majority of mCherry is localized to intracellular vesicles of unknown origin. We used a panel of endosomal markers based on RabGTPases tagged with enhanced green fluorescent protein (EGFP) to perform colocalization studies with mCherryTM. This approach proved that mCherryTM is localized to Rab7a endosomes and to a lesser extent to those positive for Rab9a. Live-cell imaging data showed the joint transport of mCherryTM-containing vesicles and EGFP-labeled Gag. Both signals were detected in a pericentriolar region as well as at the cell periphery. The results allowed us to propose a mode of intracellular trafficking of M-PMV Env and its site(s) of interaction with Gag immature particles.

2. Materials and Methods

2.1. Plasmids

The plasmids pSARMXmCherryTM (encoding whole M-PMV proviral DNA with mCherry coding sequence inserted into the extracellular region of the transmembrane domain, TM, immediately adjacent to the membrane-spanning domain [11]) and pEGFP-Rab5a were kindly provided by Dr. Paul Spearman (Cincinnati, OH, USA). pSARM-Gag-EGFP-M100A was constructed previously and is described in Clark et al. [12]. The plasmids pEGFP-Rab7a, pEGFP-Rab9a and pEGFP-Rab11a were kindly provided by Richard Pagano (Addgene plasmids # 12605, # 12663 and # 12674) [13].

2.2. The Introduction of I18A and Y22A Mutations into pSARMXmCherryTM Construct

It was shown previously that Env proteins mutated in the cytoplasmic domain (cytoplasmic tail, CT) of TM at positions 18 and 22 (I18A and Y22A) were efficiently transported to the plasma membrane, but failed to be incorporated into the released virions; suggesting that critical step(s) in the trafficking of these proteins are perturbed [9,14]. The following primers were designed to introduce I18A into pSARMXmCherryTM. Two sets of primers were designed to amplify two halves of the plasmid carrying the mutation:

Set 1:

5'-AAACCTGCACAAGTCCATTATCATCGCCTTG and

5'-AAGAGGGCCCAATATCCGAGCAAAGACG

Set 2

5'-GACTTGTGCAGGTTTGGCCTGGATGCTC and

5'-ATATTGGGCCCTCTTATCAGCAAGGCCTGG

To regenerate the plasmid, the two polymerase chain reaction (PCR) products, which had complementary 15 nucleotides ends, were joined using InFusion[®] according to the manufacturer's instructions. After incubation at 50 °C for 15 min, the mixture was transformed into *E. coli* JM109 competent cells and incubated at 30 °C.

An identical approach was used for the Y22A mutant form of pSARMXmCherryTM.

Set 1:

5'-GTCCATGCTCATCGCCTTGAACAAGAAGACAGTGG and

5'-AAGAGGGCCCAATATCCGAGCAAAGACG

Set 2

5'-GCGATGAGCATGGACTTGTATAGGTTTGGC and

5'-ATATTGGGCCCTCTTATCAGCAAGGC

2.3. Cultivation of Cells, Transfection of Plasmids and Imaging

All transfections were performed in COS-1 cells [CRL-1650]—African green monkey kidney fibroblasts transformed with SV40 (ATCC, Manassas, VA, USA). The cells were cultivated in Dulbecco's modified Eagle's medium (DMEM) supplemented with 10% fetal serum. For all imaging studies, the cells were seeded and grown on sterile coverslips placed in 6-well plates. The transfection was performed usually 24 h later using FugeneHD (Promega, Fitchburg, WI, USA) reagent in a ratio of 3 µL of reagent to 1 µg of DNA. The transfection mixture was prepared according to the manufacturer's instructions in 100 µL of OptiMem[®] (Thermo Fisher Scientific, Waltham, MA, USA) media per well and added dropwise to the cells.

For the RabGTPase colocalization studies, 100 ng of RabGTPase DNA was mixed with 1 µg of pSARMXmCherryTM plasmid variant and transfected as described above. Twenty-four hours post-transfection, the cultivation medium was replaced with fixative (4% formaldehyde in phosphate buffered saline (PBS)) and incubated for 20 min at room temperature, washed with PBS, incubated with 50 mM NH₄Cl for 5 min (to remove residual traces of formaldehyde) and again washed with PBS. The coverslips were mounted in Vectashield mounting medium (Vector Laboratories, Burlingame, CA, USA).

For studies of the membrane localization of native Env (of untagged virus), 1 µg of pSARMX construct or pTML plasmid was mixed with 3 µL of FugeneHD and transfected as above. At 24 h post-transfection, the coverslips with the living cells were placed on ice and incubated with goat anti-M-PMV antibody for 25 min to stain surface Env. To visualize the intracellular content, fixation was performed as described above. After the fixation, 1% bovine serum albumin (BSA) in PBS was added to the samples to block nonspecific interaction sites. After 20 min of incubation the cells were permeabilized using 0.1% Tween 20 in PBS for 10 min and then incubated with rabbit anti-CA antibody [15] for 30 min at room temperature. To visualize Env-bound primary antibody, the cells were incubated with secondary anti-goat IgG antibody conjugated with AlexaFluor[®] 350 (Invitrogen, Carlsbad, CA, USA) for 20 min at RT. To visualize immature capsids, the cells were incubated with secondary anti-rabbit IgG antibody conjugated with fluorescein isothiocyanate (FITC) under the same conditions. After multiple washes, the coverslips were mounted into Vectashield mounting medium.

For studies of the membrane localization of mCherry tagged Env, 1 µg of pSARMXmCherryTM wild-type (WT) or mutant variant construct was mixed with 3 µL of FugeneHD and transfected

as above. After 48 h, the living cells were incubated with goat anti-M-PMV antibody or rabbit anti-mCherry antibody (ab167453, Abcam, Cambridge, UK) on ice for 25 min. After the formaldehyde fixation, 1% BSA in PBS was added to the samples to block nonspecific interaction sites and samples were immunostained with secondary anti-goat IgG antibody conjugated with Alexa Fluor[®] 350 (Invitrogen, USA) or with secondary anti-rabbit IgG antibody conjugated with Alexa Fluor[™] Plus 488 (Thermo Fisher Scientific, Waltham, MA, USA) for 20 min at RT. After multiple washes, the coverslips were mounted into Vectashield mounting medium (with DAPI for anti-mCherry antibody staining).

For the study of the colocalization of cis/medial Golgi and mCherry[™], COS-1 cells were transfected with 1 µg of pSARMXmCherry[™] WT or mutant construct as it is described above. 48 h later were cells fixed with 4% formaldehyde, blocked with BSA and permeabilized as described above. All samples were incubated with primary antibody rabbit anti-GOLM1 (Sigma Aldrich, St. Louis, MO, USA) and after multiple washes immunostained with secondary anti-rabbit IgG antibody conjugated with Alexa Fluor[™] Plus 488 and mounted into Vectashield medium.

All fixed samples were imaged using an Olympus cell'R microscope (Olympus, Tokyo, Japan) or spinning disk confocal microscope (Andor, Belfast, UK).

2.4. Immunolabeling of Viral Proteins with Radioactive Isotopes and Immunoprecipitation (Pulse Chase Assay)

For this assay, the cells were seeded into 6-well plates in multiple sets. They were transfected using 1 µg of DNA (pSARMX-WT, pSARMXmCherry[™]-WT or mutant variants) with 3 µL of FugeneHD in 100 µL of OptiMem[®] medium per well and incubated for 48 h. The cultivation medium was then replaced with DMEM medium lacking methionine and cysteine. After 15 min of incubation, the cells were pulse-labeled with 100 µCi of [³⁵S]-labeling mix (Isolabel [³⁵S]; a mixture of [³⁵S] methionine and [³⁵S] cysteine in the ratio 4:1) per well for 30 min at 37 °C under physiological conditions. One set of samples was lysed immediately (pulse/cell lysates) and others after 2 h, 4 h and 8 h of incubation in complete DMEM. The culture media were centrifuged at 13,000 RCF for 5 min at room temperature. Lysis buffer A (8.76 g/L NaCl, 6.06 g/L Trizma base, 10 mL/L Triton X-100, 10 g/L sodium deoxycholate) was added and samples were incubated for 10 min, placed on ice for 5 min, centrifuged at 13,000 × g RCF for 2 min and supernatants were transferred into new tubes. The concentration of sodium dodecyl sulfate (SDS) was adjusted to 0.1% in both culture media and cell lysates and all the samples were incubated with a suspension of inactivated *Staphylococcus aureus* (*Staph A*) at room temperature for 30 min to remove unspecific binders. 1 µL of goat anti-M-PMV antibody was added to each sample after the pellet of *Staph A* was removed and incubated overnight at 4 °C. The immunocomplexes were precipitated with *Staph A* in lysis buffer B (Lysis buffer A + 1 g/L SDS). Viral proteins were resolved by Tris-Tricine SDS polyacrylamide gel electrophoresis (SDS PAGE). Gels were incubated in drying solution (100 mL/L acidic acid, 400 mL/L methanol, 30 mL/L) for 20 min and dried in a gel dryer (Bio-Rad, Hercules, CA, USA) for 2 h at 80 °C. The imaging screen (Molecular Imager FX[™] Imaging screen-K) was exposed to the dried gels for one week.

2.5. Live-Cell Imaging

For live-cell imaging, the cells were seeded into glass-bottomed dishes (MatTek Corporation, Ashland, MA, USA) and incubated in complete DMEM.

To determine the localization of mCherry[™] protein variants, COS-1 cells were transfected with 1 µg of pSARMXmCherry[™] WT or mutated variant with 3 µL of FugeneHD in 100 µL of OptiMem[®] medium per dish.

For studies of the co-transport of mCherry[™] and EGFP-labeled immature capsids, the cells were co-transfected with a mixture of 200 ng of pSARM-Gag-EGFP-M100A and 800 ng of pSARMXmCherry[™] WT (or mutant variant) and 3 µL of FugeneHD in 100 µL of OptiMem[®] media per dish. We showed previously that the pSARM-Gag-EGFP-M100A vector produced minimal levels of Env, likely due to a decrease in the splicing efficiency of Env mRNA since some of the potential splice branch points for Env splicing were removed during the codon-optimization of the Gag sequence.

Immediately before imaging, the culture media in all samples were replaced with phenol red lacking DMEM supplemented with 10% FBS, L-glutamine (final concentration 0.584 g/L) and 1% vitamins solution. The samples were then placed into the incubation cell of an Olympus cell'R microscope and incubated at physiological conditions while the videos were acquired. All videos were captured each second with exposure of 100 ms.

2.6. Quantification of Colocalization

Colocalization of Rab-positive vesicles and mCherryTM was analyzed with ImageJ (version 1.52g, National Institutes of Health, Bethesda, MD, USA) [16–18]. Due to the unusual type of colocalization, where both signals do not overlap, since the Rab signal is on the surface of the endosome and the mCherry signal appears to fill the inner volume of the endosome, a mask of regions of interests (ROIs) was created based on the Rab signal. This mask was applied to the mCherry channel image and the intensity of the mCherry signal was measured in all ROIs. This approach gave a yes/no answer as to whether particular ROI (or actually Rab-positive endosome) also contained an mCherry signal or only the background signal. Based on these results, the percentage of mCherry-positive Rab-positive endosomes from the total number of Rab-positive endosomes was identified.

The quantification of the colocalization of mCherryTM variants and GagEGFPWT was performed by Coloc2 analysis in ImageJ (version 1.52g, National Institutes of Health, Bethesda, MD, USA) [19–21]. The analysis was done on the first image from the time-lapse dataset of the particular virus variant (WT, I18A, Y22A). The mask of ROIs was created based on the mCherry signal (mCherry signal-positive vesicles) and then the colocalization with the GagEGFP signal was quantified by using the Coloc2 analysis tool in ImageJ (version 1.52g, National Institutes of Health, Bethesda, MD, USA).

2.7. Transmission Electron Microscopy (TEM) Analysis

Transmission electron microscopy (TEM) analysis was performed as described previously [22]. Briefly, COS-1 cells producing M-PMV were washed with PBS 48 h post-transfection and fixed with 2.5% glutaraldehyde in 0.1 M cacodylate buffer, pH 7.5 and then postfixed in 1% osmium tetroxide, dehydrated in ethanol. The material was embedded in Agar 100 epoxy resin. Ultrathin sections were contrasted with saturated uranyl acetate and analyzed with a JEOL JEM-1200EX microscope operating at 60 kV.

3. Results

3.1. mCherryTM Protein Synthesis, Processing and Incorporation into Viral Particles

The preparation of plasmid encoding the whole M-PMV genome where Env is tagged with the mCherry fluorescence protein in TM was described previously [11]. To investigate the mechanism of Env incorporation into the virus particle, we engineered the I18A and Y22A mutations into mCherryTM and compared their trafficking pathways with the wild type. COS-1 cells were transfected with plasmids harboring M-PMV proviral DNA with either untagged Env, WT mCherryTM, I18A mCherryTM, or Y22A mCherryTM. At 48 h post-transfection, the cells were metabolically labeled for 25 min and chased for 2 h, 4 h and 8 h.

The molecular weights of the expressed mCherry-tagged Env precursors (Pr86-mCherryTM) corresponded well to that expected for fully glycosylated Env with mCherry inserted (~110 kDa) (Figure 1A, lanes 3–5). The signal intensities of these products are higher than for untagged Pr86 (Figure 1A, lane 2), due to the presence of 10 additional methionines in the mCherry tag. Importantly, the M-PMV structural and enzymatic polyprotein precursors Pr78 (Gag), Pr95 (Gag-Pro) and Pr180 (Gag-Pro-Pol) were expressed at similar levels for viruses expressing both untagged Env and mCherry-tagged Env (Figure 1A, lane 2 vs. lanes 3–5).

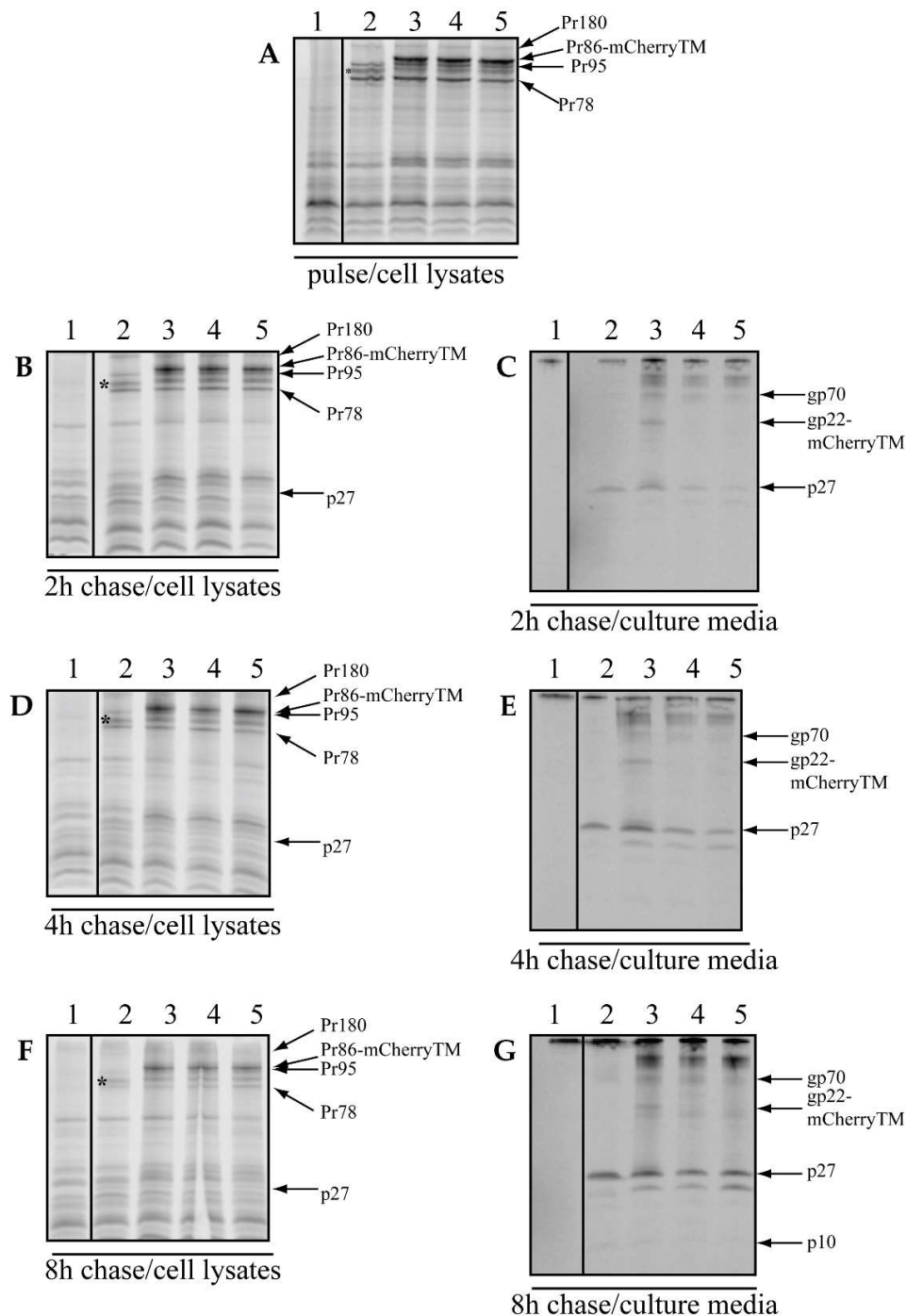


Figure 1. Sodium dodecyl sulfate polyacrylamide gel electrophoresis (SDS-PAGE) analysis of synthesis, processing and incorporation of wild-type (WT) and mutant Env with mCherry inserted into transmembrane domain (mCherryTM). COS-1 cells transfected with pSARMX-WT (untagged Env, lane 2), pSARMXmCherryTM WT (WT mCherryTM, lane 3), pSARMXmCherryTM I18A (I18A mCherryTM, lane 4) or pSARMXmCherryTM Y22A (Y22A mCherryTM, lane 5). Line 1 contains mock material corresponding to non-transfected cells. The cells were labeled 48 h posttransfection with Isolabel-³⁵S for 25 min and chased in fresh culture media for 2 h, 4 h and 8 h. Viral proteins were immunoprecipitated with goat anti-Mason-Pfizer monkey virus (M-PMV) antibody and analyzed by SDS PAGE. The positions of the precursors Pr180 (Gag-Pro-Pol), Pr95 (Gag-Pro), Pr86 (Env-labeled *), Pr78 (Gag), Pr86-mCherryTM; the product of the cleavage of Gag polyprotein, p27 (CA); product of the cleavage of Pr86, gp70 and product of the cleavage of Pr86-mCherryTM, gp22-mCherryTM are shown.

We observed a decrease in intracellular concentrations of the precursor proteins over the chase period (Figure 1B–F), which was accompanied by a reciprocal increase in signal present in the media corresponding to released virions (Figure 1C,E,G). This suggests that the precursors were efficiently incorporated and based on the presence of p27 (the Gag cleavage product originating from Pr180, Pr95 and Pr78 precursors that is linked to virus release), we conclude that virions underwent budding and the correct maturation process (Figure 1C,E,G; lines 2–5). The absence of gp22-mCherry in Figure 1C,E,G; lanes 4 and 5, is an expected result, since CT cleavage is mediated by the viral protease during maturation and neither I18A mCherryTM (line 4) nor Y22A mCherryTM (line 5) is expected to be incorporated into virions [9]. In contrast, the gp22-mCherry product was present in the culture medium collected from cells producing only the WT mCherryTM labeled virus (Figure 1C,E,G; lane 3). In both lanes 4 and 5 (Figure 1C,E,G), we also detected a protein consistent with gp70, a cleavage product of Pr86 and additional high-MW proteins likely released into the culture medium (Figure 1C,E,G; lanes 4 and 5). A western blot assay was performed to confirm the packaging of mCherryTM into virions by isolating and analyzing the proper density fractions of the iodixanol gradient to exclude any proteins which are not associated with the released particles. These experiments showed efficient incorporation of the mCherry-tagged gp22 and p27Gag into particles with the correct density for M-PMV virions (see Section SA in Supplementary Information). From these results, it is clear that WT mCherryTM was successfully transported to the plasma membrane for incorporation into viral particles and that the CT was properly processed during maturation, while this was not the case for viruses encoding the mCherry-tagged Env mutant proteins, consistent with previous work on Env lacking mCherry [9,14]. Moreover, the levels of p27 released into the culture medium were reduced for both the I18A and Y22A mutants, similar to the previous results of Song et al. [14].

3.2. The Intracellular Localization of mCherryTM and Its I18A and Y22A Mutants

Based on the above evidence that mCherryTM can serve as a relevant model for studying the trafficking of M-PMV Env, we sought to investigate its transport and localization in living cells under physiological conditions by fluorescence microscopy.

As shown in Figure 2A–C, we did not observe any detectable mCherry signal at the plasma membrane; however, a strong mCherry signal was observed in the perinuclear region of the cells expressing WT mCherryTM, specifically, at cisternae-like organelles. Based on their shape and localization (Figure 2A), they are likely Golgi cisternae. Env is a type I transmembrane protein, thus the localization of mCherryTM to the Golgi would be expected, as these proteins are transported through the ER and Golgi for posttranslational processing (glycosylation, protease processing, etc.). In addition to the static region of intense staining with WT mCherryTM, we observed some signal in vesicles of unknown origin. Due to seeming variation among intracellular distribution of the signal for the Y22A mutant (Figure 2C), we performed additional experiments to verify whether the intensive mCherry signal localization in the perinuclear area is the Golgi apparatus. We immunostained cis/medial part of this organelle with anti-GOLM1 (Golgi membrane protein 1) antibody in cells producing WT mCherryTM or the mutant variants (Figure 3). The staining of the WT and the I18A mCherryTM mutant was equally intense, but I18A mCherryTM signal was somewhat more distributed around the GOLM1-labeled area. In contrast, the Y22A mCherryTM signal was detected in distributed cytoplasm vesicles, with a less intense signal colocalizing in the GOLM1-labeled region compared to the WT and the I18A mCherryTM mutant (Figure 3).

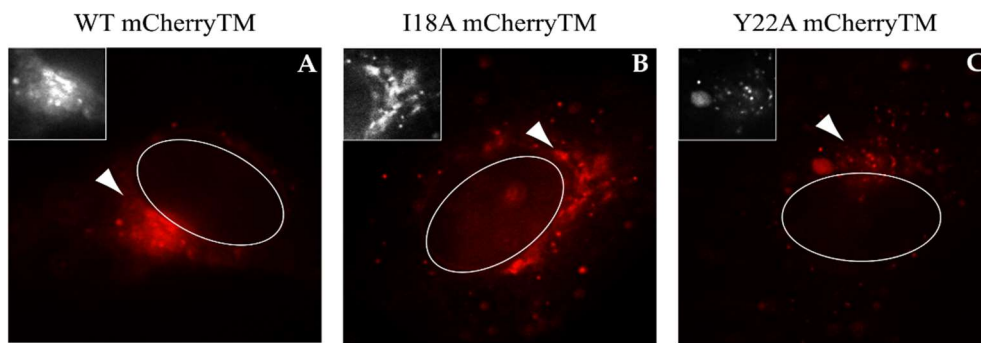


Figure 2. Intracellular localization of WT mCherryTM and I18A and Y22A mutants in living COS-1 cells. The COS-1 cells were transfected with pSARMXmCherryTM WT (A), pSARMXmCherryTM I18A (B) or pSARMXmCherryTM Y22A (C); 24 h posttransfection, they were imaged using the Olympus cell'R in real time. Each picture was captured as a single snap in the TxRed channel. All pictures were captured with the same exposure time. The magnified areas of each picture were transformed into a black-and-white version with increased contrast. The white ovals represent a nucleus. Magnification 600×; scale bar 20 μm.

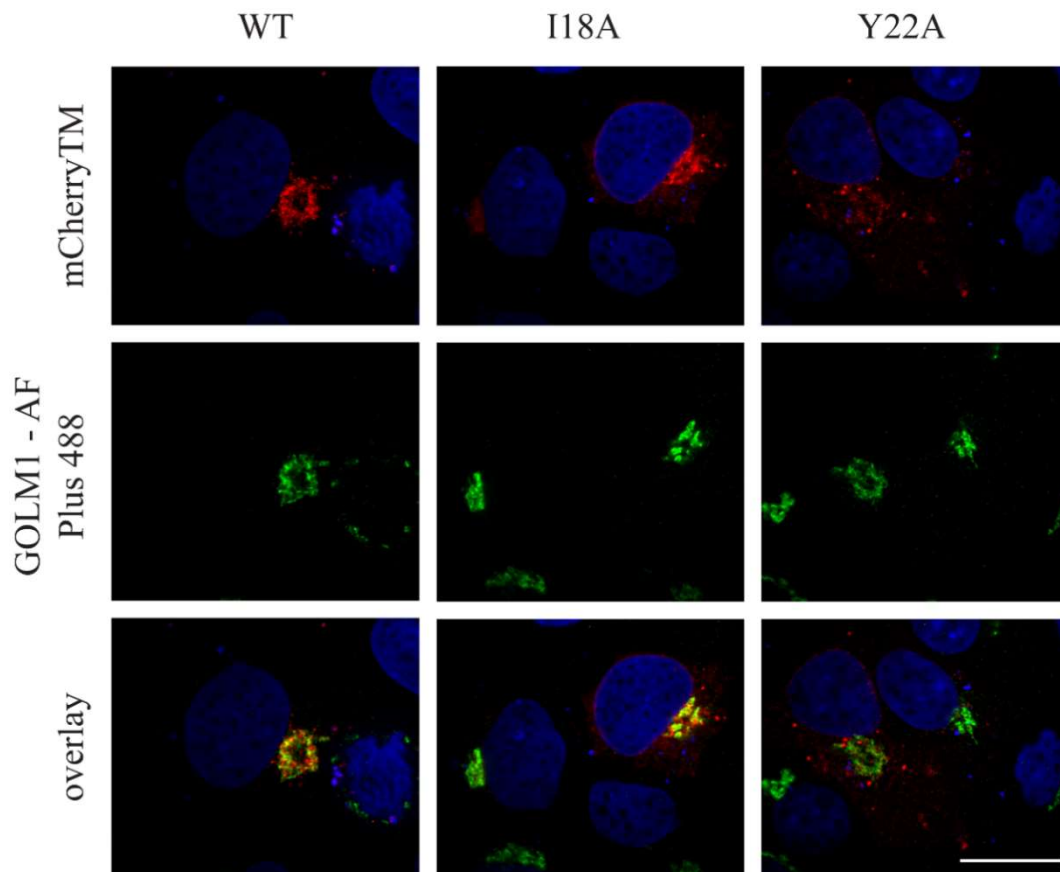


Figure 3. The colocalization of mCherryTM and cis/medial Golgi marker GOLM1. COS-1 cells were transfected with pSARMXmCherryTM WT or mutant variant. 48 h later, they were fixed with 4% formaldehyde and permeabilized with Tween 20. All samples were immunostained with primary rabbit anti-GOLM1 antibody and then with secondary antibody against rabbit IgG conjugated with Alexa FluorTM Plus 488 and mounted into Vectashield mounting medium with DAPI. Samples were imaged with spinning disk confocal microscope (Andor). Magnification 600×; scale bar 20 μm.

3.3. Env and mCherryTM Localization at the Plasma Membrane (PM)

The lack of an mCherry signal at the plasma membrane for any of the mCherryTM constructs was quite surprising, as an intense signal of immunostained Env at the PM has previously been observed [9]. However, Song et al. analyzed cells producing Env in isolation, while we sought to detect Env in the presence of additional M-PMV proteins. To clarify, we replicated the antibody staining experiments performed by Song et al. using an M-PMV molecular clone (pSARMX-WT) or Env transport-defective I18A and Y22A variants. To directly replicate the observations made by Song et al., we also included pTMT-WT, which encodes M-PMV Env alone [14].

Consistent with the findings of Song et al., we observed a largely uniform staining for M-PMV Env when expressed alone (Figure 4D). The Gag production in fixed and permeabilized cells was confirmed by counterstaining with the anti-CA antibody.

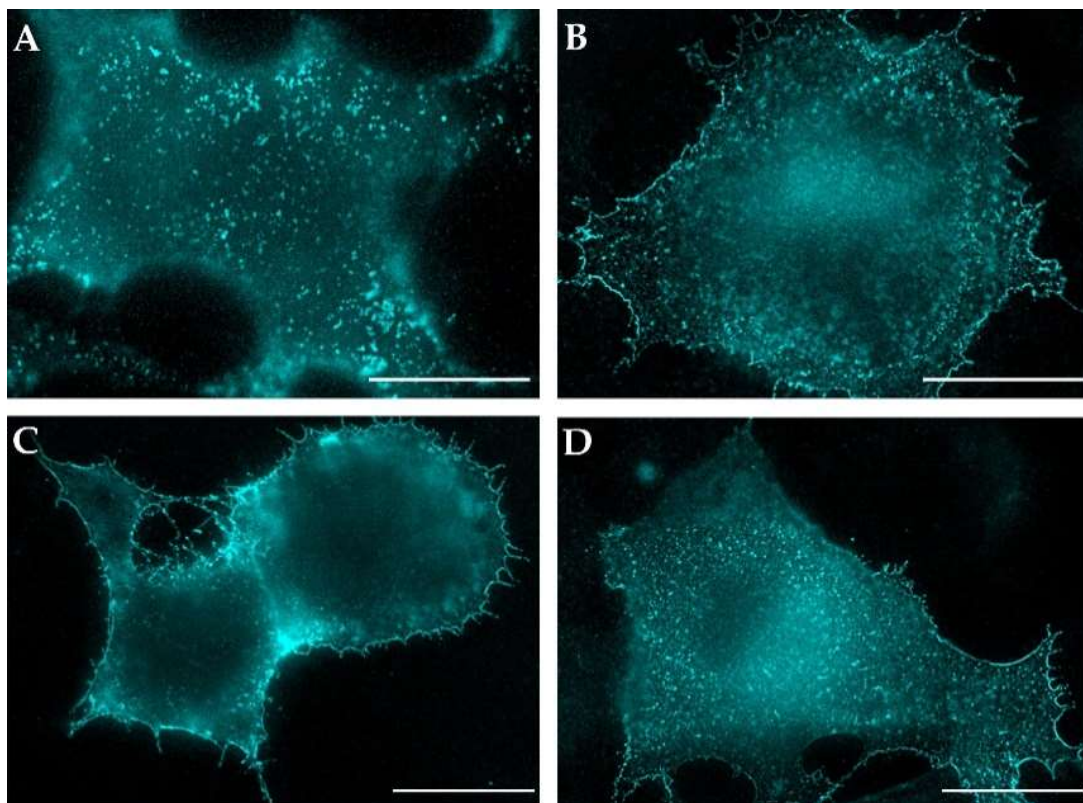


Figure 4. Plasma membrane distribution of M-PMV Env. The COS-1 cells were either transfected with plasmids encoding M-PMV genomic DNA with: WT Env (pSARMX-WT; panel A), I18A Env (pSARMX-I18A; panel B), or Y22A Env (pSARMX-Y22A; panel C) or an M-PMV Env expression vector (pTMT-WT; panel D). 48 h post-transfection cells were incubated with goat anti-M-PMV antibody on ice for 25 min to bind surface exposed M-PMV Env. Formaldehyde (4%) fixed cells were immunostained for CA protein with rabbit anti-CA antibody (except for the cells transfected with pTMT-WT). Env was visualized using secondary anti-goat IgG antibody conjugated with Alexa Fluor[®] 350. Samples were mounted in Vectashield mounting media and imaged on an Olympus cell[^]R microscope. The original blue color of the AF350 signal was changed to cyan for increased contrast. Magnification 600 \times ; scale bars 20 μ m.

Despite repeatedly observed somewhat larger speckles in panel A (Figure 4, complete virus) when compared to both mutant virus variant in panels B and C, we hesitate to speculate on relocalization of Env on the plasma membrane when Gag was co-expressed with either the wild type or the mutants, in contrast to that observed for HIV-1 [23]. The enhanced intensity of plasma membrane staining for the Y22A mutant (Figure 4C) indicates that its trafficking is retarded at the plasma membrane,

presumably due to a defect in its endocytosis. This finding is in agreement with the observations of Song et al. for this mutant [9].

As was mentioned above, we failed to detect any mCherry-related fluorescence signal of the mCherryTM protein at the PM, however, since WT mCherryTM appeared to be incorporated into virions during budding, Env should be visible at the PM. To address this discrepancy between the missing signals of the mCherry-labeled Envs at PM and positive membrane signals of all non-mCherry-labeled Env proteins, we immunostained the surface of the COS-1 cells producing WT mCherryTM and its mutant variants.

The non-permeabilized cells expressing M-PMV with mCherry-labeled Env proteins produced intense intracellular mCherry signals, but little or no evidence of an mCherry signal at the plasma membrane. In contrast, the same cells immunostained with anti-M-PMV antibody exhibited intense PM staining, with the signal homogeneously distributed over the surface of the cell (Figure 5A–C). It therefore appears that both the WT Env (Figure 4) and WT mCherryTM protein is present at the same levels at the cell surface. The lack of the mCherry signal at the PM remains to be explained. The explanation could be either its presence at low concentration that is under the detection limit of the inherent mCherry signal or a loss of its ability to fluoresce following exposure to the culture medium.

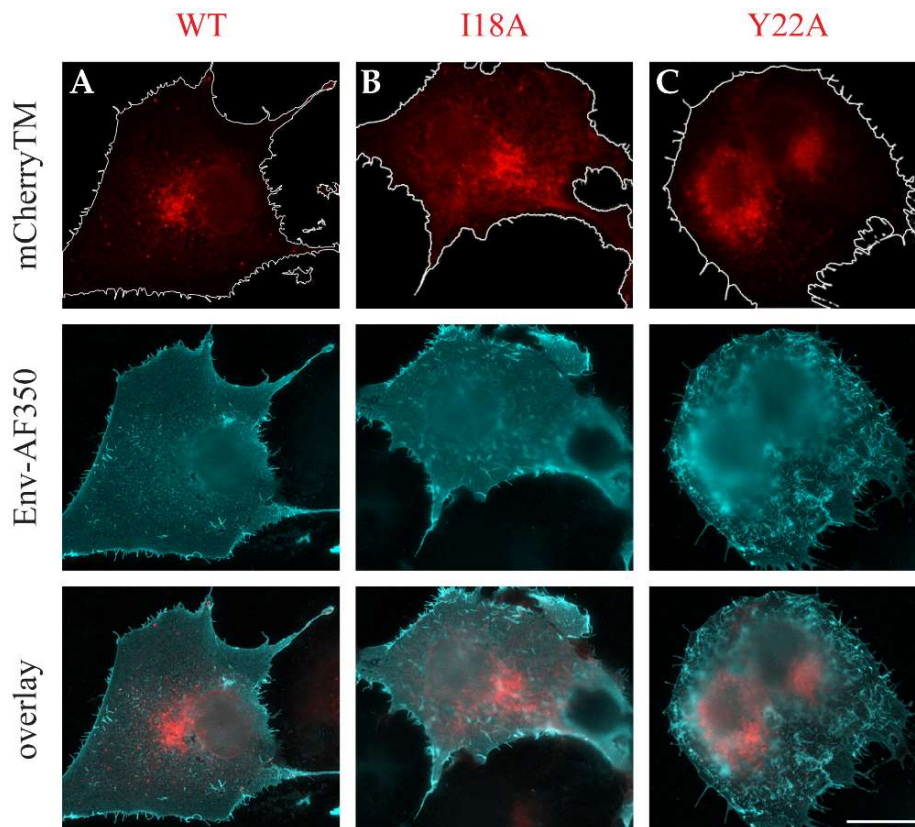


Figure 5. Immunostained mCherryTM proteins. COS-1 cells were transfected with plasmids encoding M-PMV genomic DNA with: mCherry-tagged Envs; pSARMXmCherryTM WT (A), pSARMXmCherryTM I18A (B) or pSARMXmCherryTM Y22A (C). After 48 h, the living cells were incubated with goat anti-M-PMV antibody on ice and then fixed with 4% formaldehyde and immunostained with secondary anti-goat IgG antibody conjugated with Alexa Fluor[®] 350. The upper panels show mCherry fluorescence, the middle panels show the Alexa Fluor[®] 350-staining, and the lower panels the two images overlaid. Non-transfected COS-1 cells were processed in the same set of samples, no non-specific staining was observed for this immunostaining (). The original blue color of AF350 signal was changed to cyan for increased contrast. The delineation in the upper panels highlights the plasma membrane (PM). Magnification 600 \times ; scale bar 20 μ m.

To address this question, we performed surface staining of intact non-permeabilized cells using anti-mCherry antibody labeled with the high signal-to-noise ratio fluorophore Alexa Fluor™ Plus 488. The immunofluorescence image (Figure 6, the right panel) exhibits an intensive green signal corresponding to the presence of mCherry™ at the membrane surface. As seen from the middle panel in Figure 6, the intracellular mCherry signal is substantially higher than the very faint, close to zero, mCherry signal at the membrane. Nevertheless, these experiments show that the mCherry™ is efficiently transported to the plasma membrane and argue that this protein can be employed to study the intracellular trafficking of Env.

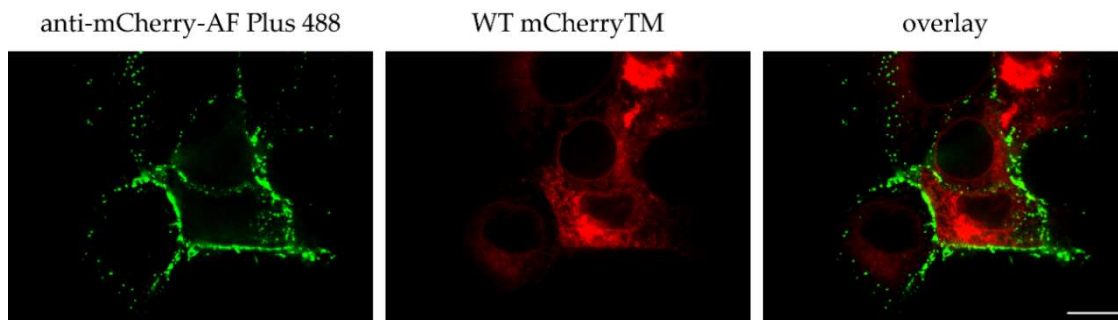


Figure 6. Membrane localization of WT mCherry™ immunostained with anti-mCherry antibody. COS-1 cells were transfected with pSARMXmCherry™ WT. After 48 h, the living cells were incubated with rabbit anti-mCherry antibody on ice and then fixed with 4% formaldehyde and immunostained with secondary anti-rabbit IgG antibody conjugated with Alexa Fluor™ Plus 488. The left panel shows surface immune-staining of mCherry, the middle panel shows the inherent mCherry fluorescence, and the right panel shows these two images overlaid. Mock-transfected COS-1 cells were processed in the same way; no signal was detected. One focal plane acquired with a spinning disk confocal microscope (Andor) is shown. Magnification 600×; scale bar 20 μm.

3.4. Characterization of Vesicles Carrying Mason-Pfizer Monkey Virus (M-PMV) Env

Based on the shape, size, and mobility in live cell imaging of the Env-containing vesicles, along with previous observations that the M-PMV Env cytoplasmic tail targets viral glycoproteins to endosomal pathways [24], we concluded that the pool of mobile mCherry™ is present in the form of endosomal vesicles. In order to explore this, Rab5a, Rab7a, Rab9a, and Rab11a, four markers of specific endosomal compartments N-terminally tagged with EGFP were co-expressed with WT or mutant mCherry™ (Figure 7). All the markers belong to the family of the Ras superfamily of G proteins (Rab GTPases) and are responsible for regulating the transport and maturation of endosomal vesicles. Rab5a regulates transport from the plasma membrane to the early endosomes [25] and is predominantly localized to the early/sorting endosomes. Rab7a moderates the maturation of certain domains of early/sorting endosomes into late endosomes [26], and so Rab7a is frequently used as a marker of late endosomes. Rab9a is involved in the retrograde transport of cargo from late endosomes to the TGN [27]. Rab11a specifically localizes to recycling endosomes, which recycle cargo from early/sorting endosomes back to the plasma membrane [10,28].

We did not observe any significant colocalization of WT mCherry™ with Rab5a-positive early/sorting endosomes (Figure 7A). Only approximately 3% of all identified Rab5-positive vesicles also contained WT mCherry™ signal. While surprising, since previous work by Song showed the rapid endocytosis of WT Env, this could have resulted from the reduced mCherry™ signal observed following its exposure on the PM. Also, approximately 7% of Rab5a-positive vesicles colocalized with the I18A mCherry™ signal (Figure 7B). As shown in the magnified field in Figure 7B, while the I18A mCherry™ and EGFP-tagged Rab5a marker were present on the same vesicles, they did not colocalize in particular subdomains.

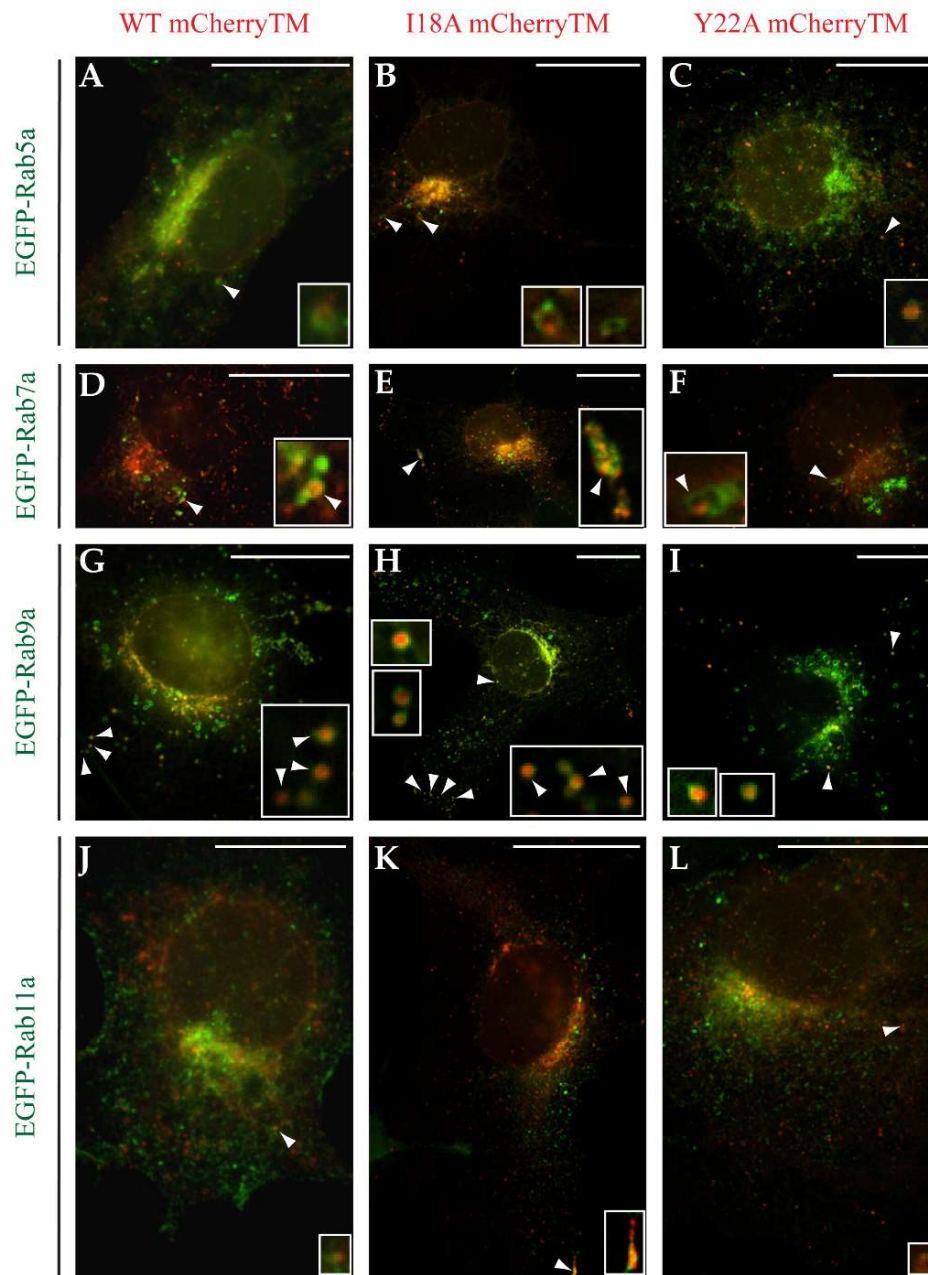


Figure 7. Rab-markers based identification of intracellular vesicles carrying mCherryTM protein variants. The COS-1 cells co-transfected with a combination of pSARMXmCherryTM and enhanced green fluorescent protein (EGFP)-tagged endosomal marker coding plasmids were fixed with 4% formaldehyde 24 h post-transfection. Upon mounting in Vectashield media the samples were imaged using an Olympus cell[^]R microscope. White arrowheads indicate colocalization of the mCherryTM signal and the corresponding marker. Magnification 600 \times ; scale bars 20 μ m.

The Y22A mutant disrupts a critical endocytic signal, and results in a significant deficiency in its removal from the plasma membrane [9]. Based on this, it was surprising that colocalization between Y22A mCherryTM and Rab5a was identified (Figure 7C). Based on the analysis, 10% of Rab5-positive vesicles contained also Y22A mCherryTM signal.

In contrast to what was observed for Rab5a, all three mCherryTM fusion proteins significantly colocalized with Rab7a. The highest degree of colocalization with Rab7a was seen for the WT Env, where 68% of Rab7a-positive vesicles also contained the WT mCherryTM signal (Figure 7D), while both the I18A (Figure 7E) and Y22A (Figure 7F) mutants colocalized with Rab7a much less efficiently

(23% for I18A variant and 9% for Y22A variant). The colocalization between mCherryTM and Rab9a-EGFP-positive endosomes was found to be 30% for WT mCherryTM, 23% for I18A mCherryTM and 25% for Y22A mCherryTM (Figure 7G–I). This confirmed a previous report that Env CT directs localization to Rab9a-positive endosomes [24], and shows that the observation applies both in the context of full-length Env and in the presence of other viral proteins. Only a minor degree of colocalization was detected for mCherryTM variants on Rab11a-positive recycling endosomes, where only about 2% of recycling endosomes contained a WT mCherryTM signal, and about 1% of such vesicles contained an I18A mCherryTM and an Y22A mCherryTM signal. (Figure 7J–L).

3.5. Live-Cell Imaging of mCherryTM and EGFP-Tagged M-PMV Virus Like Particle

pSARM-Gag-EGFP-M100A was used to monitor interactions between M-PMV Gag and mCherryTM and the trafficking properties of Gag-associated Env vesicles. This vector has been previously described; but briefly, it expresses a Gag C-terminally tagged with EGFP, does not encode Pro or Pol, and Env production is significantly decreased due to the effect of codon optimization of the Gag sequence [12]. COS-1 cells were co-transfected with pSARM-Gag-EGFP-M100A and WT or mutant mCherryTM and 24 h post-transfection samples were imaged with an Olympus cell^R microscope under physiological conditions in real time.

Figure 8A shows one time point (t_{20s}) from videos of WT mCherryTM and pSARM-Gag-EGFP-M100A co-transfected COS-1 cells (Video S1 and S2, magnified region in Video S3 and S4). The white arrowhead in this figure highlights a vesicle carrying at least two immature capsids, and in the associated video it is clear that this vesicle is being trafficked towards the plasma membrane. Another 8–13 WT mCherryTM-containing vesicles with attached immature capsids near the PM can be seen and at least three more are visible in the perinuclear area. The colocalization of WT mCherryTM with GagEGFP^{WT} was quantified with Coloc2 tool in ImageJ (version 1.52g, National Institutes of Health, Bethesda, MD, USA). A rounded estimate is that 47% of identified WT mCherryTM-positive vesicles colocalized with the GagEGFP signal. It needs to be emphasized that this particular dataset was challenging for software-based analysis, due to the very high density of GagEGFP-positive particles, resulting in a high background signal which had an impact on the measured parameters. This was not the case for both mutant variants. However, by visual analysis, we estimated that up to 73% of WT mCherryTM vesicles colocalized with GagEGFP particles.

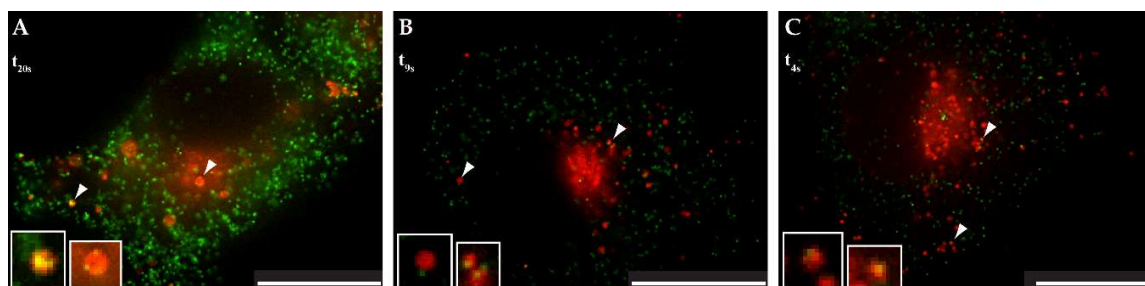


Figure 8. Localization of mCherryTM protein variants and EGFP-labeled Gag/virus like particles. The COS-1 cells were seeded into glass-bottomed dishes and co-transfected 24 h later with pSARMXmCherryTM WT (panel A) or one of the mutant variants (pSARMXmCherryTM I18A, panel B; pSARMXmCherryTM Y22A, panel C) together with the pSARM-Gag-EGFP-M100A constructs. The next day, the living cells were imaged in the Olympus cell^R microscope under physiological conditions. Panel A shows WT mCherryTM and EGFP-labeled immature capsids (see also Videos S1–S4 in Supplementary Information). Panel B shows I18A mCherryTM and EGFP-labeled immature capsids (see Video S5 in Supplementary Information). Panel C shows Y22A mCherryTM and EGFP labeled immature capsids (see Video S6 in Supplementary Information). White arrowheads indicate mCherryTM-containing vesicles colocalizing with Gag-EGFP virus-like particles. Magnification 600 \times ; scale bar 20 μ m.

With I18A, the software analysis was more accurate according to the almost zero background signal.

The colocalization rate of I18A mCherryTM and Gag-EGFP (white arrowheads in Figure 8B, shown one time point-t9s) was 33% which is significantly lower than for WT Env. This is consistent with the reduced incorporation of this mutant Env. I18A mCherryTM vesicles oscillating near the nucleus were observed (Video S5). The data documenting the vesicular co-transport of Y22A mCherryTM and GagEGFP immature capsids (Figure 8C, shown one time point-t4s) were similar to that of I18A mCherryTM (Video S6), even in that the colocalization rate was 53%, which is almost halfway between WT and I18A Env. As was observed for the I18A mutant, a majority of the vesicles associated with immature capsids were near the nucleus. To analyze the type of transport of a particular mCherry variant, particle tracking measurements were performed (see Section SB in Supplementary Information).

The association of WT immature particles with intracellular vesicles was also confirmed by the transmission electron microscopy of COS-1 cells transfected with whole M-PMV provirus vector (Figure 9).

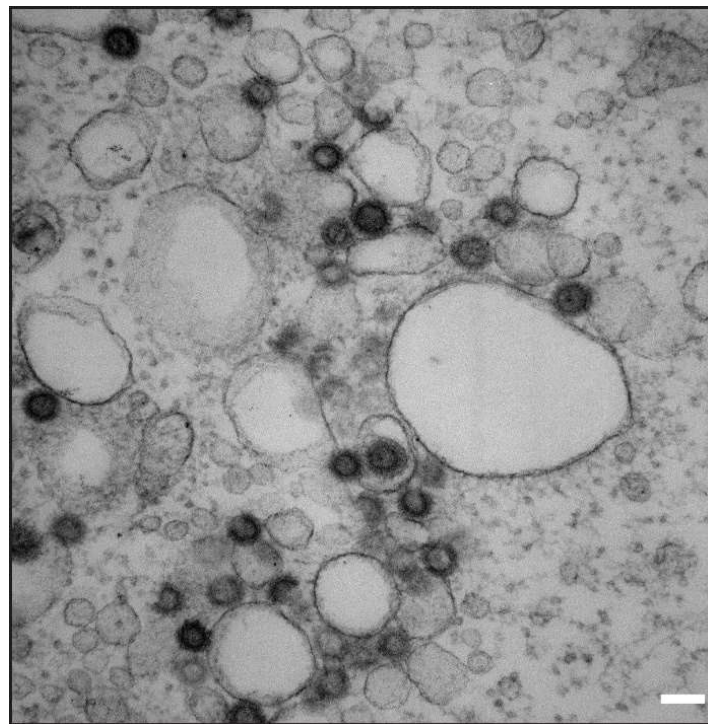


Figure 9. Transmission electron microscope (TEM) image of immature M-PMV particles associated with vesicular membranes. Scale bar represents 100 nm.

4. Discussion

Several studies focusing on the molecular mechanism of M-PMV Env intracellular trafficking and its interaction with Gag have been published [5,10,11]. The main focus of these studies was on the role of the CT since it is the only part of Env available for potential interactions with viral structural polyproteins and cytoplasmic proteins. It is important in the initiation of Env incorporation into the viral particle, and it also plays a role in anterograde and retrograde trafficking, and in the initiation of intracellular signaling cascades leading to enhanced viral gene expression [29–32].

In M-PMV, the CT is only 38 amino acids long but it contains at least two signal sequences that are important for the regulation of intracellular transport and interaction of Env with Gag [33]. Alanine-scanning mutagenesis identified three residues critical for Env incorporation into budding virions. Mutations I18A, Y22A completely disrupt incorporation and L25A mutant is poorly

incorporated [9,14]. Intracellularly assembled M-PMV immature capsids acquire their Env at the plasma membrane during budding [1,34,35], however it is still unclear where the initial contact between Env and Gag occurs and which domain of Gag is responsible for this interaction. Based on observations in HIV-1, where a single mutation in MA or deletion in the CT blocks Env incorporation, M-PMV MA is presumed to mediate this interaction [32,36–38]. Using live-cell imaging of fluorescently tagged Gag and Env, we determined dynamic intracellular interactions between Gag immature capsids and Env-containing vesicles (Figure 8A–C and Videos S1–S6). This system enables the intracellular trafficking of M-PMV Env to be tracked. The particle-tracking analysis showed that all three variants are transported via active transport (see Section SB in Supplementary Information).

Env, as a type I transmembrane protein is synthesized at the rough ER and it is glycosylated and cleaved by furin while traversing toward the *trans*-Golgi apparatus (TGN). Once Env reaches the TGN, it must be sorted to either cisterna C6 or C7 of TGN. The cargo leaving the C6 cisterna is transported to the plasma membrane via long tubules and nonclathrin buds, while cargo leaving the C7 cisterna is targeted exclusively to the endosomal pathway via clathrin-coated vesicles [39,40]. It is unclear how the sorting of transmembrane proteins into these cisternae occurs; however, the length of the membrane-spanning domain (MSD) likely plays a role in this process. It was originally shown for sorting at early endosomes that extension of the MSD of TGN38 from 21 to 24 amino acids caused an aberrant localization of proteins into distinct microdomains [41]. In addition, White et al. demonstrated that the length of the MSD together with signals in the cytoplasmic domain assist in segregating transmembrane proteins from Golgi resident proteins into distinct “cargo” regions [42]. The M-PMV MSD consists of 28 amino acids [33] and could be the factor influencing Env targeting into the distinct cisterna of the TGN.

In contrast to the C-type retroviruses, M-PMV particles assemble at the centrioles, and Env was thought to be transported from the TGN directly to the plasma membrane [9,43]. Here the endocytic signal present in the CT mediates rapid Env endocytosis. This generally prevents prolonged exposure to the immune system. Sfakianos et al. proposed that M-PMV particles assemble at the membrane of recycling endosomes [10]. This could subsequently result in the efficient targeting of both Env and Gag. Evidence for an interaction between M-PMV immature capsids and intracellular vesicles being utilized in anterograde transport has been published by our group previously [5,11]. This intracellular interaction is also consistent with the finding that M-PMV MA interacts with the plasma membrane phospholipids with significantly lower affinity [44] compared to HIV-1. We also observed an accumulation of Gag at intracellular vesicles in COS-1 cells producing wild-type untagged M-PMV soon after infection and also transmission electron microscopy has confirmed the presence of assembled M-PMV particles associated with intracellular vesicles (Figure 9).

Using the plasmid pSARMXmCherryTM encoding whole M-PMV with mCherry tagged Env, we observed Env in living cells. The majority of mCherryTM was present in intracellular vesicles and cis/medial Golgi (Figures 2 and 3). The predominant vesicular localization supports the theory that a significant fraction of Env is targeted to the C7 cisterna of TGN and then to the endosomal pathway rather than to C6 cisterna and the PM. Blot et al. published a similar observation utilizing M-PMV Env CT fused to the C terminus of the CD25 protein. They proposed that this chimera is targeted directly from the C7 cisterna to the Rab7a-positive endosomes and then (based on the length of MSD and targeting of Env into distinct microdomains on endosomal membranes) to the Rab9a-positive endosomes [24], where Rab9aGTPase moderates the recycling of cargo back to the TGN [27,45]. They suggested that Env is retained in this intracellular cycle (TGN-Endosomal pathway-TGN) to avoid its unnecessary exposure on the PM [24]. Our data are in agreement with this theory of intracytoplasmic Env recycling. All three tested mCherry tagged M-PMV variants exhibited strong colocalization with the Rab7a marker and moderate colocalization with the Rab9a marker (see Figure 7D–I). We observed only a low colocalization of all three variants with the Rab5a marker of early endosomes (Figure 7A–C), consistent with the majority of Env entering the endosomal pathway

directly from the TGN, although this could reflect the much reduced mCherry signal observed at the plasma membrane and possible quenching of the signal following extracellular exposure.

Blot et al. showed that the dileucine motif (LL or L Φ motif) mediates the targeting of M-PMV Env CT containing the chimera from the TGN to late endosomes, while a tyrosine-based motif (the Yxx Φ motif) mediates retrograde transport from Rab9a-positive endosomes to the TGN [24]. Our data confirm the importance of the Yxx Φ motif in Env transport, as we used M-PMV Env with its native trimerization domain and complete SU and TM subunits. As shown in Figures 2C and 3, the Y22A mCherryTM protein localizes predominantly in endosomal vesicles while the WT and I18A (Figure 2A,B and Figure 3) variants are concentrated more also on cisterna-like organelles, labeled with GOLM1 (cis/medial Golgi) marker, suggesting that the Y22A mutation blocks recycling from Rab9a vesicles to the TGN.

In the cells producing only Env (without other viral proteins), we observed an intense signal of immunostained Env present on the PM (Figure 4D), consistent with the observations of Song et al. [9,14]. We saw a similar result in cells producing both complete untagged WT and also mutated viruses (Figure 4A–C) and a mCherry-tagged virus-infected cell stained with anti-mCherry antibody (Figure 6), where Gag is present. This Env-related signal on plasma membrane is either highlighting spots where budding of virus particles occurs or Env that has reached the plasma membrane but failed to be incorporated to the virus.

Therefore, we hypothesize that Env can follow two intracellular routes following its synthesis; in the first, Env cycles internally via Rab9 vesicles to interact with immature capsids just assembling in the pericentriolar region, and in the second, Env is transported directly to the PM.

Based on our findings together with previously published data, we propose the mechanism depicted in Figure 10, where two subpopulations of Env leave the TGN. The first is directly transported to the PM and, because the endocytic signal is not hindered by interaction with immature capsids, Env is rapidly endocytosed and thus targeted to Rab5a-positive endosomes. Based on MSD properties and signals in the CT, Env is present in distinct microdomains at the membrane of this endosome, which matures into a Rab7a-positive endosome. Such, Rab7a-positive endosomes have been shown to recruit Rab9aGTPase into distinct microdomains [26,41,46,47], which afterwards mature into Rab9a-positive endosomes recycling cargo from late endosomes to cisterna C7 of the TGN [48]. The Rab9aGTPase remains connected with these vesicles until their fusion with the TGN membrane [27]. At least some of these Env molecules could then be transported from the TGN, likely utilizing a dileucine motif in the CT back to Rab7a endosomes. This motif was shown to interact with adaptor proteins to recruit clathrin to the site of bud formation [49,50].

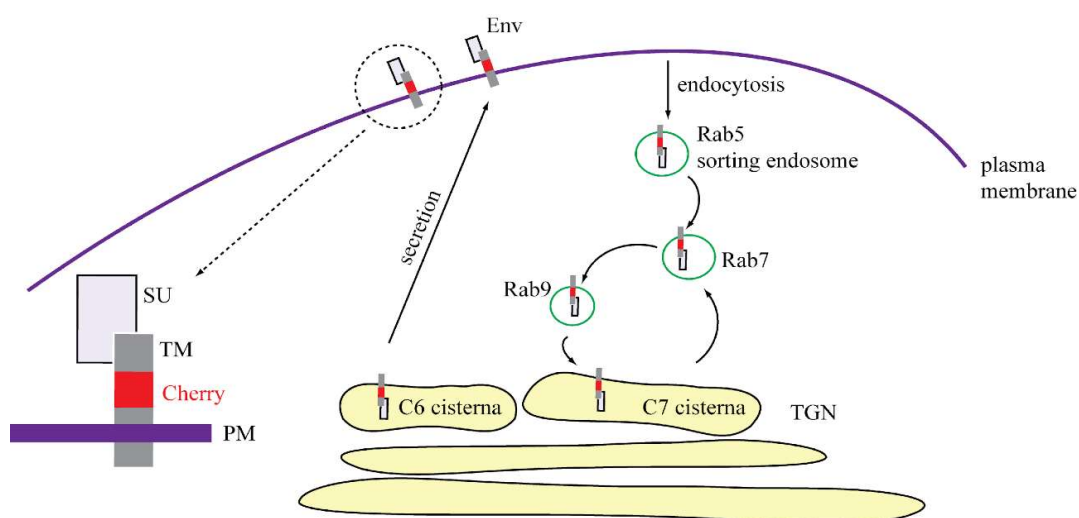


Figure 10. Proposed scheme of M-PMV Env intracellular transport when expressed in the absence of other viral components.

The existence of two independent pathways might also explain published observations that disruption of the dileucine motif did not prevent the incorporation of Env into M-PMV virions [14]. The disruption of the dileucine motif would block the targeting of Env from the TGN to the endosomal pathway but would not prevent Env transport to the PM and subsequent endocytosis back to Rab7 endosomes. In contrast, disruption of the YxxΦ motif may stop both routes at the membrane of Rab9a-positive vesicles. Since we have demonstrated the co-transport of Y22A mCherryTM with the immature capsid (Figure 8, Video S6), the Y22A mutation probably did not influence the recruitment of immature capsids to the endosomal membrane or their anchoring to the endosomal membrane. Nevertheless, it presumably prevents the recycling of Env from Rab9a endosomes back to the TGN and then transport to the PM. This would explain the lower proportion of the Y22A mutant signal in the GOLM1 labeled region, where both the WT and I18A mutant are predominantly observed (Figure 3).

We propose a model of Env transport in the M-PMV-infected cell (Figure 11), where Gag that is transported to the MTOC via interaction with a light chain of dynein (Tctex-1) [4] oligomerizes in this region into the hexameric lattice of the immature particle. These preassembled particles can bind to the adjacent Env-containing Rab9a-positive vesicles either directly through interaction with polar lipids [51] or via the cytoplasmic tail of the TM. The transport of Rab9a-positive endosomes towards both the plasma membrane and the TGN has been shown by Barbero et al. [27]. We hypothesize that the interaction of immature capsids with the Env-enriched vesicles can induce a switch in transport towards the PM. This is supported by live-cell microscopy, where we observed immature capsid-associated-Env-carrying vesicles near the nucleus as well as on the cell periphery (Figure 8, Video S1–S6).

In summary, by using biochemical methods, fluorescence microscopy including live-cell imaging, and TEM, we analyzed the intracellular trafficking of M-PMV Gag and Env and propose a scheme of intracellular trafficking of these viral components via the endocytic sorting machinery (Figure 11). The data extend and refine those published by Sfakianos et al. and Blot et al., who suggested that Env and Gag traverse jointly through the cytoplasm of infected cells [10,24].

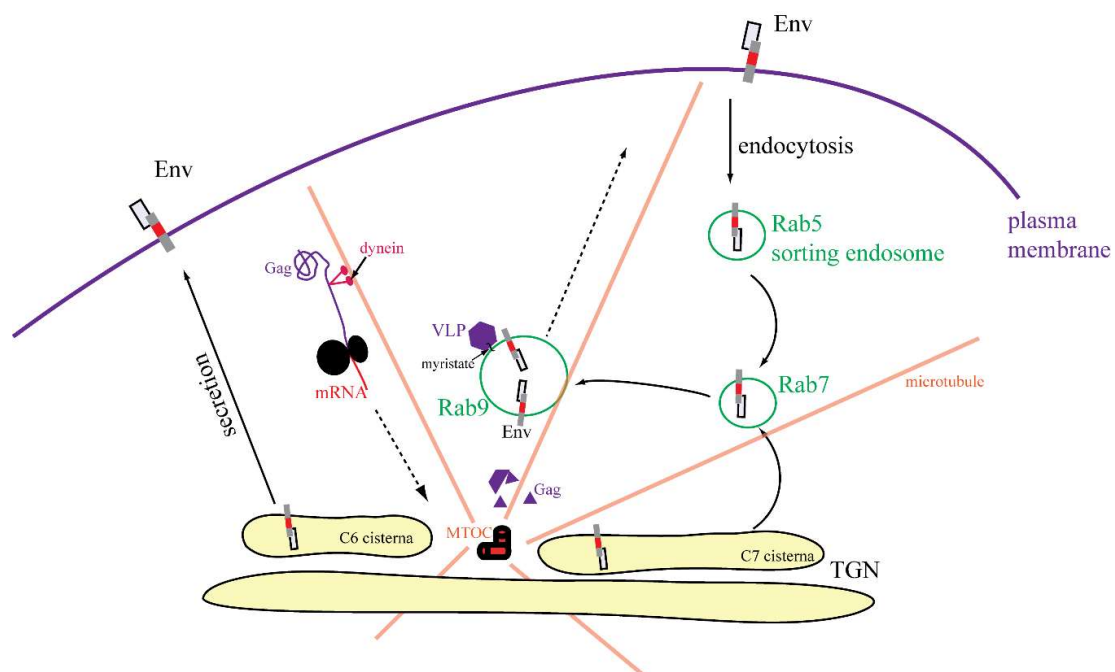


Figure 11. Proposed scheme of M-PMV Env and Gag intracellular transport.

Supplementary Materials: The following are available online at <http://www.mdpi.com/1999-4915/10/10/575/s1>, Video S1 and S2: Live imaging of COS-1 cell co-transfected with pSARMXmCherryTM WT and pSARM-Gag-EGFP-M100A to demonstrate co-transport of EGFP-tagged M-PMV capsids and WT mCherryTM-containing vesicle. Focused on the whole cell. Fast version means compression of 10 frames per second and shows real velocity of movement (Video S1). Slow version means compression of five frames per second (Video S2). Video S3 and S4: Live imaging of COS-1 cell co-transfected with pSARMXmCherryTM WT and pSARM-Gag-EGFP-M100A to demonstrate co-transport of EGFP-tagged M-PMV capsids and WT mCherryTM-containing vesicle. Focused on small region on periphery of cell. Fast version means compression of 10 frames per second and shows real velocity of movement (Video S3). Slow version means compression of five frames per second (Video S4). Video S5: Live imaging of COS-1 cell co-transfected with pSARMXmCherryTM I18A and pSARM-Gag-EGFP-M100A to demonstrate co-transport of EGFP-tagged M-PMV capsid and I18A mCherryTM-containing vesicle. Focused on the whole cell. Only one velocity provided. Video S6: Live imaging of COS-1 cell co-transfected with pSARMXmCherryTM Y22A and pSARM-Gag-EGFP-M100A to demonstrate co-transport of EGFP-tagged M-PMV capsid and Y22A mCherryTM-containing vesicle. Focused on the whole cell. Only one velocity provided. Section SA—Western blot analysis of released virions. Released virions were isolated via iodixanol gradient. Only the fractions of the proper density, corresponding to the density of the virions [52], were analyzed. Antibody against Gag and against mCherry were used to visualize particular viral components. Presence of gp22mCherry signal in isolated virions was validated. Section SB—Particle-tracking analysis was performed using Fiji plugin Mosaic: Particle tracker 2D/3D [53,54]. Two cells for each mCherry virus variant from independent experiments were selected for this analysis. In all analyzed cells, 6 to 8 mCherry signal-containing vesicles were tracked. The trajectories were filtered to only include those containing at least 50 time points. The analysis showed, according to the MSS slope values, that all three variants were using active transport.

Author Contributions: P.G.P. designed and performed the experiments and ImageJ analyses as well as writing this paper, J.L. co-designed and performed some of the experiments and contributed to discussions about the results, J.Z. performed confocal microscopy, H.L. performed TEM experiments, M.R. designed the experiments and wrote the TEM part of this paper as well as discussing TEM results, E.H. and T.R. provided all their expertise in designing the whole project and supervised all the work and writing of this paper.

Funding: This research was founded by grant from the Czech Science Foundation (GACR) no.: GA17-24281S.

Acknowledgments: We are grateful to Paul Spearman for kindly providing the plasmids pSARMXmCherryTM and pEGFP-Rab5a, to Romana Hadravova for technical assistance with electron microscopy, and to William E. Diehl for the inspiring discussion of results and review of this paper.

Conflicts of Interest: The authors declare no conflicts of interest.

References

1. Chopra, H.C.; Mason, M.M. A new virus in a spontaneous mammary tumor of a rhesus monkey. *Cancer Res.* **1970**, *30*, 2081–2086. [PubMed]
2. Kramarsky, B.; Sarkar, N.H.; Moore, D.H. Ultrastructural comparison of a virus from a Rhesus-monkey mammary carcinoma with four oncogenic RNA viruses. *Proc. Natl. Acad. Sci. USA* **1971**, *68*, 1603–1607. [CrossRef] [PubMed]
3. Kohoutova, Z.; Rumlova, M.; Andreansky, M.; Sakalian, M.; Hunter, E.; Pichova, I.; Ruml, T. The impact of altered polyprotein ratios on the assembly and infectivity of Mason-Pfizer monkey virus. *Virology* **2009**, *384*, 59–68. [CrossRef] [PubMed]
4. Vlach, J.; Lipov, J.; Rumlova, M.; Veverka, V.; Lang, J.; Srb, P.; Knejzlik, Z.; Pichova, I.; Hunter, E.; Hrabal, R.; et al. D-retrovirus morphogenetic switch driven by the targeting signal accessibility to Tctex-1 of dynein. *Proc. Natl. Acad. Sci. USA* **2008**, *105*, 10565–10570. [CrossRef] [PubMed]
5. Sfakianos, J.N.; LaCasse, R.A.; Hunter, E. The M-PMV cytoplasmic targeting-retention signal directs nascent Gag polypeptides to a pericentriolar region of the cell. *Traffic* **2003**, *4*, 660–670. [CrossRef] [PubMed]
6. Sakalian, M.; Hunter, E. Separate assembly and transport domains within the Gag precursor of Mason-Pfizer monkey virus. *J. Virol.* **1999**, *73*, 8073–8082. [PubMed]
7. Hong, S.; Choi, G.; Park, S.; Chung, A.S.; Hunter, E.; Rhee, S.S. Type D retrovirus Gag polyprotein interacts with the cytosolic chaperonin TRiC. *J. Virol.* **2001**, *75*, 2526–2534. [CrossRef] [PubMed]
8. Ulbrich, P.; Haubova, S.; Nermut, M.V.; Hunter, E.; Rumlova, M.; Ruml, T. Distinct roles for nucleic acid in in vitro assembly of purified Mason-Pfizer monkey virus CANC proteins. *J. Virol.* **2006**, *80*, 7089–7099. [CrossRef] [PubMed]
9. Song, C.; Dubay, S.R.; Hunter, E. A Tyrosine Motif in the Cytoplasmic Domain of Mason-Pfizer Monkey Virus Is Essential for the Incorporation of Glycoprotein into Virions. *J. Virol.* **2003**, *77*, 5192–5200. [CrossRef] [PubMed]

10. Sfakianos, J.N.; Hunter, E. M-PMV capsid transport is mediated by Env/Gag interactions at the pericentriolar recycling endosome. *Traffic* **2003**, *4*, 671–680. [[CrossRef](#)] [[PubMed](#)]
11. Pereira, L.E.; Clark, J.; Grznarova, P.; Wen, X.; Lacasse, R.; Ruml, T.; Spearman, P.; Hunter, E. Direct evidence for intracellular anterograde co-transport of M-PMV Gag and Env on microtubules. *Virology* **2014**, *449*, 109–119. [[CrossRef](#)] [[PubMed](#)]
12. Clark, J.; Grznarova, P.; Stansell, E.; Diehl, W.; Lipov, J.; Spearman, P.; Ruml, T.; Hunter, E. A Mason-Pfizer Monkey Virus Gag-GFP Fusion Vector Allows Visualization of Capsid Transport in Live Cells and Demonstrates a Role for Microtubules. *PLoS ONE* **2013**, *8*, e83863. [[CrossRef](#)] [[PubMed](#)]
13. Choudhury, A.; Dominguez, M.; Puri, V.; Sharma, D.K.; Narita, K.; Wheatley, C.W.; Marks, D.L.; Pagano, R.E. Rab proteins mediate Golgi transport of caveola-internalized glycosphingolipids and correct lipid trafficking in Niemann-Pick C cells. *J. Clin. Investig.* **2002**, *109*, 1541–1550. [[CrossRef](#)] [[PubMed](#)]
14. Song, C.; Micoli, K.; Bauerova, H.; Pichova, I.; Hunter, E. Amino acid residues in the cytoplasmic domain of the Mason-Pfizer monkey virus glycoprotein critical for its incorporation into virions. *J. Virol.* **2005**, *79*, 11559–11568. [[CrossRef](#)] [[PubMed](#)]
15. Rumlova, M.; Ruml, T.; Pohl, J.; Pichova, I. Specific in vitro cleavage of Mason-Pfizer monkey virus capsid protein: Evidence for a potential role of retroviral protease in early stages of infection. *Virology* **2003**, *310*, 310–318. [[CrossRef](#)]
16. Schindelin, J.; Arganda-Carreras, I.; Frise, E.; Kaynig, V.; Longair, M.; Pietzsch, T.; Preibisch, S.; Rueden, C.; Saalfeld, S.; Schmid, B.; et al. Fiji: An open-source platform for biological-image analysis. *Nat. Methods* **2012**, *9*, 676–682. [[CrossRef](#)] [[PubMed](#)]
17. Schindelin, J.; Rueden, C.T.; Hiner, M.C.; Eliceiri, K.W. The ImageJ ecosystem: An open platform for biomedical image analysis. *Mol. Reprod. Dev.* **2015**, *82*, 518–529. [[CrossRef](#)] [[PubMed](#)]
18. Schneider, C.A.; Rasband, W.S.; Eliceiri, K.W. NIH Image to ImageJ: 25 years of image analysis. *Nat. Methods* **2012**, *9*, 671–675. [[CrossRef](#)] [[PubMed](#)]
19. Costes, S.V.; Daelemans, D.; Cho, E.H.; Dobbin, Z.; Pavlakakis, G.; Lockett, S. Automatic and quantitative measurement of protein-protein colocalization in live cells. *Biophys. J.* **2004**, *86*, 3993–4003. [[CrossRef](#)] [[PubMed](#)]
20. Manders, E.M.M.; Verbeek, F.J.; Aten, J.A. Measurement of co-localization of objects in dual-colour confocal images. *J. Microsc.* **1993**, *169*, 375–382. [[CrossRef](#)]
21. Li, Q.; Lau, A.; Morris, T.J.; Guo, L.; Fordyce, C.B.; Stanley, E.F. A syntaxin 1, Galpha(o), and N-type calcium channel complex at a presynaptic nerve terminal: Analysis by quantitative immunocolocalization. *J. Neurosci. Off. J. Soc. Neurosci.* **2004**, *24*, 4070–4081. [[CrossRef](#)] [[PubMed](#)]
22. Bohmova, K.; Hadravova, R.; Stokrova, J.; Tuma, R.; Ruml, T.; Pichova, I.; Rumlova, M. Effect of dimerizing domains and basic residues on in vitro and in vivo assembly of Mason-Pfizer monkey virus and human immunodeficiency virus. *J. Virol.* **2010**, *84*, 1977–1988. [[CrossRef](#)] [[PubMed](#)]
23. Muranyi, W.; Malkusch, S.; Muller, B.; Heilemann, M.; Krausslich, H.G. Super-resolution microscopy reveals specific recruitment of HIV-1 envelope proteins to viral assembly sites dependent on the envelope C-terminal tail. *PLoS Pathog.* **2013**, *9*, e1003198. [[CrossRef](#)] [[PubMed](#)]
24. Blot, V.; Lopez-Verges, S.; Breton, M.; Pique, C.; Berlioz-Torrent, C.; Grange, M.P. The conserved dileucine- and tyrosine-based motifs in MLV and MPMV envelope glycoproteins are both important to regulate a common Env intracellular trafficking. *Retrovirology* **2006**, *3*, 62. [[CrossRef](#)] [[PubMed](#)]
25. Bucci, C.; Parton, R.G.; Mather, I.H.; Stunnenberg, H.; Simons, K.; Hoflack, B.; Zerial, M. The small GTPase rab5 functions as a regulatory factor in the early endocytic pathway. *Cell* **1992**, *70*, 715–728. [[CrossRef](#)]
26. Vanlandingham, P.A.; Ceresa, B.P. Rab7 regulates late endocytic trafficking downstream of multivesicular body biogenesis and cargo sequestration. *J. Biol. Chem.* **2009**, *284*, 12110–12124. [[CrossRef](#)] [[PubMed](#)]
27. Barbero, P.; Bittova, L.; Pfeffer, S.R. Visualization of Rab9-mediated vesicle transport from endosomes to the trans-Golgi in living cells. *J. Cell Biol.* **2002**, *156*, 511–518. [[CrossRef](#)] [[PubMed](#)]
28. Ullrich, O.; Reinsch, S.; Urbe, S.; Zerial, M.; Parton, R.G. Rab11 regulates recycling through the pericentriolar recycling endosome. *J. Cell Biol.* **1996**, *135*, 913–924. [[CrossRef](#)]
29. Postler, T.S.; Bixby, J.G.; Desrosiers, R.C.; Yuste, E. Systematic analysis of intracellular trafficking motifs located within the cytoplasmic domain of simian immunodeficiency virus glycoprotein gp41. *PLoS ONE* **2014**, *9*, e114753. [[CrossRef](#)] [[PubMed](#)]

30. Postler, T.S.; Desrosiers, R.C. The tale of the long tail: The cytoplasmic domain of HIV-1 gp41. *J. Virol.* **2013**, *87*, 2–15. [[CrossRef](#)] [[PubMed](#)]
31. Postler, T.S.; Desrosiers, R.C. The cytoplasmic domain of the HIV-1 glycoprotein gp41 induces NF-kappaB activation through TGF-beta-activated kinase 1. *Cell Host Microbe* **2012**, *11*, 181–193. [[CrossRef](#)] [[PubMed](#)]
32. Tedbury, P.R.; Freed, E.O. The cytoplasmic tail of retroviral envelope glycoproteins. *Prog. Mol. Boil. Transl. Sci.* **2015**, *129*, 253–284.
33. Sonigo, P.; Barker, C.; Hunter, E.; Wain-Hobson, S. Nucleotide sequence of Mason-Pfizer monkey virus: An immunosuppressive D-type retrovirus. *Cell* **1986**, *45*, 375–385. [[CrossRef](#)]
34. Rhee, S.S.; Hunter, E. Amino-Acid Substitutions within the Matrix Protein of Type-D Retroviruses Affect Assembly, Transport and Membrane Association of a Capsid. *EMBO J.* **1991**, *10*, 535–546. [[CrossRef](#)] [[PubMed](#)]
35. Rhee, S.S.; Hunter, E. Myristylation Is Required for Intracellular-Transport but Not for Assembly of D-Type Retrovirus Capsids. *J. Virol.* **1987**, *61*, 1045–1053. [[PubMed](#)]
36. Murakami, T.; Freed, E.O. Genetic evidence for an interaction between human immunodeficiency virus type 1 matrix and alpha-helix 2 of the gp41 cytoplasmic tail. *J. Virol.* **2000**, *74*, 3548–3554. [[CrossRef](#)] [[PubMed](#)]
37. Freed, E.O.; Martin, M.A. Virion incorporation of envelope glycoproteins with long but not short cytoplasmic tails is blocked by specific, single amino acid substitutions in the human immunodeficiency virus type 1 matrix. *J. Virol.* **1995**, *69*, 1984–1989. [[PubMed](#)]
38. Mammano, F.; Kondo, E.; Sodroski, J.; Bukovsky, A.; Gottlinger, H.G. Rescue of human immunodeficiency virus type 1 matrix protein mutants by envelope glycoproteins with short cytoplasmic domains. *J. Virol.* **1995**, *69*, 3824–3830. [[PubMed](#)]
39. Ladinsky, M.S.; Kremer, J.R.; Furcinitti, P.S.; McIntosh, J.R.; Howell, K.E. HVEM tomography of the trans-Golgi network: Structural insights and identification of a lace-like vesicle coat. *J. Cell Boil.* **1994**, *127*, 29–38. [[CrossRef](#)]
40. Ladinsky, M.S.; Mastronarde, D.N.; McIntosh, J.R.; Howell, K.E.; Staehelin, L.A. Golgi structure in three dimensions: Functional insights from the normal rat kidney cell. *J. Cell Boil.* **1999**, *144*, 1135–1149. [[CrossRef](#)]
41. Chia, P.Z.; Gasnereau, I.; Lieu, Z.Z.; Gleeson, P.A. Rab9-dependent retrograde transport and endosomal sorting of the endopeptidase furin. *J. Cell Sci.* **2011**, *124*, 2401–2413. [[CrossRef](#)] [[PubMed](#)]
42. White, J.; Keller, P.; Stelzer, E.H. Spatial partitioning of secretory cargo from Golgi resident proteins in live cells. *BMC Cell Boil.* **2001**, *2*, 19.
43. Hunter, E.; Swanstrom, R. Retrovirus envelope glycoproteins. *Curr. Top. Microbiol. Immunol.* **1990**, *157*, 187–253. [[PubMed](#)]
44. Prchal, J.; Srb, P.; Hunter, E.; Ruml, T.; Hrabal, R. The structure of myristoylated Mason-Pfizer monkey virus matrix protein and the role of phosphatidylinositol-(4,5)-biphosphate in its membrane binding. *J. Mol. Boil.* **2012**, *423*, 427–438. [[CrossRef](#)] [[PubMed](#)]
45. Lombardi, D.; Soldati, T.; Riederer, M.A.; Goda, Y.; Zerial, M.; Pfeffer, S.R. Rab9 functions in transport between late endosomes and the trans Golgi network. *EMBO J.* **1993**, *12*, 677–682. [[CrossRef](#)] [[PubMed](#)]
46. Sharma, D.K.; Choudhury, A.; Singh, R.D.; Wheatley, C.L.; Marks, D.L.; Pagano, R.E. Glycosphingolipids internalized via caveolar-related endocytosis rapidly merge with the clathrin pathway in early endosomes and form microdomains for recycling. *J. Boil. Chem.* **2003**, *278*, 7564–7572. [[CrossRef](#)] [[PubMed](#)]
47. Cheryl Chia, P.Z.; Gleeson, P.A. The Regulation of Endosome-to-Golgi Retrograde Transport by Tethers and Scaffolds. *Traffic* **2011**, *12*, 939–947. [[CrossRef](#)] [[PubMed](#)]
48. Patterson, G.H.; Hirschberg, K.; Polishchuk, R.S.; Gerlich, D.; Phair, R.D.; Lippincott-Schwartz, J. Transport through the Golgi apparatus by rapid partitioning within a two-phase membrane system. *Cell* **2008**, *133*, 1055–1067. [[CrossRef](#)] [[PubMed](#)]
49. Bonifacino, J.S.; Glick, B.S. The mechanisms of vesicle budding and fusion. *Cell* **2004**, *116*, 153–166. [[CrossRef](#)]
50. Bonifacino, J.S.; Traub, L.M. Signals for sorting of transmembrane proteins to endosomes and lysosomes. *Annu. Rev. Biochem.* **2003**, *72*, 395–447. [[CrossRef](#)] [[PubMed](#)]
51. Stansell, E.; Apkarian, R.; Haubova, S.; Diehl, W.E.; Tytler, E.M.; Hunter, E. Basic residues in the Mason-Pfizer monkey virus gag matrix domain regulate intracellular trafficking and capsid-membrane interactions. *J. Virol.* **2007**, *81*, 8977–8988. [[CrossRef](#)] [[PubMed](#)]

52. Dostalkova, A.; Kaufman, F.; Krizova, I.; Kultova, A.; Strohalmova, K.; Hadravova, R.; Ruml, T.; Rumlova, M. Mutations in the Basic Region of the Mason-Pfizer Monkey Virus Nucleocapsid Protein Affect Reverse Transcription, Genomic RNA Packaging, and the Virus Assembly Site. *J. Virol.* **2018**. [[CrossRef](#)] [[PubMed](#)]
53. Sbalzarini, I.F.; Koumoutsakos, P. Feature point tracking and trajectory analysis for video imaging in cell biology. *J. Struct. Biol.* **2005**, *151*, 182–195. [[CrossRef](#)] [[PubMed](#)]
54. Chenouard, N.; Smal, I.; de Chaumont, F.; Maska, M.; Sbalzarini, I.F.; Gong, Y.; Cardinale, J.; Carthel, C.; Coraluppi, S.; Winter, M.; et al. Objective comparison of particle tracking methods. *Nat. Methods* **2014**, *11*, 281–289. [[CrossRef](#)] [[PubMed](#)]



© 2018 by the authors. Licensee MDPI, Basel, Switzerland. This article is an open access article distributed under the terms and conditions of the Creative Commons Attribution (CC BY) license (<http://creativecommons.org/licenses/by/4.0/>).

Příloha 6



Contents lists available at SciVerse ScienceDirect

Materials Science and Engineering C

journal homepage: www.elsevier.com/locate/msec

Structure, mechanical properties, corrosion behavior and cytotoxicity of biodegradable Mg–X (X = Sn, Ga, In) alloys

J. Kubásek^{a,*}, D. Vojtěch^a, J. Lipov^b, T. Ruml^b

^a Department of Metals and Corrosion Engineering, Institute of Chemical Technology, Prague, Technická 5, 166 28 Prague 6, Czech Republic

^b Department of Biochemistry and Microbiology, Institute of Chemical Technology, Prague, Technická 5, 166 28 Prague 6, Czech Republic

ARTICLE INFO

Article history:

Received 22 October 2012

Received in revised form 15 January 2013

Accepted 4 February 2013

Available online xxxx

Keywords:

Magnesium
Biodegradable alloy
Mechanical properties
Corrosion
Cytotoxicity

ABSTRACT

As-cast Mg–Sn, Mg–Ga and Mg–In alloys containing 1–7 wt.% of alloying elements were studied in this work. Structural and chemical analysis of the alloys was performed by using light and scanning electron microscopy, energy dispersive spectrometry, x-ray diffraction, x-ray photoelectron spectroscopy and glow discharge spectrometry. Mechanical properties were determined by Vickers hardness measurements and tensile testing. Corrosion behavior in a simulated physiological solution (9 g/l NaCl) was studied by immersion tests and potentiodynamic measurements. The cytotoxicity effect of the alloys on human osteosarcoma cells (U-2 OS) was determined by an indirect contact assay. Structural investigation revealed the dendritic morphology of the as-cast alloys with the presence of secondary eutectic phases in the Mg–Sn and Mg–Ga alloys. All the alloying elements showed hardening and strengthening effects on magnesium. This effect was the most pronounced in the case of Ga. All the alloying elements at low concentrations of approximately 1 wt.% were also shown to positively affect the corrosion resistance of Mg. But at higher concentrations of Ga and Sn the corrosion resistance worsened due to galvanic effects of secondary phases. Cytotoxicity tests indicated that Ga had the lowest toxicity, followed by Sn. The most severe toxicity was observed in the case of In.

© 2013 Elsevier B.V. All rights reserved.

1. Introduction

Magnesium alloys show a good combination of strength and low weight making them of interest in many structural applications in automotive and aerospace industries. Besides, a relative non-toxicity and degradability of magnesium in the human body make magnesium based alloys promising materials for the production of temporary biodegradable medical implants like stents in vascular medicine or fixation devices for fractured bones in osteosynthesis. For this purpose, many Mg-based alloying systems, such as AZ, AM, AE, ZE, WE, MZ, WZ, LAE, ZK (according to ASTM designation), Mg–Ca, Mg–RE, and Mg–Zn–Ca [1–3], have been studied. The design and introduction of a new implant into the medical practice require deep knowledge of chemical, physical, mechanical, corrosion and biological characteristics of the new material. In this study we focus our attention on binary Mg-based alloys containing low-melting metals (LMMs), namely tin, gallium and indium. Among them, Mg–Sn alloys have been the most widely studied so far. However, additions of tin into Mg-based alloys are mainly aimed in improving strength and creep resistance for elevated temperature applications [4–7]. Tin forms a Mg₂Sn intermetallic phase with a high melting point of 770 °C [8], therefore,

this phase shows morphological and thermal stabilities and enhances the elevated temperature performance of Mg-based alloys. Tin also improves the castability and corrosion resistance of Mg alloys [4,5]. Regarding the biocompatibility, tin is generally considered as a relatively non-toxic metal. The reason is that tin and its compounds are poorly absorbed and accumulated in human tissues and that tin is rapidly excreted mainly by kidneys [9]. There are only a few reports on Mg–Sn alloys in the context of biodegradable materials. It was reported by Gu et al. [10] that a binary Mg–1Sn alloy showed a good in vitro biocompatibility and that it had no adverse effects on cell viability.

Mg-based alloys containing gallium are mainly studied for applications in seawater batteries and sacrificial anodes [11,12]. In these applications, gallium was reported to improve the strength and hardness of Mg-based alloys due to both solid solution and precipitation strengthening [13]. In vivo and in vitro biocompatibility was mainly studied for Ga-based semiconductor compounds like GaP or GaN potentially applicable to monitor and control neural functions [14,15]. It was reported that the GaN semiconductor had a better stability and biocompatibility than the GaP one. Gallium ions are also known to be effective against bone resorption and for the treatment of osteoporosis, and to increase calcium and phosphorus contents in bones [16]. However, to our knowledge, Mg–Ga alloys have not yet been studied as potential biodegradable materials for osteosynthesis.

Regarding indium, a number of studies show that insoluble indium compounds may induce toxicity and even carcinogenic effects

* Corresponding author. Tel.: +420 220444055; fax: +420 220444400.
E-mail address: Jiri.Kubasek@vscht.cz (J. Kubásek).

when directly inhaled by lung [17]. On the other hand, there are only a limited number of studies of Mg–In alloys related to biodegradable implants. Some results are promising, because they indicate a positive effect of In on the strength and relatively low effects of In on the viability of cell lines [10]. For these reasons, Mg–In alloys are still subject of experimental research.

As indicated above, in available literature there is little information on Mg–Sn, Mg–Ga and Mg–In alloys in the context to biodegradable implants. For this reason, the present study is intended to characterize structural, mechanical, corrosion and biological properties of as-cast Mg–Sn, Mg–Ga and Mg–In biodegradable alloys containing various concentrations of alloying elements. The main objective is to select the most prospective system for load-bearing implants in osteosynthesis. Simple gravity casting was used to prepare the alloys, because it represents a simple and inexpensive alternative for the production of small and complex-shaped implants. Moreover, due to relatively high solid solubility of Sn, Ga and In in the α -Mg solid solution (14.5, 8.5 and 53.5 wt.%, respectively) [8], the influence of solution heat-treatment (T4) on the properties of the alloys is also investigated.

2. Materials and methods

Binary Mg–Sn, Mg–Ga and Mg–In alloys with various contents of LMMs were investigated in our work. Concentrations of alloying elements were selected to be lower than their maximum solid solubility in α -Mg. Alloy designations and chemical compositions are summarized in Table 1.

The investigated alloys were prepared by melting of pure metals in an induction furnace under argon atmosphere. After a sufficient homogenization of the melt, the alloy was poured into a not preheated brass metal mold to produce a cylindrical ingot of 20 mm in diameter. Structure, mechanical and corrosion properties were studied in the as-cast state.

Mechanical properties were characterized by Vickers hardness tests with a loading of 5 kg (HV5) and by tensile tests (LabTest 5.250SP1-VM). Rod samples for tensile testing of 10 mm in diameter and 100 mm in length were directly machined from the cast ingots.

The corrosion behavior of the alloys was studied by immersion tests and potentiodynamic measurements in a simple simulated physiological solution (9 g/l NaCl). However, it's worth mentioning that blood plasma and intercellular fluid in human organism contain in addition to Cl^- anion K^+ , Ca^{2+} , Mg^{2+} , HCO_3^- , HPO_4^{2-} , H_2PO_4^- or SO_4^{2-} ions and some organic components such amino acids or proteins. Therefore, degradation of magnesium alloys in these fluids is a much complicated phenomenon compared to that in a simple salt solution. In our corrosion experiment we did not use any simulated body fluid (SBF). Besides Cl^- anions, SBFs mostly proposed in literature also contain HCO_3^- , HPO_4^{2-} or H_2PO_4^- anions. It is known that

these anions would bring about the formation of insoluble corrosion products (carbonates and phosphates) on the surface of corroded Mg alloys. These products would slow down the corrosion rates of the investigated materials [18] and the differences between them would be partially diminished. For this reason we used a solution containing only the most aggressive Cl^- anions to assess differences between corrosion performances of the alloys. Moreover it looks like that corrosion of biodegradable materials in human organism can differ from the corrosion process in simulated body fluids, even in DMEM [19]. Therefore, we used only simple simulated physiological solution, allowing an easy comparison of corrosion rate. In the immersion tests, coupons (20 mm in diameter, 2 mm thick) were immersed in 250 ml of the solution for 168 h at 37 °C. To prevent evaporation loss of the corrosion medium immersion tests were carried out in closed vessels. The exposition in a closed system also better simulates a biodegradable implant tightly surrounded by a hard tissue like, for example, a screw for fixation of fractured bone. The immersion tests were supplemented by pH measurements at certain times during exposure. After immersion tests, corrosion products were removed using a solution of 200 g/l CrO_3 , 10 g/l AgNO_3 and 20 g/l $\text{Ba}(\text{NO}_3)_2$ according to ISO 8407. The corrosion rates were calculated (mm/year) using the weight losses measured on a balance with an accuracy of 0.1 mg according to ASTM G31-72. Each immersion test was performed three times. The potentiodynamic curves of the alloys were measured on a potentiostat (FAS1 Gamry). Experiments were performed in a standard three-electrode setup: the sample (circle surface area with 10 mm in diameter) as the working electrode, platinum wire as counter electrode and $\text{Ag}/\text{AgCl}/\text{KCl}$ (3 mol/l) as the reference electrode (SSCE) with a potential of 0.199 V/SHE. All potentials presented in this paper were measured against SSCE. Potentiodynamic curves were scanned at a rate of 2 mV/s.

The structure and elemental distributions of the alloys, as well as the corroded surfaces, were studied by light microscopy (LM) and scanning electron microscopy (SEM, Tescan Vega 3) with energy dispersion spectrometry (EDS, Oxford Instruments Inca 350). The phase composition was determined by X-ray diffraction (XRD) analysis using an X'Pert Pro diffractometer (30 mA, 40 kV, X-ray radiation $\text{Cu K}\alpha$). Concentration profiles of corrosion products were also analyzed by glow discharge spectrometry (GDS, GD Profiler 2, Ar pressure of 650 Pa, source operating at 50 W, approximate sputtering rate of 2.5 $\mu\text{m}/\text{min}$). Additionally, chemical composition of the surface and sub-surface regions of corroded alloys was characterized by x-ray photoelectron spectroscopy (XPS, ESCA Probe P, pressure in the analytical chamber of 2×10^{-8} Pa, monochromatic $\text{Al K}\alpha$ X-ray source, binding energy calibration with respect to the energy of $\text{Au 4f}_{7/2}$ peak).

Human osteosarcoma cells (U-2 OS) were used to evaluate the cytotoxicity of the alloys containing 1% of LMMs. Cells were cultured in Dulbecco's modified Eagle's medium (DMEM) supplemented with 10% fetal bovine serum (FBS), 100 U/ml penicillin, 1 mg/ml

Table 1
Designations and chemical compositions (in wt.%, including cathodic impurities) of the investigated alloys.

Alloy designation	Element											
	Sn	Ga	In	Al	Si	Mn	Zn	Fe	Ni	Cu	Co	Mg
Mg	–	–	–	0.018	0.015	0.015	0.003	<0.001	<0.001	<0.001	<0.001	bal.
Mg–1Sn	1.335	–	–	0.021	0.015	0.040	0.003	<0.001	<0.001	<0.001	<0.001	bal.
Mg–5Sn	4.697	–	–	0.020	–	0.020	0.003	<0.001	<0.001	0.001	<0.001	bal.
Mg–7Sn	7.238	–	–	0.027	0.010	0.035	0.003	<0.001	<0.001	<0.001	<0.001	bal.
Mg–1Ga	–	1.210	–	0.025	0.024	0.020	0.003	<0.001	<0.001	<0.001	<0.001	bal.
Mg–4Ga	–	3.889	–	0.017	0.020	0.013	0.003	<0.001	<0.001	<0.001	<0.001	bal.
Mg–7Ga	–	6.733	–	0.014	0.023	0.017	0.003	0.001	<0.001	<0.001	<0.001	bal.
Mg–1In	–	–	0.863	0.018	0.032	0.027	0.003	<0.001	<0.001	<0.001	<0.001	bal.
Mg–3In	–	–	2.636	0.013	0.011	0.015	0.003	<0.001	<0.001	<0.001	<0.001	bal.
Mg–7In	–	–	7.363	0.015	0.011	0.010	0.002	<0.001	<0.001	<0.001	<0.001	bal.

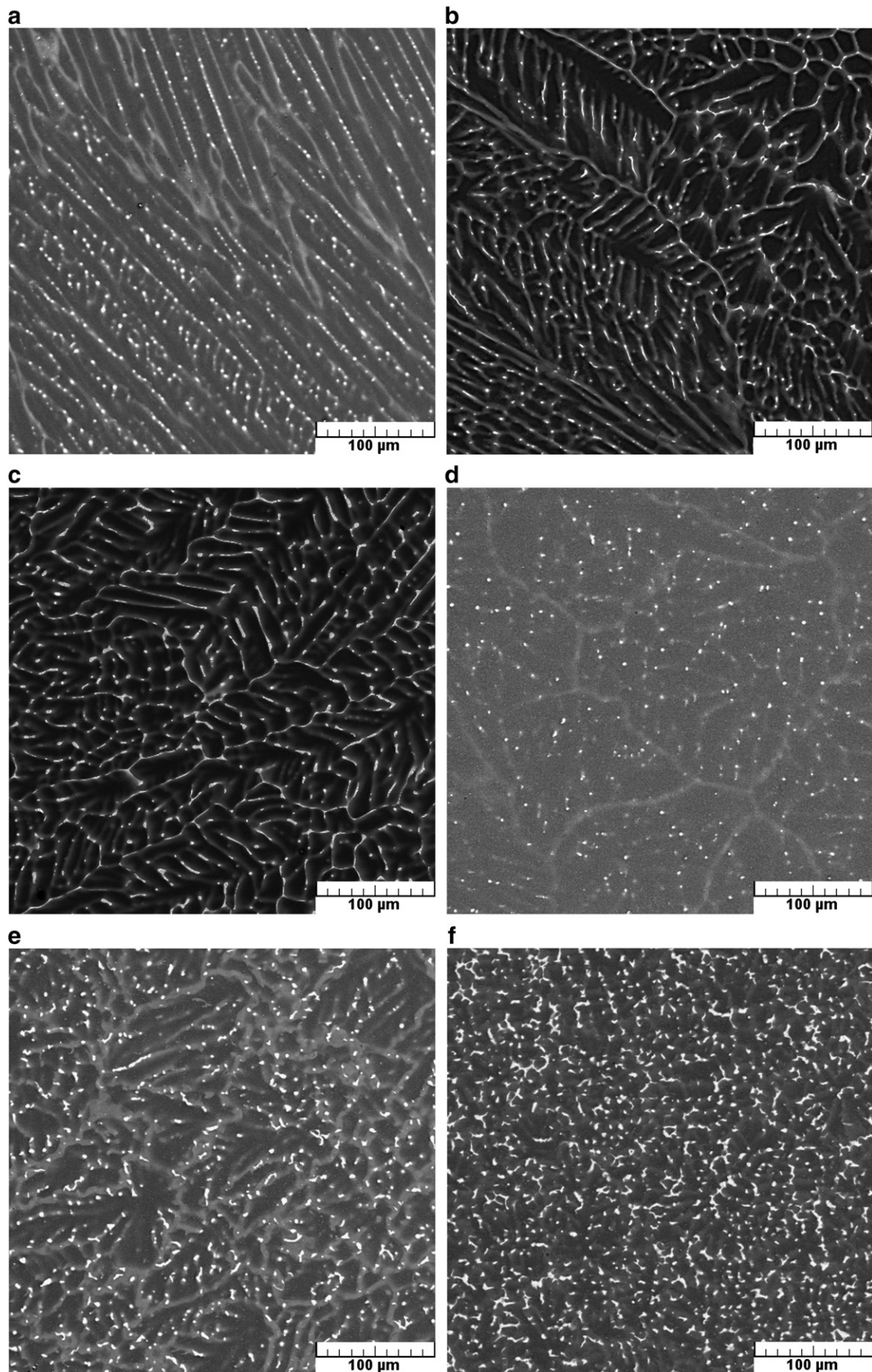


Fig. 1. SEM micrographs of the as-cast alloys: a) Mg-1Sn, b) Mg-5Sn, c) Mg-7Sn, d) Mg-1 Ga, e) Mg-4Ga, f) Mg-7Ga, g) Mg-1In, h) Mg-3In, and i) Mg-7In.

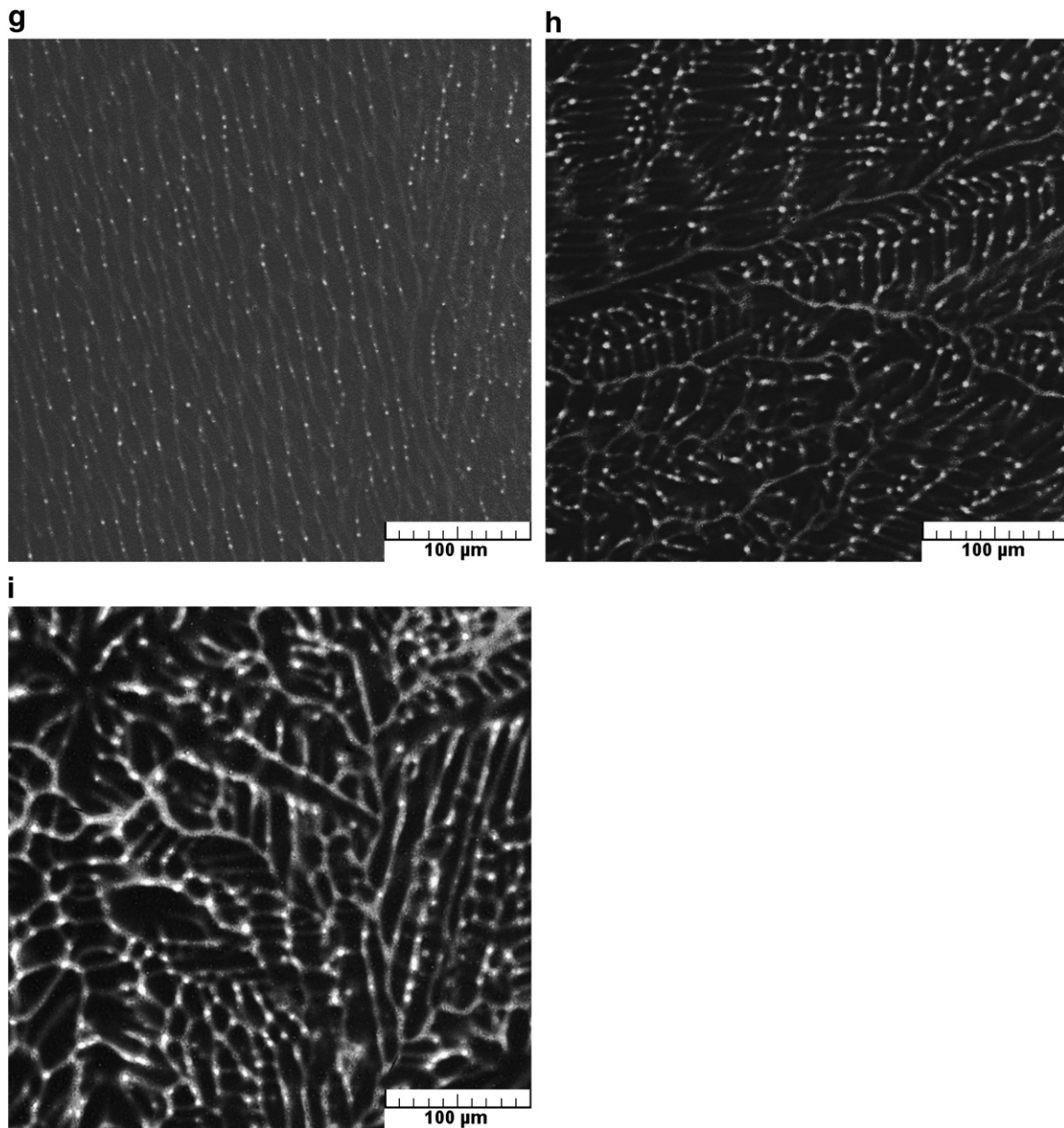


Fig. 1 (continued).

streptomycin and 250 ng/ml amphotericin B at 37 °C in a humidified atmosphere of 5% CO₂. The cytotoxicity was evaluated by an indirect contact assay. Extracts were prepared using DMEM medium containing 5% FBS and antibiotics at 37 °C for 168 h. The ratio of surface area of alloy samples to the extraction medium was 1 cm²/ml. The extract was then withdrawn and either used directly for the cytotoxicity test or; alternatively, stored at 4 °C. Cytotoxicity tests were also performed after twofold and fifteen fold dilutions of the original extracts. The concentrations of eluted metal ions were determined using inductively coupled plasma mass spectrometry. Cells were seeded at a density of 2.5×10^4 cells/ml and incubated in 96-well cell culture plates for 24 h to allow attachment. The medium was then replaced with 100 μl of the extracts. The controls involved either DMEM medium as mock or 0.64% phenol in DMEM medium as a negative control. Following the incubation of the cells in a humidified atmosphere of 5% CO₂ at 37 °C for 2 and 5 days the extracts were removed. The cells were then washed twice using phosphate buffered saline (PBS) and overlaid with phenol red-free DMEM medium

containing 5 μl of WST-1 reagent (Roche) per well. The plates were incubated with WST-1 for 4 h at 37 °C. The assay is based on the reduction of tetrazolium salt to soluble formazan by mitochondrial enzymes of viable cells. The absorbance of the samples characterizing the cell viability was measured using microplate reader at 450 nm with a reference wavelength of 630 nm.

3. Results and discussion

3.1. Structure

Fig. 1 shows as-cast microstructures of the investigated alloys. The α-Mg phase in the as-cast alloys (Fig. 1(a) to (i)) has a typical dendritic morphology with an average dendrite arm thickness of approximately 20 μm. In Mg–Sn (Fig. 1(a) to (c)) and Mg–Ga (Fig. 1(d) to (f)) alloys, Mg₂Sn and Mg₅Ga₂ eutectic particles (light) are observed in interdendritic regions. The volume fractions of eutectic phases increase with increasing concentrations of Sn and Ga in alloys.

Table 2
Concentrations (in wt.%) of the main alloying elements in α -Mg dendrites of the as-cast alloys (EDS).

	As-cast alloy								
	Mg–1Sn	Mg–5Sn	Mg–7Sn	Mg–1Ga	Mg–4Ga	Mg–7Ga	Mg–1In	Mg–3In	Mg–7In
Dendrite cores	0.9	3.0	4.4	0.8	3.2	4.2	0.8	1.5	5.0
Dendrite edges	1.8	7.4	8.9	3.6	6.4	8.6	1.9	5.5	11.7

Moreover, the volume fraction of the Mg_5Ga_2 eutectic particles is higher than that of Mg_2Sn particles at the same concentrations of alloying elements (Fig. 1(c) and (f)). The reason is a higher solid solubility of Sn in Mg (14.5%) than that of Ga in Mg (8.5%) [8]. In the Mg–In alloys (Fig. 1 from (g) to (i)), no secondary phases are visible due to a high solid solubility of In in α -Mg (53.5 wt.%) [8]. SEM micrographs in Fig. 1 also indicate a dendritic microsegregation in the as-cast alloys which appears as light shadows at dendrite edges corresponding to an enrichment in alloying elements. Chemical compositions of dendrite cores and edges are summarized in Table 2. As expected, concentration gradients increase with increasing concentrations of alloying elements. Moreover, the highest concentration gradient is observed in the as-cast Mg–7In alloy, because this alloy does not contain any In-rich secondary phases (Fig. 1(i)).

3.2. Mechanical properties

Mechanical properties of selected as-cast alloys are summarized in Fig. 2. It is observed that the LMMs influence mechanical properties in different ways. Both gallium and tin increase the yield strength that belongs to 0.2% of relative deformation (TYS), ultimate tensile strength (UTS) and hardness. But the hardening effect is more pronounced in the case of gallium, because hardness, yield and tensile strength of the Mg–4Ga alloy are higher than the same parameters of the Mg–5Sn alloy. Three hardening contributions can be expected in the Mg–Ga and Mg–Sn alloys: 1. Hall–Petch (H–P) hardening, 2. solid solution hardening and 3. hardening by secondary Mg_2Sn and Mg_5Ga_2 eutectic particles (Fig. 1). The H–P contribution is similar for both the alloys because of the observed similarity in dendrite dimensions (Fig. 1). Solid solution hardening is caused by an elastic stress induced by substitution atoms introduced into the Mg lattice. In the first approach, the elastic stress is proportional to the atomic size mismatch between Mg and alloying elements. Atomic radii of

Mg, Sn and Ga are 0.160, 0.158 and 0.135 nm, respectively [8]. Apparently, gallium atoms which are smaller than magnesium atoms by 16% induce a higher stress in magnesium lattice than tin atoms whose dimensions are similar to magnesium. Hardness and strength are also influenced by the volume fraction of secondary eutectic phases. By comparing Fig. 1(b) and (e) one can observe that the volume fraction of the Mg_5Ga_2 phase in the Mg–4Ga alloy is slightly higher than that of the Mg_2Sn phase in the Mg–5Sn alloy. As was mentioned before, this is caused by a higher solid solubility of Sn in Mg [8]. Besides the hardening and strengthening effects of gallium, this element also improves plasticity, because the elongation of the Mg–4Ga alloy (7.2%) is the highest from all the measured alloys (Fig. 2). Plasticity of Mg-based alloys is influenced by slip systems available in the magnesium lattice. It was shown by Liu et al. [13] that small gallium atoms introduced into hexagonal magnesium lattice reduce the c/a ratio leading to the activation of additional slip planes and to an improvement of the plasticity.

In contrast to gallium and tin, the influence of indium on the strength and hardness is smaller because both parameters are similar to those of pure Mg. The reasons are: 1. the similarity between In and Mg atomic radii (0.157 and 0.160 nm, respectively) [8] resulting in a low solid solution hardening effect, 2. the absence of hard secondary phases due to a high solid solubility of indium in magnesium (Fig. 1(g) to (i)). Modulus of elasticity for all studied materials ranged from 42 GPa for Mg to 45 GPa for Mg–5Sn alloy. Due to low concentrations of alloying elements, there were no differences in the values of modulus of elasticity.

In Table 3 mechanical properties of different materials that have been studied for possible applications as biodegradable implant materials are shown, pure magnesium and Mg–In alloy were characterized by quite poor TYS and UTS. On the contrary Mg–Ga alloy was characterized by improved mechanical properties in comparison with biodegradable polymer materials and improved or comparable

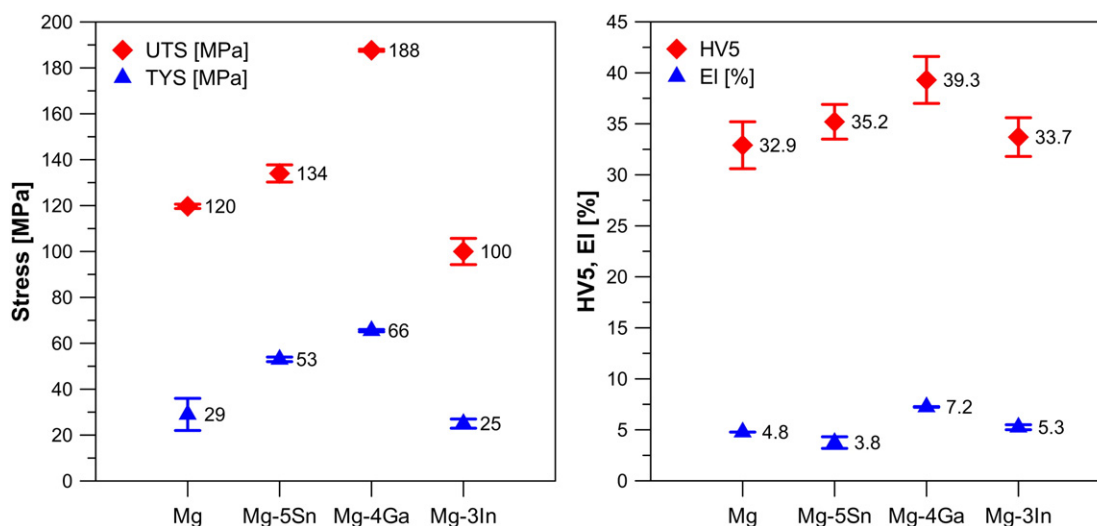


Fig. 2. Mechanical properties of the as-cast alloys (TYS – Tensile Yield Strength, UTS – Ultimate Tensile Strength, EI – plastic Elongation, HV5 – Vickers Hardness).

Table 3
Mechanical properties of selected materials considered for applications in medicine.

		TYS [MPa]	UTS [MPa]	El [%]	EM [GPa]
Cortical bone [29]		104.9–114.3	35–283	1.07–2.10	5–23
Cancellous bone [29]			1.5–38		0.010–1.570
Ti6Al4V [30]	Annealed conditions	795	860	10	116
Stainless steel 316L type [2]	Annealed conditions	190	490	40	193
Synthetic HA [29]			40–200		70–120
DL-PLA [29]			29–35		1.9–2.4
PLLA (poly-L-lactid acid) [31]		11–72			
PGA (polyglycolic acid) [31]		57			
PCL (poly-C-caprolactone) [31]		19–21			
Mg [29]	As-cast		87	21	41
Mg [10]	As-cast	20	85	13	
Mg–1Al [10]	As-cast	40	160	16	
Mg–1Ag [10]	As-cast	25	115	13	
Mg–1In [10]	As-cast	35	145	15	
Mg–1Mn [10]	As-cast	28	87	7.5	
Mg–1Si [10]	As-cast	80	195	15	
Mg–1Sn [10]	As-cast	35	145	20	
Mg–1Y [10]	As-cast	25	75	10	
Mg–1Zn [10]	As-cast	25	130	18	
Mg–1Zr [10]	As-cast	65	170	27	
Mg–5Gd [32]	As-cast	45	125	4.5	
Mg–10Gd [32]	As-cast	80	125	2.5	
Mg–1Zn [33]	As-cast	20	102	7	
Mg–4Zn [33]	As-cast	58	217	16	
Mg–4Zn–0.5Ca [33]	As-cast	70	180	12	
Mg–4Zn–1.5Ca [33]	As-cast	83	167	7	
Mg–0.5Sr [34]	T4	37	74	3	
Mg–1.5Sr [34]	T4	40	81	2.6	
Mg–2.0Zn–0.5Sr [34]	T6	62	142	8.9	
Mg–6.0Zn–0.5Sr [34]	T6	128	209	3.6	
Mg–2Sr [35]	Rollled state	145	210	3	
WE43 [36]	T6	170	220	2	44
Mg–2Ca [37]	Extruded	165	230	11	
Mg–4Ca [37]	Extruded	200	240	5	
Mg–3Nd–0.2Zn–0.4Zr [38]	T4	90	194	12	
Mg–3Nd–0.2Zn–0.4Zr [38]	Extruded	162	234	12	
Mg–2Zn–0.46Y [39]	Extruded	160	270	20	
Mg–2Zn–0.46Y–1Nd [39]	Extruded	170	280	16	
Mg–4Y–1Zn–1Mn [40]	As-cast	140	175	8	
AZ91 [41]	Diecast	150	230	3	
AM60 [41]	Diecast	115	205	6	
ZE41 [41]	T5	140	205	3.5	
WE54 [41]	T6	172	250	2	
WE43 [41]	T6	165	250	2	
AE42 [41]	Diecast	110	244	17	

mechanical properties with other studied materials based on Mg–Zn, Mg–Ca or Mg–Zn–Nd system. Moreover, mechanical properties of Mg–Ga were studied only in the cast state. It can be assumed that after sufficient treatment, for example using extrusion process, mechanical properties especially TYS should be significantly improved. In [20] Pellicer et al. compared compressive yield stress and Young's modulus of potential biodegradable materials. Although our materials were studied using tensile tests, observed properties are close to some other biodegradable magnesium alloys in crystalline state. Therefore, values of compressive stress should be also comparable. Based on our assumptions and using reference [20], it is evident that especially Mg–Ga alloys appear as competitive material for other biodegradable materials. However, mechanical properties of biodegradable metallic glasses are still superior because these materials are characterized by closer modulus of elasticity compared to bones and higher Yield strength than magnesium crystalline alloys. Unfortunately, the main problem in this case is the preparation of larger volumes of these materials.

Fig. 3 illustrates fracture surfaces of the alloys after tensile tests. A combination of inter- and trans-crystalline failures is observed for the pure Mg (Fig. 3(a)). In the case of binary alloys (Fig. 3(b) to (d)), fracture cracks evidently grew along dendrite boundaries. In the Mg–Sn

and Mg–Ga alloys these boundaries are occupied by hard eutectic particles acting as stress concentrators. More detailed views indicate the occurrence of local plastic deformation during the fracture of the alloys. This deformation is mainly observed on the fracture surface of the Mg–4Ga alloy showing a typical dimple-like morphology (Fig. 3(c)). The presence of small and deep dimples surrounding hard Mg₅Ga₂ eutectic particles is in accordance with the high elongation of the Mg–Ga alloy determined by tensile tests (Fig. 2). On the other hand, in the case of the Mg–5Sn alloy there is only an indication of shallow dimples on the fracture surface (Fig. 3b) corresponding to the low elongation of this alloy (Fig. 2).

3.3. Corrosion behavior

Corrosion rates of studied alloys are summarized in Fig. 4a. Fig. 5 illustrates potentiodynamic curves of the alloys containing the highest concentrations of LMMs. It is observed in Fig. 4a that all the LMMs improve the corrosion resistance in the simulated physiological solution. Additions of 1 wt.% of Sn and In are enough to reduce the corrosion rate by a factor of 5 and 6, respectively. The addition of 1 wt.% of Ga is even able to slow down the corrosion rate by one order of magnitude. Gallium thus appears to be the most effective in

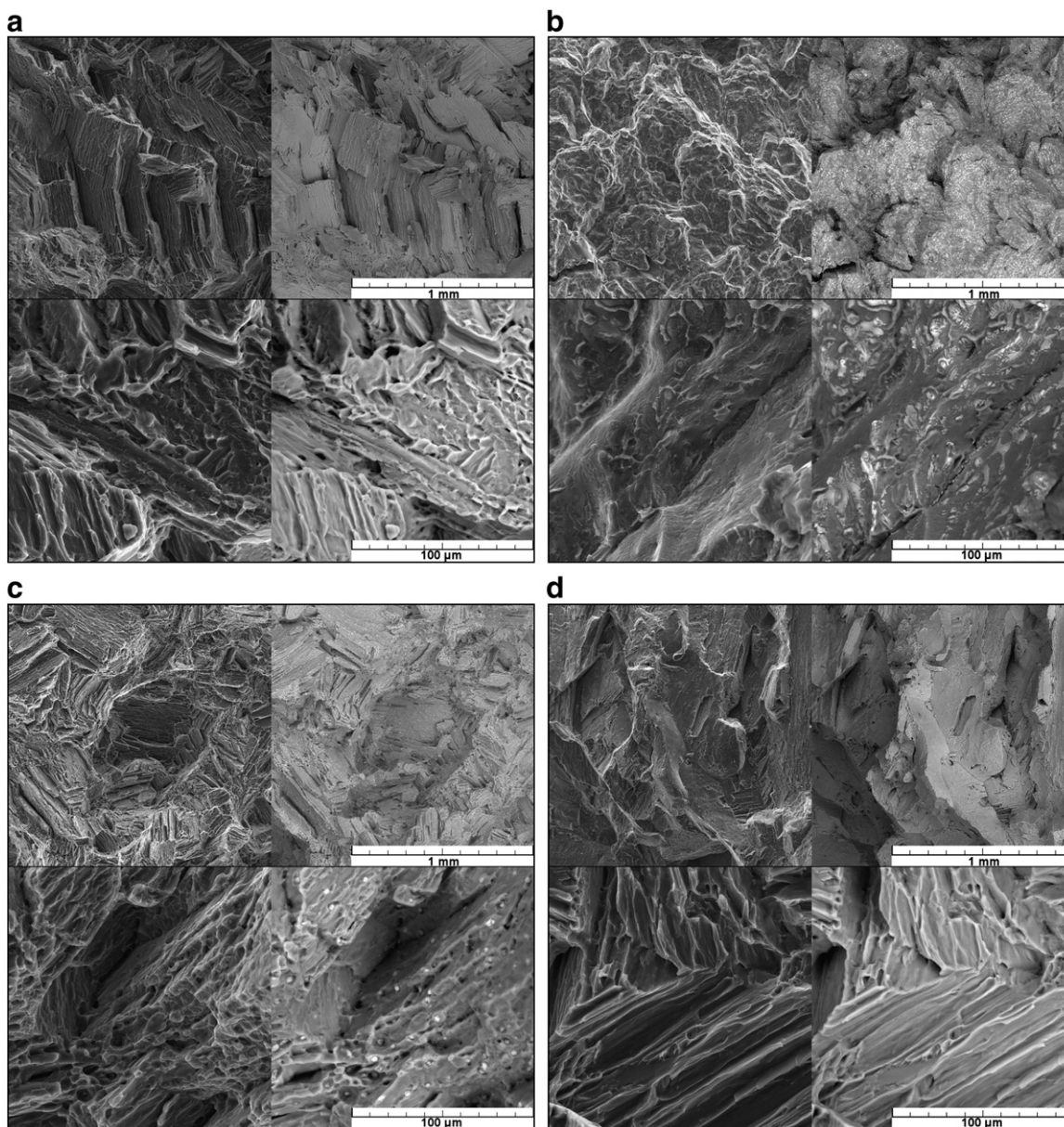


Fig. 3. Fracture surfaces of the alloys after tensile tests: a) Mg, b) Mg–5Sn, c) Mg–4Ga, and d) Mg–3In (SEM).

terms of corrosion resistance. Further increase of LMMs concentrations above 1 wt.% worsens the corrosion resistance. But in the case of Mg–In alloys this change is relatively small. During immersion tests pH was regularly measured (Fig. 4b). The highest increase in pH was observed for pure Mg, compared to the lowest increase in pH for Mg–1Ga alloy. The corrosion of magnesium is accompanied by pH increase. For this reason it can be assumed that higher increase in pH is connected with higher corrosion rate of alloy. In this case, based on the final pH values, studied alloys are in the same order as in the case of corrosion rates. LMMs used in our study are more noble than Mg (standard potentials of Mg, Ga, In and Sn are -2.38 V, -0.55 V, -0.49 V and $+0.15$ V, respectively [21]). For these reasons, corrosion potentials of Mg–LMMs alloys are shifted to positive values in comparison with those of Mg (Fig. 5). This shift is the most pronounced for the Mg–7Sn alloy, because of the most noble nature of Sn from all the LMMs. Potentiodynamic curves also demonstrate a reduction of anodic current density caused by additions of Sn and Ga.

Corroded surfaces of selected alloys are illustrated in Fig. 6. Pure Mg is covered by relatively massive corrosion products containing relatively large ($5\text{--}10\ \mu\text{m}$) clusters of flake-like crystals (Fig. 6(a)). In contrast, corrosion products on the Mg–LMMs alloys are thinner and more compact (Fig. 6(b) to (d)). The most corrosion resistant Mg–1Ga alloy is covered by an almost flat layer of dense corrosion products which is only locally broken by short cracks (Fig. 6(d)). The composition of corrosion products was studied by different methods (EDS, XRD, XPS and GDS). According to these measurements the corrosion products contained magnesium and oxygen, low amount of Cl and main alloying element in concentration that were similar with the as-cast state of the alloy. For all of the studied alloys, any enrichment of surface layer caused by alloying element was not observed. Diffraction analyses (not shown) confirmed $\text{Mg}(\text{OH})_2$ (brucite). Detailed XPS spectra are showed in Fig. 7. These results confirmed the presence of magnesium in the form of hydroxide and oxide. Moreover tin, gallium and indium are presented in the form of SnO_2 , Ga_2O_3 and In_2O_3 respectively.

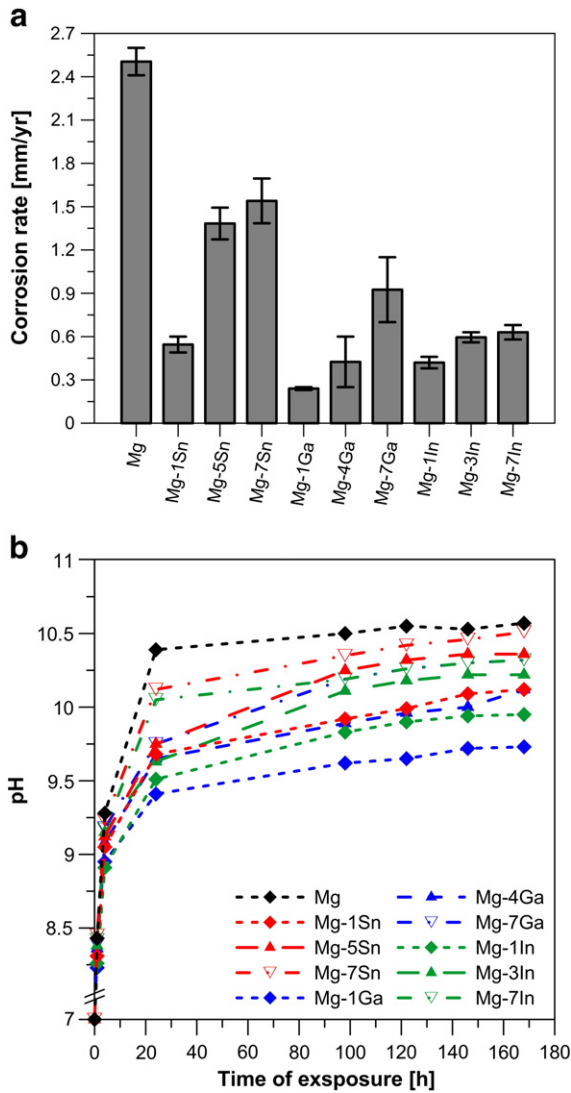
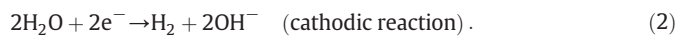
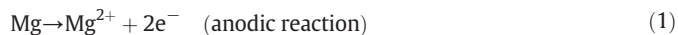


Fig. 4. Corrosion rates of the investigated alloys in the simulated physiological solution determined from the weight losses.

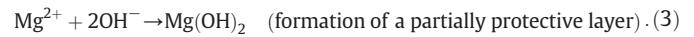
It is known that the corrosion process of magnesium based alloys generally occurs via cathodic and anodic reactions given below:



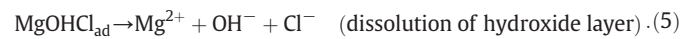
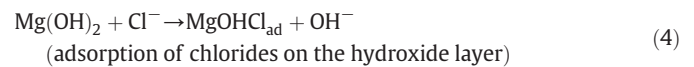
Corrosion of magnesium is accompanied by hydrogen release. The amount of hydrogen is proportional to the corrosion rate of magnesium or its alloys. One molecule of hydrogen gas is formed per one atom of Mg, which is about 920 mm³ H₂ generated by the degradation of 1 mg Mg. Therefore, measurement of hydrogen release is used as other method to determine the corrosion rate. In fact, the values of corrosion rate determined from hydrogen release are similar as corrosion rates estimated from weight changes. Differences can be observed if some particles such as intermetallic phases fall from the surface during immersion tests. Degradation of magnesium and its alloys generally results in considerable gas accumulations in the surrounding tissue [22]. Gas bubbles are able to impede a good connectivity of osteocytes with alloy. Besides disturbing the bone implant connectivity, gas pocket can increase the inner mechanical pressure near bone which can result in callus formation [23]. Moreover there

is the potential for gas gangrene to occur [24]. The creation of hydrogen bubbles is influenced by diffusion and solubility coefficient of hydrogen in biological tissue. The numerical value of diffusion coefficient depends on viscosity and tissue components or structures such as lipids, proteins and glycosaminoglycans [25]. In any case, corrosion rate of magnesium and its alloys should be sufficiently low in order to avoid accumulation of hydrogen in the gas pockets.

Corrosion of magnesium is also accompanied by pH increase. A local increase of pH near the surface leads to precipitation of solid magnesium hydroxide on the surface:



Although magnesium hydroxide may show a partial protective effect against further corrosion, it is strongly attacked in the presence of chloride anions to produce soluble compounds [26]:



The observed incorporation of Sn^{IV}, Ga^{III} and In^{III} atoms in the Mg(OH)₂ lattice (Fig. 7) apparently slows down the corrosion process given by Eqs. (1)–(5), as is indicated by Figs. 4 and 6. The positive effects of LMMs on the corrosion resistance can be explained on the following basis:

1. According to the Pourbaix E-pH diagrams of Sn, Ga, In and Mg [27], SnO₂, Ga₂O₃ and also In₂O₃ oxides are thermodynamically stable in significantly broader ranges of pH than Mg(OH)₂. Therefore, mixed Mg(OH)₂-LMM oxide (and perhaps hydroxide) layers are more stable than pure Mg(OH)₂.
2. Dissolution of the surface layer is suppressed by LMMs because the solubility product (K_s) of Mg(OH)₂ is higher than those of LMM oxides and hydroxides by many orders of magnitude [28]. Mixed Mg(OH)₂-LMM oxide (hydroxide) layers thus represent more efficient barriers against corrosion than pure Mg(OH)₂.
3. Incorporation of Sn, Ga and In atoms whose oxidation states are higher than that of Mg in the Mg(OH)₂ lattice (Fig. 7) locally increases positive charge in the brucite lattice. This increase is balanced by the interaction of LMM atoms with adsorbed harmful

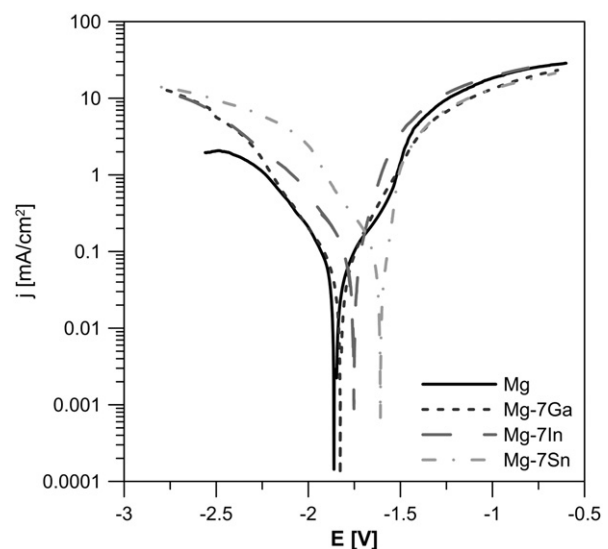


Fig. 5. Potentiodynamic curves of the investigated alloys.

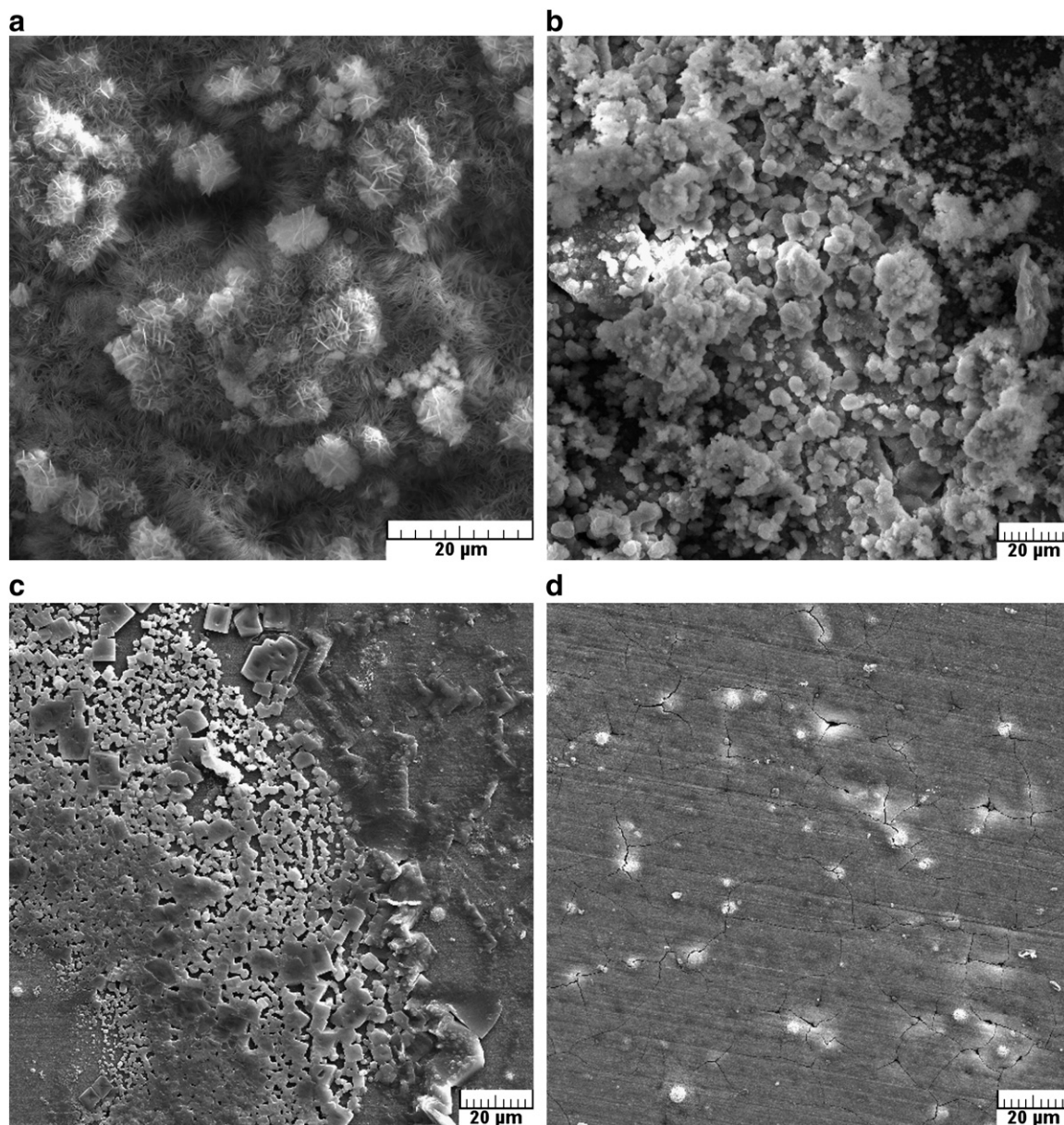


Fig. 6. Corroded surfaces of the investigated alloys after immersion tests (SEM): a) Mg, b) Mg–1Sn, c) Mg–1In, and d) Mg–1Ga.

Cl^- anions (Eq. (4)) which slows down the penetration of Cl^- deeper into the hydroxide layer. Consequently, dissolution of hydroxide layer given by Eq. (5) is inhibited.

4. Tin and gallium are known to exhibit high hydrogen overpotentials [12,26], therefore, they inhibit the cathodic reaction given by Eq. (2). A similar effect may be expected for indium.

It was stated before that the increase of LMM concentrations above 1% leads to an increase of the corrosion rate (Fig. 4). This is caused by an increase of galvanic corrosion due to Mg_2Sn and Mg_5Ga_2 phases which are cathodic to magnesium [21,26]. A similar finding was reported recently for Mg–Sn alloys by Liu et al. [26] who demonstrated a direct relationship between the volume fraction of Mg_2Sn phase and the corrosion rate. Fig. 8 confirms that the corrosion attack occurs most rapidly in the vicinity of cathodic phases. By an increase of Sn and Ga contents, the number of fast attacked sites increases. In the case of Mg–In alloys, the increase of corrosion rate due to addition of In above 1% is not significant, because of the

absence of eutectic phases (Fig. 1). For this reason the appearance of corroded surfaces of Mg–1In and Mg–7In alloys is similar. Due to a less noble nature of gallium as compared to tin and due to a lower content of Ga in the intermetallic phase, the galvanic corrosion is more pronounced in the Mg–Sn alloys than in the Mg–Ga alloys. This may be a reason for the best corrosion performance of the Mg–1Ga alloy (Fig. 4).

3.4. Cytotoxicity

Table 4 lists the element concentrations in both the original and diluted extracts used for cytotoxicity tests. It is observed that the amounts of released Ga and In are relatively low in comparison with Sn. It is in accordance with a higher corrosion rate of the Mg–Sn alloy (Fig. 4).

Fig. 9 illustrates the cytotoxic effect of the extracts and their dilutions on the U-2 OS cells, expressed as the percent absorbance of the DMEM control. Results obtained confirm the known fact that Mg

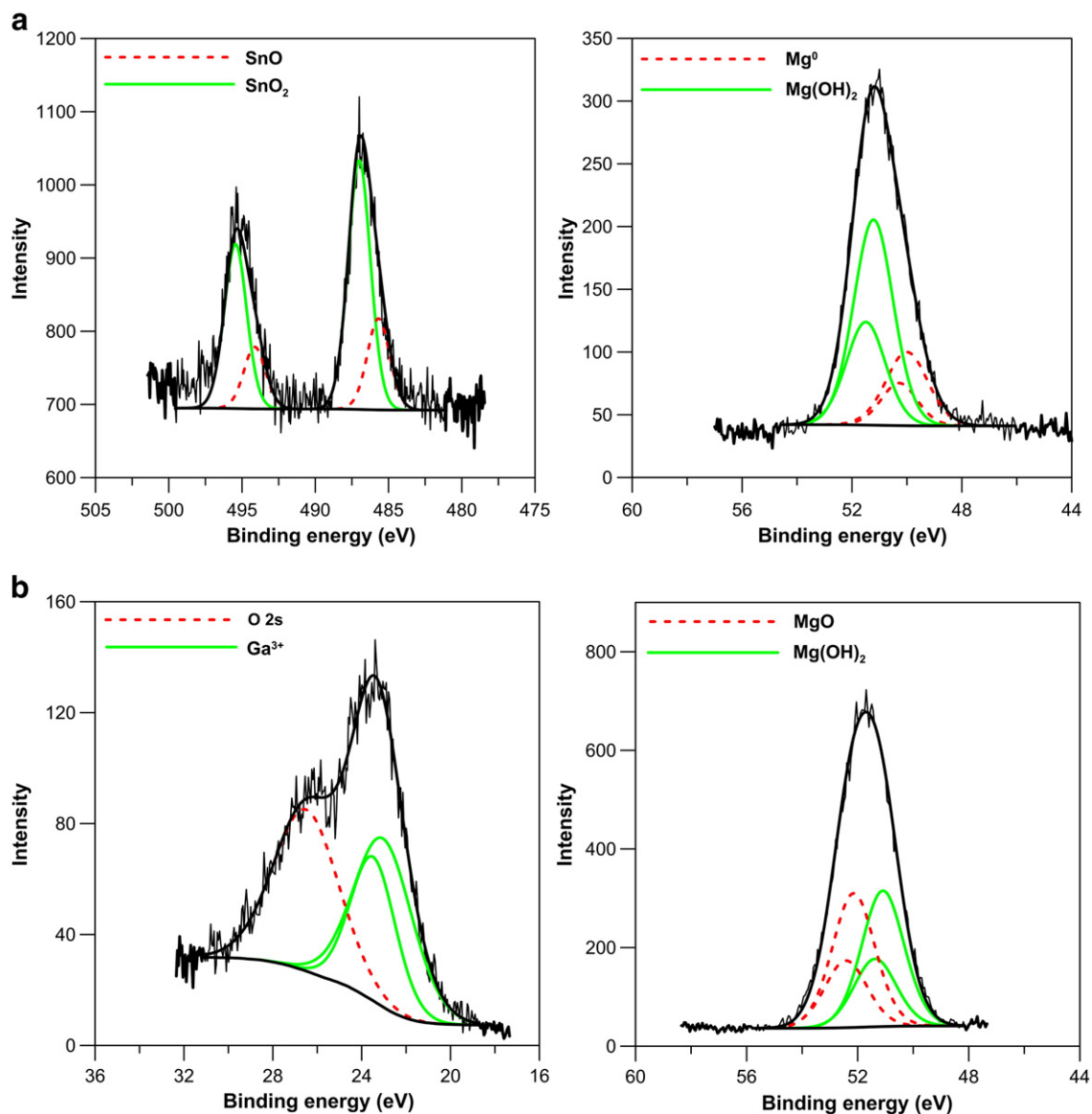


Fig. 7. Detailed XPS spectra of corroded Mg-1Sn and Mg-1Ga alloys.

is well tolerated by human cell lines. Even at concentrations of 160×10^3 ng/ml of total Mg in the extract the cells were fully viable. The Mg-1Ga alloy did not show acute toxicity at the highest concentration of 640 ng/ml, but after 5 days of incubation, the metabolic activity was comparable to the phenol control. The toxic effect of Ga seems to drop rapidly after the twofold dilution (310 ng/ml of total Ga), because 75% of the cells were viable after 5 days. The dilution of 1:15 was also very well tolerated. Regarding the Mg-1Sn alloy, a relatively high concentration of Sn in the original extract (2520 ng/ml) causes a severe toxic effect on the cells. After twofold dilution of the original extract to a Sn concentration of 1310 ng/ml the cell activity is also very low. But when the Sn amount decreases to 163 ng/ml the cells remain viable even after 5 days similarly to the control. In the case of the Mg-1In alloy, the maximum concentration of total In in the original extract was 164 ng/ml, but even at this concentration, the toxic effect is rather dramatic. It suggests that In shows a significantly higher toxicity to cells than tin. The viability comparable to the control was reached only at the minimum In concentration of 12 ng/ml. The above results indicate that the cytotoxic effects of LMMS on the U-2 OS cells increase from Ga to Sn and to In.

4. Conclusions

Mg-Sn, Mg-Ga and Mg-In alloys were studied in the context to biodegradable metallic implants potentially applicable in osteosynthesis. Sufficient hardness, strength, toughness, corrosion resistance and biocompatibility are the most important characteristics of these implants. The results obtained in our study indicate that alloying with indium is not favorable, because the effect of this element on mechanical properties is small. Moreover, indium shows the most severe toxic effect on osteosarcoma cells from all the low-melting metals studied. In contrast, our study shows that the addition of a low amount of gallium is the most effective to improve the above characteristics. For this reason, Mg-Ga alloys seem to be the most prospective for biodegradable implants. But, in contrast to tin, a problem arises from a lack of information on long-term health effect of gallium. Therefore, further extensive studies devoted to the biocompatibility of Mg-Ga-based alloys are needed. Another problem with Mg-Ga alloys is a high cost of metallic gallium. It was shown in this study that the effects of tin on strength, hardness and corrosion resistance are weaker than those of gallium. Moreover, tin has a more toxic effect on osteosarcoma cells than gallium. But the

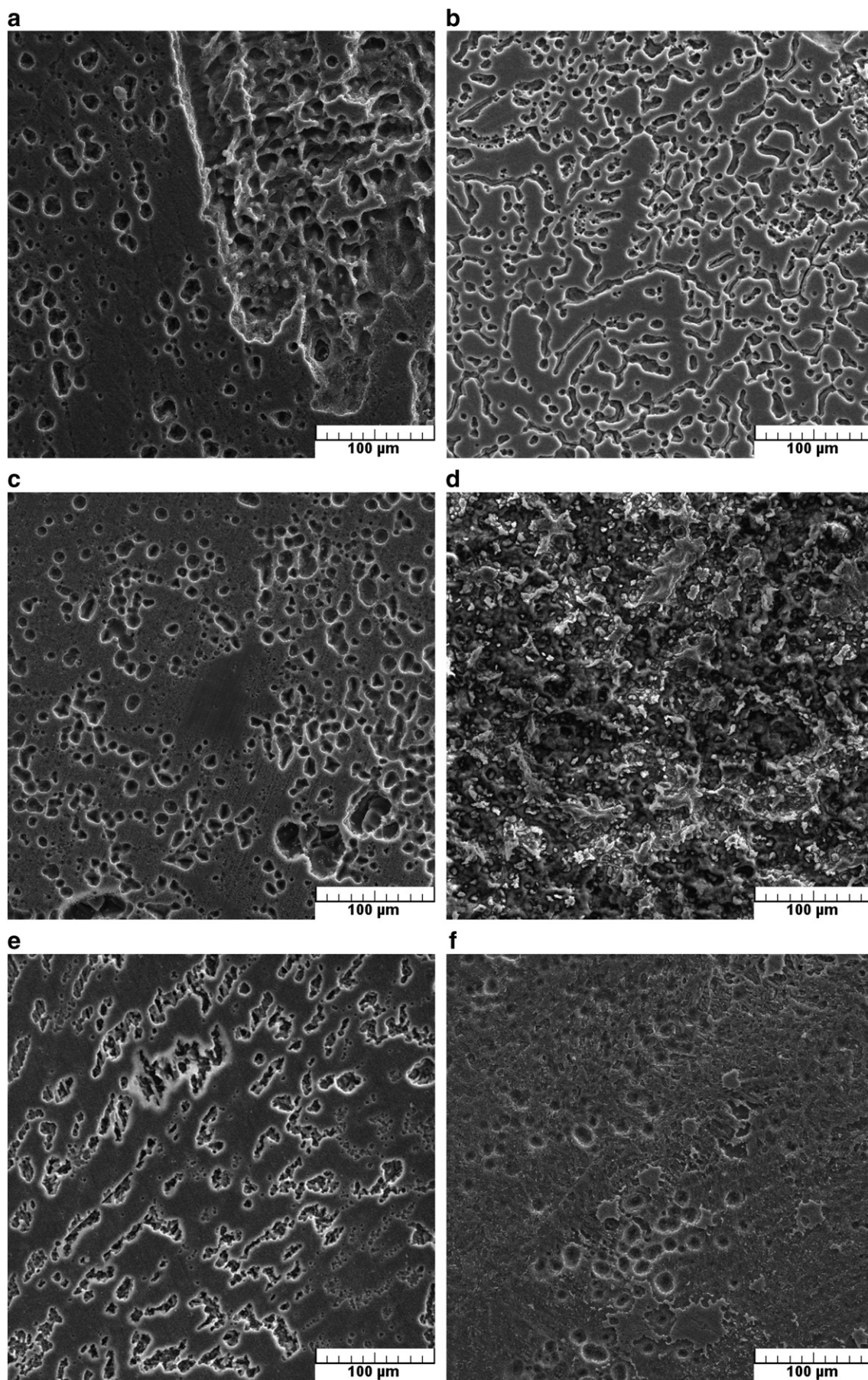


Fig. 8. Corroded surfaces after chemical removing corrosion products: a) Mg–1Sn, b) Mg–7Sn, c) Mg–1Ga, d) Mg–7Ga, e) Mg–1In and f) Mg–7In.

Table 4
Element concentrations (ng/ml) in extracts used for cytotoxicity tests.

Alloy	Mg	Mg–1 Ga	Mg–1In	Mg–1Sn			
Element	Mg	Mg	Ga	In	Mg	Sn	
Concentration in the original extract	160×10^3	121×10^3	640	144×10^3	164	455×10^3	2520
Concentration in the twofold diluted extract	75×10^3	65×10^3	310	80×10^3	87	70×10^3	1310
Concentration in the fifteen fold diluted extract	12×10^3	9×10^3	45	11×10^3	12	28×10^3	163

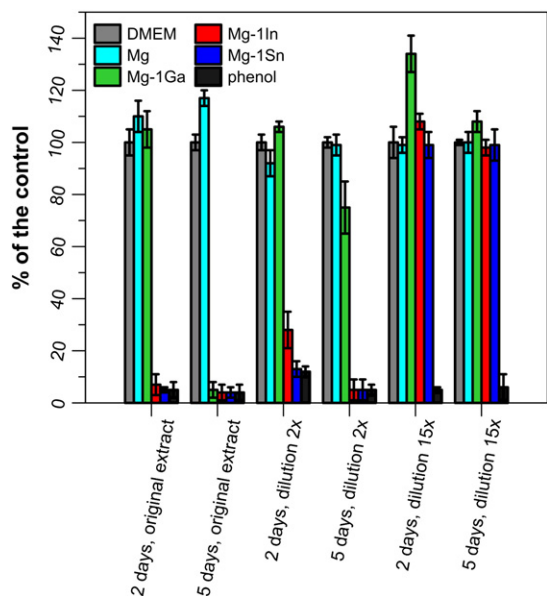


Fig. 9. The cytotoxic effects of the extracts and their dilutions on the U-2 OS cells, expressed as the percent absorbance of the DMEM control.

advantage of Mg–Sn alloys is in a lower cost of tin. Mg–Sn-based biodegradable alloys are thus still a subject of extensive studies.

Acknowledgments

The research of biodegradable Mg-based alloys was financially supported by the Czech Science Foundation under the project no. P108/12/G043.

References

- [1] R.C. Zeng, W. Dietzel, F. Witte, N. Hort, C. Blawert, *Adv. Eng. Mater.* 10 (2008) B3–B14.
- [2] F. Witte, *Acta. Biomater.* 6 (2010) 1680–1692.
- [3] D. Vojtěch, H. Čížová, K. Volenec, *Kov. Mater.* 44 (2006) 211–223.
- [4] J. Chen, Z. Chen, H. Yan, F. Zhang, K. Liao, *J. Alloys Compd.* 461 (2008) 209–215.
- [5] M.B. Yang, F.S. Pan, *Mater. Des.* 31 (2010) 68–75.
- [6] G. Nayyeri, R. Mahmudi, *Mat. Sci. Eng. A-Struct.* 527 (2010) 669–678.
- [7] M.B. Yang, X.F. Liang, Z. Yi, F.S. Pan, *Mater. Des.* 32 (2011) 1967–1973.
- [8] W.F. Gale, T.C. Totemeier, *Smithells Metals Reference Book*, 8th ed., Elsevier Publishers, 2004.
- [9] Inorganic Tin in Drinking-water, Background document for development of WHO for Guidelines Drinking-water Quality, 2004. http://www.who.int/water_sanitation_health/dwq/chemicals/tin.pdf, last accessed 20.2.2013.
- [10] X. Gu, Y. Zheng, Y. Cheng, S. Zhong, T. Xi, *Biomaterials* 30 (2009) 484–498.
- [11] F.G. Meng, J. Wang, M.H. Rong, L.B. Liu, Z.P. Jin, *Trans. Nonferrous Met. Soc. China* 20 (2010) 450–457.
- [12] Y. Feng, R.C. Wang, C.Q. Peng, *Trans. Nonferrous Met. Soc. China* 21 (2011) 1047–1051.
- [13] H. Liu, G. Qi, Y. Ma, H. Hao, F. Jia, S. Ji, H. Zhang, X. Zhang, *Mater. Sci. Eng., A* 526 (2009) 7–10.
- [14] S.A. Jewett, M.S. Makowski, B. Andrews, M.J. Manfra, A. Ivanisevic, *Acta. Biomater.* 8 (2012) 728–733.
- [15] C.E. Linsmeier, L. Wallman, L. Faxius, J. Schouenborg, L.M. Bjursten, N. Danielsen, *Biomaterials* 29 (2008) 4598–4604.
- [16] P. Melnikov, A.R. Teixeira, A. Malzac, M.D. Coelho, *Mater. Chem. Phys.* 117 (2009) 86–90.
- [17] A. Tanaka, M. Hirata, Y. Kiyohara, M. Nakano, K. Omae, M. Shiratani, K. Koga, *Thin Solid Films* 518 (2010) 2934–2936.
- [18] Y. Xin, T. Hu, P.K. Chu, *Acta. Biomater.* 7 (2011) 1452–1459.
- [19] A. Yamamoto, S. Hiromoto, *Mater. Sci. Eng. C* 29 (2009) 1559–1568.
- [20] E. Pellicer, S. González, A. Blanquer, S. Suriñach, M.D. Baró, L. Barrios, E. Ibáñez, C. Nogués, J. Sort, *J. Biomed. Mater. Res. A* 101A (2013) 502–517.
- [21] S.G. Bratsch, *J. Phys. Chem. Ref. Data* 18 (1989) 1–21.
- [22] F. Witte, V. Kaese, H. Haferkamp, E. Switzer, A. Meyer-Lindenberg, C.J. Wirth, H. Windhagen, *Biomaterials* 26 (2005) 3557–3563.
- [23] T. Kraus, S.F. Fischerauer, A.C. Hänzli, P.J. Uggowitzer, J.F. Löffler, A.M. Weinberg, *Acta. Biomater.* 8 (2012) 1230–1238.
- [24] C.K. Seal, et al., *IOP Conf. Ser. Mater. Sci. Eng.* 4 (2009) 012011.
- [25] F. Witte, N. Hort, C. Vogt, S. Cohen, K.U. Kainer, R. Willumeit, F. Feyerabend, *Curr. Opin. Solid State Mater. Sci.* 12 (2008) 63–72.
- [26] X. Liu, D. Shan, Y. Song, R. Chen, E. Han, *Electrochim. Acta* 56 (2011) 2582–2590.
- [27] M. Pourbaix, *Atlas of Electrochemical Equilibria in Aqueous Solutions*, ed. 2nd English ed. National Association of Corrosion Engineers, Houston, Tex, 1974.
- [28] L. Lide, *CRC Handbook of Chemistry and Physics*, CRC Handbook of Chemistry & Physics, 88th edition, CRC Press, 2007.
- [29] X.N. Gu, Y.F. Zheng, *Front. Mater. Sci. China* 4 (2010) 111–115.
- [30] H. Hermawan, D. Ramdan, J.R.P. Djuansjah, in: R. Fazel-Rezai (Ed.), *Biomedical Engineering – From Theory to Applications*, 2011.
- [31] L.E. Claes, *Clin. Mater.* 10 (1992) 41–46.
- [32] N. Hort, Y. Huang, D. Fechner, M. Störmer, C. Blawert, F. Witte, C. Vogt, H. Drücker, R. Willumeit, K.U. Kainer, F. Feyerabend, *Acta. Biomater.* 6 (2010) 1714–1725.
- [33] B.P. Zhang, Y. Wang, L. Geng, in: R. Pignatello (Ed.), *Biomaterials – Physics and Chemistry*, 2011.
- [34] H.S. Brar, J. Wong, M.V. Manuel, *J. Mech. Behav. Biomed. Mater.* 7 (2012) 87–95.
- [35] X.N. Gu, X.H. Xie, N. Li, Y.F. Zheng, L. Qin, *Acta. Biomater.* 8 (2012) 2360–2374.
- [36] H. Hermawan, Springer, Berlin Heidelberg, 2012, pp. 13–22.
- [37] M. Salahshoor, Y. Guo, *Mater.* 5 (2012) 135–155.
- [38] X. Zhang, G. Yuan, L. Mao, J. Niu, P. Fu, W. Ding, *J. Mech. Behav. Biomed. Mater.* 7 (2012) 77–86.
- [39] B. Wang, S.K. Guan, J. Wang, L.G. Wang, S.J. Zhu, *Mater. Sci. Eng. B-Adv.* 176 (2011) 1673–1678.
- [40] I. Stulikova, B. Smola, *Mater. Charact.* 61 (2010) 952–958.
- [41] A. Luo, M.O. Pegguleryuz, *J. Mater. Sci.* 29 (1994) 5259–5271.

Příloha 7



Microstructural, mechanical, corrosion and cytotoxicity characterization of the hot forged FeMn30(wt.%) alloy



Jaroslav Čapek^{a,b,*}, Jiří Kubásek^a, Dalibor Vojtěch^a, Eva Jablonská^c, Jan Lipov^c, Tomáš Ruml^c

^a Department of Metals and Corrosion Engineering, University of Chemistry and Technology Prague, Technická 5, 166 28 Prague 6, Czech Republic

^b Institute of Physics, Academy of Sciences of the Czech Republic (AS CR), Na Slovance 1999/2, 182 21, Prague 8, Czech Republic

^c Department of Biochemistry and Microbiology, University of Chemistry and Technology Prague, Technická 5, 166 28 Prague 6, Czech Republic

ARTICLE INFO

Article history:

Received 26 June 2015

Received in revised form 2 September 2015

Accepted 10 September 2015

Available online 12 September 2015

Keywords:

FeMn alloys
Biodegradability
Cytotoxicity
Microstructure
Mechanical properties

ABSTRACT

An interest in biodegradable metallic materials has been increasing in the last two decades. Besides magnesium based materials, iron-manganese alloys have been considered as possible candidates for fabrication of biodegradable stents and orthopedic implants. In this study, we prepared a hot forged FeMn30 (wt.%) alloy and investigated its microstructural, mechanical and corrosion characteristics as well as cytotoxicity towards mouse L 929 fibroblasts. The obtained results were compared with those of iron. The FeMn30 alloy was composed of antiferromagnetic γ -austenite and ϵ -martensite phases and possessed better mechanical properties than iron and even that of 316L steel. The potentiodynamic measurements in simulated body fluids showed that alloying with manganese lowered the free corrosion potential and enhanced the corrosion rate, compared to iron. On the other hand, the corrosion rate of FeMn30 obtained by a semi-static immersion test was significantly lower than that of iron, most likely due to a higher degree of alkalization in sample surrounding. The presence of manganese in the alloy slightly enhanced toxicity towards the L 929 cells; however, the toxicity did not exceed the allowed limit and FeMn30 alloy fulfilled the requirements of the ISO 10993-5 standard.

© 2015 Elsevier B.V. All rights reserved.

1. Introduction

The idea of biodegradable metallic implants has been resurrected at the end of the 20th century [1–3]. Namely, magnesium based materials have been investigated very extensively as candidates for orthopedic implants and cardiovascular stents. As a result of various investigations, the German company Syntellix AG introduced to the market a new biodegradable and bioresorbable material called Magnezix®. This material is based on the Mg-Y-RE-Zr system and is used for fabrication of screws intended for temporary fixation of small bones [1,4]. Even though a lot of other types of magnesium based materials have been tested *in vivo* [1,2,5–8]; to the best of our knowledge, none of them have been successfully used in the clinical practice.

With respect to the mechanical properties, iron based alloys seem to be more suitable for some types of implants, especially cardiovascular stents or porous orthopedic implants [9]. Iron also belongs to essential elements of human body and is necessary for proper functions of enzymes and oxygen transport [10–12]. In contrast to magnesium alloys, corrosion of iron in body fluids is significantly slower, is not connected with hydrogen evolution and dramatic increase of pH [13,14]. On the other hand, excess of iron in human body may cause heart, joint, liver, pancreas and nervous system diseases. Some *in vitro* cytotoxicity

studies suggest that iron may be problematic in higher concentration [14], but majority of studies concerned with degradable iron proved its acceptable non-toxicity at concentrations reached in these systems [13,15]. This was confirmed by *in vivo* studies on pure iron and some iron alloys which were used as stents and orthopedic implants; therefore, iron has been predicted as a promising candidate for biodegradable material [16–21].

Insufficient degradation rate and ferromagnetic behavior of pure iron are more serious issues preventing its use as biodegradable implantable material [5,13,19,21–24]. Due to the low degradation rate, the implants may cause the same problem as stents fabricated from a bioinert material (e.g. 316L steel); moreover, ferromagnetic behavior is not compatible with magnetic resonance imaging (MRI), which is an useful diagnostic method for many diseases [5,20,24]. When iron occurs in the face-centered cubic (fcc), usually called austenitic, structure, it becomes antiferromagnetic. Alloying by a sufficient amount of nickel or manganese allows stabilization of the austenitic structure to room temperature [20,23,25]. Nickel is a strong allergen and it is also suspected as a carcinogen making it unusable as an alloying element for biodegradable materials [20,25,26]. In contrast to nickel, manganese is a trace element of human body and acts as a cofactor of many enzymes [20,27,28]. The austenitic structure is stabilized by approximately 30 wt.% of manganese, although hexagonal (hcp) ϵ -martensite can form as a stress-induced phase in the Fe–Mn system. The formation of this phase is not necessarily undesirable because it is antiferromagnetic

* Corresponding author.

E-mail address: capekj@fzu.cz (J. Čapek).

and may enhance mechanical properties as well as degradation rate [23, 24,29–31]. The *in vitro* and *in vivo* studies performed on Fe–Mn alloys showed their applicability, despite the fact that manganese can be toxic in excessive amount. Moreover, the Fe–Mn based alloys possess mechanical properties comparable to those of the stainless steel 316L, whose mechanical behavior is considered as ideal for stent fabrication. Alloying with manganese also shifts the corrosion potential of iron to lower values making it less noble and many studies have indicated that the Fe–Mn based alloys degraded faster than pure iron *in vitro* [19,24,32]. Degradation rate of such alloys can be further enhanced by an addition of other elements, for example palladium or silicon; moreover, alloying with these elements enhanced mechanical properties as well [17,19,20,24,32,33].

In this study, a wrought FeMn30(wt.%) alloy was prepared as a suitable semi-product for potential manufacturing of stents or fixation screws. The microstructure, mechanical and corrosion behavior as well as *in vitro* cytotoxicity were investigated. The studied characteristics were compared with those of wrought iron with commercial purity to evaluate the influence of Mn on mechanical, chemical and biological characteristics.

2. Experimental

2.1. Material preparation

The FeMn30(wt.%) alloy was prepared by induction melting of appropriate amounts of elemental iron and manganese. Melting was performed in a silica crucible under an argon atmosphere and the melt was cast into a sand cylindrical mold with a diameter of 80 mm. After cooling the ingot was heated to 850 °C and open-die drop forged to a rod of squared cross-section with a side of 20 mm. The rod was mechanically machined and cut into shapes required for the particular tests and measurements.

The wrought iron (Fe) was obtained from a supplier in a form of cylindrical rods with a diameter of 16 mm. Its chemical composition declared by the supplier is shown in Table 1.

2.2. Microstructure

Few millimeters thick flat pieces were cut from the wrought rods using a metallographic saw with a diamond blade. Subsequently, the samples were grinded using SiC grinding papers P120–P4000, ultrasonically cleaned in ethanol, mechanically polished on a diamond paste (particle size $\leq 1 \mu\text{m}$) and finally polished using colloidal silica. After polishing, the samples were ultrasonically cleaned and etched in order to remove Beilby layer and reveal microstructure. The FeMn30 alloy was etched in Viella's reagent (100 ml of ethanol, 5 ml of hydrochloric and 1 g of picric acid) and the iron in picral (saturated solution of picric acid in ethanol). Phase composition was investigated by the X-ray diffraction method using a PANalytical X'Pert PRO X-ray diffractometer equipped with a Cu anode (XRD) and microstructure was documented by light and scanning electron microscopy using an OLYMPUS PME3 light metallographic microscope (LM) and a TESCAN VEGA-3 LMU scanning electron microscope (SEM), respectively.

2.3. Mechanical properties

Tensile and compression tests were performed using a LabTest 5.250SP1-VM universal loading machine at room temperature and the engineering stress–strain curves were recorded. For both tests, the

Table 2

Ionic composition of SBF and DMEM (Sigma-Aldrich, cat. no. D0819). SBF was buffered with Tris–HCl and was preserved with 0.1% NaN₃. DMEM contains also amino acids, vitamins, glucose (4.5 g/l) and 5% FBS (fetal bovine serum) was added.

Ion/Concentration [mmol/l]	Na ⁺	K ⁺	Ca ²⁺	Mg ²⁺	Cl [−]	HPO ₄ ^{2−}	HCO ₃ [−]	SO ₄ ^{2−}
SBF	142.0	5.0	2.5	1.0	109.0	1.0	27.0	1.0
DMEM	124.5	5.4	1.8	0.8	89.8	0.9	44.0	0.8

samples were cylindrical shaped and their dimensions (diameter × length) were 4 × 25 mm and 10 × 15 mm for tensile and compression tests, respectively. The deformation rates were 1 mm/min for both tests. Three samples of each material were used in each test, yield and ultimate strengths were determined from the obtained tensile and compressive stress–strain curves and average values and standard deviations were calculated from the obtained data. The fracture surfaces obtained by the tensile tests were observed by SEM. One FeMn30 sample was longitudinally cut after the compression test. Then it was subjected to the metallographic investigation in the same way as described in Section 2.2 in order to observe differences in microstructure before and after loading. Hardness was measured by the Brinell method using a load of 62.5 kg and a WC indenter with a diameter of 2.5 mm; 10 measurements were done for each sample and average values and standard deviations were calculated.

2.4. *In vitro* corrosion behavior

Disk samples with a diameter of 10 mm and a thickness of 2 mm for corrosion tests were cut and grinded using SiC grinding papers P120–P2500, ultrasonically cleaned in ethanol, dried by flowing hot air and weighed using an analytical balance. All corrosion investigations were conducted at a temperature of 37 °C.

2.4.1. Potentiodynamic test

Potentiodynamic tests were performed using a Gammy reference 600 system. Simulated body fluid (SBF) prepared according to Müller (ionic composition shown in Table 2) buffered with Tris–HCl with initial pH 7.4 and preserved with NaN₃ was chosen as the corrosion environment and a rounded area of 1 cm² was exposed to the corrosion medium. A platinum wire was used as a counter electrode and a silver chloride electrode (ACIE) as a reference electrode. Firstly, the free corrosion potential was stabilized for a time period of 1 h; subsequently, the sample was polarized (1 mV/s). Corrosion rates were determined from Tafel slopes.

2.4.1.1. Long-term immersion test. Immersion tests were performed in a semi-static regime. One sample of each material was immersed in SBF (see Table 2) for 10 weeks at 37 °C. The used volume of corrosion medium was 150 ml per 1 cm² of the sample surface. The medium was replaced by new one every week.

2.4.1.2. Immersion test at physiological conditions. *In vitro* immersion tests were also performed at conditions mimicking physiological situation (in CO₂ atmosphere). Tests were performed in 24-well plate in order to establish the system, which could be used for direct *in vitro* cytotoxicity testing in the future. Two samples of each type were firstly sterilized in hot air (180 °C) for 2 h and then submersed into Dulbecco's modified Eagle's medium (DMEM, Sigma-Aldrich, cat. no. D0819, ionic concentrations are shown in Table 2) and SBF (see Table 2) for 2 weeks at 37 °C in

Table 1

Chemical composition of wrought Fe.

Element	C	Mn	Si	P	S	Cu	Cr	Ni	Al	V	Nb	Zr	N	Fe
Amount (wt.%)	0.040	0.41	0.03	0.018	0.023	0.05	0.071	0.032	<0.010	<0.004	<0.003	<0.002	<0.0088	Balance

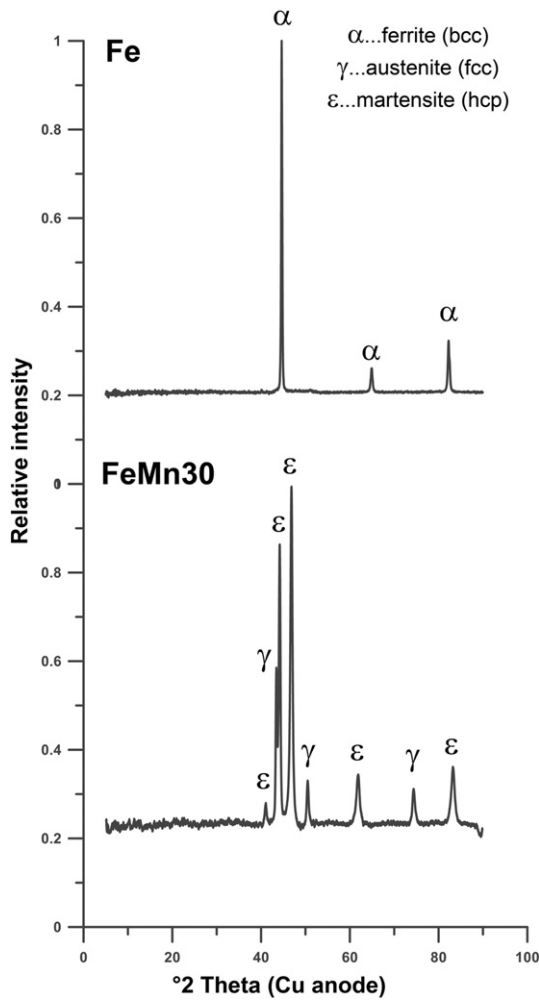


Fig. 1. XRD patterns of studied samples.

5% CO₂ atmosphere with surface to volume ratio of 1.1 ml per 1 cm². The medium was replaced by new one after 1 week.

2.4.2. Corrosion rate evaluation

After both immersion tests, ion release into the solution was measured after 2 and 10 weeks of exposition by Inductively coupled plasma mass spectrometry (ICP-MS) using a Perkin Elmer Elan 6000 spectrometer (three measurements for each sample). Prior to the measurement, ultrapure HNO₃ was added to the extracts in order to dissolve majority of solid corrosion products. After the expositions, samples were rinsed by distilled water, ethanol and dried by flowing hot air. The corrosion

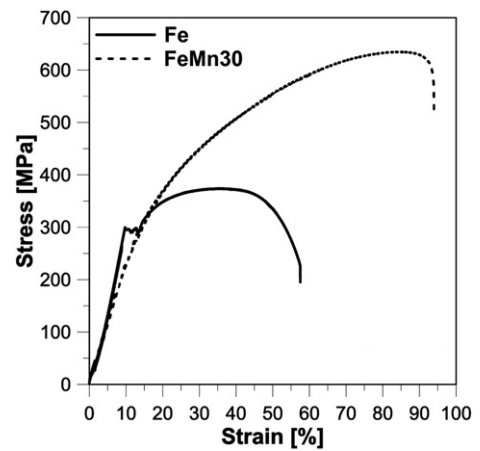


Fig. 3. Tensile stress–strain curves.

products were chemically removed according to ISO 8407 using Clark solution (100 ml HCl, 5 g SnCl₂ and 2 g Sb₂O₃) and samples were rinsed and dried in the same way as after exposition. Subsequently the samples were weighed and corrosion rates were calculated from the mass losses. The corrosion products were documented and analyzed using SEM equipped with an Oxford Instruments INCA 350 EDX analyzer (SEM-EDX).

2.4.3. In vitro cytotoxicity

In vitro cytotoxicity was tested using indirect test evaluated by WST-1 assay according to ISO 10993-5 standard. Disk samples with a diameter of 10 mm and thickness of 2 mm were firstly sterilized in hot air (180 °C) for 2 h. Subsequently, each sample was exposed to 2.5 ml of Eagle's minimum essential medium (MEM) with an addition of 5% of fetal bovine serum (FBS) for 1 day at a temperature of 37 °C on an orbital shaker at 125 RPM. Three samples from each type (Fe and FeMn30) were used. Meanwhile, L929 cells (murine fibroblasts, ATCC® CCL-1™) were seeded into 96-well plates (100 μl/well) in density of 1 × 10⁵ cells/ml and incubated at 37 °C for 24 h in MEM + 10% FBS to allow cell adhesion. Thereafter, the medium was replaced by the extracts in MEM medium with 5% FBS. Concentrated extracts and 50% extracts diluted with fresh cultivation medium were used and MEM with 5% FBS was used as a negative control. After 24 h incubation with the extracts, the cells were washed with phosphate buffer saline (PBS) and incubated with WST-1 reagent (5% WST-1 in MEM without phenol red) for 4 h. The yellow formazan product created by metabolic reduction was photometrically quantified using an ELISA reader at the absorption wavelength 450 nm. Cytotoxic effect was depicted as a decrease in metabolic activity compared to the negative control. Cytotoxic measurement was done in six replicates for each sample. Metabolic activity 70% of the control was taken as a minimum value of cytocompatibility.

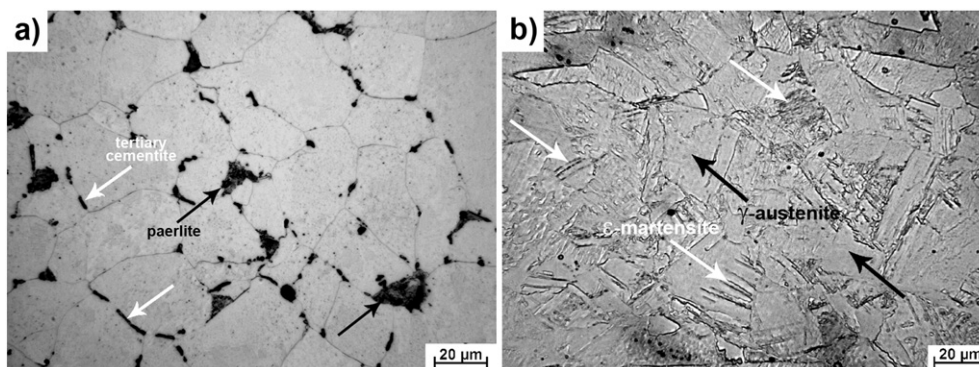


Fig. 2. Microstructures (LM) of a) Fe and b) FeMn30 alloy.

Table 3
Mechanical characteristics of the studied materials.

Sample/Property	TYS [MPa]	UTS [MPa]	Tensile rupture elongation [%]	CYS [MPa]	HBW
Fe	299 ± 11	372 ± 18	57 ± 3	441 ± 6	96 ± 1
FeMn30	242 ± 14	632 ± 12	94 ± 6	413 ± 7	175 ± 7

3. Results and discussions

3.1. Microstructure

3.1.1. Mechanical properties

Fig. 1 shows the XRD patterns of the studied materials. According to the XRD analysis, the Fe sample consisted mainly of α -ferrite (bcc structure). The FeMn30 alloy consisted of austenite (γ , fcc structure) and hexagonal martensite (ϵ , hcp structure). These phases are also observable in micrographs shown in Fig. 2. In the case of Fe, cementite was found beside α -ferrite by metallographic investigation. Cementite was not detected by XRD (Fig. 1) because its content in Fe was under the detection limit of XRD. Cementite occurred in a lamellar structure as a part of pearlite (marked by black arrows in Fig. 2a) and as tertiary cementite precipitated at grain boundaries (marked by white arrows in Fig. 2a). The FeMn30 alloy consisted of austenitic grains (marked by black arrow in Fig. 2b) in which needles of ϵ -martensite were observed (marked by white arrows in Fig. 2b).

3.1.2. Tensile test

Fig. 3 shows the tensile stress–strain curves and the values of selected tensile characteristics are listed in Table 3. Substantial differences in tensile behavior of the studied materials were observed. The FeMn30 alloy possessed slightly lower modulus of elasticity, lower tensile yield strength (TYS) and significantly higher ultimate tensile strength (UTS) than Fe. In the case of Fe, TYS was determined as the peak at the end of the elastic (linear) part of the stress–strain curve. Such peak is typical for alloys containing interstitial alloying elements or impurities and is caused by dislocation escaping from Cottrell atmospheres. Because no decrease of stress after linear deformation took place during deformation of the FeMn30 alloy, TYS was determined as the stress at 0.2% of plastic deformation (proof stress). The curves of both materials (Fig. 3) contain regions of plastic deformation and the plastic deformation is connected with strain hardening. The region of strain hardening is significantly larger in the case of the FeMn30 alloy, whose deformation finished in this stage at a rupture elongation about 90%. Fe was strain hardened to a lower extent; however, the engineering stress decreased after reaching UTS suggesting that necking took place before the rupture at an elongation of approximately 55%. The significantly higher strain hardening, UTS and rupture elongation of the FeMn30 alloy can be explained by the stress induced phase transformation of austenite to ϵ -martensite. This is also connected with twinning, which leads to a large elongation at the rupture [34–36]. Moreover, ϵ -martensite belongs to the hexagonal closed packed (hcp) phases; therefore it possesses significantly less slip systems than Fe (bcc structure).

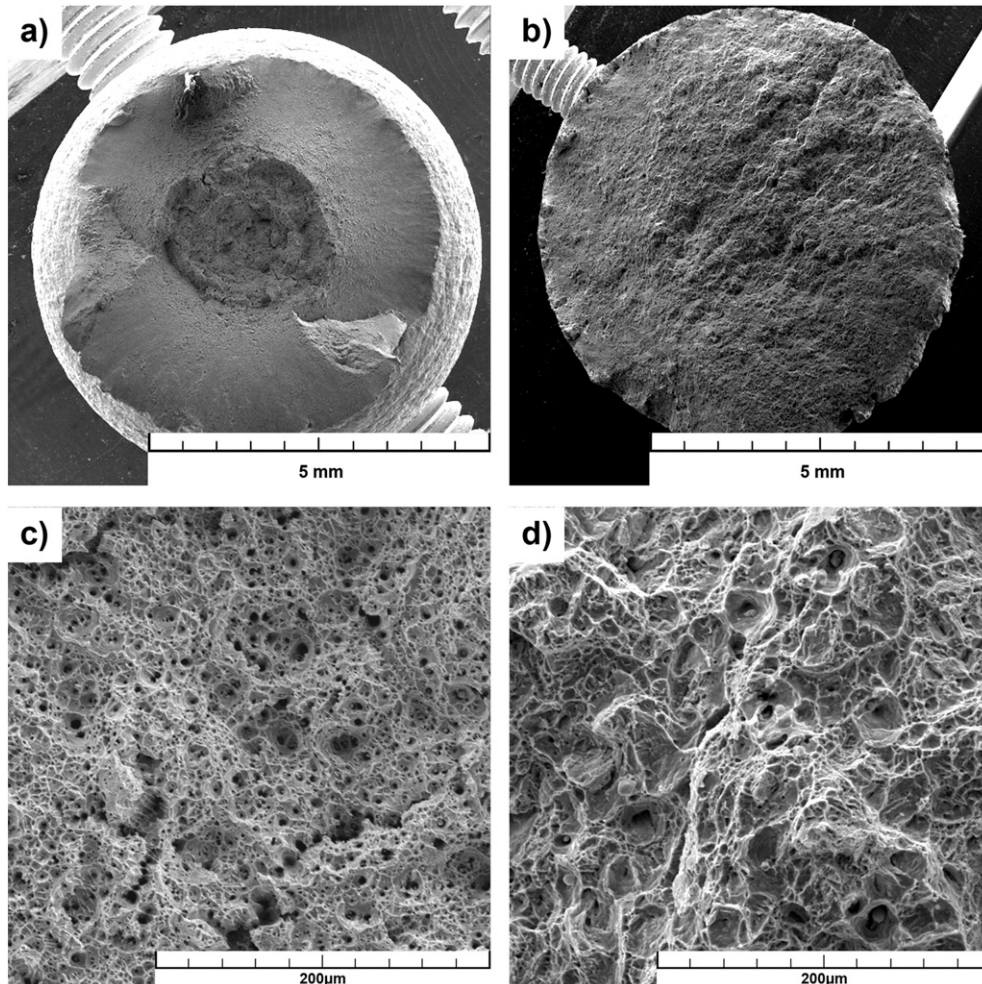


Fig. 4. Fracture surfaces of Fe (a, c) and FeMn30 (b, d).

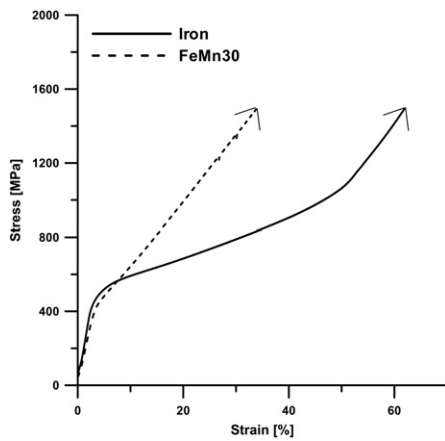


Fig. 5. Compressive stress–strain curves.

As a consequence almost no necking (i.e. the decrease of engineering stress after UTS reaching) takes place during its deformation as a consequence.

The statements above were confirmed by SEM observation of fracture surfaces (Fig. 4). At low magnification, significant necking is clearly visible on the fracture surface of Fe (Fig. 4a); while in the case of the FeMn30 alloy, no distinctive necking is observed (Fig. 4b). At higher magnification (Fig. 4c and d) a lot of dimples are observed suggesting that the crack growth was accompanied by plastic deformation. These observations are in a good agreement with the high elongation of both materials.

3.1.3. Compressive test

Fig. 5 shows compressive stress–strain curves of the studied samples. The tests were canceled before rupture because the used forces were close to the machine limit. The trend in compressive behavior was similar to that in tension—Fe possesses slightly higher modulus of elasticity and compressive yield strength (CYS) than the FeMn30 alloy (see Table 3). As in the tensile stress–strain curves the strain hardening of the FeMn30 alloy was higher than that of Fe. To confirm the assumption that the hardening is caused by the phase transformation of austenite to ϵ -martensite, the microstructure of the FeMn30 alloy was studied after the compression test (see Fig. 6).

It is obvious in Fig. 6 that significantly higher amount of martensite was present in the microstructure of the sample after the compression test than in that of the noncompressed one (Fig. 2). As indicated before, the substantial strain hardening is caused by the formation of hexagonal ϵ -martensite with limited number of slip systems.

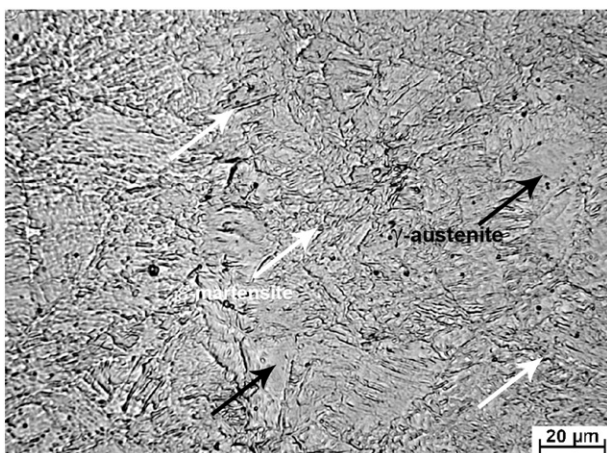


Fig. 6. Microstructure of the FeMn30 alloy after compression test (LM).

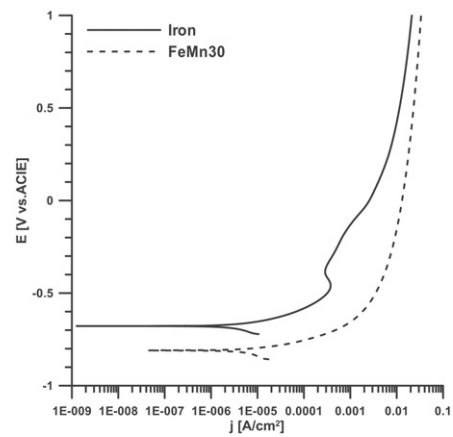


Fig. 7. Potentiodynamic curves of the studied samples.

3.1.4. Hardness

FeMn30 was almost two times harder than Fe (see Table 3). This may be explained by the differences in phase composition of the alloys. The content of cementite in the Fe sample was very small (Fig. 2); therefore, its hardening effect was weak. On the other hand, the FeMn30 alloy contained relatively large amount of ϵ -martensite, which is relatively hard phase due to a limited number of slip systems [24]. The presence of this phase and the ϵ/γ phase boundaries significantly hardened the material. Moreover, the indentation causes the phase transformation from a relatively soft austenite to a hard martensite (Fig. 6) and this transformation consumes a lot of energy inserted by the loading.

3.2. In vitro corrosion behavior

3.2.1. Potentiodynamic test

The potentiodynamic curves plotted in Fig. 7 and corrosion parameters given in Table 4 show that Fe behaved as a nobler material compared to FeMn30. This observation is in a good agreement with the majority of available literature data concerned on this topic. Table 4 also illustrates that the corrosion rate of the FeMn30 alloy obtained from Tafel extrapolation was almost 20 times higher than that of Fe (0.899 vs. 0.041 mm/a—see Table 4). Both materials corroded in passivity at potentials typical for body environment [37]. The potentiodynamic curves also suggest that FeMn30 possessed higher current density (i.e. corrosion rate) than Fe in the passive region suggesting that FeMn30 would corrode faster under physiological conditions. Moreover, no pitting was observed during the potentiodynamic tests of both materials. FeMn30 showed higher corrosion current density ($I_{\text{corr}} = 7.6 \cdot 10^{-5} \text{ A/cm}^2$) compared to 316L stainless steel ($I_{\text{corr}} = 3.5 \cdot 10^{-6} \text{ A/cm}^2$) studied by Motalebi et al. [38]. This suggests that FeMn30 may possess corrosion properties suitable for application as possible biodegradable material.

3.2.2. Immersion test

The results of immersion test are plotted in Fig. 8 and listed in Table 5. The relative mass losses were slightly higher than relative ion releases. It is because a portion of ions was retained in the form of solid corrosion products. In Fig. 8 and Table 5, it is also obvious that the corrosion rate in SBF was slightly higher after 10 weeks than after 2 weeks. We are aware of the fact that measurements were not

Table 4
Results of potentiodynamic test.

Sample/Characteristic	E_{corr} [mV vs. ACIE]	v_{corr} [mg/cm ² /day]	v_{corr} [mm/a]
Fe	−678.0	0.087	0.041
FeMn30	−809.7	1.891	0.899

conducted at the same conditions. Nevertheless, we could suppose that the difference was also caused by a localized corrosion under solid corrosion products. Localized forms of corrosion (e.g. pitting and crevice corrosion) become usually more evident after longer exposition times when solid corrosion products are formed and aggressive ions as chlorides are present in the corrosion medium [39]. Contrary to the potentiodynamic measurements, corrosion rates of the FeMn30 alloy obtained by the immersion tests were lower than those of Fe in both corrosion media (SBF and DMEM). Moreover, the corrosion rates obtained by the immersion tests were different than those, especially in case of FeMn30, obtained by Tafel extrapolation (Table 4). The corrosion rates obtained by the immersion tests were different because the access of corrosion medium to the sample surface was strongly limited by the solid corrosion products. On the other hand, the partially protective corrosion products did not form during the potentiodynamic measurements because the exposition time was not sufficient to change the chemistry of corrosion media (composition and pH) significantly, which would be necessary to induce the formation of protective compounds.

Figs 9 and 10 show SEM images, X-ray elemental maps and EDX spectra of the samples after 10 weeks of immersion in SBF. In these pictures one can see that the corrosion products were rich in O and that they also contained Na, Ca and P. It can be thus assumed that the corrosion products consisted of hydrated iron and iron–manganese oxides; moreover, they also contained precipitates rich in Ca and P, which could be beneficial for orthopedic applications, where formation of CaP layers is desirable since it can enhance bone formation [40]. The corrosion products detached from the surface locally; therefore, we were able to observe their layered structure and estimate elemental distribution in these layers using EDX. In the X-ray elemental maps (Figs. 9 and 10), it is obvious that oxygen is distributed homogeneously through the corrosion products and low concentration of phosphorus was detected in the corrosion products (see EDX spectra and quantitative analyses in Figs. 9 and 10). The external surface layer was rich in calcium and enriched in manganese (in the case of FeMn30); whereas the layer adjacent to the metal was rich in Fe. Small amount of manganese was also detected by the EDS analysis of Fe after the immersion test; this was because the sample contained 0.41 wt.% of manganese (see Table 1). Compared to FeMn30, no significant influence of such negligible amount of manganese on material properties can be supposed. As will be given below, the fact that manganese accumulates in the outer surface layer may cause a higher pH increase in the vicinity of the sample surface. This may inhibit the corrosion process of the FeMn30 alloy during the immersion tests.

Table 5

Corrosion rate [mm/year] calculated from mass loss after the immersion tests.

Corrosion rate [mm/year]	Two weeks	Ten weeks
Iron SBF	0.082	0.101
Fe30Mn SBF	0.019	0.028
Iron DMEM	0.060	N/A
Fe30Mn DMEM	0.035	N/A

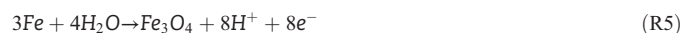
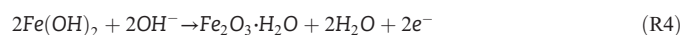
The fact that the corrosion rate of FeMn30 obtained by immersion test was lower than that of Fe may be explained by different pH changes at the sample surface. As indicated in Figs. 9 and 10, the corrosion products contained mainly hydrated Fe and Mn oxides and hydroxides. By comparing the solubility of these compounds (Table 6), one can see that manganese hydroxide is much more soluble than iron hydroxides [41]. Therefore, the pH of corrosion medium in contact with the sample surface tends to be higher when the alloy contains high amount of manganese. Consequently, the higher pH slows the corrosion process by slowing down the cathodic reaction (R1).



The increase in pH also influences composition of corrosion products. At lower pH, iron is oxidized forming ferrous ions (R2); after they exceed solubility limit, ferrous hydroxide is formed by the reaction with hydroxyl anions (R3) [42].



At higher pH, ferrous hydroxide is oxidized forming ferric oxide (R4). In anoxic and alkali environment, iron is oxidized by water forming magnetite (R5) [42]. Anoxic environment can occur under corrosion products after longer exposition times because the corrosion products strongly limit oxygen transport to the metal surface. Magnetite formed under such conditions is dense and acts as a passive layer and slows the corrosion process [42].



Similar difference between potentiodynamic and immersion corrosion measurements of Fe and FeMn30 was also observed by Liu et al.

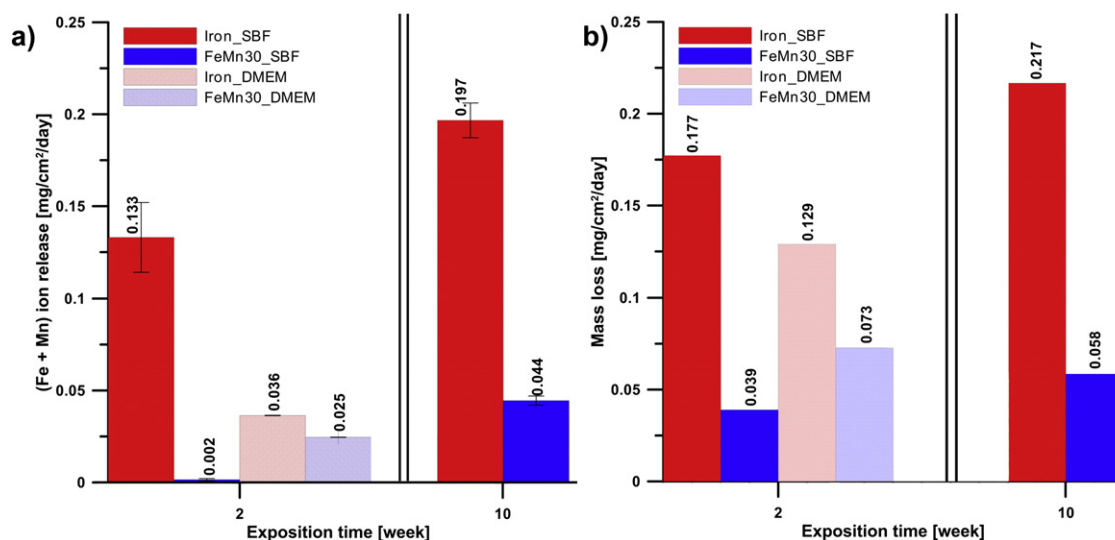


Fig. 8. Ion release [mg/cm²/day] vs. exposition time after immersion tests calculated from released ions (a) and mass losses (b).

[19]; although, they accounted this behavior to a different distribution of the corrosion products through the surface [19]. In our study we did not observe any significant differences in the distribution of corrosion products (see Figs. 9 and 10); therefore, we favor the explanation that pH differences cause the observed differences in corrosion behavior of Fe and FeMn30. To support this assumption, we also tried to measure pH of the corrosion media. However, no significant changes were observed due to the buffer capacity of SBF and DMEM in the whole volume. For this reason, we immersed Fe and FeMn30 samples in an unbuffered simulated physiological solution (9 g/l NaCl) and measured evolution of pH during 1 week. The initial pH of the solution was 5.7 and after 1 day of exposition it increased to 5.8 and 7.1 in the case of Fe and FeMn30, respectively. The pH changes in other days were negligible compared to the increase in the first day. These results support our assumption that corrosion of the FeMn30 alloy significantly increases pH of corrosion medium in contact with the alloy surface and influences the corrosion process [43]. In the whole volume of buffered medium, such increase is not detected.

The assumption, that pH increases in the vicinity of FeMn30 surface and its corrosion rate is slowed compared to pure iron during the semistatic test, is supported by the fact that Liu et al. obtained similar results by a static immersion test [19], while Hermawan et al., who

performed dynamic immersion tests [20,24], found that FeMn alloys corrode faster than pure Fe. The flowing environment most likely ensures a displacement of dissolved corrosion products and an intake of fresh corrosion medium. This prevents to changes in composition of the environment in surface vicinity and corrosion mechanisms during long term testing. Consequently, this leads to different results compared to static tests. Based on the comparison between our study and the study of Liu et al. [19], where semi-static or static immersion tests were used, and by Hermawan et al. [20,24], where dynamic immersion tests were performed, we can suggest that alloying with manganese is more suitable for implants exposed flowing medium (e.g. stents) rather than for orthopedic implants, where the movement of the corrosion medium and access of oxygen is limited. The same conclusion is indicated by Kraus et al. [18] who reported the results of their *in vivo* study.

3.3. *In vitro* cytotoxicity

Fig. 11 shows the metabolic activity of L 929 cells after 1-day incubation with the diluted (50%) and non-diluted extracts of both samples. In the figure it is obvious that pure Fe was non-toxic, as the metabolic activity of L 929 cells in Fe extract was equal to the control (sole cultivation medium). We could observe slight decrease in the metabolic

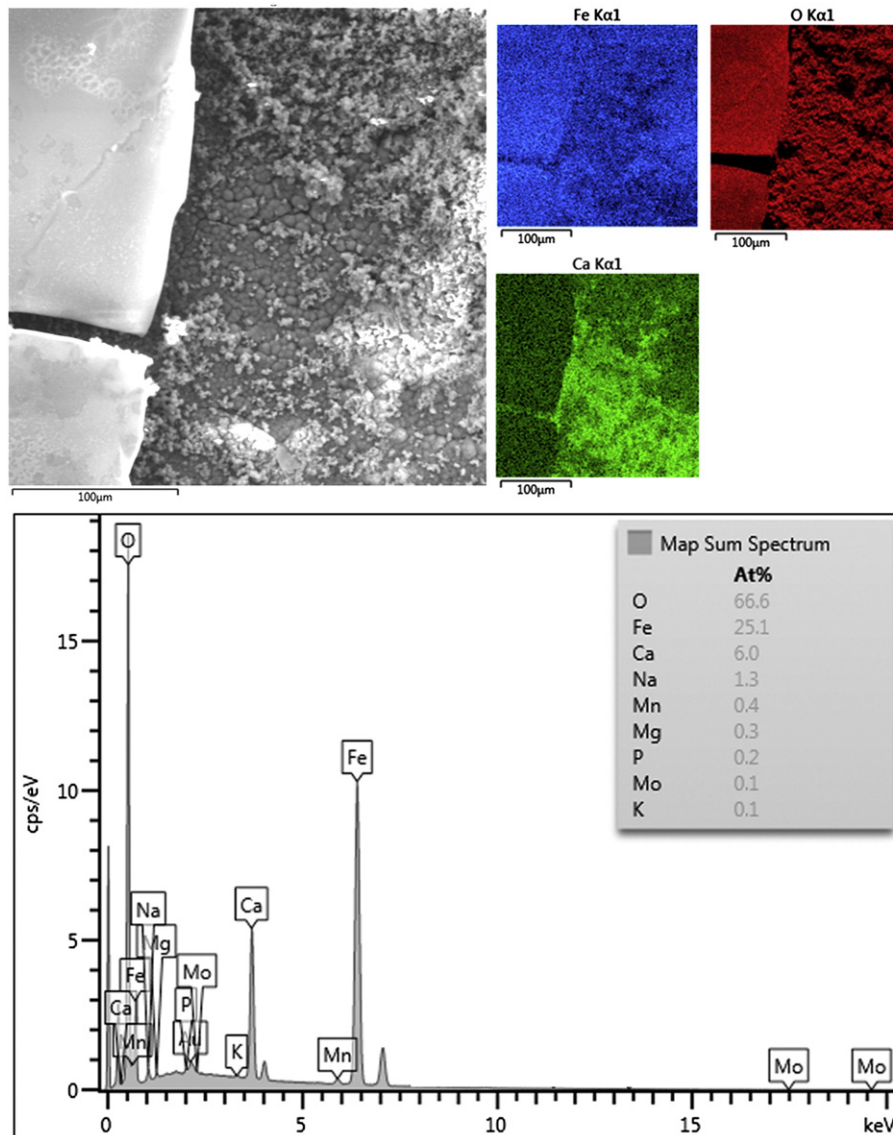


Fig. 9. SEM image, X-ray elemental maps and EDX spectrum of the corroded surface of Fe after 10 weeks of immersion in SBF.

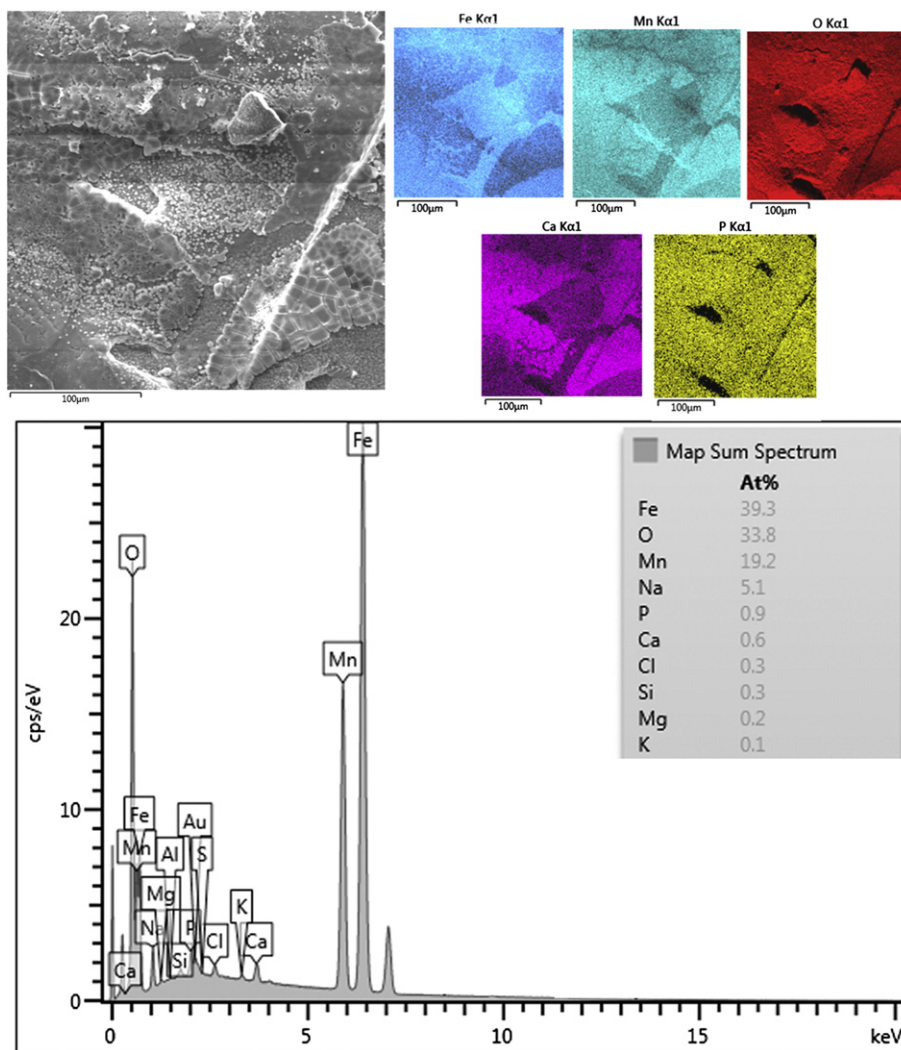


Fig. 10. SEM image, X-ray elemental maps and EDX spectrum of the corroded surface of FeMn30 after 10 weeks of immersion in SBF.

activity in the case of the extracts of the FeMn30 alloy (90% of the control), which was probably caused by released Mn ions. Nevertheless, this value is still significantly higher than the standard limit of 70% below which an extract is considered toxic. The concentration of released Fe ions in the extracts was $19.6 \pm 7.5 \mu\text{g/ml}$ ($351 \pm 134 \mu\text{mol/l}$) and $9.7 \pm 1.1 \mu\text{g/ml}$ ($175 \pm 19 \mu\text{mol/l}$) for Fe and FeMn30, respectively. The cell response to these concentrations of iron is in a good agreement with the data of other authors: Zhu et al. [44] observed no cytotoxic effect of iron on human endothelial cells after one day, when the concentration of iron was below $50 \mu\text{g/ml}$ and Hallab determined LC_{50} for osteoblast-like cells MG-63 to be approximately $300 \mu\text{mol/l}$ [14].

Concentration of released Mn ions in the extracts of FeMn30 was $4.6 \pm 0.6 \mu\text{g/ml}$ ($82 \pm 11 \mu\text{mol/l}$). We assume that sensitivity to manganese is probably strongly cell type dependent: when normal human lung epithelial cells were used, concentration of Mn above $20 \mu\text{mol/l}$ was cytotoxic after two days [45], whereas mouse brain cells tolerated concentration of Mn up to $200 \mu\text{mol/l}$ when measured after 24 h [46].

Table 6
Solubility product constants of probable corrosion products at 25 °C [41].

Hydroxide	Solubility product constant
Mn(OH) ₂	$1.6 \cdot 10^{-13}$
Fe(OH) ₂	$7.9 \cdot 10^{-16}$
Fe(OH) ₃	$1.6 \cdot 10^{-39}$

Also Schinhammer observed adverse effect of Mn on HUVEC when the concentration was higher than $500 \mu\text{mol/l}$ after 2 days [15].

These preliminary cytotoxicity results indicate that FeMn30 alloy would meet the requirements dictated by the ISO 10993-5 standard [47]. Fe–Mn based alloys have been found as suitable in several *in vitro* studies [15,20] as well as in the *in vivo* study performed by Kraus et al. [18].

4. Conclusion

In this study, the hot-forged FeMn30(wt.%) alloy was studied as a potential biodegradable material for orthopedic applications. Microstructural characteristics, mechanical and *in vitro* corrosion behavior and *in vitro* cytotoxicity of the alloy to L 929 cells were studied and compared with those of Fe. The FeMn30 alloy consisted of γ -austenitic and ϵ -martensitic phases. It possessed better mechanical properties than Fe and even better than 316L stainless steel, which is the most commonly used biomaterial. The potentiodynamic measurements showed that alloying by manganese shifts the free corrosion potential to the less noble values and increases the corrosion rate in the initial stage of the corrosion process. Contrary to the results of potentiodynamic tests, semi-static immersion tests showed that the FeMn30 alloy corroded more slowly than Fe which was attributed to a local increase of pH in surface surrounding due to a higher solubility of manganese hydroxide compared to iron hydroxides. The extracts of FeMn30 were slightly

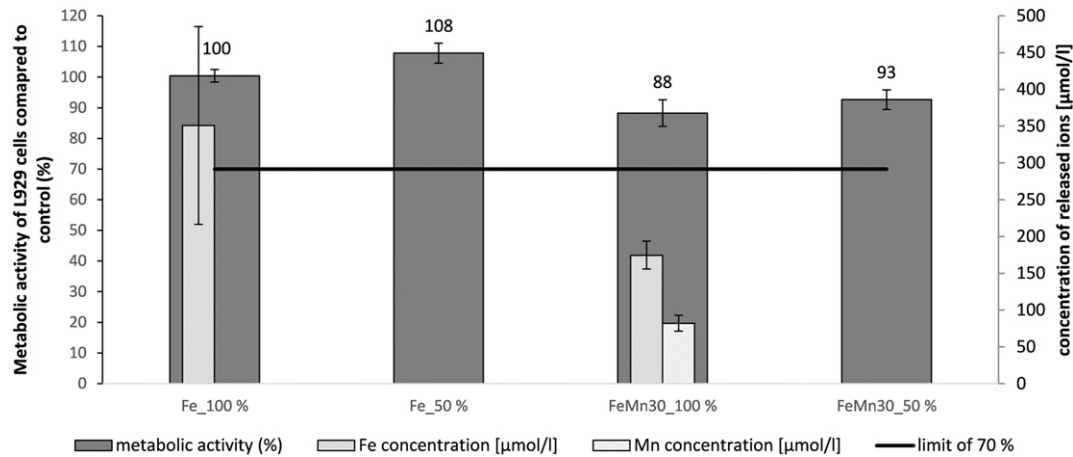


Fig. 11. Left Y-axis: percent of the metabolic activity of L929 cells after 1 day of exposition to the extracts (100% undiluted and 50% diluted extract) compared to the control (sole cultivation medium). Right Y-axis: concentration of released Fe and Mn ions in extracts [µmol/l] measured by ICP-MS Three samples from each type (Fe and FeMn30) were used. Error bars represent SSD. Black line indicates the cytotoxicity limit according to ISO 10993-5 standard.

more toxic than those of iron; however, metabolic activity of L929 cells was still above the tolerable 70% limit. Based on the results obtained in this work and results obtained by other authors we can also conclude that the FeMn30 alloy may possess good cytocompatibility. It also achieves sufficient mechanical properties but the main drawback lies in too low degradation rate for the use as a biodegradable material. The degradation rate should be significantly enhanced, most likely by alloying with other elements, and this is the topic of our future studies.

Acknowledgments

The authors would like to thank the Czech Science Foundation (project no. P108/12/G043) for supporting this research.

References

- [1] Y. Chen, Z. Xu, C. Smith, J. Sankar, *Acta Biomater.* 10 (2014) 4561–4573.
- [2] Y.F. Zheng, X.N. Gu, F. Witte, *Mater. Sci. Eng. R* 77 (2014) 1–34.
- [3] M. Moravej, D. Mantovani, *Int. J. Mol. Sci.* 12 (2011) 4250–4270.
- [4] <http://syntellix.de/en/>, 16. 6. 2015.
- [5] H. Hermawan, D. Dube, D. Mantovani, *Acta Biomater.* 6 (2010) 1693–1697.
- [6] Y.G. Chen, J. Yan, X.H. Wang, S. Yu, Z.G. Wang, X.N. Zhang, S.X. Zhang, Y.F. Zheng, C.L. Zhao, Q. Zheng, *Biomaterials* 27 (2014) 1217–1230.
- [7] F. Witte, J. Fischer, J. Nellesen, C. Vogt, J. Vogt, T. Donath, F. Beckmann, *Acta Biomater.* 6 (2010) 1792–1799.
- [8] F. Witte, J. Fischer, J. Nellesen, H.A. Crostack, V. Kaese, A. Pisch, F. Beckmann, H. Windhagen, *Biomaterials* 27 (2006) 1013–1018.
- [9] B. Wegener, B. Sievers, S. Utschneider, P. Müller, V. Jansson, S. Rößler, B. Nies, G. Stephani, B. Kieback, P. Quadbeck, *Mater. Sci. Eng. B* 176 (2011) 1789–1796.
- [10] T. Ganz, *Physiol. Rev.* 93 (2013) 1721–1741.
- [11] N. Abbaspour, R. Hurrell, R. Kelishadi, *J. Res. Med. Sci.* 19 (2014) 164–174.
- [12] D. Luchowska-Kocot, *J. Elem.* 19 (2014) 889–901.
- [13] B. Liu, Y.F. Zheng, *Acta Biomater.* 7 (2011) 1407–1420.
- [14] N.J. Hallab, C. Vermes, C. Messina, K.A. Roebuck, T.T. Glant, J.J. Jacobs, *J. Biomed. Mater.* 60 (2002) 420–433.
- [15] M. Schinhammer, I. Gerber, A.C. Hänzli, P.J. Uggowitzer, *Mater. Sci. Eng. C* 33 (2013) 782–789.
- [16] R. Waksman, R. Pakala, R. Baffour, R. Seabron, D. Hellinga, F.O. Tio, *J. Interv. Cardiol.* 21 (2008) 15–20.
- [17] P. Quadbeck, R. Hauser, K. Kümmel, G. Standke, G. Stephani, B. Nies, S. Rößler, B. Wegener, PM2010 World Congress, Florenz, Italy, 2010.
- [18] T. Kraus, F. Moszner, S. Fischerauer, M. Fiedler, E. Martinelli, J. Eichler, F. Witte, E. Willbold, M. Schinhammer, M. Meischel, P.J. Uggowitzer, J.F. Löffler, A. Weinberg, *Acta Biomater.* 10 (2014) 3346–3353.
- [19] B. Liu, Y.F. Zheng, L. Ruan, *Mater. Lett.* 65 (2011) 540–543.
- [20] H. Hermawan, A. Purnama, D. Dube, J. Couet, D. Mantovani, *Acta Biomater.* 6 (2010) 1852–1860.
- [21] M. Peuster, P. Wohlsein, M. Brüggemann, M. Eherding, K. Seidler, C. Fink, H. Brauer, A. Fischer, G. Hausdorf, *Heart* 86 (2001) 563–569.
- [22] H. Kitabata, R. Waksman, B. Warnack, *Cardiovasc. Revasc. Med.* 15 (2014) 109–116.
- [23] M. Schinhammer, A.C. Hänzli, J.F. Löffler, P.J. Uggowitzer, *Acta Biomater.* 6 (2010) 1705–1713.
- [24] H. Hermawan, D. Dube, D. Mantovani, *J. Biomed. Mater. Part A* 93 (2010) 1–11.
- [25] M. Talha, C.K. Behera, O.P. Sinha, *Mater. Sci. Eng. C* 33 (2013) 3563–3575.
- [26] K. Yang, Y. Ren, *Sci. Technol. Adv. Mater.* 11 (2010) (13 pp.).
- [27] J. Crossgrove, W. Zheng, *NMR Biomed.* 17 (2004) 544–553.
- [28] M. Aschner, T.R. Guilarde, J.S. Schneider, W. Zheng, *Toxicol. Appl. Pharmacol.* 221 (2007) 131–147.
- [29] Y.K. Lee, J.H. Jun, C.S. Choi, *ISIJ Int.* 37 (1997) 1023–1030.
- [30] A. Cladera, B. Weber, C. Leinenbach, C. Czaderski, M. Shahverdi, M. Motavalli, *Constr. Build. Mater.* 63 (2014) 281–293.
- [31] H. Hermawan, D. Dube, D. Mantovani, *Thermec 2006 Supplement: 5th International Conference on Processing and Manufacturing of Advanced Materials*, 15–17 2007, pp. 107–112.
- [32] M. Schinhammer, P. Steiger, F. Moszner, J.F. Löffler, P.J. Uggowitzer, *Mater. Sci. Eng. C* 33 (2013) 1882–1893.
- [33] M. Schinhammer, C.M. Pecnik, F. Rechberger, A.C. Hänzli, J.F. Löffler, P.J. Uggowitzer, *Acta Mater.* 60 (2012) 2746–2756.
- [34] O. Grässel, L. Krüger, G. Frommeyer, L.W. Meyer, *Int. J. Plast.* 16 (2000) 1391–1409.
- [35] S. Cotes, M. Sade, A.F. Guilletmet, *Metall. Mater. Trans. A* 26 (1995) 1957–1969.
- [36] H. Ding, Z.-Y. Tang, W. Li, M. Wang, D. Song, *J. Iron Steel Res. Int.* 13 (2006) 66–70.
- [37] D.J. Blackwood, 2.27 - Corrosion in Body Fluids, in: B. Stott, et al., (Eds.), *Shreir's Corrosion*, Elsevier, Oxford 2010, pp. 1308–1322.
- [38] A. Motalebi, M. Nasr-Esfahani, R. Ali, M. Pourriahi, *Prog. Nat. Sci.* 22 (2012) 392–400.
- [39] D.A. Jones, *Principles and Prevention of Corrosion*, Prentice Hall, 1996.
- [40] R.Z. LeGeros, *Clin. Orthop. Relat. Res.* 395 (2002) 81–98.
- [41] M. Olia, A.S. Casparian, *How to Prepare for the Fundamentals of Engineering, FE/EIT Exam*, Barron's, Hauppauge, N.Y., 2000.
- [42] D. Talbot, J. Talbot, *Corrosion Science and Technology*, CRC Press, 1998.
- [43] A.T. Kuhn, C.Y. Chan, *J. Appl. Electrochem.* 13 (1983) 189–207.
- [44] S. Zhu, N. Huang, L. Xu, Y. Zhang, H. Liu, H. Sun, Y. Leng, *Mater. Sci. Eng. C* 29 (2009) 1589–1592.
- [45] L.E. Pascal, D.M. Tessier, *Toxicol. Lett.* 147 (2004) 143–151.
- [46] N.M. Filipov, R.F. Seegal, D.A. Lawrence, *Toxicol. Sci.* 84 (2005) 139–148.
- [47] ISO 10993-5: Biological Evaluation of Medical Devices—Part 5: Tests for *In vitro* Cytotoxicity, International Organization for Standardization, 2009.

Příloha 8



Structure, mechanical characteristics and in vitro degradation, cytotoxicity, genotoxicity and mutagenicity of novel biodegradable Zn–Mg alloys



J. Kubásek^{a,*}, D. Vojtěch^a, E. Jablonská^b, I. Pospíšilová^a, J. Lipov^b, T. Ruml^b

^a Department of Metals and Corrosion Engineering, Institute of Chemical Technology, Prague, Technická 5, 166 28 Prague 6, Czech Republic

^b Department of Biochemistry and Microbiology, Institute of Chemical Technology, Prague, Technická 5, 166 28 Prague 6, Czech Republic

ARTICLE INFO

Article history:

Received 22 September 2014

Received in revised form 4 August 2015

Accepted 11 August 2015

Available online 17 August 2015

Keywords:

Zinc

Mechanical properties

In vitro testing

Cytotoxicity

Genotoxicity

ABSTRACT

Zn–(0–1.6)Mg (in wt.%) alloys were prepared by hot extrusion at 300 °C. The structure, mechanical properties and in vitro biocompatibility of the alloys were investigated. The hot-extruded magnesium-based WE43 alloy was used as a control. Mechanical properties were evaluated by hardness, compressive and tensile testing. The cytotoxicity, genotoxicity (comet assay) and mutagenicity (Ames test) of the alloy extracts and ZnCl₂ solutions were evaluated with the use of murine fibroblasts L929 and human osteosarcoma cell line U-2 OS. The microstructure of the Zn alloys consisted of recrystallized Zn grains of 12 μm in size and fine Mg₂Zn₁₁ particles arranged parallel to the hot extrusion direction. Mechanical tests revealed that the hardness and strength increased with increasing Mg concentration. The Zn–0.8 Mg alloys showed the best combination of tensile mechanical properties (tensile yield strength of 203 MPa, ultimate tensile strength of 301 MPa and elongation of 15%). At higher Mg concentrations the plasticity of Zn–Mg alloys was deteriorated. Cytotoxicity tests with alloy extracts and ZnCl₂ solutions proved the maximum safe Zn²⁺ concentrations of 120 μM and 80 μM for the U-2 OS and L929 cell lines, respectively. Ames test with extracts of alloys indicated that the extracts were not mutagenic. The comet assay demonstrated that 1-day extracts of alloys were not genotoxic for U-2 OS and L929 cell lines after 1-day incubation.

© 2015 Elsevier B.V. All rights reserved.

1. Introduction

The use of metallic biodegradable implants represents an innovative approach in orthopedic or cardiovascular surgical applications. The main advantages of metallic biodegradable materials over polymers (PLA) and ceramics (HA) are significantly higher strength, hardness, wear resistance and fracture toughness. Most widely studied biodegradable metals include magnesium and iron [1–7]. Although biodegradable magnesium implants for bone fixations have recently been commercially introduced by Syntellix, concerns still remain in biomaterial engineering community regarding excessive biocorrosion rates of magnesium alloys [1,2,5,7–14]. On the other hand, iron corrodes too slowly in body fluids which is partially caused by the presence of iron oxide products with a larger volume that resists biodegradation, therefore, possible ways for accelerating the degradation rate are still searched for. They include additions of manganese, phosphorus, and noble metals [3,15–17].

Besides magnesium and iron, zinc has been explored as the newest metallic alternative to biodegradable magnesium alloys and polymers. Zinc, as an essential element in the human body, is involved in various

aspects of cellular metabolism. Zinc is important to the proper functions of numerous enzymes; it supports immune functions, protein and DNA syntheses. It also supports normal growth, wound healing and a proper sense of taste and smell [2,18]. The recommended daily value of Zn ranges from 10 mg per day for adults to 2 mg per day for infants. The upper limit for zinc is 40 mg per day [19]. The consumption of zinc in amounts higher than this value is generally considered relatively non-toxic, and amounts approaching 100 mg per day can be tolerated for few days period [20]. In scientific and patent sources, there are numerous biodegradable Mg-based alloys containing zinc in amounts of several wt.%, like Mg–Zn, Mg–Zn–Mn–Ca, Mg–Zn–Y, and Mg–Zn–Si [1,2,5,7]. Additions of Zn to these alloys improve the corrosion resistance and strength [18]. In the Mg–Zn phase diagram, there is a deep eutectic at about 51 wt.% Zn [21] that is the basic factor supporting the high glass-forming ability of Mg–Zn-based alloys [10,14]. It was shown by Z. Bruno et al. [14] that amorphous Mg–Zn-based alloys containing about 50 wt.% of Zn have excellent strength, high corrosion resistance, low hydrogen evolution rate and good biocompatibility in animals, therefore, they become promising candidates for biodegradable bone implants. But problems arise from a quite difficult preparation of metallic glasses and especially forming them to a final product. Common processes involve rapid solidification of melt that limits the maximum thickness of amorphous alloys to hundreds of micrometers [14].

* Corresponding author.

E-mail address: Jiri.Kubasek@vscht.cz (J. Kubásek).

The fact that zinc is biologically tolerated even at concentrations approaching 50 wt.% in Mg-based alloys [10,14] indicate that Zn-based alloys may also be promising candidates for biodegradable implants. The advantages of Zn-based alloys are low melting point and low reactivity in a molten state. Therefore, they can be prepared by simple melting, gravity or die-casting in air atmosphere and hot forming. To our best knowledge, we reported for the first time structural, mechanical and corrosion studies on biodegradable Zn-based alloys [22]. A series of as-cast binary Zn–Mg alloys containing 0–8 wt.% Zn were investigated in our studies [22–24]. Tensile, compressive, bending, as well as hardness mechanical tests, were carried out to find an optimum Mg concentration. We have found that magnesium has a strong strengthening effect on zinc. As-cast alloys with 1–2 wt.% Mg showed the best combination of tensile strength (180 MPa) and ductility (almost 2%). However, it is known that some kinds of implants should possess higher strength levels of approximately 300 MPa and also higher plasticity of 15% [19]. Unfortunately, it is not possible to use higher Mg-concentrations in Zn–Mg alloys because magnesium forms a brittle eutectic phase reducing strength, plasticity and toughness of Zn–Mg alloys [24]. Attempts to improve mechanical properties of zinc were recently made by Yu et al. [25]. They incorporated nano-diamond particles into zinc, but no positive effects were observed. Another way to improve mechanical strength is applying hot extrusion in processing alloys and this is the subject of the present study. Thermo-mechanical processing such as extrusion or rolling has been already successfully used to prepare Zn–Mg alloys with up to 1 wt.% of Mg [26,27]. To our best knowledge, alloys with higher concentrations of Zn have not been studied yet. We have also shown previously [22] that Zn–Mg alloys corrode in a neutral simulated body fluid at considerably lower rates than pure Mg and AZ91HP alloy. This was also confirmed by other studies [28].

The national approval procedures for any material with potential use in human medicine require a complete set of biocompatibility tests. Both in vitro and in vivo testing are necessary processes in the evaluation of biocompatibility of novel biomaterials. General in vitro biocompatibility testing includes cytotoxicity and genotoxicity testing as defined in ISO 10993-1 standard [29]. The term cytotoxicity refers to toxic effects at the cellular level comprising death, changes in cellular membrane permeability, enzymatic inhibition, etc. [30]. Cytotoxicity is quantified as a decrease in metabolic activity of cells exposed to alloy sample extract compared with control. Genotoxicity is defined as a harmful action on a cell's genetic material affecting its integrity. Genotoxic substances are potentially mutagenic [31] and can cause damage to the germ line resulting in mutations in future generations and are also capable of inducing cancer [32]. Since bones are a source of mesenchymal stem cells important for physiological self-regeneration of the body [33,34], mutagenicity testing of biomaterials for orthopedic applications is of great importance. The *Salmonella typhimurium* assay (well known as Ames test) is a widely accepted short-term bacterial assay for identifying substances that can cause genetic damage leading to gene mutations [32]. Testing of genotoxicity using Ames test is recommended by ISO standard 10993-3 [35] and should be performed according to OECD guidelines [36].

Our preliminary in vitro cytotoxicity tests with as-cast Zn alloys revealed that the U-2 OS cells exposed to the extract from the Zn–0.8 Mg alloys containing 70 $\mu\text{mol/l}$ Zn showed a good viability of 80% [24]. Zinc in vitro cytotoxicity has also been studied on other kinds of human and animal cells. Wu et al. [37] observed a 70% viability of human endometrial epithelial cells at 150 $\mu\text{mol/l}$ Zn. A similar reduction of viability was however detected for rat retinal cells at only 50 $\mu\text{mol/l}$ Zn [38]. Human proximal tubular cells exhibited a viability of less than 50% in a 100 $\mu\text{mol/l}$ Zn solution [39]. A recent study of Cheng et al. [28] indicated that 1 $\mu\text{g/ml}$ (i. e. 15 μM) Zn is not toxic to ECV304 cells, but it reduced viability of L929 cells in the same extract. Li et al. [27] showed in their research very good viability of ECV304, VSCM and MG63 cells in extracts from extruded Zn–1 Mg alloy. They also showed that ECV304 and MG63 cells cultured 24 h directly on the surface of Zn–

1 Mg behaved healthy. On the contrary VSCM cells were characterized by unhealthy and dead morphology after 24 h on the surface of the Zn–1 Mg alloys [27]. Gong et al. showed that viability of L-929 in diluted extracts (1:15) performed at DMEM with 10% FBS after 24 and 72 h is excellent. However, information about concentrations of Zn and Mg ions after extraction is missing [26]. Murni et al. [40] studied cytotoxicity on Zn–3 Mg alloy. Extracts were prepared by incubating of 0.75 mg of Mg–3Zn powder in cell culture for 72 h and the prepared extract from Zn–3 Mg contained 0.49 ppm of Zn ions. Viability tests on NHOst cells showed poor viability ($47 \pm 12\%$) after 1-day incubation time. Cell viability increased above 100% compared with control group after three days of incubation, however, it was again reduced after 7 days of incubation [40]. Dambatta et al. studied NHOst cell viability in extracts prepared by incubating 0.1–2 mg/ml of the powder of Zn–3 Mg alloys in cell media. The results revealed that concentrations of 0.1 and 0.5 mg/ml led to the improved cell viability higher than 100%. On the contrary, concentrations of 1 and 2 mg/ml Zn–3 Mg alloys induced significant toxicity [41]. Although presented research contain important information about biocompatibility of Zn-based materials for different types of cells, exact compositions of extracts from studied materials measured by ICP are missing in many cases which partially cause ambiguity of estimated properties. Also the utilization of different kinds of cells can bring different results. Therefore, additional in vitro tests are needed to better characterize Zn biocompatibility prior to its possible applications in human medicine.

In vivo tests of zinc were reported recently in a pioneering work of Bowen et al. [19] and also the work of Li et al. [27]. Bowen et al. applied thin zinc wires to the abdominal aorta of adult rats and studied corrosion rates, corrosion products and tissue adherence. It was observed that the in vivo corrosion rate ranged between 10 and 50 $\mu\text{m/year}$ and that it progressively increased during six months of exposition. Another important finding was that the implant remained intact for at least four months after implantation. Post-corrosion investigation revealed the presence of compact corrosion products facilitating a good adherence of the surrounding tissue. Li et al. [27] confirmed that application of Zn–1 Mg alloys in mouse femora has no negative effect on the health of mice. Moreover, strong new bone formation during process has been observed. These results imply that zinc or zinc alloys are promising materials for biodegradable vascular stent applications.

In the present work, structural, mechanical, in vitro corrosion and biological characteristics of Zn and Zn–Mg alloys were studied systematically. Zn–Mg alloys containing 0–1.6 wt.% Mg were selected for this study, because their plasticity and formability are significantly impaired at higher Mg concentrations [24]. The alloys were studied in the as-hot extruded state to achieve high mechanical strength. Mechanical properties of the Zn–Mg alloys were compared with the WE43 alloy that has been extensively studied in the context to biodegradable implants. The WE43 alloy also appears as one of promising candidates for designing these implants [1,2,5,7,11]. For in vitro biocompatibility testing, we have chosen two cell lines: (1) murine fibroblasts L929 (ATCC® CCL-1™) explicitly recommended for in vitro cytotoxicity testing by ISO standard 10993-5 [42] and (2) human osteosarcoma cell line U-2 OS (ATCC® HTB-96™) resembling osteoblasts due to intended use of the alloys. We have first tested toxicity of a broad range of concentrations of ZnCl_2 , covering the possible peak concentrations of zinc released from the alloy during corrosion.

2. Materials and methods

Pure Zn, Zn–0.8 Mg, Zn–1.6 Mg, and Mg–4Y–3RE–0.4Zr (WE43, according to the ASTM designation) alloys were studied in this work. Zinc and zinc alloys were prepared by melting pure Zn (99.99 wt.%) and Mg (99.99 wt.%) in an electric resistance furnace under air atmosphere. After sufficient homogenization, the melted alloys were gravity cast into a cast-iron mold to prepare cylindrical ingots of 20 mm in diameter and 150 mm in length. Chemical compositions of ingots are

given in Table 1. The WE43 alloy was purchased from an industrial supplier in the form of rectangular ingots of $200 \times 100 \times 500$ mm in size. To ensure identical preparation of both kinds of materials, the alloy was re-melted in a vacuum induction furnace under a protective argon (4N) atmosphere and gravity cast into cast iron mold. Prepared cylindrical ingots had the same dimensions as those of Zn alloys. Subsequent processing step was hot extrusion. Cylinders of 20 mm in diameter and 15 mm in height were cut from as-cast ingots and hot extruded in a hydraulic press at an extrusion ratio and rate of 10:1 and 2 mm/min, respectively, to produce rods of 6 mm in diameter. Before hot extrusion, the WE 43 alloy was heat-treated by the T4 regime, i.e., solutionized at $525^\circ\text{C}/8$ h and water quenched to improve the formability of the material. Extrusion temperatures of zinc and WE43 alloys were 300 and 400°C , respectively.

2.1. Structure and mechanical properties

The microstructures of the alloys were examined by light and scanning electron microscopy (SEM, Tescan Vega 3) equipped with energy dispersion spectrometry (Oxford Instruments Inca 350). For this purpose, the samples were grinded using SiC abrasive papers (P180–P4000), polished by diamond pastes with 2 and $0.7\ \mu\text{m}$ particles and etched in a 2 ml $\text{HNO}_3 + 100$ ml H_2O solution. Phase composition of alloys was determined by X-ray diffraction (X'Pert Philips, 30 mA, 40 kV, X-ray radiation $\text{Cu K}\alpha$). Mechanical properties of alloys were examined by Vickers hardness (loading of 5 kg), tensile and compressive testing. Tensile tests were conducted on rods of 6 mm in diameter and 70 mm in length. Samples for compressive tests had a diameter and length of 6 and 12 mm, respectively. Both types of mechanical tests were carried out on LabTest 5.25OSP1-VM universal loading machine at a deformation rate of 1 mm/min.

2.2. Corrosion properties

In vitro corrosion tests can be carried out in numerous solutions simulating human body fluids [2,7,9,12]. However, any extrapolation of in vitro corrosion rates of biomaterials to in vivo conditions is problematic and may be inaccurate. For this reason, we estimated in vitro corrosion rates only from released ions during preparation of extracts in DMEM (Dulbecco's modified Eagle's medium, Sigma-Aldrich) and MEM (minimum essential medium, Sigma-Aldrich) for cytotoxicity tests. Cylindrical samples were sterilized by immersion into 70% ethanol followed by UV irradiation for at least 2 h. The extracts of the tested alloys were prepared according to ISO 10993-5 standard [43]. Cultivation medium DMEM or MEM was used depending on a cell type tested. Lower (5%) concentration of FBS was used because proteins in FBS can mask toxicity [44]. Volume to surface ratio ($1\ \text{ml}/88\ \text{cm}^2$) was fixed for all tested samples. The alloys were agitated (125 rpm) in closed vessels at 37°C for 24 h. Thereafter, the resulting extracts were centrifuged ($1500 \times g$, 5 min, RT) in order to remove solid parts of corroded materials. Extracts were used within 24 h after extraction for all tests. The amount of metal ions in extracts was measured using ICP-MS.

Such conditions are closely related to the conditions in human organism, although flow is not included. Estimated corrosion rates directly correspond to the observed cytotoxicity of selected materials. The corrosion rates were calculated, in $\text{mg}/\text{cm}^2/\text{day}$. The surface of samples after immersion was monitored using SEM equipped by energy dispersion spectrometry (Oxford Instruments Inca 350). Also X-ray diffraction

(X'Pert Philips, 30 mA, 40 kV, X-ray radiation $\text{Cu K}\alpha$) was used to characterize the phase composition of corrosion products.

Corrosion rates were calculated directly from released magnesium ions. For this purpose, a sample of the solution after the immersion of zinc alloy in DMEM or MEM was taken. This solution was subsequently stabilized by HNO_3 (Suprapur) and diluted with demineralized water. The amount of metal ions in prepared samples was measured using ICP-MS. The measured concentration was used for the calculation of weight of magnesium ions released during exposure and this weight was related to the original surface area of the sample and the time of exposure. As a result, corrosion rate in $\text{mg}/\text{cm}^2/\text{day}$ was estimated.

2.3. In vitro biocompatibility

- 1) Cell lines and cultivation. U-2 OS cells (human cell line derived from osteosarcoma, ATCC® HTB-96™) were maintained in Dulbecco's modified Eagle's medium and L929 cells (murine fibroblasts, ATCC® CCL-1™) were maintained in minimum essential medium. Both media were supplemented with 10% fetal bovine serum (FBS, Invitrogen) and cells were incubated at 37°C in a humidified atmosphere of 5% CO_2 . Cells were passaged at subconfluency. Cells from the 3rd passage were used for cell culture experiments.
- 2) Cytotoxicity assay. WST-1 assay is based on metabolic reduction of tetrazolium salt resulting in colored formazan product. Cytotoxicity is measured spectrophotometrically as the decrease in metabolic activity of the cells [45]. U-2 OS and L929 cells were seeded into 96-well plates ($100\ \mu\text{l}/\text{well}$) in densities of 0.8×10^5 and 1×10^5 cells/ml, respectively. The densities were chosen depending on the cell size so that tested agent could be added to the cells at subconfluency, as recommended by standard ISO 10993-5 [46]. After seeding, the cells were incubated at 37°C for 24 h to allow cell adhesion. Thereafter, a medium was replaced by the solutions of ZnCl_2 prepared in DMEM/MEM with 5% FBS ($2\text{--}300\ \mu\text{mol}/\text{l}$ Zn) or by the extracts in DMEM/MEM medium with 5% FBS. The extraction process was performed without 5% CO_2 atmosphere as it is recommended in standard ISO 10993-5 [46]. The pH changes were controlled after extraction process and confirmed similar values in the case of DMEM + FBS with Zn-0.8 Mg alloys and DMEM + FBS alone and increase about 1 unit of pH after the extraction process of WE43 compared with the DMEM + FBS alone. Such increase in pH value during extraction can partially affect the corrosion rate of WE43 although this could be partially neglected for such short tests. On the contrary, the viability of cell in cytotoxicity tests is not affected by this pH change due to the fact, that samples were during cytotoxic tests in incubator with CO_2 that cause the compensation of pH to the initial value of 7.4 for both studied materials. Concentrated extracts and extracts diluted with a fresh cultivation medium (75%, 50% and 25% extracts) were used for cytotoxicity studies. After 24 h, the cells were washed with PBS and incubated with a WST-1 reagent (5% WST-1 in DMEM without phenol red) for 4 h. The formazan product was photometrically quantified using an ELISA reader at the absorption wavelength 450 nm with a reference wavelength of 630 nm. DMEM/MEM with 5% FBS was used as a negative control and 0.64% phenol in DMEM with 5% FBS as a positive control. Cytotoxic effect was depicted as a decrease in metabolic activity (decrease in the amount of the formed formazan) compared with the negative control. All samples were processed in 6 replicates. According to standard ISO 10993-5, a decrease greater than 30% is considered as the cut-off between non-toxic and toxic effects.
- 3) Mutagenicity assay—Ames test. The Ames test is a short-term bacterial reverse mutation assay designed to detect potential mutagens. The test employs histidine (His) dependent *Salmonella* strains carrying different mutations in genes in the His operon. When a mutagen is added to the plate containing only a trace of His, the number of revertant colonies (those bacteria that revert to His independence) per plate is increased [32]. The Ames test in a form of plate incorporation

Table 1
Chemical compositions of the studied materials (in wt.%).

Material designation	Zn	Mg	Si	Ca
Zn	99.97	–	0.02	0.2
Zn-0.8 Mg	99.12	0.84	0.02	0.1
Zn-1.6 Mg	98.38	1.59	0.02	0.2

assay without metabolic activation was carried out according to Mortelmans and Zeiger [32] and OECD guidelines [47]. The extracts of alloys prepared as described above were used for testing. Two strains TA98 and TA100 considered as strains of the first choice [44] were used. Overnight cultures were centrifuged, resuspended in 0.9% NaCl and diluted to a final optical density of 0.4. Two milliliters of molten top agar (0.6% NaCl, 0.6% agar, 0.05 mM biotin and 0.05 mM histidine), 0.1 ml of the extract of tested alloys, 0.1 ml of phosphate buffer and 0.1 ml of tested strain suspension were mixed and poured onto the surface of glucose minimal agar plates. They were inverted and incubated at 37 °C for 72 h. Three triplicates were prepared for each sample. A buffer was used as a negative control and daunomycin (TA98) or sodium azide (TA100) was used as positive control. Revertant colonies per plate were hand-counted and the ratio of a negative control to a sample was calculated. The ratio of revertants higher than 3 was considered as the cut-off between mutagenic and non-mutagenic responses.

4) Genotoxicity assay–Comet assay. Cells exposed to the extracts were embedded in agarose on a microscope slide and lysed and the presence of DNA breaks was determined by electrophoresis at high pH. The percentage of DNA in a comet tail reflects the degree of DNA damage [45]. Specifically; U-2 OS and L929 cells were seeded into 24-well plates (500 μ l/well) in the same manner as for cytotoxicity assay. Following one day incubation, the medium was replaced by the extracts of alloys in DMEM/MEM medium with 5% FBS and cells were incubated for 24 h. DMEM/MEM with 5% FBS was used as a negative control and H₂O₂ (4.2 mg/l, 10 min) in PBS as a positive control. The comet assay was performed according to Olive and Banáth [46] with slight modifications. Briefly, cells were washed with PBS,

trypsinized and the density of the suspension was adjusted to about $2\text{--}3 \times 10^5$ cells/ml. The cell suspension was mixed with 1% low melting-point agarose (LMPA, 2-hydroxyethylagarose, type VII, Sigma-Aldrich), laid on a microscopic slide precoated with agarose (Type I-A, low EEO, Sigma-Aldrich), covered with a coverslip and allowed to form a thin solid layer. Slices with gels were submerged into an alkaline lysis solution (pH over 12) for 1 h. The positive control was lysed in a separate vessel. Rinsed slides were then submerged into an electrophoresis solution (pH over 12) and electrophoresis was conducted for 25 min at 0.6 V/cm. Washed slides were allowed to dry, covered with a fresh layer of LMPA, stained with ethidium bromide (100 μ g/ml) and analyzed using a fluorescence microscope. CASP freeware [47] was used for evaluation of the images according to Cortes-Gutierrez et al. [48]. At least 50 comets from each sample were evaluated. Comets were sorted into five categories (0–4) depending on the percentage of DNA in the tail of the comet (0 corresponding to 0–20% damage etc.). The amount of comets in each category was multiplied by the appropriate number of the category. The degree of DNA damage (single- and double-strand breaks) was depicted using arbitrary units (0 = no damage, 200 = 100% damage). Three independent measurements were done for each sample.

3. Results and discussion

3.1. Structures

The structures of the hot-extruded alloys are illustrated in Fig. 1. Pure zinc is composed of fine recrystallized equi-axed grains with an

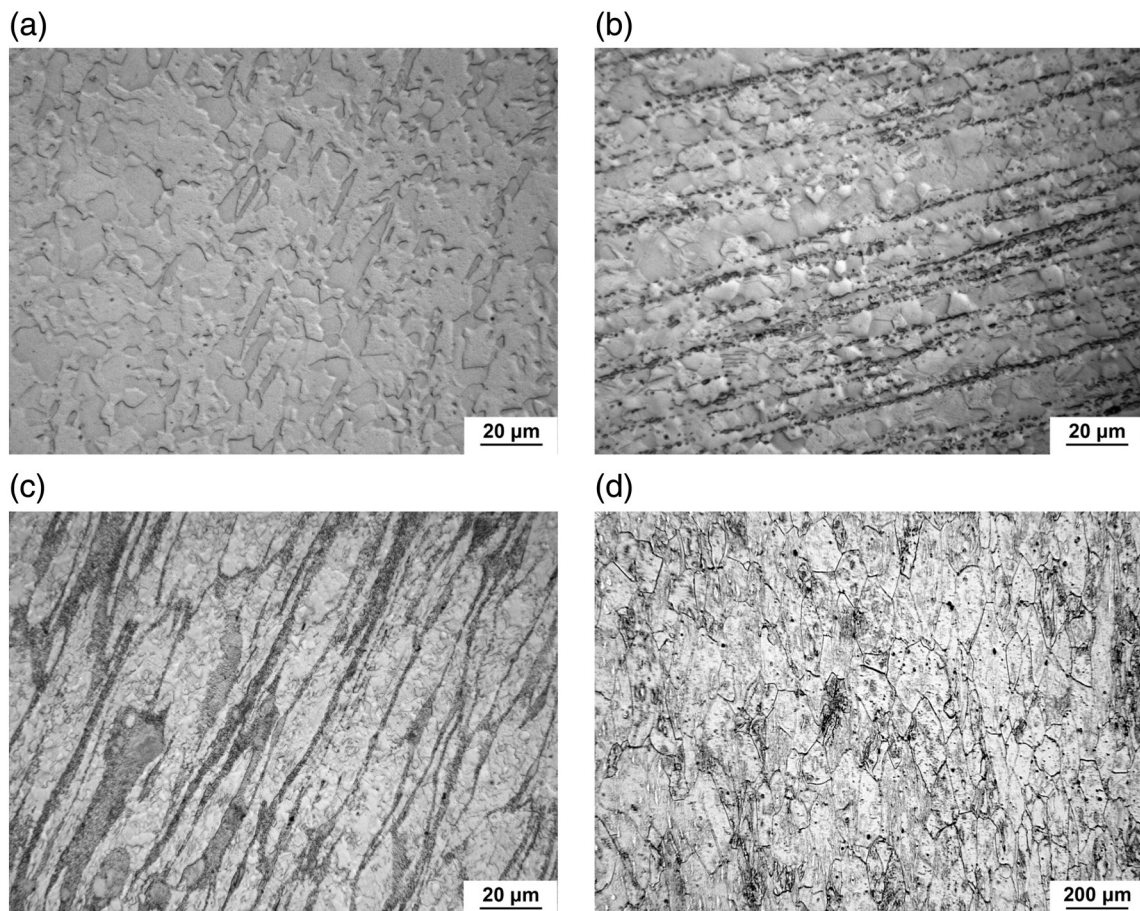


Fig. 1. Light micrographs of the hot-extruded alloys: a) Zn, b) Zn–0.8 Mg, c) Zn–1.6 Mg, and d) WE 43 (LM).

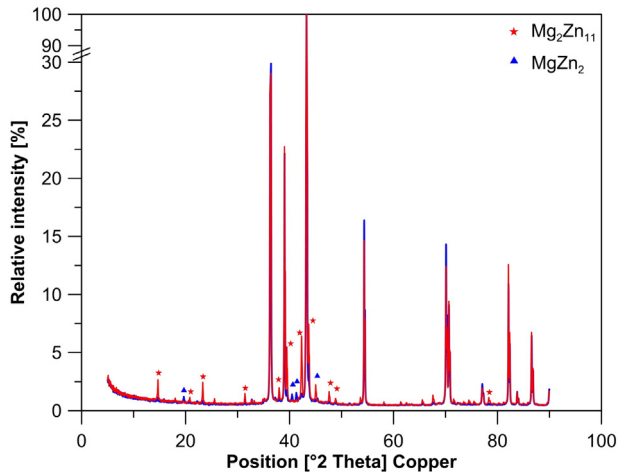


Fig. 2. XRD spectra of Zn–Mg alloys with 0.8 and 1.6 wt.% of Mg.

average grain size of 20 μm (Fig. 1a). The visual absence of deformation texture suggests that dynamic recrystallization was completed during the hot extrusion process. We illustrated in our previous study [22] that the as-cast Zn contained large grains ranging between 100 and 1000 μm . The observed grain size of 20 μm indicates that the parameters of hot-extrusion were selected properly to refine the microstructure

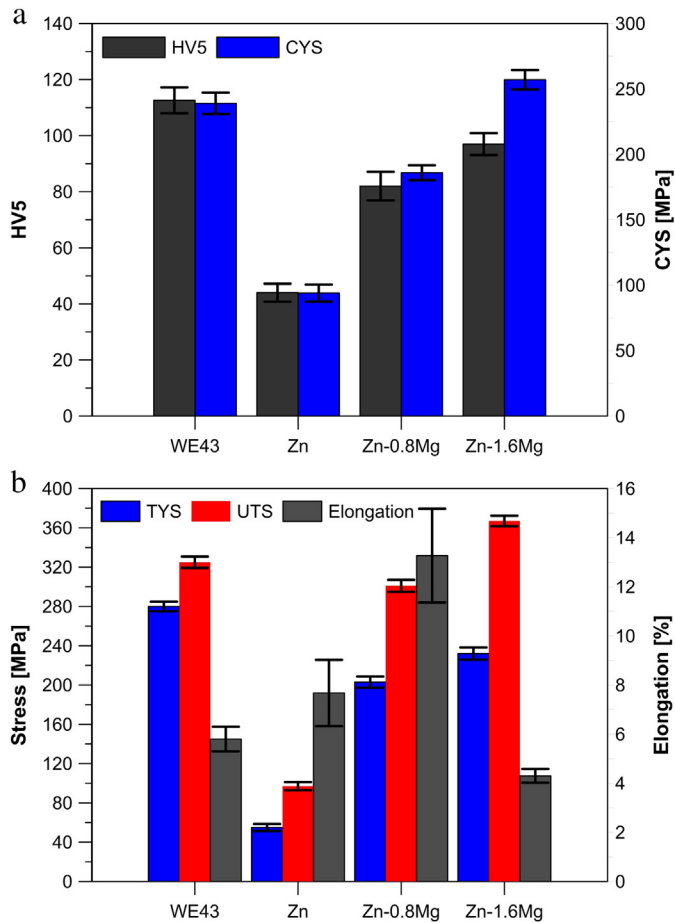


Fig. 3. Mechanical properties of the alloys: a) Vickers hardness (HV 5) and compressive yield strength (CYS), and b) tensile yield strength (TYS), ultimate tensile strength (UTS) and elongation (E).

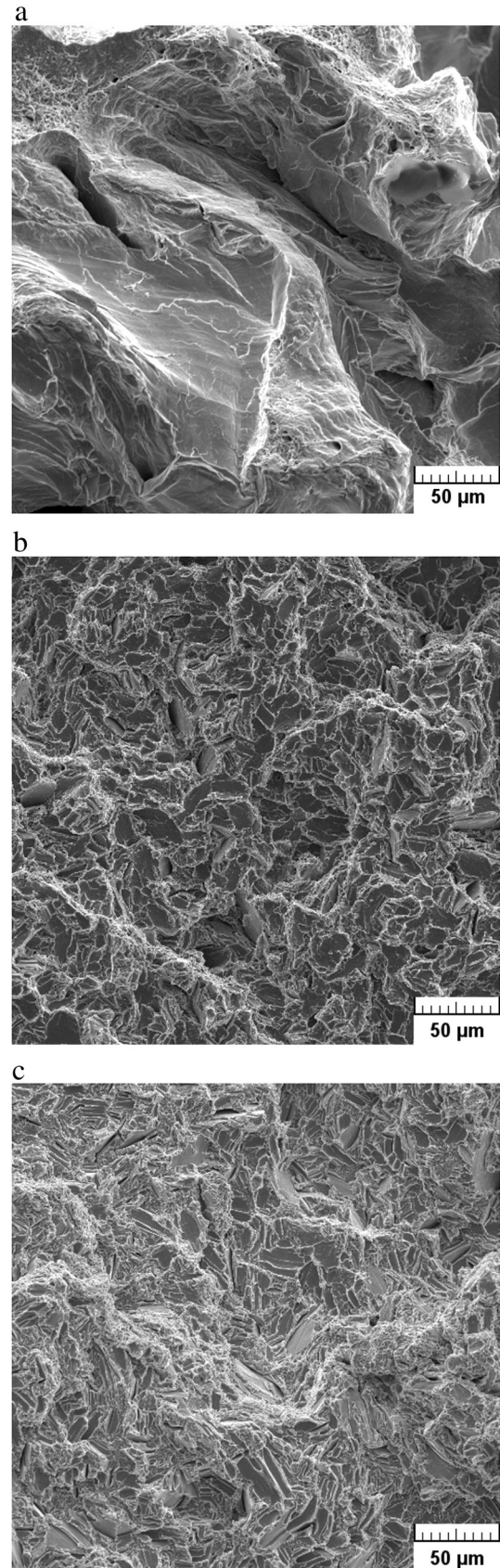


Fig. 4. Fracture surfaces of the alloys after tensile tests: a) Zn, b) Zn–0.8 Mg, and c) Zn–1.6 Mg (SEM).

Table 2

Basic mechanical properties of various biomaterials and natural bones (PLA – polylactic acid) [1,2,5,50,51].

Materials	Density (g/cm ³)	Tensile strength (MPa)	Elastic modulus (GPa)	Elongation (%)
Bones	~2	30–280	5–20	1–2
PLA	~1	~30	~2	–
Wrought Mg-based (WE43)	~3	320	~50	6
Wrought Zn–0.8 Mg	~7	300	~90	15
Wrought Ti-based	~5	800–1100	110	~10
Wrought Co-based	~9	700–1200	220	~10
Wrought stainless steels	~8	600–1000	200	~20

sufficiently. It was also shown in our previous work [22] that the Zn–0.8 Mg alloys in the as-cast state were hypoeutectic, i.e., it contained primary Zn dendrites and Zn + Mg₂Zn₁₁ eutectic mixture forming a continuous interdendritic network. A light micrograph of the hot extruded Zn–0.8 Mg alloys in Fig. 1b shows that the hot extrusion process breaks down the interdendritic network and arranges the Mg₂Zn₁₁ particles (dark) into thin rows parallel to the hot extrusion direction. The primary Zn dendrites vanish during hot extrusion and are replaced by dynamically recrystallized regions (light) elongated in the extrusion direction. Recrystallized regions are composed of equi-axed Zn grains of 12 μm in diameter, i.e., slightly smaller than those in pure Zn. Apparently, fine Mg₂Zn₁₁ particles partially hinder the grain boundary movement and grain growth during hot extrusion. Another important observation is that the rows of intermetallic phases are separated from each other and this has a direct impact on mechanical behavior of the Zn–0.8 Mg alloy, as will be shown later. Fig. 1c illustrates the as-hot extruded Zn–1.6 Mg alloy. In the initial as-cast state, the structural constituents of this alloy are primary Zn dendrites and Zn + Mg₂Zn₁₁ interdendritic eutectic network [22]. The volume fraction of the eutectic mixture is approximately double that of the previous material. After hot extrusion, eutectic regions (dark) become oriented in the extrusion direction but they still remain relatively thick and create a continuous network around deformed and dynamically recrystallized Zn (light). The average grain size in these regions of 12 μm is identical to the Zn–0.8 Mg alloy. The Mg-based WE 43 alloy is illustrated in Fig. 1d. It is composed of recrystallized slightly textured Mg grains of approximately 50 μm in thickness and 100 μm in length. EDS chemical analysis of Mg grains determined concentrations of Y and RE of 3.8 and 3.2 wt.% indicating that the Mg₄₁Nd₅, Mg₁₄Nd₂Y and Mg₂₄Y₅ intermetallic phases originally present in the as-cast WE 43 alloy [49] dissolved during the T4 heat treatment at 525 °C/8 h. Observed spectra from XRD measurements are shown in Fig. 2 as dependence of relative intensity to ²Theta. It is evident that there is a slight difference between the Zn–0.8 Mg and Zn–1.5 Mg alloy. XRD measurements clearly confirmed the presence of Mg₂Zn₁₁ intermetallic phase in both zinc-based alloys and also some amounts of MgZn₂ phase in as-extruded Zn–0.8 Mg. Such results are also in consistency with our previous work that has been oriented on the as-cast Zn–TaMg alloys [22].

3.2. Mechanical properties

Fig. 3 summarizes hardness, compressive and tensile mechanical properties of extruded alloys. There is a direct relationship between Mg-concentration and mechanical properties. Hardness increases with increasing Mg-content from 44 HV5 for pure Zn to 97 HV5 for the Zn–1.6 Mg alloys (Fig. 3a). A similar situation is observed in compressive behavior where pure Zn shows a compressive yield strength (CYS) of 120 MPa, while that of the Zn–1.6 Mg alloys reaches more than 380 MPa. It is also important to note that both hardness and CYS of the reference WE43 alloy are slightly lower as compared with the Zn–1.6 Mg alloy. Tensile behavior follows a similar trend, i.e., both the tensile yield strength (TYS) and ultimate tensile strength (UTS) increase

with increasing Mg-content (Fig. 3b). The Zn–1.6 Mg alloys reach a maximum UTS of 367 MPa. However, elongation (E) of near zero proves an excessive brittleness of the Zn–1.6 Mg alloys showing no plastic strain during loading. The reason of this behavior is the presence of continuous network of hard and brittle Mg₂Zn₁₁ intermetallic phases (Fig. 1c) facilitating the growth of fracture cracks before the onset of plastic strain. In contrast to the Zn–1.6 Mg alloy, the Zn–0.8 Mg alloys show TYS and UTS values of 203 and 301 MPa, respectively. It also shows a good plasticity and E of 15% because of the absence of the network of intermetallic phases (Figs. 1b, 2b). Gong et al. [26] studied the Zn–1 Mg alloys in extruded state and postulated values for TYS and UTS as 180 MPa 250 MPa respectively. The reason is that slightly lower values of mechanical properties can be connected with different conditions of extrusion (temperature = 200 °C, ram speed = 20 mm/s, extrusion ratio = 16). Li et al. [27] prepared Zn–1 Mg alloys with almost similar mechanical properties compared with the present paper by extrusion process at 210 °C, and at extrusion ratio equal to 8, which are close conditions to our procedure. The extruded WE43 alloy exhibits slightly higher TYS and UTS (280 and 325 MPa, respectively) but a significantly lower elongation of 6%. Although present paper deals with Zn–Mg alloys containing up to 1.6 wt.% of Mg, higher amounts of Mg can be added to Zn to significantly affect mechanical properties. Based on the phase diagram [21], zinc solubility in Mg is almost negligible and due to the eutectic point near 3 wt.% of Mg in zinc, eutectic mixture of α-Mg and Mg₂Zn₁₁ phase is strongly presented in the structure and the amount of Mg₂Zn₁₁ phase is increased significantly with an increasing Mg amount in the alloy. This cause a decrease of plasticity, however other mechanical properties such as hardness and compressive properties (CYS and UCS) can be increased noticeably. It has been shown that Vickers hardness (HV5) reached about 200 MPa for Zn–3.4 Mg alloys in the as cast state [22]. Although the experiments were performed for as-cast states, HV5 was increased regularly with an increased Mg content in alloys [22]. The same trend was observed for as-cast states in reference [24]. Moreover in [24] authors showed that CYS is improved up to 3.4 wt.% of Mg in alloy and reached almost 650 MPa. When Mg concentration was increased to higher values than at eutectic composition, plasticity of material disappeared and only UCS was observed at lower values of about 230 MPa [24]. It can be assumed that due to this specific brittleness, extrusion of materials with more than 3 wt.% of Mg will be almost impossible. The trends which are observed for as-cast Zn–Mg up to 3 wt.% of Mg will be probably very similar for extruded materials although to our best knowledge, there does not exist a sufficient date which can confirm this statement.

Fracture surfaces after tensile tests shown in Fig. 4 confirm the above findings. Pure zinc (Fig. 4a) is characterized by a relatively coarse transcrystalline fracture surface with plastic deformation traces corresponding to the moderate elongation of 8% measured for pure Zn (Fig. 3b). The fracture surface of the Zn–0.8 Mg alloys (Fig. 4b) is very fine and exhibits a dimple-like morphology with dimples created around hard Mg₂Zn₁₁ intermetallic phases. Dimples are surrounded by areas of plastic deformation of Zn phase (light). Plastic zones are dense and well developed suggesting good plasticity and high elongation (15%) of the Zn–0.8 Mg alloys (Fig. 3b). A quite different fracture morphology is observed for the Zn–1.6 Mg alloys (Fig. 4c) where a high density of flat brittle facets appears which is consistent with a macroscopic brittleness and negligible elongation of this alloy (Fig. 3b). Brittle facets are created by the fracture occurring in the eutectic network retained after hot extrusion (Fig. 1c).

The results above indicate considerable hardening and strengthening effects of Mg due to the presence of fine and hard Mg₂Zn₁₁ intermetallic phases (Fig. 1b, c). Solid solution strengthening can be neglected because of very low solid solubility of Mg in Zn [21]. By comparing structures and mechanical properties of the extruded and cast Zn–Mg alloys given in our previous study [22] one can observe that hot extrusion brings about a considerable improvement of both strength and plasticity of the Zn–0.8 Mg alloy. The as-cast alloy has UTS and E of less than

180 MPa and 2%, respectively [22], but hot extrusion leads to almost two-fold increase in UTS and even seven-fold increase in E (Fig. 3b). During hot extrusion, the dynamic recrystallization occurs leading to a significant grain refinement. The as-cast structure with average dendritic branch thickness of 30 μm [22] vanishes and is replaced by equi-axed grains of 12 μm in size (Fig. 1b). Moreover, eutectic networks disappear which further contributes to the strength and plasticity of the Zn–0.8 Mg alloy. The Hall–Petch (H–P) relationship between TYS and grain size (d) for pure Zn has been reported in the following form [50]:

$$\text{TYS (MPa)} = 32 \text{ (MPa)} + 6.9 \left(\text{N/mm}^3 \right)^{1/2} \times [d \text{ (mm)}]^{-1/2}. \quad (1)$$

The grain size of 0.012 mm in the Zn–0.8 Mg suggests that the H–P contribution to the TYS is 95 MPa. This value is only half of the measured TYS of this alloy (203 MPa) and the remaining part can be attributed to the presence of arranged Mg-enriched intermetallic phases (Fig. 1b) and, perhaps, also to some crystallographic orientation of Zn induced by hot extrusion.

Based on the above statements the Zn–0.8 Mg alloys appear as a promising material for designing biodegradable implants. It is worth noting, that mechanical characteristics of the Zn–0.8 Mg alloys fulfill the general requirements for materials of biodegradable stents (TYS – 200 MPa, UTS – 300 MPa and E – 15% [19]). The requirements for load-bearing implants like fixation devices for fractured bones cannot be generalized, because of a complexity of possible locations and applications in the human body. It thus remains to compare mechanical characteristics of the new material with other inert, biodegradable materials and hard bone tissue, as summarized in Table 2. One can see that the new Zn–Mg alloys have a lower strength than inert biomaterials and similar strength to the WE43 alloy. Nevertheless, the strength of 300 MPa considerably exceeds that of poly-lactic acid (PLA) which is a commercial biodegradable material currently used for bone fixations or other polymeric materials. Importantly, the plasticity of the new material is fully comparable with Ti, Co alloys and stainless steels. From the mechanical point of view, the wrought Zn–0.8 Mg alloys thus appear as a good candidate for designing small bone fixation devices like screws, plates and other implants. As it will be demonstrated in the following paragraph, the essential advantage of the Zn alloy over the Mg alloy is related to its different corrosion behavior.

3.3. Corrosion behavior

For corrosion and also biological experiments only Zn–0.8 Mg and WE43 alloys were selected. This was done due to the observed mechanical properties of Zn-based alloy and the best combination of them in the case of Zn–0.8 Mg. Corrosion rates in DMEM and MEM calculated from released Zn ions in the case of the Zn–0.8 Mg and Mg ions in the case of WE43 are 0.0134 ± 0.0003 and 0.2011 ± 0.0114 $\text{mg/cm}^2/\text{day}$, respectively. Calculated values were similar for both extracts in DMEM and MEM, therefore, average values are calculated. It is clearly evident that the Zn-based alloy corroded at a significantly lower corrosion rate compared with the magnesium-based alloy.

Corrosion properties of rolled Zn–1 Mg alloys in a Hank's solution have been previously reported by Li et al. [27]. Corrosion rate estimated from weight changes reached the value of about 0.085 mm/year which corresponds to the value 0.0165 $\text{mg/cm}^2/\text{day}$. This is very close to the calculated value of 0.0134 $\text{mg/cm}^2/\text{day}$ presented in this work. Gong et al. [26] studied the corrosion of Mg–1Zn and WE43 extruded alloys in SBF. Estimated corrosion rates from weight changes were 0.12 and 0.34 mm/year which corresponds to the 0.023 and 0.2012 $\text{mg/cm}^2/\text{day}$ for Zn–1 Mg and WE43 respectively. The reason for higher corrosion rate of zinc alloy compared with the present results can be connected with the occurrence of a higher amount of eutectic phases in the structure. These phases are corroded firstly [26,41], and therefore, observed corrosion rate can be higher compared with the results in this work. Dambatta et al. [41] studied the corrosion of Zn–3 Mg, however, their calculations were performed only from electrochemical measurements, such as potentiodynamic measurements and EIS (electrochemical impedance spectroscopy). Previous research [27] revealed that corrosion rates estimated based on weight changes and electrochemistry can be significantly different for zinc alloys. This was also reported in the past for magnesium alloys [9]. Therefore, observed corrosion rates cannot be compared regularly with presented results. Corrosion processes of Zn–Mg alloys and magnesium alloys are different. Magnesium is insensitive to oxygen dissolved in the corrosion medium and the following anodic and cathodic reactions can be written for Mg [52–54]:

Anodic reaction:

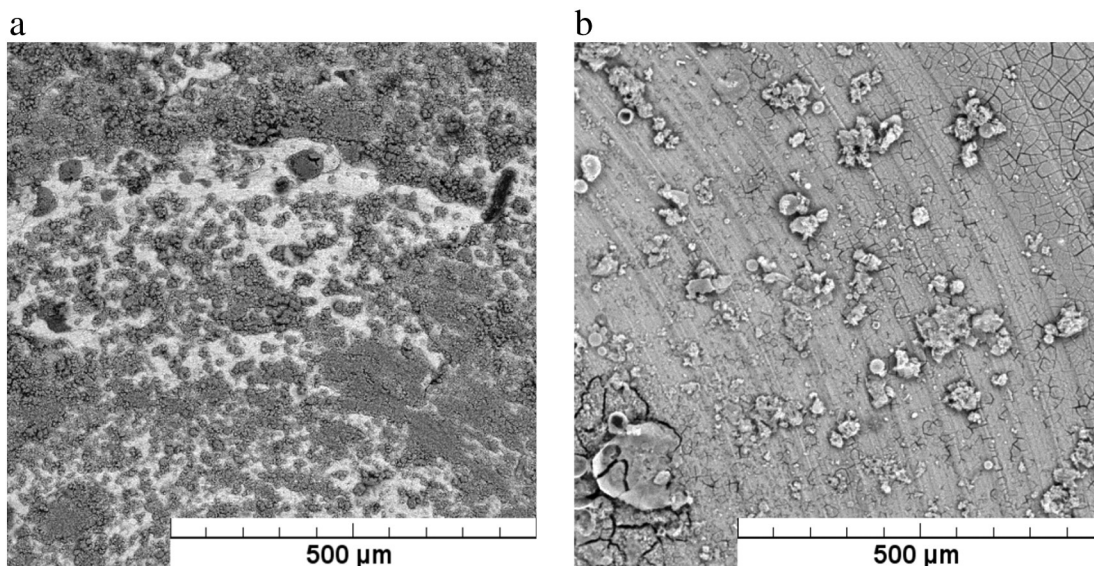


Fig. 5. Surface of alloys after immersion in DMEM/MEM solution: a), c) Zn–0.8 Mg and b), d) WE43 alloy.

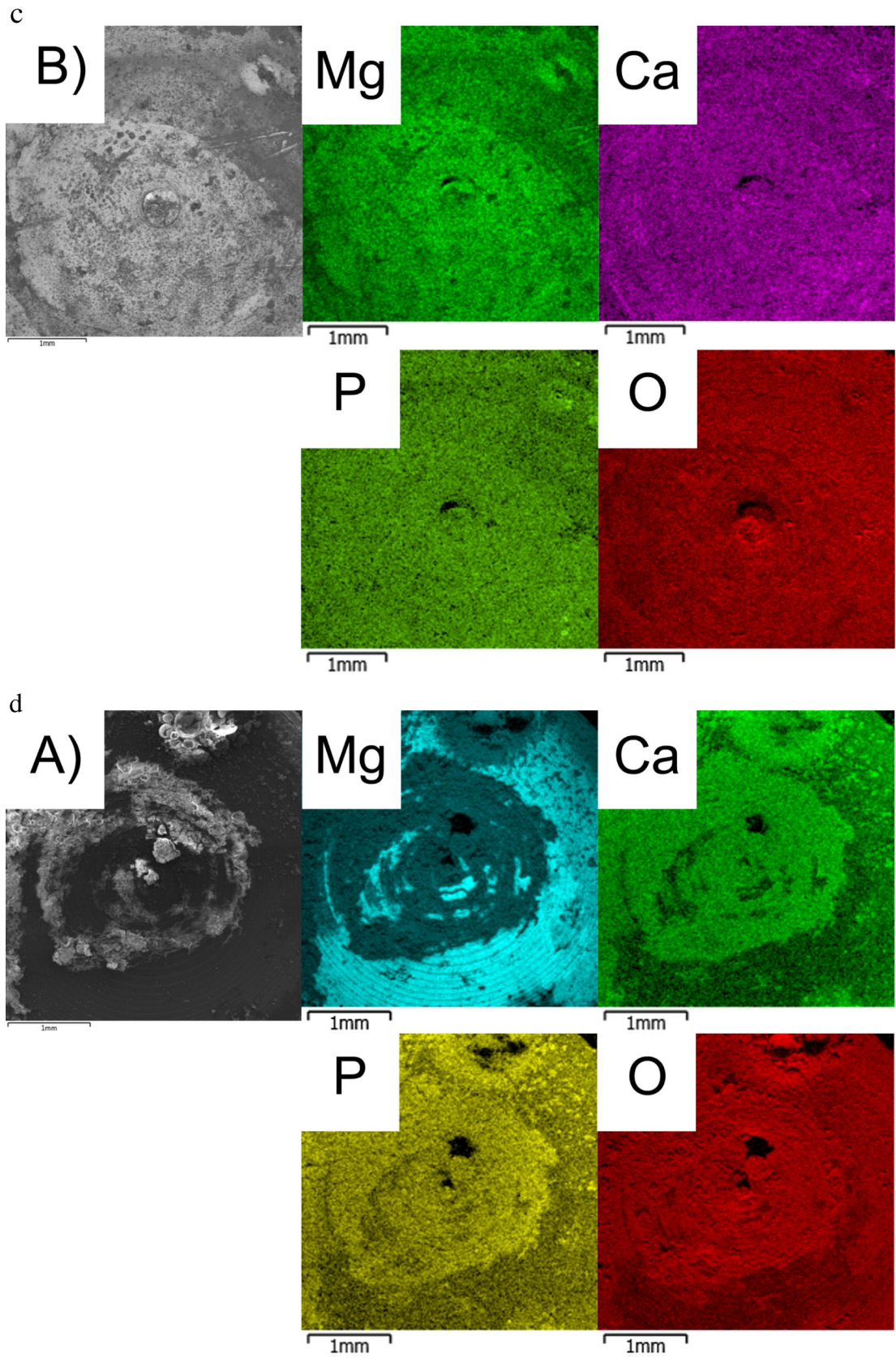


Fig. 5 (continued).

Table 3
Composition of corrosion products after immersion in DMEM or MEM solution.

at.%	O	Mg	Zn	Ca	P	Y	Nd	Na	Cl	K	Gd	Dy
WE43	44.7	44.5	–	2.7	2.6	1.4	0.4	0.4	0.2	0.1	0.1	0.1
Zn–0.8 Mg	49.8	1.5	42.4	0.6	0.6	–	–	3.9	1.2	–	–	–

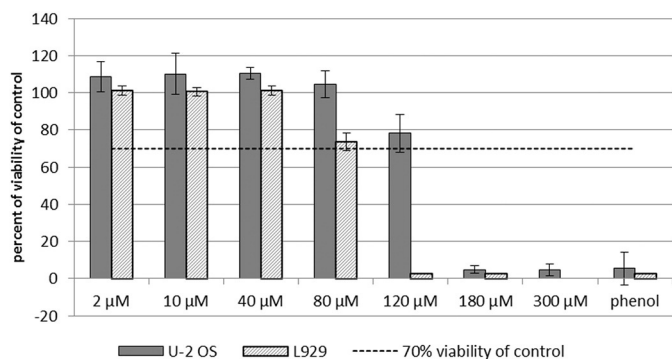


Fig. 6. Effect of Zn^{2+} ions on viability of U-2 OS and L929 cells. Relative viability of cells after 1-day incubation with Zn^{2+} in DMEM/MEM + 5% FBS was related to untreated cells cultivated in DMEM/MEM + 5% FBS which were used as a negative control. Cells treated with 0.64% (72 mM) phenol as a positive control. Dashed line stands for the cut-off between non-toxic and toxic responses. Error bars represent sample standard deviation.

Cathodic reaction:



Similarly, the anodic reaction of zinc is dissolution of the metal. But, hydrogen evolution in the nearly neutral solution, which is stabilized in the human body, is not expected for zinc, and the cathodic reaction is based on the reduction of oxygen [52,53]:

Anodic reaction:



Cathodic reaction:



It can be concluded from the corrosion experiments that the Zn alloys are considerably more corrosion resistant than the magnesium alloy. Firstly, zinc is less reactive than magnesium. The standard potentials of Zn and Mg are -0.762 and -2.372 V (versus SHE), respectively [46]. Secondly, zinc exhibits a high hydrogen overpotential suppressing the cathodic evolution of hydrogen. The cathodic reaction occurring on the zinc surface is dominated by a reduction of dissolved oxygen (Eq. (4)) and, therefore, it is controlled by the diffusion rate of oxygen.

Table 4
Zinc cytotoxicity (zinc was added in form of $ZnCl_2$). MTT = 3-(4,5-dimethylthiazol-2-yl)-2,5-diphenyltetrazolium bromide, LDH = lactate dehydrogenase, WST-1 = water soluble tetrazolium salt, EC_{50} , TC_{50} = the concentration required to reduce viability by 50%.

Concentration of Zn (in μM)	Cells	Test	Exposition time	Result	Reference
5–300 μM in complete cell–culture medium	Primary human endometrial epithelial cells	MTT	24 h	$TC_{50} = 215 \mu M$, 70% viability at 150 μM	[37]
20–80 μM in serum-free medium	Rat retinal cells	LDH	24 h	70% viability at 50 μM , 100% cell death at 60–80 μM	[38]
1–100 μM in serum-free medium	Human proximal tubular cells	MTT	24 h	Significant reduction in the viability at 100 μM	[39]
50–300 μM in serum-free medium (2 h) followed by incubation in medium with serum	Neuronal PC12 cells	MTT	2 h exposure, 22 h incubation	$EC_{50} = 185 \mu M$	[56]
2–300 μM	U-2 OS	WST-1	24 h	The highest safe concentration of 120 μM	This work
2–180 μM	L929	WST-1	24 h	The highest safe concentration of 80 μM	This work

As stated before, zinc alloys are considered mainly for load-bearing and stent applications. Typical dimensions of a biodegradable zinc screw or nail may be 4 mm in diameter and 20 mm in length. Assuming, for simplicity, uniform in vivo corrosion at a rate of 0.0134 mg/cm²/day provides a Zn dose of 0.038 mg per day which is far below the tolerable limit of 40 mg per day. The recent in vivo study with zinc wires implanted to the rat's artery [17] reported corrosion rates of approximately 0.05 mm/year which correspond to 0.097 mg/cm²/day. Such values are higher than that measured in our study although protective insoluble surface films composed of zinc oxide, phosphate and carbonate were observed after the in vivo exposition of zinc [17]. Such variety can be connected with differences between conditions in human organism and static and also very short immersion tests.

Therefore it is important to note that estimated corrosion rates are only approximate values for direct comparison between the Zn and Mg alloys which directly relate to the cytotoxicity testing.

Taking the mechanical performance of zinc implants into consideration, it is not a simple task to define the acceptable corrosion rate because it depends on the implant type, function, size, location in the body and other factors. Assume again that a biodegradable fixation screw has a diameter of 4 mm. The surgical requirement may be that the screw must keep 95% of its original load-bearing capability for at least 6 weeks after implantation. In other words, corrosion of the screw should not reduce its cross-section by more than 5% per 6 weeks giving a maximum acceptable corrosion rate of 0.4 mm/year which corresponds to the 0.78 mg/cm²/day. In this case, the observed degradation rate of the Zn alloy is significantly lower. Also the WE43 alloy corrodes at an acceptable corrosion rate, although this rate approaches 0.20 mg/cm²/day which correspond to the value 0.42 mm/year. However it is worth mentioning that such prediction is reliable only in the case of a uniform corrosion on the surface, which is not often satisfied especially in the case of Mg-based alloys.

Corrosion products of both alloys (Fig. 5a–d) after immersion test were predominantly composed of matrix element (Zn or Mg) and other elements such as oxygen, phosphorus and calcium (Table 3). Such composition points to oxides and hydrated oxides of Zn or Mg and also phosphates product on the surface. Distribution of mentioned elements on the surface of immersed samples is shown in Fig. 5. Corrosion products in this case cover almost the entire surface. It is also evident from Table 3 that the surface products on WE43 after immersion contain higher amounts of P and Ca compared with the Zn–0.8 Mg alloy. Human bone is composed of phosphates. Therefore, superior creation of phosphates on the surface of alloy can cause improved connection between alloy and bone. From this point of view, Zn-based alloys seem to have lower tendency to create phosphates on the surface. We also try to perform XRD measurement, however due to the low

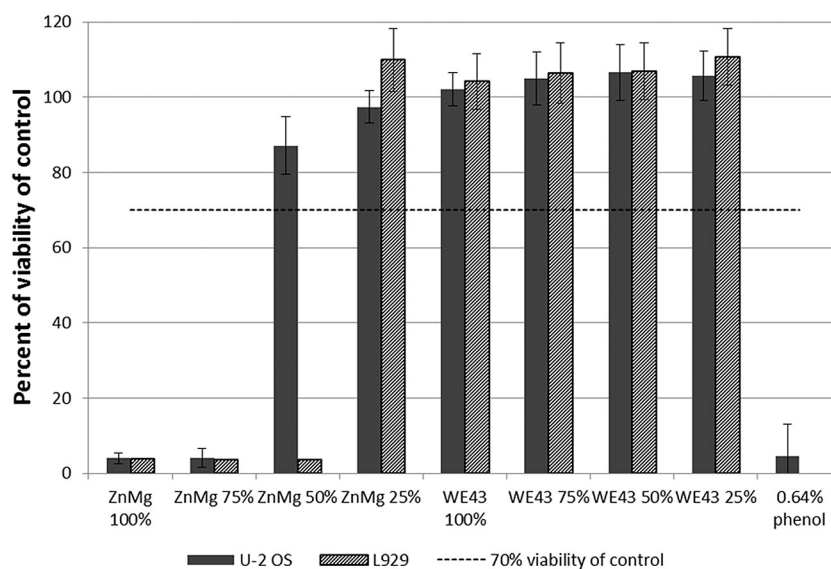


Fig. 7. Effect of the Zn–0.8 Mg and WE43 extracts on U-2 OS and L929 cells. The columns demonstrate relative viability of U-2 OS and L929 cells treated 1-day with extracts (extracted in DMEM for 1-day) of the Zn–0.8 Mg and WE43 alloys in DMEM + 5% FBS. The results are related to the viability of the cells incubated in DMEM + 5% FBS, which was used as a negative control. Dashed line stands for the cut-off between non-toxic and toxic responses. Error bars represent sample standard deviation.

thickness of corrosion products, results contained only small signs of MgO and ZnO on the surface and spectra were predominantly occupied by the peaks of matrix element and observed intermetallic phases.

3.4. Cytotoxicity of salt solutions

Firstly, we tested cytotoxicity of various concentrations of zinc on U-2 OS and L929 cell line to predict in vitro toxicity of extracts of alloys. Generally it is necessary to prepare the extracts to get information which Zn concentration can be reached during corrosion process. It is also clear that other agents (increased pH, the formation of toxic products in the corrosion medium, oxidative stress) can be critical to decreased cell viability. However; the purpose of these tests was to confirm if the behavior of cells in prepared solutions will be similar at the same concentrations of Zn ions to the behavior in prepared extracts, and therefore, if such arrangement can serve as a simple possible testing method for approximate determination of cytotoxicity. In Fig. 6 the cytotoxicity is depicted as a decrease in metabolic activity evaluated by WST-1 test compared with negative control (sole cultivation medium). There seems to be a rather sharp transition from non-toxic to toxic concentrations, 120 μM and 80 μM concentrations being the highest safe concentrations, for U-2 OS and L929 cell line, respectively. The results of cytotoxicity testing always depend on the cell line and the experimental setup. Despite this, our observations are in a good agreement with other toxicology studies performed with various cell lines [37, 55], see Table 4. They also show that L929 are more responsive than U-2 OS and therefore are a good model for cytotoxicity testing.

Table 5

Concentrations of Zn and Mg ions in extracts of the Zn–0.8 Mg alloys (1-day extracts in DMEM or MEM with 5% FBS) measured by ICP-MS.

Element	Concentration in $\mu\text{mol/l}$	
	DMEM	MEM
Zn	184	176
Mg	1020	868

3.5. Cytotoxicity of alloy extracts

We tested cytotoxicity and genotoxicity of extracts of the Zn–0.8 Mg alloy, see Fig. 7 and Table 5. Commercially available Mg-based alloy WE43 served as a control. As expected, the extracts of the reference WE43 alloy (Table 6) demonstrate no cytotoxicity for the U-2 OS and L929 cells. In contrast, we observe toxic effect upon 1-day treatment of U-2 OS cells with the Zn–0.8 Mg alloy extracts both undiluted and in 75% concentration which correspond to the Zn ion concentrations of 184 μM and 138 μM , respectively (Table 4). On the other hand, the solution of 92 μM Zn obtained by 50% dilution of the original extract reduces the cell viability by less than 20%. It is consistent with the results of the tests with ZnCl_2 solutions which proved the maximum safe Zn concentration of 120 μM (Fig. 6). Therefore, the approach of simulating alloy extracts with ZnCl_2 salt solutions seems to be a valuable tool for assessing the toxicity of degradation products of the Zn-based alloys. Fig. 7 also indicates that the L929 cells are more sensitive to Zn than the U-2 OS cell line, since its viability decreases during 1-day incubation with any of the tested concentrations except the 25% extract (44 μM Zn). Cheng [28] observed a toxic effect when using the extract of Zn on L929 at a concentration of 15 μM . This discrepancy is probably caused by the fact, that the authors used an extraction medium without FBS. Cells cultivated completely without FBS can be more sensitive to tested substances.

Unfortunately, a direct comparison with other research papers is complicated. Gong et al. [26] did not measure the concentrations of ions in extracts. In another papers [27,41] authors dealt with cytotoxicity measurements but they did not postulate concentrations of ions in

Table 6

Concentrations of Mg and RE ions in extracts of the WE43 alloy (1-day extracts in DMEM or MEM with 5% FBS) measured by ICP-MS.

Element	Concentration in $\mu\text{mol/l}$	
	DMEM	MEM
Mg	7653	6830
Y	1830×10^{-3}	540×10^{-3}
Dy	80×10^{-3}	20×10^{-3}
Gd	90×10^{-3}	30×10^{-3}
Nd	450×10^{-3}	110×10^{-3}

Table 7

Number of revertant colonies after the Ames test and the ratio of the sample to the positive control. The ratio of revertant colonies greater than 3 is considered as the cut-off.

	TA 98		TA 100	
	Average number of revertants	Ratio of sample to control	Average number of revertants	Ratio of sample to control
Negative control	9.5 ± 0.7	1	100.7 ± 13.3	1
Zn–0.8 Mg	17.3 ± 2.1	1.8 ± 0.3	119.3 ± 37.9	1.2 ± 0.5
WE43	8.7 ± 5.5	0.9 ± 0.5	91.7 ± 17.5	0.9 ± 0.1
Positive control	180.0	18.9	1600.0	15.9

extracts. In all cases, they only revealed the amount of the powder of the alloy which was used to prepare extracts but there was no evidence as to what amount of the powder was really dissolved during incubation. Murni et al. [40] postulated the concentration of Zn ions as 0.49 ppm, which corresponds approximately to the amount of dissolved Zn equal to 8 µmol/l. This concentration caused a toxic effect on cells after 1-day incubation. However, based on our results, such low amount of zinc ions should not cause a toxic effect. There can be two explanations. Firstly, the cells which were used in the present study and in the work by Murni et al. [40] were different. Secondly, we performed extraction in the culture cell medium with FBS (fetal bovine serum) but Murni et al. [40] performed extractions only in the solution containing a culture cell medium. As a consequence, during subsequent tests of cytotoxicity, FBS can in our case partially mask toxic effect, and therefore, a higher accepted concentration of Zn is estimated.

A question remains whether the cytotoxic concentrations of the above 44 µM (good viability of L929 cells) are achievable or not in the vicinity of the implant when applied in situ. According to the recent in vivo study on zinc biocompatibility reported by Bowen et al. [19], bio-corrosion products of zinc contain, apart from Zn, mainly O, C and P, therefore, zinc oxide, hydroxide, carbonate and phosphate compounds can be expected to dominate. Assuming that these compounds cover the entire surface of the alloy, the local Zn concentration in the surrounding fluid can be roughly estimated from the solubility product constants (K_{SP}) of these compounds. The K_{SP} values for ZnO, Zn(OH)₂, ZnCO₃ and Zn₃(PO₄)₂ are $4 \cdot 10^{-10}$, $5 \cdot 10^{-17}$, $2 \cdot 10^{-10}$ and $9 \cdot 10^{-33}$, respectively [7]. Resulting local Zn concentration of approximately 20 µM is still lower than the safe limits given above. This may be the reason why the Bowen's study showed a good adherence of the tissue to the corroded zinc surface [19].

3.6. Genotoxicity and mutagenicity of alloy's extracts

Genotoxicity and mutagenicity were tested using the Ames test and the comet assay as described in the Materials and methods section.

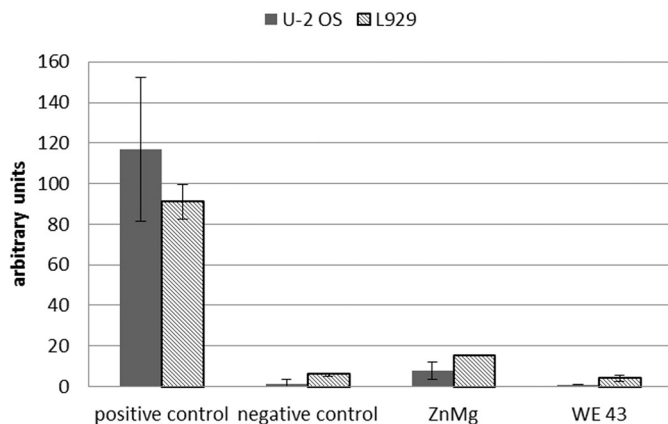


Fig. 8. Genotoxic effect of extracts of alloys on U-2 OS and L929 cells. The degree of DNA damage (single- and double-strand breaks) was depicted using arbitrary units (0 = no damage, 200 = 100% damage). Average values were calculated from three independent measurements. Error bars represent sample standard deviation.

Ames test was performed with 1-day extracts of alloys and *S. typhimurium* strains TA 98 and TA 100 were used without metabolic activation. Table 7 shows the number of revertant colonies and the ratio of the sample to the positive control. The ratio of revertants for all samples is below the critical value of 3, indicating that the extracts of tested alloys were not mutagenic. This result was expected, since other published microbial tests concerning mutagenicity of zinc were also negative [56,57].

The comet assay was performed to test the genotoxicity. The data shown in Fig. 8 demonstrate that 1-day extracts of alloys are genotoxic neither for U-2 OS nor L929 cell lines after 1-day incubation. Murni et al. [40] performed Comet assay test on NHOst cells after 1, 3 and 7 days of incubation in extracts from Zn–3 Mg alloy. Although authors used different methods of evaluation of their results compared with the present paper, both results confirmed that the extracts from zinc alloys did not significantly induce DNA fragmentation. On the contrary pure Zn has a serious impact on DNA fragmentation especially after 7 days of incubation [40].

Published data on genotoxicity testing on mammalian systems are heterogeneous. Chromosomal aberrations were observed in vitro in human lymphocytes [58]. On the contrary, no mutagenicity potential of zinc was observed when using L5178YTK^{+/-} mouse lymphoma-TK assay [59]. Nevertheless, it can be concluded from the above cytotoxicity, genotoxicity and mutagenicity tests that the Zn–0.8 Mg alloys could be designated as relatively safe or at least promising for further in vivo biocompatibility testing.

4. Conclusions

Based on the results obtained in this study, the following conclusions can be made:

1. The hot extruded Zn–0.8 Mg alloys possess the best combination of tensile strength (301 MPa) and plasticity (15%) among all the examined Zn-based alloys. These mechanical characteristics meet the general requirements defined for biodegradable implants.
2. The corrosion rates of the Zn–0.8 Mg alloys are significantly lower compared with that of the WE43 alloy. Possible zinc doses caused by the corrosion of fixation implants are far below the toxic doses of zinc for humans. In addition, the low corrosion rates of zinc alloys ensure that the implants maintain a 95%-load-bearing capacity for at least 6 weeks after implantation.
3. The in vitro cytotoxicity tests determined that zinc is less biocompatible than magnesium and the maximum safe concentrations of Zn²⁺ for the U-2 OS and L929 cells are 120 µM and 80 µM, respectively. Genotoxicity and mutagenicity tests did not indicate any negative effects connected with the use of zinc. Hence, zinc appears as a promising biomaterial for designing biodegradable implants.

Acknowledgments

The authors wish to thank the Czech Science Foundation for the financial support of this research (project no. P108/12/G043).

References

- [1] X.-N. Gu, Y.-F. Zheng, A review on magnesium alloys as biodegradable materials, *Front. Mater. Sci. Chin.* 4 (2010) 111–115.
- [2] F. Witte, N. Hort, C. Vogt, S. Cohen, K.U. Kainer, R. Willumeit, F. Feyerabend, Degradable biomaterials based on magnesium corrosion, *Curr. Opin. Solid State Mater. Sci.* 12 (2008) 63–72.
- [3] M. Schinhammer, A.C. Hanzi, J.F. Löffler, P.J. Uggowitzer, Design strategy for biodegradable Fe-based alloys for medical applications, *Acta Biomater.* 6 (2010) 1705–1713.
- [4] D. Persaud-Sharma, A. McGoron, Biodegradable magnesium alloys: a review of material development and applications, *J. Biomimetics Biomater. Tissue Eng.* 12 (2012) 25–39.
- [5] G.E.J. Poinern, S. Brundavanam, D. Fawcett, Biomedical magnesium alloys: a review of material properties, surface modifications and potential as a biodegradable orthopaedic implant, *Am. J. Biomed. Eng.* 2 (2012) 218.
- [6] C.-Y. Zhao, F.-S. Pan, S. Zhao, H.-C. Pan, K. Song, A.-T. Tang, Microstructure, corrosion behavior and cytotoxicity of biodegradable Mg-Sn implant alloys prepared by sub-rapid solidification, *Mat Sci Eng C-Mater* 54 (2015) 245–251.
- [7] Y.F. Zheng, X.N. Gu, F. Witte, Biodegradable metals, *Mater. Sci. Eng. R. Rep.* 77 (2014) 1–34.
- [8] H. Waizy, J.M. Seitz, J. Reifenrath, A. Weizbauer, F.W. Bach, A. Meyer-Lindenberg, B. Denkena, H. Windhagen, Biodegradable magnesium implants for orthopedic applications, *J. Mater. Sci.* 48 (2013) 39–50.
- [9] A. Atrens, M. Liu, N.I. Zainal Abidin, Corrosion mechanism applicable to biodegradable magnesium implants, *Mater. Sci. Eng. B* 176 (2011) 1609–1636.
- [10] X. Gu, Y. Zheng, S. Zhong, T. Xi, J. Wang, W. Wang, Corrosion of, and cellular responses to Mg–Zn–Ca bulk metallic glasses, *Biomaterials* 31 (2010) 1093–1103.
- [11] F. Witte, The history of biodegradable magnesium implants: a review, *Acta Biomater.* 6 (2010) 1680–1692.
- [12] Y. Xin, T. Hu, P.K. Chu, In vitro studies of biomedical magnesium alloys in a simulated physiological environment: a review, *Acta Biomater.* 7 (2011) 1452–1459.
- [13] N. Hort, Y. Huang, D. Fechner, M. Störmer, C. Blawert, F. Witte, C. Vogt, H. Drücker, R. Willumeit, K.U. Kainer, F. Feyerabend, Magnesium alloys as implant materials – principles of property design for Mg–RE alloys, *Acta Biomater.* 6 (2010) 1714–1725.
- [14] Z. Bruno, J.U. Peter, F.L. Jörg, MgZnCa glasses without clinically observable hydrogen evolution for biodegradable implants, *Nat. Mater.* 8 (2009) 887–891.
- [15] M. Moravej, D. Mantovani, Biodegradable metals for cardiovascular stent application: interests and new opportunities, *Int. J. Mol. Sci.* 12 (2011) 4250–4270.
- [16] H. Hermawan, D. Dubé, D. Mantovani, Developments in metallic biodegradable stents, *Acta Biomater.* 6 (2010) 1693–1697.
- [17] B. Wegener, B. Sievers, S. Utzschneider, P. Müller, V. Jansson, S. Rossler, B. Nies, G. Stephani, B. Kieback, P. Quadbeck, Microstructure, cytotoxicity and corrosion of powder–metallurgical iron alloys for biodegradable bone replacement materials, *Mater. Sci. Eng. B Adv.* 176 (2011) 1789–1796.
- [18] S. Zhang, X. Zhang, C. Zhao, J. Li, Y. Song, C. Xie, H. Tao, Y. Zhang, Y. He, Y. Jiang, Y. Bian, Research on an Mg–Zn alloy as a degradable biomaterial, *Acta Biomater.* 6 (2010) 626–640.
- [19] P.K. Bowen, J. Drelich, J. Goldman, Zinc exhibits ideal physiological corrosion behavior for bioabsorbable stents, *Adv. Mater.* 25 (2013) 2577–2582.
- [20] G.J. Fosmire, Zinc toxicity, *Am. J. Clin. Nutr.* 51 (1990) 225–227.
- [21] C.J. Smithells, W.F. Gale, T.C. Totemeier, *Smithells Metals Reference Book*, 8th ed. Elsevier Butterworth-Heinemann, Amsterdam, 2004.
- [22] D. Vojtech, J. Kubasek, J. Serak, P. Novak, Mechanical and corrosion properties of newly developed biodegradable Zn-based alloys for bone fixation, *Acta Biomater.* 7 (2011) 3515–3522.
- [23] J. Kubasek, D. Vojtech, L.T.D. Tanger, *Zn-based Alloys as an Alternative Biodegradable Materials*, Tanger Ltd, Slezska, 2012.
- [24] J. Kubasek, I. Pospíšilová, D. Vojtěch, E. Jablonská, T. Ruml, Structural, mechanical and cytotoxicity characterization of as-cast biodegradable Zn–xMg (x = 0.8–8.3 wt.%) alloys, *Mater. Tehnol.* 48 (2014) 623–629.
- [25] M. Yu, C. George, Y.N. Cao, D. Wootton, J. Zhou, Microstructure, corrosion, and mechanical properties of compression-molded zinc-nanodiamond composites, *J. Mater. Sci.* 49 (2014) 3629–3641.
- [26] H. Gong, K. Wang, R. Strich, J.G. Zhou, In vitro biodegradation behavior, mechanical properties, and cytotoxicity of biodegradable Zn–Mg alloy, *J. Biomed. Mater. Res. B Appl. Biomater.* (2015), <http://dx.doi.org/10.1002/jbm.b.33341> (n/a–n/a).
- [27] H.F. Li, X.H. Xie, Y.F. Zheng, Y. Cong, F.Y. Zhou, K.J. Qiu, X. Wang, S.H. Chen, L. Huang, L. Tian, L. Qin, Development of biodegradable Zn–1X binary alloys with nutrient alloying elements Mg, Ca and Sr, *Sci. Rep.* 5 (2015) 10719.
- [28] J. Cheng, B. Liu, Y.H. Wu, Y.F. Zheng, Comparative in vitro study on pure metals (Fe, Mn, Mg, Zn and W) as biodegradable metals, *J. Mater. Sci. Technol.* 29 (2013) 619–627.
- [29] I.O.f. Standardization, ISO 10993-1. Biological evaluation of medical devices. Part 1, Evaluation and testing within a risk management process, Geneva, Switzerland 2009, p. 21.
- [30] B.D. Ratner, A.S. Hoffman, F.J. Schoen, J.E. Lemons, *Biomaterials Science: An Introduction to Materials in Medicine*, Elsevier Science, 2004.
- [31] G. Lawton, D.R. Witty, Progress in medicinal chemistry preface, *Prog. Med. Chem.* 52 (2013) V–Vii.
- [32] K. Mortelmans, E. Zeiger, The Ames *Salmonella*/microsome mutagenicity assay, *Mutat. Res. Fundam. Mol. Mech. Mutagen.* 455 (2000) 29–60.
- [33] S.A. Wexler, C. Donaldson, P. Denning-Kendall, C. Rice, B. Bradley, J.M. Hows, Adult bone marrow is a rich source of human mesenchymal 'stem' cells but umbilical cord and mobilized adult blood are not, *Brit. J. Haematol.* 121 (2003) 368–374.
- [34] I. Catacchio, S. Berardi, A. Reale, A. De Luisi, V. Racanelli, A. Vacca, R. Ria, Evidence for bone marrow adult stem cell plasticity: properties, molecular mechanisms, negative aspects, and clinical applications of hematopoietic and mesenchymal stem cells transdifferentiation, *Stem Cells Int.* (2013), <http://dx.doi.org/10.1155/2013/589139> (Unsp 589139).
- [35] I.O.f. Standardization, ISO 10993-3. Biological evaluation of medical devices. Part 3, Tests for genotoxicity, carcinogenicity and reproductive toxicity, Geneva, Switzerland 2003, p. 16.
- [36] OECD, Test No. 471: Bacterial Reverse Mutation Test, OECD Publishing, Paris, 1997, <http://dx.doi.org/10.1787/9789264071247-en>.
- [37] J. Wu, L. Wang, J. He, C. Zhu, In vitro cytotoxicity of Cu(2)(+), Zn(2)(+), Ag(+) and their mixtures on primary human endometrial epithelial cells, *Contraception* 85 (2012) 509–518.
- [38] M.H. Yoo, J.Y. Lee, S.E. Lee, J.Y. Koh, Y.H. Yoon, Protection by pyruvate of rat retinal cells against zinc toxicity in vitro, and pressure-induced ischemia in vivo, *Invest. Ophthalmol. Vis. Sci.* 45 (2004) 1523–1530.
- [39] V. Rodilla, A.T. Miles, W. Jenner, G.M. Hawksworth, Exposure of cultured human proximal tubular cells to cadmium, mercury, zinc and bismuth: toxicity and metallothionein induction, *Chem. Biol. Interact.* 115 (1998) 71–83.
- [40] N.S. Murni, M.S. Dambatta, S.K. Yeap, G.R.A. Froemming, H. Hermawan, Cytotoxicity evaluation of biodegradable Zn–3 Mg alloy toward normal human osteoblast cells, *Mater. Sci. Eng. C* 49 (2015) 560–566.
- [41] M. Dambatta, N. Murni, S. Izman, D. Kurniawan, G. Froemming, H. Hermawan, In vitro degradation and cell viability assessment of Zn–3 Mg alloy for biodegradable bone implants, *Proc. Inst. Mech. Eng. H J. Eng. Med.* 229 (2015) 335–342.
- [42] I.O.f. Standardization, ISO 10993-5. Biological evaluation of medical devices. Part 5, Tests for in vitro cytotoxicity, Geneva, Switzerland 2009, p. 34.
- [43] M.V. Berridge, P.M. Herst, A.S. Tan, Tetrazolium dyes as tools in cell biology: new insights into their cellular reduction, in: M.R. El-Gewely (Ed.), *Biotechnology Annual Review*, Elsevier 2005, pp. 127–152.
- [44] E. Zeiger, K.J. Risko, B.H. Margolin, Strategies to reduce the cost of mutagenicity screening with the *Salmonella* assay, *Environ. Mutagen.* 7 (1985) 901–911.
- [45] A.R. Collins, The comet assay for DNA damage and repair – principles, applications, and limitations, *Mol. Biotechnol.* 26 (2004) 249–261.
- [46] P.L. Olive, J.P. Banath, The comet assay: a method to measure DNA damage in individual cells, *Nat. Protoc.* 1 (2006) 23–29.
- [47] K. Konca, A. Lankoff, A. Banasik, H. Lisowska, T. Kuszewski, S. Gozdz, Z. Koza, A. Wojcik, A cross-platform public domain PC image-analysis program for the comet assay, *Mutat. Res. Genet. Toxicol. Environ.* 534 (2003) 15–20.
- [48] E.I. Cortes-Gutierrez, F. Hernandez-Garza, J.O. Garcia-Perez, M.I. Davila-Rodriguez, M.E. Aguado-Barrera, R.M. Cerda-Flores, Evaluation of DNA single and double strand breaks in women with cervical neoplasia based on alkaline and neutral comet assay techniques, *J. Biomed. Biotechnol.* (2012), <http://dx.doi.org/10.1155/2012/385245>.
- [49] J. Kubasek, D. Vojtech, M. Martinek, Structural characteristics and elevated temperature mechanical properties of AJ62 Mg alloy, *Mater. Charact.* 86 (2013) 270–282.
- [50] A.S.M., International Handbook Committee, *ASM Handbook, Volume 02 – Properties and Selection: Nonferrous Alloys and Special-purpose Materials*, ASM International, 1990.
- [51] J.R. Davis, *Handbook of Materials for Medical Devices*, ASM International, 2003.
- [52] D.A. Jones, *Principles and Prevention of Corrosion*, Prentice Hall, 1996.
- [53] D.E.J. Talbot, J.D.R. Talbot, *Corrosion Science and Technology*, CRC Press, 2007.
- [54] C. Yao, Z. Wang, S.L. Tay, T. Zhu, W. Gao, Effects of Mg on microstructure and corrosion properties of Zn–Mg alloy, *J. Alloys Compd.* 602 (2014) 101–107.
- [55] S. Pavlica, F. Gaunitz, R. Gebhardt, Comparative in vitro toxicity of seven zinc–salts towards neuronal PC12 cells, *Toxicol. in Vitro* 23 (2009) 653–659.
- [56] P.K. Wong, Mutagenicity of heavy metals, *Bull. Environ. Contam. Toxicol.* 40 (1988) 597–603.
- [57] H. Nishioka, Mutagenic activities of metal compounds in bacteria, *Mutat. Res.* 31 (1975) 185–189.
- [58] G. Deknudt, M. Deminatti, Chromosome studies in human lymphocytes after in vitro exposure to metal salts, *Toxicology* 10 (1978) 67–75.
- [59] D.E. Amacher, S.C. Paillet, Induction of trifluorothymidine-resistant mutants by metal ions in L5178Y/TK^{+/–} cells, *Mutat. Res.* 78 (1980) 279–288.

Příloha 9



Influence of surface pre-treatment on the cytocompatibility of a novel biodegradable ZnMg alloy



Eva Jablonská^{a,*}, Dalibor Vojtěch^b, Michaela Fousová^b, Jiří Kubásek^b, Jan Lipov^a, Jaroslav Fojt^b, Tomáš Ruml^a

^a Department of Biochemistry and Microbiology, University of Chemistry and Technology, Prague, Technická 5, 166 28 Prague 6, Czech Republic

^b Department of Metals and Corrosion Engineering, University of Chemistry and Technology, Prague, Technická 5, 166 28 Prague 6, Czech Republic

ARTICLE INFO

Article history:

Received 12 February 2016

Received in revised form 28 April 2016

Accepted 24 May 2016

Available online 26 May 2016

Keywords:

Biodegradable alloys

Zinc

In vitro testing

Cytocompatibility

ABSTRACT

Degradable zinc-based alloys with an appropriate corrosion rate are promising materials for the preparation of temporary orthopaedic implants. Previously, we prepared and characterised a novel Zn1.5Mg alloy. This paper is focused on the characterisation of this alloy after a surface pre-treatment, which should mimic processes occurring *in vivo*.

The samples of the Zn1.5Mg alloy were immersed in a simulated body fluid (SBF) at 37 °C for 14 days in order to form a protective layer of corrosion products. Thereafter, these samples were used for the corrosion rate determination, an indirect *in vitro* cytotoxicity test, as well as for a direct contact test and were compared with the non-treated samples. The protective layer was characterized by SEM and its chemical composition was determined by EDS and XPS analysis.

The corrosion rate was significantly decreased after the pre-incubation. The protective layer of corrosion products was rich in Ca and P. The pre-incubated samples exhibited increased cytocompatibility in the indirect test (metabolic activity of L929 cells was above 70%) and we also observed osteoblast-like cell growth directly on the samples during the contact tests. Thus, the pre-incubation in SBF leading to improved cytocompatibility could represent more appropriate model to *in vivo* testing.

© 2016 Elsevier B.V. All rights reserved.

1. Introduction

Degradable metallic biomaterials for temporary load-bearing orthopaedic applications have been attracting great attention (reviewed in [1]). Compared to non-biodegradable metals, there is the obvious advantage of no need for a reoperation since the temporary implants (usually in the form of screws, plates or pins) are fully degraded after they fulfil their mission to assist bone tissue healing. When designing biodegradable materials for load-bearing applications, factors such as mechanical properties, corrosion rate and cytocompatibility/toxicity must be taken into account. In this regard, better mechanical strength is the main advantage of biodegradable metals over the thus-far used biodegradable polymers [1].

The most extensively studied degradable metallic biomaterials are based mainly on magnesium (reviewed in [2]), iron (reviewed in [3]) and zinc. Magnesium is a biogenic element, which is easily excreted from the body and is even considered to be osteogenic [4–6]. However, the corrosion rate of Mg-based materials is usually too high, which leads to the premature loss of implant integrity. Moreover, the corrosion mechanism involves pH increase and hydrogen evolution, the latter leading to the gaseous hydrogen accumulation and gas pocket formation

around the implant. These unwanted events subsequently impair the healing process [7]. Fe-based materials have been also studied, but conversely, their corrosion rate is much lower than desired [8,9]. Therefore, there is an effort to develop metallic materials without the aforementioned drawbacks. In this regard, zinc-based materials seem to be promising candidates in the field of biodegradable metals.

The corrosion rate of Zn is lower than the one of Mg [10–12]. Moreover corrosion of Zn is accompanied by oxygen depolarization reaction and, therefore, problems with hydrogen are precluded. Similar to magnesium, zinc is in small amounts also an essential nutrient in human body, where it influences various processes for example by enabling the function of numerous metalloenzymes, transcription factors and other proteins [13]. The recommended dietary allowances (RDAs) for zinc are 0.16, resp. 0.13 mg/kg/day, which means approximately 11, resp. 8 mg/day, for men and women, respectively. An amount of 0.3 mg zinc/kg/day was determined as a minimal risk level (MRL) for intermediate-duration exposure (15–364 days). The levels of zinc that produce adverse health effects are 1.6–2.4 mg/kg/day. Normally, zinc does not accumulate in the body and is excreted *via* urine and faeces [14], which is its another advantage over iron.

The first step towards development of zinc biomaterials was done in 2009 by Zberg et al. [15] who prepared Zn-rich (up to 35 at.%) MgZnCa glass with high corrosion resistance and high mechanical strength and observed no inflammation or hydrogen evolution *in vivo*. However,

* Corresponding author.

E-mail address: eva.jablonska@vscht.cz (E. Jablonská).

complicated preparation of metallic glasses, limited final product thickness and requirements for mechanical homogeneity [11] hinder the manufacturing of the final implant. Bowen et al. performed a long term examination of the corrosion behaviour of pure zinc intended for cardiovascular applications. They observed no necrosis in the aorta of rats at the tissue-implant interface and found zinc corrosion parameters to be optimal in terms of the rate and corrosion layers formed [11].

Nevertheless, pure Zn is soft, brittle and has insufficient mechanical strength for load-bearing applications and, therefore, must be alloyed with other, preferably also biogenic, elements. To our best knowledge, our group was first to report structural, mechanical and corrosion studies on conventionally prepared biodegradable Zn-based alloys [12]. Testing of cast and extruded ZnMg alloys containing up to 3 wt.% of Mg showed that optimal mechanical properties were achieved at Mg contents of approximately 1 wt.%. The corrosion rates of the ZnMg alloys were significantly lower than those of Mg alloys. Subsequently, the Zn1.5Mg alloy was tested using extracts in the *in vitro* indirect test. Cytotoxicity of the extracts was found to be dependent on the amount of Zn released [16].

Meanwhile, cast and hot extruded Zn1Mg [17], Zn1Mg, Zn1Ca and Zn1Sr alloys [18] and a cast Zn3Mg alloy [19] were prepared and studied by other research groups. The authors observed diverse cytocompatibility; however, data comparison is difficult since various methods of *in vitro* testing were used (fifteen-fold dilution of the extracts before the indirect test, preparation of the extracts from the powdered alloy) and concentrations of released ions are often not shown [17–19]. Impaired cell morphology of rodent vascular smooth muscle cells (VSCM) seeded directly onto the Zn alloys was observed [18] as well as a cytotoxic effect towards human osteoblasts of the alloy extracts at day 1 [19]. On the other hand, human cells derived from osteosarcoma (MG63 cells) and human urinary bladder carcinoma cell line EC304 on Zn alloys exhibited a healthy morphology [18].

From all of the above mentioned, it can be assumed that zinc-based alloys show good mechanical properties and that their corrosion rate is usually low enough resulting in zinc concentrations even below the RDA limit and, therefore, causing no systemic toxicity *in vivo* [18]. On the other hand, the *in vitro* cytocompatibility data are inconsistent and it appears that the corrosion rate may lead to local Zn concentrations higher than desirable. This discrepancy between the *in vivo* and *in vitro* results is influenced by different corrosion behaviour of Zn alloys in a tissue culture plate and in the body. It was found that corrosion rate of degradable magnesium alloys *in vivo* is 1–5 times lower than *in vitro* [20]. Presuming similar problem for zinc-based alloys, our aim was to perform *in vitro* tests that would closer mimic the situation *in vivo*.

In our work, we focused on the surface pre-treatment of the Zn1.5Mg alloy and its influence on the corrosion rate and characterisation of the corrosion layer. We presume that *in vivo*, body fluids support development of the corrosion layer concurrently or before cell attachment. Therefore, we used pre-incubation in simulated body fluid (SBF) to mimic the initial moments after implantation and showed that the corrosion protective layer had a positive effect on initial corrosion resistance and cell adhesion.

2. Material and methods

2.1. Sample preparation

Zn1.5Mg alloy was prepared as described previously [16]. Briefly, pure Zn (99.99 wt.%) and Mg (99.99 wt.%) were melted in an electric resistance furnace under air atmosphere. After sufficient homogenization, the melted alloy was gravity cast to prepare cylindrical ingots of 20 mm in diameter which were subsequently hot extruded at 300 °C in a hydraulic press at an extrusion ratio and rate of 10:1 and 2 mm min⁻¹, respectively, to produce rods of 6 mm in diameter.

2.2. Sample cleaning, sterilisation and treatment

Cylindrical samples (5 mm in diameter and 12 or 3 mm in height) of Zn1.5Mg alloy were grinded (SiC paper, up to P4000), cleaned and sterilised by immersing into 70% ethanol (2 h) and by subsequent UV exposition (2 h). Thereafter, samples were either stored in closed vessels as a control until the tests or submerged into SBF prepared according to Müller et al. [21] (composition given in Table 1) for two weeks in order to create a protective corrosion layer. Surface to volume ratio was 80 mm² ml⁻¹. Both types of samples (pre-incubated and untreated) were further compared in terms of surface composition, corrosion rate and cytocompatibility.

2.3. Analysis of the surface

The chemical composition and surface morphology of the untreated and pre-incubated samples were analysed by scanning electron microscopy (SEM, Tescan Vega 3) equipped with energy dispersion spectrometer (EDS, Oxford Instruments Inca 350).

For more accurate quantitative evaluation of chemical composition of the formed corrosion layer and determination of binding status, the surface of the samples was studied using a XPS spectrometer ESCAprobe P (Omicron Nanotechnology Ltd.) equipped with Al K α ($\lambda = 1486.7$ eV) X-ray source. The spectra were measured with an energy step of 0.05 eV and normalized to the binding energy of C1s peak (285.0 eV). The samples were thoroughly washed with distilled water, ethanol and acetone before entering the spectroscope. The data for the chemical state evaluation were obtained from the NIST X-ray Photoelectron Spectroscopy Database.

2.4. Preparation of the extracts

Untreated and pre-incubated samples (5 mm in diameter and 12 mm in height) prepared as described in 2.2 were transferred to MEM cultivation medium with 5% foetal bovine serum (FBS) and agitated (130 RPM) at 37 °C in closed vessels for 24 h. The surface to volume ratio was 87.5 cm ml⁻¹ for all samples. The extracts were further used for indirect *in vitro* cytotoxicity tests and for corrosion rate determination.

2.5. Corrosion rate determination

The extracts were analysed by ICP-MS (Perkin Elmer Elan 6000 spectrometer, three measurements for each sample). Prior to the measurement, ultrapure HNO₃ was added to the extracts in order to dissolve solid corrosion products. Corrosion rate was expressed in mg cm⁻² day⁻¹ and was calculated from released ions using Eq. (1)

$$\text{corrosion rate} = \frac{m}{S \times t} \quad (1)$$

where m is mass of released Zn in mg, S is surface of the samples in cm² and t is time of the incubation in days. Three samples of each type were used for each procedure.

Corrosion rate was determined only for comparison between the untreated and pre-incubated samples. Determination was done in

Table 1
Ion composition of SBF according to Müller et al. [21].

Ion concentration (mmol dm ⁻³)							
K ⁺	Na ⁺	Ca ²⁺	Mg ²⁺	Cl ⁻	HCO ₃ ⁻	H ₂ PO ₄ ⁻	SO ₄ ²⁻
5.0	142.4	2.5	1.0	109.0	27.0	1.0	1.0

cultivation medium after 24 h exposition. However, for accurate corrosion rate value, longer exposition time would be necessary.

2.6. Indirect *in vitro* cytotoxicity test

Indirect *in vitro* cytotoxicity tests were performed according to ISO 10993-5 standard [22]. Murine fibroblasts L929 (ATCC® CCL-1™) were seeded into 96-well plate in a density of $1 \cdot 10^4$ cells per well one day prior to the test and were cultured at standard conditions in MEM + 10% FBS. After one day, the medium was replaced by the centrifuged ($1500 \times g$, 5 min, RT) extracts prepared as described in Section 2.4. Undiluted (100%) and diluted (50%) extracts were used. Sole MEM + 5% FBS served as a control. After one day of incubation with the extracts, cell metabolic activity was evaluated using WST-1 assay. Cells were washed by PBS and 5% WST-1 (Roche) in MEM was added. After 2.5 h of incubation, absorbance at 450 nm was measured. Measurements were done in six replicates for each sample. Cytotoxicity of the extracts was depicted as a percentage of metabolic activity of the control. Extracts causing the decrease below 70% of the activity of the control were considered cytotoxic, as described in the ISO standard.

2.7. Contact *in vitro* cytocompatibility tests

Both untreated and pre-incubated samples (5 mm in diameter and 3 mm in height) prepared as described in Sections 2.1 and 2.2 were placed in six-well plates. Human osteosarcoma cells U-2 OS (ATCC® HTB-96™) were resuspended in DMEM supplemented with 10% FBS and seeded directly onto the samples. The seeding density was $24,000 \text{ cells cm}^{-2}$. Human osteosarcoma cells U-2 OS were used instead of L929 cells due to their closer resemblance to osteoblasts.

After 24 h, the medium was removed and used for corrosion rate determination described in Section 2.5 and the samples (four samples of each type) were rinsed with PBS and fixed with 4% formaldehyde for 20 min at RT. Thereafter, nuclei were stained with DAPI and samples were observed using Olympus AX70 Provis fluorescence microscope. 20 fields of view at magnification of $100\times$ were taken for each sample. Number of nuclei was determined using ImageJ software.

After 24 h, samples (one sample of each type) were also fixed for electron microscopy as described previously [23]. Samples were rinsed with PBS and fixed with Karnovsky's fixative (2% formaldehyde, 2.5% glutaraldehyde and 2.5% sucrose in 0.2 M cacodylate buffer) for 1.5 h. Samples were then rinsed with 0.1 M cacodylate buffer and dehydrated in series of ethanol (50%, 70%, 80% and 100%). Finally, samples were covered with hexamethyldisilazane followed by drying at 45°C for 4 h. Before SEM analysis, samples were sputter coated with gold (2 nm thick layer).

2.8. Statistical analysis

The results from corrosion studies and both indirect and contact tests obtained with untreated and pre-incubated samples were compared using Two Sample *t*-test in R software. *p*-Value > 0.05 was considered significant.

3. Results

3.1. Surface analysis of Zn1.5Mg alloy

The surface composition of Zn1.5Mg alloy before and after pre-treatment in SBF for 14 days was examined using XPS (Fig. 1). P and Ca were detected on the pre-incubated sample and their binding energies clearly indicate that the surface was covered by a phosphate layer (Table 2). A small peak representing calcium was also found in the spectrum of the untreated sample. This is probably caused by the contamination of zinc by Ca. In binding energy region up to 100 eV

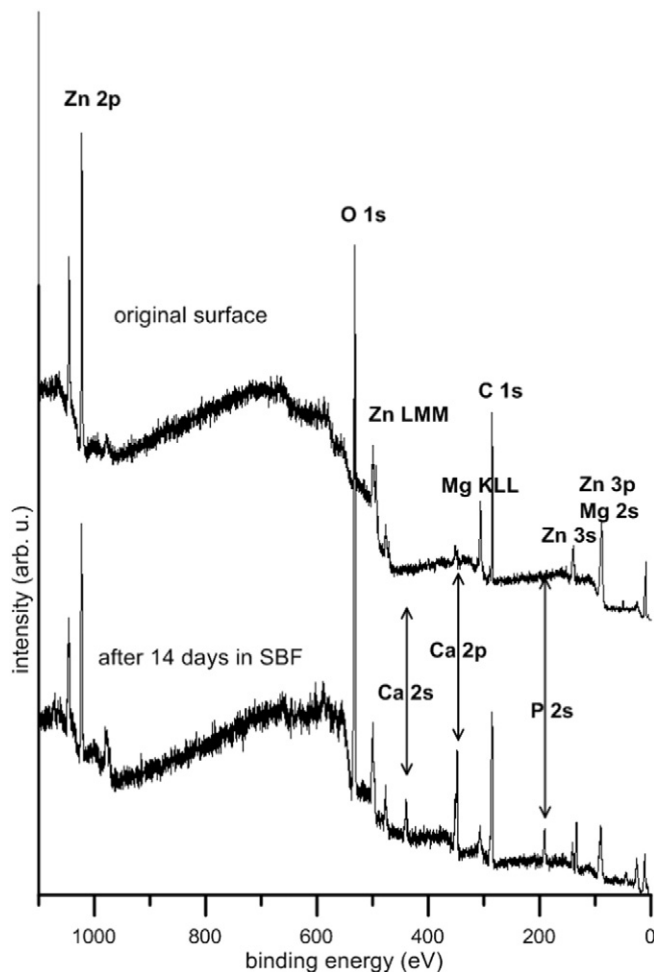


Fig. 1. XPS spectrum for untreated and pre-incubated sample.

Zn, Mg, P and Ca peaks were not labelled in the figure. The binding energy of the carbon peaks corresponded only to adventitious carbon contamination and no peaks are related to carbonates. On the preincubated sample, zinc and magnesium were only detected in the form of oxides or hydroxides. Because the analysis did not reveal any of these metals in their elemental state, it can be assumed that the layer of corrosion products is thicker than 10 nm, which is the maximal resolution depth of the XPS analysis.

Table 2
Binding energies of elements detected by XPS.

Peak	Untreated surface		Pre-incubated surface	
	B.E. (eV)		B.E. (eV)	
Zn 2p _{3/2}	1020.6	Zn	–	–
	1022.2	ZnO	1022.4	ZnO
–	–	1023.9	Zn(OH) ₂	
Mg 2p _{3/2}	50.1	Mg/MgO	–	–
Mg	–	–	50.9	MgO
Ca 2p _{3/2}	–	–	347.6	Ca ²⁺ in Ca ₃ (PO ₄) ₂
P 2p _{3/2}	–	–	133.6	PO ₄ ³⁻

Table 3
Surface chemical composition determined by XPS analysis (C not included).

Sample	Element (wt.%)				
	Zn	Mg	O	Ca	P
Untreated	22.4	31.1	44.7	1.8	0
Pre-incubated	7.4	4.0	39.1	21.6	27.9

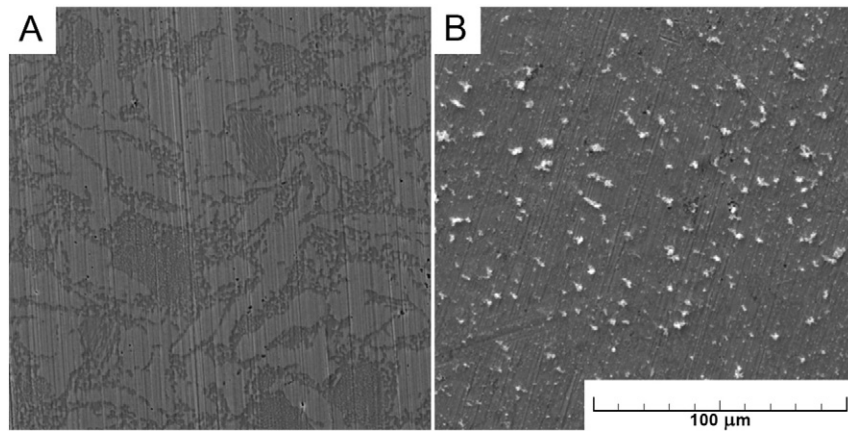


Fig. 2. Surface morphology A) before and B) after pre-incubation in SBF.

The quantification of the surface composition (Table 3, contaminating carbon is not included in the analysis) showed a relatively high amount of oxygen even in the case of the untreated sample. According to the binding energies (Table 2), oxygen corresponds to oxides of the constituting metal elements, which is connected with surface oxidation.

The surface morphology of Zn1.5Mg, before and after pre-treatment in SBF, was also examined using SEM (Fig. 2). After pre-incubation, it was possible to distinguish only small flaky precipitates composed of Ca, P and O, as can be seen in EDS map in Fig. 3. In agreement with XPS analysis, it can be concluded that these are calcium phosphates. Continuous layer of corrosion products (Fig. 2B) is not visible, probably because it is very thin to be detected by EDS. Nevertheless, point analysis (Table 4) indicated that the calcium phosphates are not present only within flaky particles but are forming the layer covering the entire surface. However, it must be noted that quantitative evaluation is not very accurate due to the both EDS resolution (the quantitative results are strongly affected by surroundings of measured points) and also the participation of O in analysis.

3.2. Corrosion rate

The corrosion rates of the pre-incubated and untreated Zn1.5Mg alloys were calculated from the ions released in extracts after one day of incubation at 37 °C after indirect (closed vessels) and also after contact tests (CO₂ atmosphere, decreased surface-to-volume ratio). Under both conditions, the corrosion rates of the pre-incubated samples were significantly lower than those of the untreated control (Fig. 4). After the pre-incubation of the samples in SBF, the corrosion rate determined in the CO₂ atmosphere was $0.019 \pm 0.011 \text{ mg cm}^{-2} \text{ day}^{-1}$ compared to $0.052 \pm 0.010 \text{ mg cm}^{-2} \text{ day}^{-1}$ for the untreated control, which is 2.7 fold deceleration. Without the CO₂ atmosphere, the deceleration of the corrosion rate of the pre-incubated samples was even more pronounced ($0.004 \pm 0.002 \text{ mg cm}^{-2} \text{ day}^{-1}$ compared to $0.012 \pm 0.001 \text{ mg cm}^{-2} \text{ day}^{-1}$ for untreated control, which is threefold reduction). Higher corrosion rate in the presence of CO₂ was also observed in the case of pure zinc [24]. The difference could be also ascribed to the changed surface-to-volume ratio. pH values were also measured but changes in both cases were negligible compared to the sole medium. We are aware of

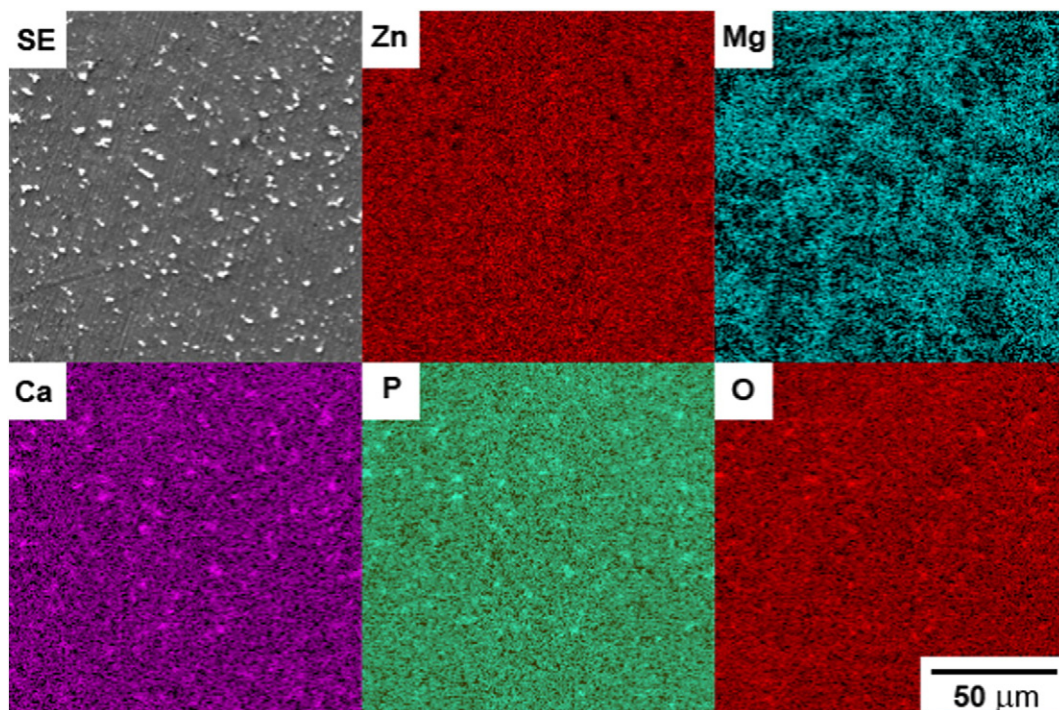


Fig. 3. EDS maps of pre-incubated Zn1.5Mg sample with formed layer of corrosion products.

Table 4
EDS analysis of the surface after pre-incubation in SBF.

Spectrum	O	Mg	P	Ca	Zn	Total
1 Surface	3.89	1.26	0.91	0.81	93.13	100
2 Surface	4.74	1.37	0.55	0.55	92.78	100
3 Surface	2.2	0.51	0.46	0.43	96.4	100
4 Surface	3.44	2.52	0.47	0.47	93.09	100
5 Surface	3.86	0.53	1.02	1.24	93.35	100
6 Flaky particle	3.45	1	1.53	1.66	92.37	100
7 Flaky particle	7.12	0.26	2.1	2.62	87.9	100
8 Flaky particle	18.29	0.9	16.19	16.44	48.18	100

the fact that the corrosion rate (CR) determination from the released ions can be affected by the corrosion products attached on the sample; however, the determination of CR from the mass loss was not possible due to the fact that we compared untreated and pre-incubated samples and after removal of the corrosion layer the results would not be comparable. We were also interested in the ion release with respect to the situation in the body.

3.3. Indirect *in vitro* cytotoxicity test

The indirect *in vitro* cytotoxicity test with a mouse fibroblast L929 cell line performed according to the ISO 10993-5 standard [22] clearly showed that Zn1.5Mg pre-incubation in SBF led to enhanced cytocompatibility of the alloy (Fig. 5). The extracts prepared from

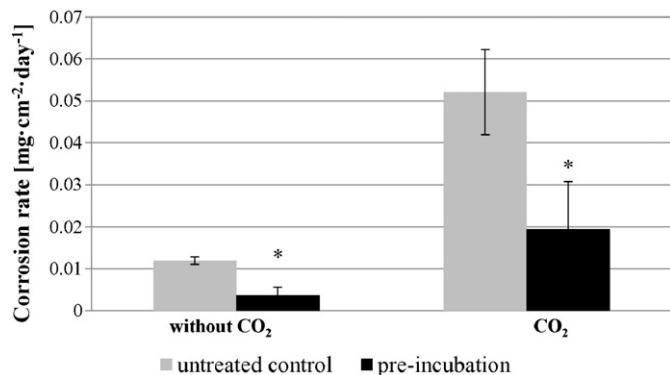


Fig. 4. Corrosion rate of the Zn1.5Mg alloy in cultivation media (MEM/DMEM) calculated from released ions: error bars represent SSD from three replicates; asterisk stands for $p > 0.05$.

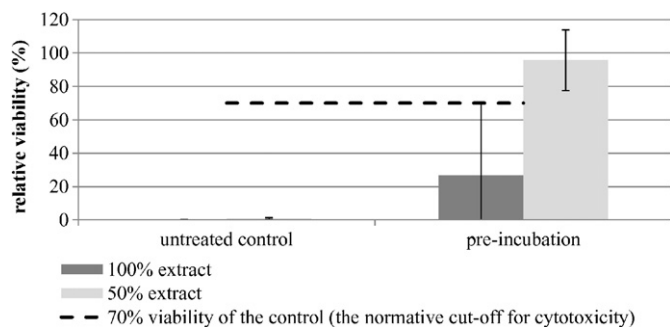


Fig. 5. Cytotoxicity of extracts of Zn1.5Mg alloys with and without pre-incubation depicted as the metabolic activity of L929 cells compared to control (sole medium) after one-day incubation with undiluted and diluted extracts: error bars represent 95% confidence interval using three independent samples measured in hexaplicates.

Table 5
Concentration of released Zn ions in concentrated extracts after one day.

	$\mu\text{g ml}^{-1}$	$\mu\text{mol l}^{-1}$
Untreated control	10.5 ± 0.8	160 ± 12
Pre-incubated sample	3.2 ± 1.7	49 ± 26

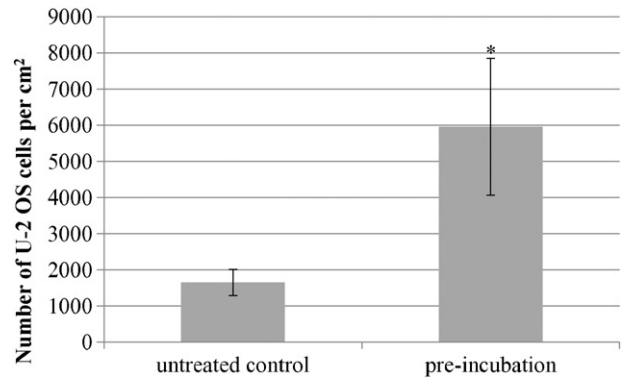


Fig. 6. Number of U-2 OS cells per cm^2 adhered on the untreated and pre-incubated samples after one day of growth: error bars represent SSD from four replicates; asterisk stands for $p > 0.05$.

untreated samples caused 100% cytotoxicity (determined as zero metabolic activity), whereas the cells treated with extracts from pre-incubated samples had significantly higher metabolic activity. Considerable standard error is caused by differences in corrosion rate within the replicates. In the case of twofold diluted extract, the metabolic activity was $96 \pm 18\%$ of the control, which is even higher than the minimal normative limit of 70% (dashed line). Cytotoxic effect was dependent on the Zn concentration in the extracts (Table 5).

3.4. Contact *in vitro* cytocompatibility test

Compared to the untreated control, pre-incubation in SBF led to surface changes that resulted in a significant increase (3.6 fold) in the number of U-2 OS cells adhered onto the samples after 24 h (Fig. 6). The cells after one day of incubation directly onto the samples were also observed by SEM. The number of cells on the untreated sample was lower and cells were round (Fig. 7A, B). Cells grown on the pre-incubated sample were more abundant and more spread (Fig. 7C, D), however, compared to the control (cover slip, Fig. 7E, F), some cells on the preincubated sample exhibited a rather unhealthy morphology – they were shrunk and did not spread (Fig. 7C). This could be caused by the local concentration of the zinc at the surface, which was low enough to allow cell attachment, but still higher than desirable. This observation is in contrast with Li et al. [18], who observed the normal morphology of ECV304 and MG63 cells on Zn-1X alloys including Zn-1Mg. However, no direct comparison for U-2 OS cells is available.

Table 6
Solubility product constants of hydroxides and phosphates.

Compound	Formula	Solubility product constants
Zinc hydroxide	$\text{Zn}(\text{OH})_2$	$3 \cdot 10^{-17}$
Calcium phosphate	$\text{Ca}_3(\text{PO}_4)_2$	$2.07 \cdot 10^{-33}$
Magnesium hydroxide	$\text{Mg}(\text{OH})_2$	$5.6 \cdot 10^{-12}$
Zinc phosphate	$\text{Zn}_3(\text{PO}_4)_2$	$9.0 \cdot 10^{-33}$

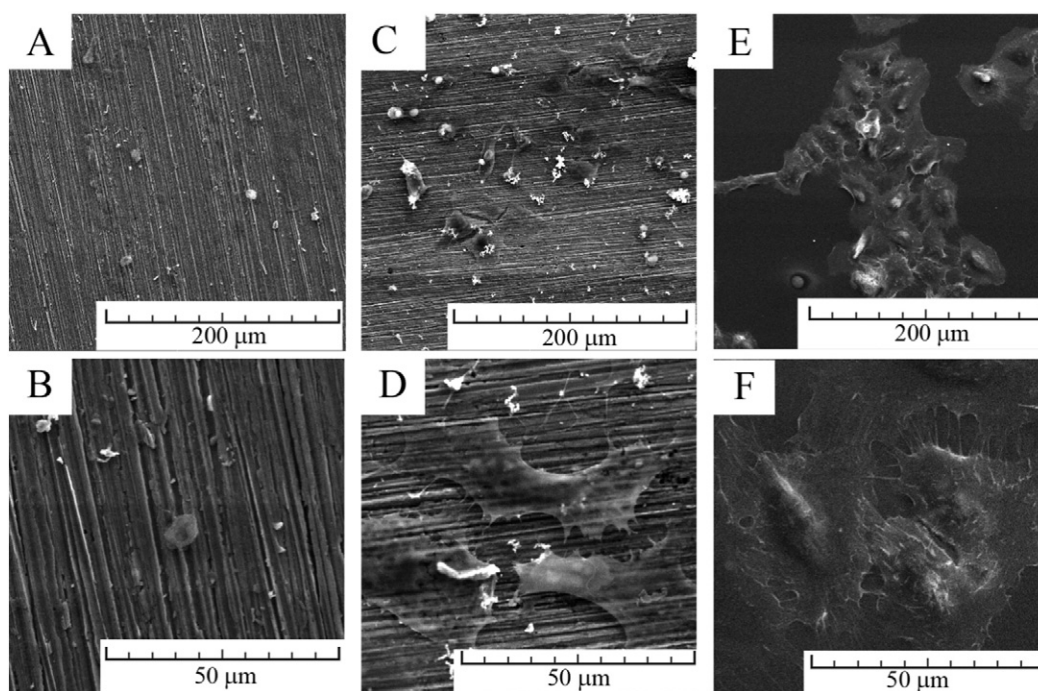


Fig. 7. SEM images of U-2 OS adhered on untreated (A, B) and pre-incubated (C, D) samples after one day. Cover slip served as a control (E, F).

4. Discussion

Zn-based biomaterials are known to represent a viable alternative to Mg-based materials for orthopaedic applications. Due to their low corrosion rate, zinc-based materials are usually tolerated *in vivo* causing no systemic toxicity [11,15,18]. Even if the highest corrosion rate observed in this study ($0.052 \pm 0.010 \text{ mg cm}^{-2} \text{ day}^{-1}$ for untreated control in CO_2 atmosphere) is taken into account, a typical screw of 5 mm diameter and 50 mm length made of zinc with a surface of 8 cm^2 would release 0.4 mg of zinc per day. This would represent an insignificant contribution to the oral intake and means that the RDA value (11 mg/day for men and 8 mg/day for women, [13]) would not be exceeded.

However, as we have shown, both previously [16] and in this study (Section 3.3) concentrations much lower than RDA cause cytotoxicity *in vitro*. It is known that the corrosion behaviour of Mg-based alloys differs *in vivo* and *in vitro* [5,20]. Thus, a similar problem can be expected in the case of Zn-based alloys. As in the case of Mg-based alloys, one of the reasons for this is probably the *in vivo* formation of the protective layer composed of phosphates [5].

The formation of phosphates decelerated the corrosion rate, probably due to their lower solubility product constant compared to hydroxides (Table 6). Another benefit is the bioactive behaviour of phosphates. Calcium phosphates exist as components of hard tissues and positively influence the adhesion and growth of bone cells on biomaterials [25]. Despite the incomparability of different types of materials, we can speculate that after pre-incubation in SBF, Ca/P layer formation could achieve a similar effect in Zn-based alloys as in Mg-based alloys [26]. Gong et al. using EDS also observed that the corrosion layer of a Zn-1Mg alloy after pre-incubation in SBF was mainly composed of Zn, O, P, and Ca [17]. Interestingly, according to Bowen who performed elemental mapping with EDS of a zinc stent, the calcium/phosphorus layer is not thought to play a significant role in pure zinc bio-corrosion *in vivo* [11]. However, no such analysis has been performed on Zn-based alloys since Li et al. examined (XPS) the exact composition of the corrosion layer formed on Zn-1X alloys after immersion tests, but not after *in vivo* tests [18]. Nevertheless, the formation of a Ca/P rich corrosion layer on Zn-based materials appears to be an advantage of zinc

alloys over, for example, iron alloys, where oxides are predominantly formed [9]. It must be noted that the Ca/P-rich layer formation is probably only one of the factors that contribute to the discrepancy between *in vivo* and *in vitro* results. Other factors could include surface exposition, fluid circulation and also the reactions with many aspects that occur between the numerous compounds, proteins and amino acids and these will be the objects of further research.

5. Conclusions

We prepared and pre-incubated the Zn1.5Mg alloy in SBF in order to create the protective surface layer. Pre-incubation significantly decreased the initial corrosion rate of the alloy and increased metabolic activity of L929 after indirect test as well as number of U-2 OS cell adhered onto the surface of the alloy. We propose that this relatively simple procedure used for the samples prior to the *in vitro* tests mimics the spontaneous formation of the protective surface layer *in vivo*. This probably decreases the ion release and subsequently also local toxicity and enhances initial cell adhesion *in vivo*. Although *in vitro* tests have limitations and do not fully mimic the complexity of the body, the economical and, more importantly, ethical questions justify their use as preliminary testing prior to the tests on animal models. We believe that our proposed treatment can reduce the discrepancy between *in vitro* and *in vivo* results obtained with Zn-based alloys.

Acknowledgements

Authors wish to thank to the Czech Science Foundation (project no. P108/12/G043) for financial support of this research.

References

- [1] Y.F. Zheng, X.N. Gu, F. Witte, Mater. Sci. Eng. R. Rep. 77 (2014) 1–34.
- [2] J. Walker, S. Shadanbaz, T.B. Woodfield, M.P. Staiger, G.J. Dias, J. Biomed. Mater. Res. B Appl. Biomater. 102 (2014) 1316–1331.
- [3] M. Schinhammer, A.C. Hanzi, J.F. Löffler, P.J. Uggowitzer, Acta Biomater. 6 (2010) 1705–1713.
- [4] S. Yoshizawa, A. Brown, A. Barchowsky, C. Sfeir, Acta Biomater. 10 (2014) 2834–2842.

- [5] F. Witte, V. Kaese, H. Haferkamp, E. Switzer, A. Meyer-Lindenberg, C.J. Wirth, H. Windhagen, *Biomaterials* 26 (2005) 3557–3563.
- [6] T. Kraus, S.F. Fischerauer, A.C. Hanzi, P.J. Uggowitzer, J.F. Löffler, A.M. Weinberg, *Acta Biomater.* 8 (2012) 1230–1238.
- [7] F. Witte, J. Fischer, J. Nellesen, H.A. Crostack, V. Kaese, A. Pisch, F. Beckmann, H. Windhagen, *Biomaterials* 27 (2006) 1013–1018.
- [8] T. Kraus, F. Moszner, S. Fischerauer, M. Fiedler, E. Martinelli, J. Eichler, F. Witte, E. Willbold, M. Schinhammer, M. Meischel, *Acta Biomater.* 10 (2014) 3346–3353.
- [9] J. Capek, J. Kubasek, D. Vojtech, E. Jablonska, J. Lipov, T. Ruml, *Mater. Sci. Eng. C Mater. Biol. Appl.* 58 (2016) 900–908.
- [10] X. Gu, Y. Zheng, S. Zhong, T. Xi, J. Wang, W. Wang, *Biomaterials* 31 (2010) 1093–1103.
- [11] P.K. Bowen, J. Drelich, J. Goldman, *Adv. Mater.* 25 (2013) 2577–2582.
- [12] D. Vojtech, J. Kubasek, J. Serak, P. Novak, *Acta Biomater.* 7 (2011) 3515–3522.
- [13] J. Nriagu, Zinc Toxicity in Humans, in: J.O. Nriagu (Ed.), *Encyclopedia of Environmental Health*, Elsevier, Burlington 2011, pp. 801–807.
- [14] J.L. Gerberding, Public Health Statement for Zinc U.S. DEPARTMENT OF HEALTH AND HUMAN SERVICES, Agency for Toxic Substances and Disease Registry, 2005.
- [15] B. Zberg, P.J. Uggowitzer, J.F. Löffler, *Nat. Mater.* 8 (2009) 887–891.
- [16] J. Kubásek, D. Vojtěch, E. Jablonská, I. Pospíšilová, J. Lipov, T. Ruml, *Mater. Sci. Eng. C* 58 (2015) 24–35.
- [17] H. Gong, K. Wang, R. Strich, J.G. Zhou, *J. Biomed. Mater. Res. B Appl. Biomater.* 103 (2015) 1632–1640.
- [18] H.F. Li, X.H. Xie, Y.F. Zheng, Y. Cong, F.Y. Zhou, K.J. Qiu, X. Wang, S.H. Chen, L. Huang, L. Tian, L. Qin, *Sci. Rep.* 5 (2015) 10719.
- [19] N.S. Murni, M.S. Dambatta, S.K. Yeap, G.R.A. Froemming, H. Hermawan, *Mater. Sci. Eng. C Mater. Biol. Appl.* 49 (2015) 560–566.
- [20] A.H.M. Sanchez, B.J.C. Luthringer, F. Feyerabend, R. Willumeit, *Acta Biomater.* 13 (2015) 16–31.
- [21] L. Muller, F.A. Muller, *Acta Biomater.* 2 (2006) 181–189.
- [22] ISO 10993-5, Biological Evaluation of Medical Devices—Part 5: Tests for In Vitro Cytotoxicity, International Organization for Standardization, 2009.
- [23] I. Michaljaníčová, P. Slepíčka, S. Rimpelová, N. Slepíčková Kasálková, V. Švorčík, *Appl. Surf. Sci.* 370 (2016) 131–141.
- [24] X.G. Zhang, *Corrosion and Electrochemistry of Zinc*, Springer, US, 1996.
- [25] S.V. Dorozhkin, *Acta Biomater.* 8 (2012) 963–977.
- [26] R. Rettig, S. Virtanen, *J. Biomed. Mater. Res. A* 88 (2009) 359–369.

Příloha 10



Effect of equal channel angular pressing on *in vitro* degradation of LAE442 magnesium alloy



Peter Minárik^{a,*}, Eva Jablonská^b, Robert Král^a, Jan Lipov^b, Tomáš Ruml^b, Carsten Blawert^c, Branislav Hadzima^d, František Chmelík^a

^a Department of Physics of Materials, Faculty of Mathematics and Physics, Charles University, Ke Karlovu 5, 121 16 Prague 2, Czech Republic

^b Department of Biochemistry and Microbiology, University of Chemistry and Technology Prague, Technická 5, 166 28 Prague 6, Czech Republic

^c Helmholtz-Zentrum Geesthacht, Zentrum für Material- und Küstenforschung GmbH, Institut für Werkstoffforschung, Max-Planck-Straße 1, Geesthacht, Germany

^d University of Žilina, Univerzitná 8215/1, 010 26 Žilina, Slovakia

ARTICLE INFO

Article history:

Received 4 October 2016

Received in revised form 1 December 2016

Accepted 22 December 2016

Available online 28 December 2016

Keywords:

Magnesium

Biodegradation

In vitro

Cytotoxicity

Implant material

ABSTRACT

Effect of processing by equal channel angular pressing (ECAP) on the degradation behaviour of extruded LAE442 magnesium alloy was investigated in a 0.1 M NaCl solution, Kirkland's biocorrosion medium (KBM) and Minimum Essential Medium (MEM), both with and without 10% of foetal bovine serum (FBS). Uniform degradation of as extruded and ECAP processed samples in NaCl solution was observed, nevertheless higher corrosion resistance was found in the latter material. The increase of corrosion resistance due to ECAP was observed also after 14-days immersion in all media used. Higher compactness of the corrosion layer formed on the samples after ECAP was responsible for the observed decrease of corrosion resistance, which was proven by scanning electron microscope investigation. Lower corrosion rate in media with FBS was observed and was explained by additional effect of protein incorporation on the corrosion layer stability. A cytotoxicity test using L929 cells was carried out to investigate possible effect of processing on the cell viability. Sufficient cytocompatibility of the extruded samples was observed with no adverse effects of the subsequent ECAP processing. In conclusion, this *in vitro* study proved that the degradation behaviour of the LAE442 alloy could be improved by subsequent ECAP processing and this material is a good candidate for future *in vivo* investigation.

© 2016 Elsevier B.V. All rights reserved.

1. Introduction

Magnesium alloys are nowadays intensively investigated as a potential material for degradable implants [1,2]. Until now, a high number of different Mg alloys have been investigated in different *in vitro* and *in vivo* studies [3], from which LAE442 alloy (Mg-4Li-4Al-2RE, wt%) is one of the most often investigated *in vivo* [4–11]. Relatively low and uniform degradation rate and no negative effect on the surrounding tissue and internal organs make this alloy one of the most suitable Mg alloys for orthopaedic applications. So far, all studies have been conducted on as-cast and extruded material. Comparative *in vivo* studies with as-cast LAE442 alloy showed superior performance compared to other alloys (AZ31, AZ91, WE43) after 18 weeks of implantation period [4,5]. However, gas cavities of evolved H₂ were observed in the surrounding tissue as a result of too rapid degradation rate. Improved *in vivo* degradation behaviour was found in the material after subsequent extrusion. A decrease of degradation rate and no presence of gas cavities after 12 weeks of implantation period were reported [6]. It was concluded that grain refinement and homogenization of alloying elements rich

secondary phases were responsible for such improvement. Moreover, long-term *in vivo* studies showed superior degradation behaviour of extruded LAE442 alloy after 6 months [7] and 12 months [8] of implantation period in a rabbit model. Furthermore, the LAE442 alloy was found to have lower degradation rate than the WE43 alloy, which is currently considered as one of the most promising ones. The WE type alloy MAGNEZIX® is the first absorbable alloy which obtained the CE marking of Medical Devices for medical applications within Europe [12]. The significance of the LAE442 alloy in the orthopaedic implant research has been proven by a comprehensive *in vivo* study, in which degradation behaviour of intramedullary interlocked nailing system implanted in an adult sheep for 24-week period was investigated [9]. After a thorough investigation of implant volume development, *ex vivo* mechanical and histological examinations and elemental analyses of alloying elements in inner organs, the authors concluded that the extruded LAE442 alloy can be considered as a suitable degradable implant material. Additionally, the beneficial effect of grain refinement on the *in vivo* corrosion of the LAE442 alloy was demonstrated after implantation of a single extruded and a double extruded material into rabbits [10].

As mentioned, decrease of the degradation rate of the LAE442 alloy was observed after subsequent extrusion, which led to decrease of the grain size and more uniform distribution of secondary phases in the

* Corresponding author.

E-mail address: peter.minarik@mff.cuni.cz (P. Minárik).

material. It was reported that even further improved grain refinement could be achieved in the LAE442 alloy after subsequent equal channel angular pressing (ECAP) [13]. Uniform distribution of equiaxed grains of $\sim 1.5 \mu\text{m}$ in diameter and much more uniform distribution of secondary phases was observed after 12 passes through ECAP. ECAP was already found to be an effective method to increase corrosion resistance of different magnesium alloys [14–16]. Therefore, further increase of the corrosion resistance of the LAE442 alloy is expected when compared to the extruded samples. Moreover, substantial increase of the yield strength was observed in the fine-grained samples of the LAE442 alloy after ECAP [17]. Increase in mechanical strength could have beneficial effect on minimizing the implant size, which is important in particular applications. Furthermore, substantial grain refinement had a positive effect on the fatigue resistance, which was found to be possibly insufficient in the extruded samples of the LAE442 alloy [18]. Therefore, the ECAP processing of LAE442 alloy may enhance the degradable properties of the implant even further. To the best of our knowledge, the present study is the first one that aims to investigate the effect of ECAP on the *in vitro* degradation behaviour of the LAE442 magnesium alloy.

2. Experimental methods

2.1. Material

The investigated material was an extruded magnesium alloy LAE442 with the composition of 4.03 wt% Li – 3.56 wt% Al – 0.76 wt% La – 0.44 wt% Nd – 1.26 wt% Ce – 0.15 wt% Ca – 0.18 wt% Mn – < 0.0001 wt% Fe – < 0.002 wt% Cu – < 0.0002 Ni and balance Mg. Extrusion was performed at 350 °C with an extrusion ratio of 22. Billets with the dimensions of $10 \times 10 \times 100 \text{ mm}^3$ were machined from the extruded bars and processed by ECAP. The ECAP processing direction was parallel to the extrusion direction. The processing was performed up to twelve passes (12P) following route B_c [19] in the temperature range of 185–230 °C and ram speed of 5–10 mm·min⁻¹. The angle θ between two intersecting channels and the corner angle ψ of the ECAP die were 90° and 0°, respectively. The samples of LAE442, which were extruded only, are designated Ex and the samples of LAE442, which were extruded and subsequently processed by ECAP, are designated 12P throughout the article.

2.2. Microstructure analysis

Microstructure of the specimens and corrosion layers after corrosion exposure were observed by scanning electron microscope (SEM) Zeiss AURIGA equipped by electron back scattered diffraction (EBSD) detector and energy-dispersive X-ray spectroscopy (EDS). Samples for microstructure observation were mechanically polished down to 50 nm alumina solution. Additional ion polishing was performed for EBSD specimens using Gatan PIPS™.

2.3. Corrosion in NaCl

Initial corrosion resistance of the studied samples was investigated by electrochemical impedance spectroscopy (EIS). The measurement was performed using three-electrode setup and controlled by the potentiostat AUTOLAB 120 N. Samples were cut perpendicular to the processing direction and exposed surface was ground with SiC1200 (15 μm) prior to each measurement. The measurement was performed in 0.1 M NaCl solution after 5 min of stabilization. EIS tests were executed at room temperature in the frequency range of 100 kHz–20 mHz with 10 mV amplitude with respect to the open circuit potential (OCP). Additional rotation of 1000 rpm was introduced to obtain better homogenization of the measurement. At least five measurements were performed for each sample/condition.

Hydrogen evolution was measured in 0.1 M NaCl solution at room temperature for one week of immersion. Samples with dimensions

$8 \times 8 \times 3 \text{ mm}^3$ were cut from the extruded and 12P bars. Subsequently they were ground (SiC1200, 15 μm) in ethanol in order to remove naturally occurring corrosion layer, measured and weighted.

2.4. Corrosion in biological media

Corrosion performance in biological media was investigated in Kirkland's biocorrosion medium (KBM, prepared according to [3] and buffered with NaHCO₃), in KBM + 10% FBS, in MEM (Sigma no. M0446) and MEM + 10% FBS. The ionic composition of both media in comparison with human plasma is given in Table 1. Samples with dimensions of $6 \times 6 \times 1.5 \text{ mm}^3$ were cut from extruded and 12P bars. Before the tests, samples were ground (SiC1200, 15 μm) in ethanol in order to remove naturally occurring corrosion layer, measured, weighted and sonicated two times for 15 min in 96% ethanol. Three and two replicates of each sample type were used for corrosion rate determination and for corrosion layer examination, respectively. Samples were immersed into 40 ml (S/V $\approx 2.8 \text{ mm}^2/\text{ml}$, i.e. V/S = 36 ml/cm²) of media in falcon tubes with vented caps (Corning) and incubated in 5% CO₂ atmosphere at 37 °C on an orbital shaker for 14 days.

After 14 days, the medium was removed and concentration of released Mg was measured using Atomic absorption spectrometer (AAS, Varian 220), while the pH of media was also recorded. Samples were immersed into a mixture of H₂CrO₄, AgNO₃ and BaSO₄ for 60 min at room temperature in order to remove the corrosion products. After drying, samples were weighted.

Corrosion rate (CR) was determined from the mass loss and was expressed in mg/cm²/day. The corrosion rate was calculated using following Formula (1):

$$\text{CR} = \frac{\Delta m}{A \times t} \quad (1)$$

CR: corrosion rate (mg/cm²/day), Δm : weight change in milligrams, A: surface area in cm², t: immersion time in days.

2.5. In vitro cytotoxicity testing

In vitro cytotoxicity of extracts (indirect test) was tested according to ISO 10993-5 standard. Samples ($6 \times 6 \times 1.5 \text{ mm}^3$) were sterilized in ethanol for 2 h and then dried. Various surface-to-volume ratios and periods of incubation were used. In the first case, samples were immersed into 1 ml (S/V = 100 mm²/ml) of cultivation media (MEM, Sigma M0446) without FBS, which is surface-to-volume ratio closer to that recommended in ISO 10993-12 standard. Samples were agitated on an orbital shaker (125 rpm) at 37 °C for 1 day. Thereafter, the extracts were centrifuged (5 min, 1500 $\times g$), supplemented with 10% FBS and immediately used for cytotoxicity testing. Three samples from each type (Ex and 12P) were used. Meanwhile, L929 cells (murine fibroblasts, ATCC® CCL-1™) were seeded into 96-well plates (100 μl /well) in the density of 1×10^5 cells/ml and incubated at 37 °C for 24 h in

Table 1

Ionic concentrations of KBM prepared according to [3] and of MEM + 10% FBS in comparison with human plasma.

Medium	KBM	MEM	Human plasma
Component	Concentration [mmol/l]		
Cl ⁻	102.5	126.9	103
Na ⁺	120.3	143.6	142
Ca ²⁺	2.5	1.8	2.5
K ⁺	5.1	5.4	5.0
Mg ²⁺	0.5	0.8	1.5
HPO ₄ ²⁻	0.9	1.0	1.0
SO ₄ ²⁻	0.5	0.8	0.5
HCO ₃ ²⁻	26.2	26.2	22–30
Glucose	5.0	5.6	5.0

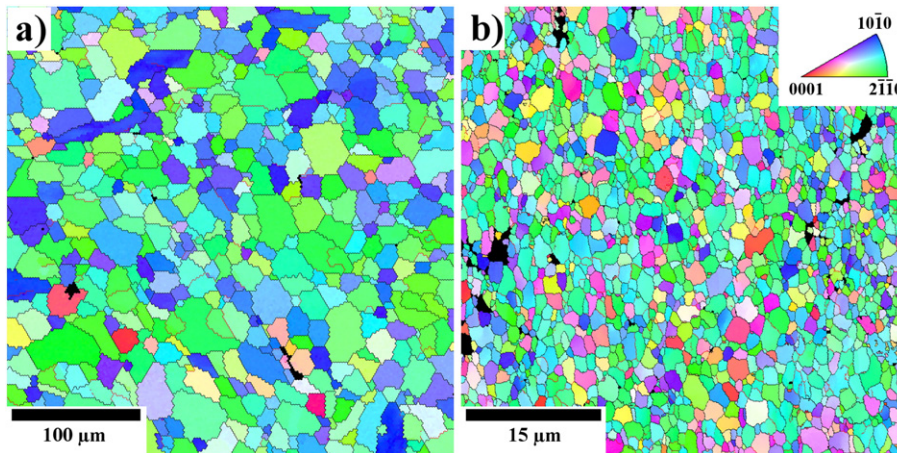


Fig. 1. EBSD micrographs of a) LAE442 Ex and b) LAE442 12P.

MEM + 10% FBS to allow cell adhesion. Thereafter, medium was replaced by the extracts in MEM medium with 10% FBS. MEM with 10% FBS only was used as a negative control.

In the second case, the conditions were more appropriate for magnesium alloys – *i.e.* higher amount of media for extraction and longer extraction time to simulate prolonged exposition of the samples in the body. Therefore, samples were immersed into 6 ml ($S/V = 17 \text{ mm}^2/\text{ml}$) of cultivation media (MEM, Sigma M0446) supplemented with 5% FBS and agitated on an orbital shaker (125 rpm) at 37 °C for 3 and also for 7 days. The decreased concentration of FBS was chosen according to ISO 10993-5 (higher concentration of FBS can mask the toxicity of the extracted substances). Three samples from each type (Ex and 12P) were used. Thereafter, the extracts were immediately used for cytotoxicity testing. Meanwhile, L929 cells were seeded into 96-well plates in the density of 1×10^5 cells/ml or 0.4×10^5 cells/ml and incubated at 37 °C for 24 h in MEM + 10% FBS to allow cell adhesion. Consequently, medium was replaced by the extracts in MEM medium with 5% FBS. MEM with 5% FBS only was used as a negative control.

The evaluation of the test was the same in both cases. After one and four days of incubation with the extracts, the cells were washed with phosphate buffer saline (PBS) and incubated with WST-1 reagent (5% WST-1 in MEM without phenol red) for 2.5 h. The yellow formazan product created by metabolic reduction was photometrically quantified using an ELISA reader at the absorption wavelength of 450 nm. Cytotoxic effect was depicted as a decrease in metabolic activity compared to the negative control. Cytotoxic measurement was done in 6 replicates for each sample. The limitary value of cytocompatibility was set as 70% of metabolic activity of the untreated control (ISO 10993-5).

The results from corrosion studies in various media for the samples after extrusion and after additional ECAP processing were compared using ANOVA followed by Tukey's honest significance test in R software. A p -value < 0.05 was considered significant.

3. Results

3.1. Microstructure

EBSD micrographs of the investigated alloy after extrusion and twelve passes through ECAP are presented in Fig. 1. The initial microstructure of the extruded material was formed by fully recrystallized equiaxed grains with the average grain size of 21 μm. The severe plastic deformation introduced to the material during processing through ECAP resulted in substantial grain refinement. Homogenous microstructure with uniform distribution of fine grains with average grain size of 1.7 μm was observed in the case of the 12P sample. Thorough characterization of the microstructure evolution, together with detailed analysis of the secondary phases, of the LAE442 alloy processed by ECAP is shown elsewhere [13]. Nevertheless, substantial fragmentation and homogenization of distribution of the secondary phase particles within the matrix after ECAP should be noted, as depicted in Fig. 2.

3.2. Corrosion in NaCl

The effect of ECAP processing on the degradation behaviour of the LAE442 alloy was first investigated in 0.1 M NaCl salt solution. The initial corrosion attack after 5 min of immersion was studied by EIS. The

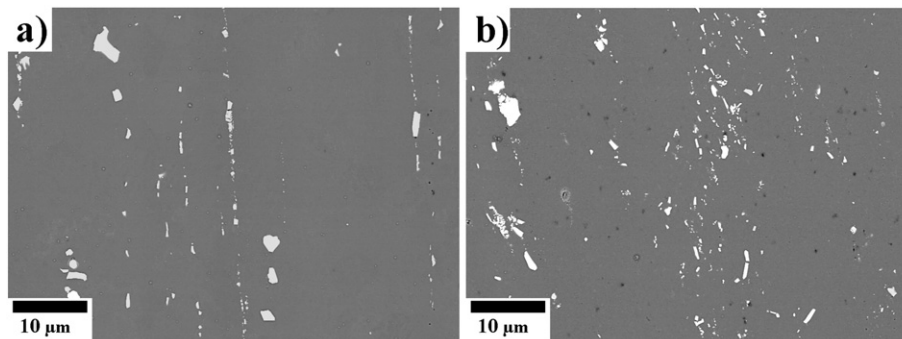


Fig. 2. Secondary phase particles distribution in a) LAE442 Ex and b) LAE442 12P (SEM, plane parallel to extrusion and ECAP direction).

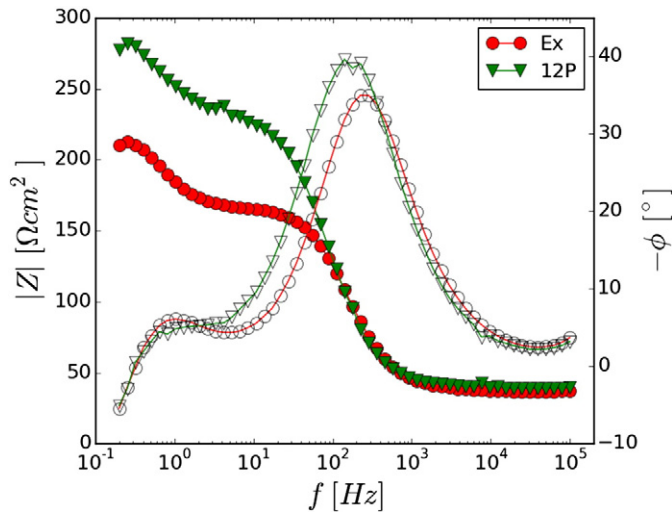


Fig. 3. Bode plots for the extruded and 12P sample, measured in 0.1 M NaCl solution after 5 min of stabilization (full symbols – magnitude, empty symbols – phase angle).

results are shown in the form of Bode plot as Fig. 3. The resulting values of total polarization resistance R_p were calculated as $142 \pm 4 \Omega \text{ cm}^2$ and $202 \pm 14 \Omega \text{ cm}^2$ for the extruded and 12P samples, respectively. The analysis of EIS data is shown in detail elsewhere [16]. The corrosion resistance resulting from EIS analysis was found to be much higher in the 12P sample than in the Ex one. Higher corrosion resistance of the 12P sample in the 0.1 M NaCl solution was observed also using hydrogen evolution measurement, as depicted in Fig. 4. This method was employed in order to observe the evolution of the degradation rate over a one-week immersion. After one day of incubation period, volume of evolved hydrogen as a function of time was linear in both samples. Corrosion rate calculated from the linear part of the plot was $2.87 \pm 0.03 \text{ mg/cm}^2/\text{day}$ and $2.49 \pm 0.02 \text{ mg/cm}^2/\text{day}$ for the Ex and 12P samples, respectively.

3.3. Corrosion in biological media

In order to investigate the degradation rate in biological media, four types of solutions were used. KBM was chosen as a simulated body fluid

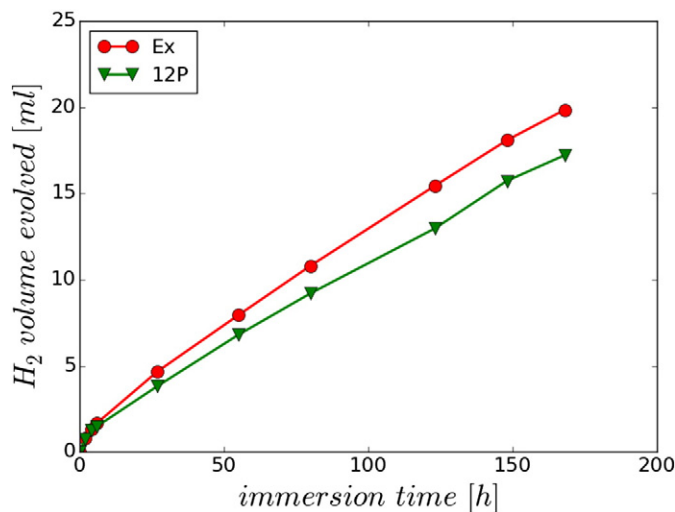


Fig. 4. Volume of hydrogen gas evolved as a function of immersion time in 0.1 M NaCl solution.

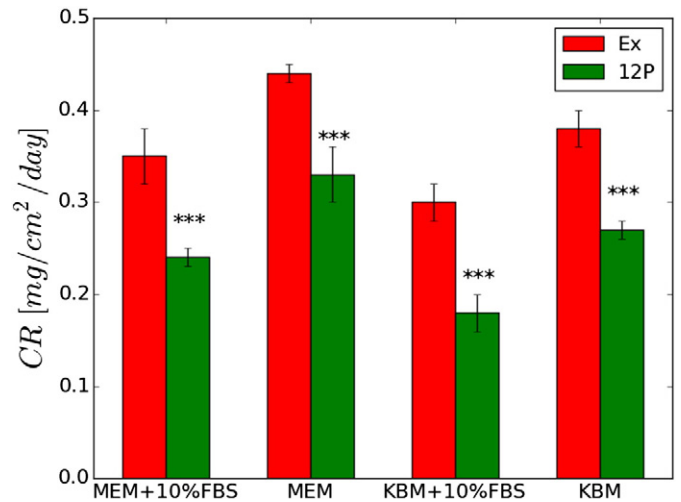


Fig. 5. Corrosion rate of LAE442 calculated from mass loss [$\text{mg/cm}^2/\text{day}$] after 14 days in 40 ml of media (KBM or MEM, with or without 10% FBS) in 5% CO_2 (error bars represent standard deviation, *** stands for $p < 0.001$).

(SBF) because, as mentioned in [3], it closely reflects ionic composition of the human plasma, especially concentration of Cl^- (contrary to other SBFs). Minimal essential medium (MEM) + 10% FBS was chosen as a cultivation medium and was also used for *in vitro* cytotoxicity testing of the investigated samples. In order to study the influence of FBS, KBM + 10% FBS and MEM without FBS was also used. Both the Ex and 12P samples were immersed into all solutions for 14 days. Afterwards, corrosion rate from mass loss was calculated. The results are presented in Fig. 5. The lowest degradation rate was found for 12P samples immersed in KBM + 10% FBS. Importantly, the 12P samples had lower corrosion rate than the Ex samples in all investigated media. It is important to note that after the immersion period, pH of each solution was below 7.6 for all tested samples and experimental setups.

3.4. Analysis of the corrosion layer morphology and composition

To better understand the reason for the differences in the degradation rate between investigated samples and different media, SEM images of the surfaces after the immersion were taken, see Fig. 6. The major difference in the observed corrosion layers formed on Ex and 12P samples was between the immersion in KBM and in other media. The samples immersed in KBM had rough surface with advanced disintegration, while in the other media, the corrosion layers had a dry, cracked earth structure. Generally, there was a major difference between the Ex and the 12P sample. The surface layers formed on the 12P samples were more compact after corrosion in all media. In KBM, this difference is primarily due to deeper and more pronounced cracks in the extruded sample. In MEM, we observed advanced disintegration of the surface layer formed on the Ex sample contrary to the 12P sample. In case of both media with FBS addition, the difference between the extruded and 12P sample is mainly due to significantly higher density of cracks of the compact surface layer observed on the Ex sample.

Not only the morphology of the corrosion layers formed in KBM and the other media were different, but there were also significant differences in their composition. Substantially higher content of Mg was observed in the layer formed in KBM, while in the other media, high content of Ca and P was measured. Calcium phosphate (CaP) compounds preferentially nucleates on $\text{Mg}(\text{OH})_2$ [20], therefore differences between Mg and Ca + P concentration indicate a limited stability of CaP on the samples immersed in KBM media but much better stability in all other media. In MEM, comparable ratio between $\text{Mg}(\text{OH})_2$ and CaP was observed. Composition of the corrosion layer was quite homogeneous

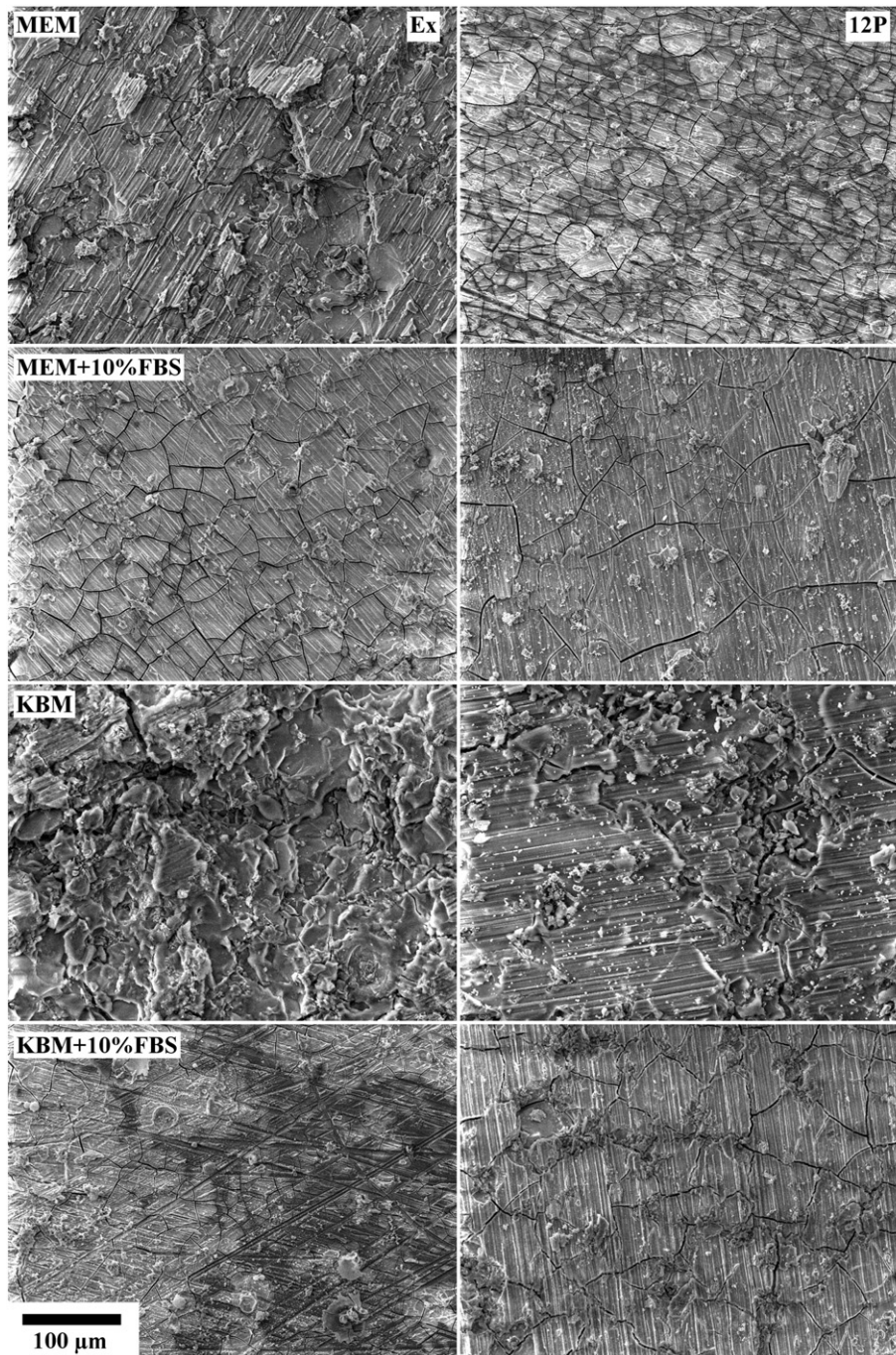


Fig. 6. Corrosion layers formed on the surface of the investigated samples after 14-days immersion in different biological media.

throughout the surfaces of all studied samples, and there was no significant difference between the extruded and 12P samples immersed in the same media. Table 2 shows composition difference between the corrosion layers formed on the 12P samples immersed in different media.

3.5. *In vitro* cytotoxicity testing

The metabolic activity of the L929 cells was not altered after exposure to the extracts of tested samples (Fig. 7); moreover, the relative cell viability was far above 70% limit stated in ISO standard. There were no differences in the cell response using various extraction media, extraction volumes, extraction periods or cultivation periods. Most importantly, there was no difference in cytotoxicity between the

samples before and after ECAP processing. We can therefore assume that the cytocompatibility of LAE442 alloy in extruded state is sufficient and that additional ECAP processing has no adverse effects on the cytocompatibility of this alloy.

4. Discussion

4.1. Corrosion in NaCl

Increase in the corrosion resistance after ECAP was already observed in a number of magnesium alloys, as mentioned above. The major reason was found to be a combination of better distribution of corrosion layer stabilizing alloying elements through the material, together with

Table 2

Elemental composition of the corrosion layers formed on the 12P samples after 14 days of immersion in different media.

at.%	KBM	KBM + 10%FBS	MEM	MEM + 10%FBS
O	61.6 ± 0.4	58.8 ± 0.2	59.7 ± 0.6	58.5 ± 0.7
Na	1.8 ± 0.3	2.0 ± 0.1	1.2 ± 0.2	1.4 ± 0.3
Mg	16.0 ± 0.4	8.0 ± 0.1	11.7 ± 0.8	7.5 ± 0.3
Al	7.3 ± 0.1	2.4 ± 0.1	3.3 ± 0.3	2.4 ± 0.3
P	6.8 ± 0.2	13.1 ± 0.1	11.4 ± 0.3	13.3 ± 0.6
Cl	0.5 ± 0.1	0.2 ± 0.1	0.4 ± 0.1	0.1 ± 0.1
Ca	6.0 ± 0.3	15.7 ± 0.1	12.3 ± 0.6	16.6 ± 0.3

reduced grain size [16,21]. The decrease in the grain size has two major impacts on the corrosion behaviour. Higher density of lattice defects leads to an increased severity of the corrosion attack, but it also leads to a decrease in the mismatch between the corrosion layer and matrix. Therefore, a decrease in the corrosion layer cracking occurs [22]. As a result, more stable protective surface films form faster [16]. Aluminium contained in the investigated alloy is an element that could positively affect corrosion resistance, as shown previously [21,23–25]. Aluminium oxides tend to fill pores of the porous $Mg(OH)_2$ corrosion layer and increase its protection ability. Nevertheless, it should be noted that the concentration of aluminium must exceed a certain threshold level in order to enhance the corrosion resistance after ECAP [16]. Similar functionality of lithium was also previously reported. $Li(OH)$ corrosion products increased corrosion resistance due to the deposition within the porous surface layer [26–29]. However, the detection of $Li(OH)$ is experimentally challenging and its deposition within the corrosion layer of the LAE442 alloy has not been proven yet. Nevertheless, the increase of the polarization resistance of the LAE442 alloy after ECAP was much higher than the increase previously observed in the lithium free AE42 alloy, which was measured under the same conditions [16]. Therefore, faster formation of corrosion layer stabilized by Al oxides together with Li hydroxides in the 12P sample explains higher corrosion resistance achieved in the LAE442 alloy compared to the AE42 alloy. The significant increase of the corrosion resistance after ECAP in the LAE442 alloy was therefore achieved by i) better distribution of Al-rich secondary phases due to fragmentation (Fig. 2), similar as observed in the AE42 alloy, ii) formation of fine distribution of aluminium rich particles within the matrix [13] and possibly iii) the enhancing effect of Li. Combination of all these factors resulted in faster formation of more stable protective surface film.

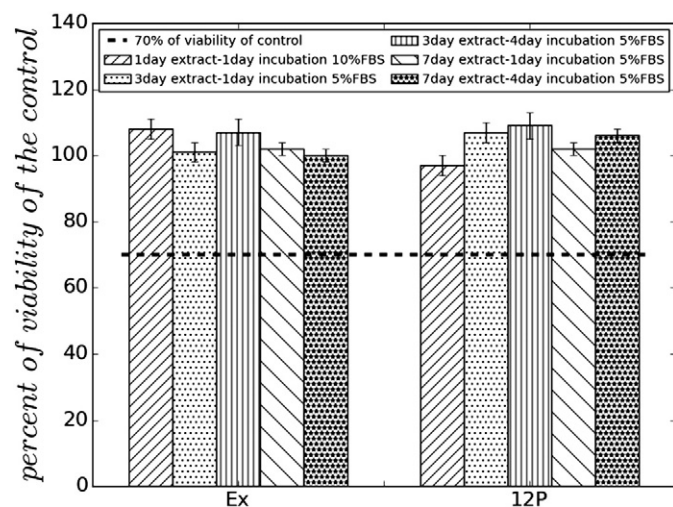


Fig. 7. Metabolic activity of L929 after 1-day or 4-day exposition to LAE442 extracts prepared using various media and extraction periods. Dashed line stands for the cut-off between non-toxic and toxic response. Error bars represent sample standard deviation from six replicates.

Higher corrosion resistance of the 12P sample was observed not only immediately after the immersion, as demonstrated by the hydrogen evolution measurement. The linear character of both plots indicates uniform degradation in both investigated samples after one day of immersion. Higher corrosion rate of the extruded sample is directly visible from the higher volume of evolved hydrogen. This hypothesis is supported also by the values of the calculated corrosion rates. The higher corrosion resistance found in the 12P sample together with the uniform degradation in 0.1 M NaCl solution is an important information that predestines this material for subsequent corrosion tests in biological media.

4.2. Corrosion in biological media

Degradation behaviour in biological media was investigated using immersion tests and corrosion rate was calculated from mass loss evaluation. Corrosion rate was significantly ($p < 0.01$) lower in the presence of 10% FBS for both types of samples in both media used (KBM and MEM). 10% FBS corresponds approximately to the protein concentration of 3.2–7 mg/ml. Our observation is in a good agreement with the published data [30] where lower corrosion rate of pure magnesium in the presence of FBS was observed. Kirkland and Birbilis observed even three times lower corrosion rates of various magnesium alloys in MEM + 10% FBS compared to sole MEM [3]. This can be explained by the formation of more uniform, thicker and more protective layer resulting from protein adsorption [3], since proteins readily interact with Mg divalent ions [31]. More stable and protective layer was also observed by SEM of samples immersed in both media with FBS, see Fig. 6. Adding 10% of FBS into the KBM resulted in a significant change of the corrosion layer character, while in the case of the MEM, the difference was not so pronounced. Nevertheless, in the case of both media EDX analysis showed (Table 2) that the addition of FBS led to an increase of stability of CaP on the surface, which has higher protection ability than the sole $Mg(OH)_2$. Therefore, it is assumed that the higher stability of the corrosion layer formed in both media with FBS led to the higher corrosion resistance of the samples.

Corrosion rate was significantly ($p < 0.05$) lower in KBM than in MEM. This is probably caused by slightly higher concentration of Cl^- in MEM (Table 1). As mentioned in [3], higher concentration of Cl^- accelerates the corrosion rate of Mg alloys.

The most important result is that the corrosion rate after ECAP processing was significantly ($p < 0.001$) lower in all used media, which is consistent with results obtained by EIS and H_2 evolution in NaCl. Investigation of the corrosion layers by SEM has shown higher stability of the corrosion layer formed on 12P samples in all used media, when compared to the extruded ones. Therefore, microstructure of the studied samples had a direct impact on the stability of the corrosion layer, as discussed above in Section 4.1. After ECAP, the density of cracks substantially decreased. This is in accordance with the previous results, which point out that substantial grain refinement leads to a decrease of the mismatch between the corrosion layer and the matrix, resulting in increase of the corrosion layer protection ability [21].

The pH values of media after the immersion period were below 7.6 for all tested samples and solutions. Thus, crucial requirement for maintaining the physiological pH range (7.4–7.6), as recommended in [3], was complied. This is important, because higher pH generally results in more stable and protective CaP surface film that could significantly decrease the corrosion rate of the studied material, and subsequently affect the results.

4.3. In vitro cytotoxicity testing

Under the selected conditions, we observed no cytotoxic effect of extracts prepared from LAE442 after both types of processing. Our results indicate that even the extruded state of the LAE442 alloy has a sufficient cytocompatibility, which is in agreement with previously published observation [32] where the cytocompatibility of extruded magnesium

alloys with Li, Al and RE was studied. The relative viability of ECV304 and VSMC cells after one-day incubation with extracts of Mg-3.5Li-4Al-2RE exceeded 70%. In another study, *in vitro* cytotoxicity tests with an extruded LAE442 alloy were performed [18]. Only slightly reduced viability (70% viability of the control) of L929 cells after incubation with 100% (undiluted) extracts of the extruded LAE442 alloy was observed. This could be caused by a smaller extraction volume used. As mentioned in the introduction, as-cast and extruded LAE442 alloy were also tested *in vivo* and were clinically well tolerated. Therefore, a positive influence of ECAP processing on *in vivo* behaviour can be assumed.

5. Conclusions

We have demonstrated that the ECAP processing decelerates the corrosion rate of the LAE442 magnesium alloy not only during short-term electrochemical experiments in NaCl, but also in longer-term experiments in more complex biological media, such as Kirkland's biocorrosion medium and Minimum Essential Medium, both with and without the addition of 10% FBS. Thus, it is concluded that ECAP processing can be used to improve corrosion resistance of the LAE442 magnesium alloy as a material for temporary orthopaedic implants. These results, together with our successful *in vitro* cytotoxicity tests, let us to conclude that future work should focus on *in vivo* corrosion testing and biocompatibility of LAE442 after ECAP.

Acknowledgement

The present work is a part of the Czech Science Foundation project 14-13415S, Operational Programme CZ.2.16/3.1.00/24503 and NPU I LO1601 - No.: MSMT-43760/2015. B.H. acknowledges the financial support for Slovak Research and Development Agency under the project No. APVV-14-0772 and for Slovak Scientific Grant Agency under the project No.1/0720/14. Authors wish to thank Dr. Eva Mištová for AAS measurements.

References

- [1] Y.F. Zheng, X.N. Gu, F. Witte, Biodegradable metals, *Mater. Sci. Eng. R. Rep.* 77 (2014) 1–34, <http://dx.doi.org/10.1016/j.mser.2014.01.001>.
- [2] F. Witte, N. Hort, C. Vogt, S. Cohen, K.U. Kainer, R. Willumeit, F. Feyerabend, Degradable biomaterials based on magnesium corrosion, *Curr. Opin. Solid State Mater. Sci.* 12 (2008) 63–72, <http://dx.doi.org/10.1016/j.cossms.2009.04.001>.
- [3] N.T. Kirkland, N. Birbilis, Introduction to magnesium biomaterials, *Magnes. Biomater.*, Springer International Publishing 2014, pp. 1–12 (http://link.springer.com/chapter/10.1007/978-3-319-02123-2_1 accessed March 19, 2015).
- [4] F. Witte, V. Kaese, H. Haferkamp, E. Switzer, A. Meyer-Lindenberg, C.J. Wirth, H. Windhagen, In vivo corrosion of four magnesium alloys and the associated bone response, *Biomaterials* 26 (2005) 3557–3563, <http://dx.doi.org/10.1016/j.biomaterials.2004.09.049>.
- [5] F. Witte, J. Fischer, J. Nellesen, H.-A. Crostack, V. Kaese, A. Pisch, F. Beckmann, H. Windhagen, In vitro and in vivo corrosion measurements of magnesium alloys, *Biomaterials* 27 (2006) 1013–1018, <http://dx.doi.org/10.1016/j.biomaterials.2005.07.037>.
- [6] F. Witte, J. Fischer, J. Nellesen, C. Vogt, J. Vogt, T. Donath, F. Beckmann, In vivo corrosion and corrosion protection of magnesium alloy LAE442, *Acta Biomater.* 6 (2010) 1792–1799, <http://dx.doi.org/10.1016/j.actbio.2009.10.012>.
- [7] A. Krause, N. von der Höh, D. Bormann, C. Krause, F.-W. Bach, H. Windhagen, A. Meyer-Lindenberg, Degradation behaviour and mechanical properties of magnesium implants in rabbit tibiae, *J. Mater. Sci.* 45 (2010) 624–632, <http://dx.doi.org/10.1007/s10853-009-3936-3>.
- [8] M. Thomann, C. Krause, D. Bormann, N. von der Höh, H. Windhagen, A. Meyer-Lindenberg, Comparison of the resorbable magnesium alloys LAE442 und MgCa0.8 concerning their mechanical properties, their progress of degradation and the bone-implant-contact after 12 months implantation duration in a rabbit model, *Mater. Werkst.* 40 (2009) 82–87, <http://dx.doi.org/10.1002/mawe.200800412>.
- [9] C. Rössig, N. Angrisani, P. Helmecke, S. Besdo, J.-M. Seitz, B. Welke, N. Fedchenko, H. Kock, J. Reifenrath, In vivo evaluation of a magnesium-based degradable intramedullary nailing system in a sheep model, *Acta Biomater.* 25 (2015) 369–383, <http://dx.doi.org/10.1016/j.actbio.2015.07.025>.
- [10] B. Ullmann, J. Reifenrath, J.-M. Seitz, D. Bormann, A. Meyer-Lindenberg, Influence of the grain size on the in vivo degradation behaviour of the magnesium alloy LAE442, *Proc. Inst. Mech. Eng. H.* 227 (2013) 317–326.
- [11] N. Angrisani, J. Reifenrath, F. Zimmermann, R. Eifler, A. Meyer-Lindenberg, K. Vano-Herrera, C. Vogt, Biocompatibility and degradation of LAE442-based magnesium alloys after implantation of up to 3.5 years in a rabbit model, *Acta Biomater.* 44 (2016) 355–365, <http://dx.doi.org/10.1016/j.actbio.2016.08.002>.
- [12] H. Windhagen, K. Radtke, A. Weizbauer, J. Diekmann, Y. Noll, U. Kreimeyer, R. Schavan, C. Stukenborg-Colsman, H. Waizy, Biodegradable magnesium-based screw clinically equivalent to titanium screw in hallux valgus surgery: short term results of the first prospective, randomized, controlled clinical pilot study, *Biomed. Eng. Online* 12 (2013) 62, <http://dx.doi.org/10.1186/1475-925X-12-62>.
- [13] P. Minárik, R. Král, J. Pešička, S. Daniš, M. Janeček, Microstructure characterization of LAE442 magnesium alloy processed by extrusion and ECAP, *Mater. Charact.* 112 (2016) 1–10, <http://dx.doi.org/10.1016/j.matchar.2015.12.002>.
- [14] J. Jiang, A. Ma, N. Saito, Z. Shen, D. Song, F. Lu, Y. Nishida, D. Yang, P. Lin, Improving corrosion resistance of RE-containing magnesium alloy ZE41A through ECAP, *J. Rare Earths* 27 (2009) 848–852, [http://dx.doi.org/10.1016/S1002-0721\(08\)60348-8](http://dx.doi.org/10.1016/S1002-0721(08)60348-8).
- [15] B. Hadzima, M. Janeček, M. Bukovina, R. Kral, Electrochemical properties of fine-grained AZ31 magnesium alloy, *Int. J. Mater. Res.* 100 (2009) 1213–1216, <http://dx.doi.org/10.3139/146.110186>.
- [16] P. Minárik, R. Král, M. Janeček, Effect of ECAP processing on corrosion resistance of AE21 and AE42 magnesium alloys, *Appl. Surf. Sci.* 281 (2013) 44–48, <http://dx.doi.org/10.1016/j.apsusc.2012.12.096>.
- [17] P. Minárik, R. Král, J. Čížek, F. Chmelík, Effect of different c/a ratio on the microstructure and mechanical properties in magnesium alloys processed by ECAP, *Acta Mater.* 107 (2016) 83–95, <http://dx.doi.org/10.1016/j.actamat.2015.12.050>.
- [18] M. Krámer, M. Schilling, R. Eifler, B. Hering, J. Reifenrath, S. Besdo, H. Windhagen, E. Willbold, A. Weizbauer, Corrosion behavior, biocompatibility and biomechanical stability of a prototype magnesium-based biodegradable intramedullary nailing system, *Mater. Sci. Eng. C* 59 (2016) 129–135, <http://dx.doi.org/10.1016/j.msec.2015.10.006>.
- [19] K. Nakashima, Z. Horita, M. Nemoto, T.G. Langdon, Development of a multi-pass facility for equal-channel angular pressing to high total strains, *Mater. Sci. Eng. A* 281 (2000) 82–87, [http://dx.doi.org/10.1016/S0921-5093\(99\)00744-3](http://dx.doi.org/10.1016/S0921-5093(99)00744-3).
- [20] J.X. Yang, F.Z. Cui, Q.S. Yin, Y. Zhang, T. Zhang, X.M. Wang, Characterization and degradation study of calcium phosphate coating on magnesium alloy bone implant in vitro, *IEEE Trans. Plasma Sci.* 37 (2009) 1161–1168, <http://dx.doi.org/10.1109/TPS.2009.2016664>.
- [21] A. Pardo, M.C. Merino, A.E. Coy, R. Arrabal, F. Viejo, E. Matykina, Corrosion behaviour of magnesium/aluminium alloys in 3.5 wt.% NaCl, *Corros. Sci.* 50 (2008) 823–834, <http://dx.doi.org/10.1016/j.corsci.2007.11.005>.
- [22] N. Birbilis, K.D. Ralston, S. Virtanen, H.L. Fraser, C.H.J. Davies, Grain character influences on corrosion of ECAPed pure magnesium, *Corros. Eng. Sci. Technol.* 45 (2010) 224–230, <http://dx.doi.org/10.1179/147842209X12559428167805>.
- [23] M. Liu, P.J. Uggowitzer, A.V. Nagasekhar, P. Schmutz, M. Easton, G.-L. Song, A. Atrens, Calculated phase diagrams and the corrosion of die-cast Mg–Al alloys, *Corros. Sci.* 51 (2009) 602–619, <http://dx.doi.org/10.1016/j.corsci.2008.12.015>.
- [24] G. Wu, Y. Fan, H. Gao, C. Zhai, Y.P. Zhu, The effect of Ca and rare earth elements on the microstructure, mechanical properties and corrosion behavior of AZ91D, *Mater. Sci. Eng. A* 408 (2005) 255–263, <http://dx.doi.org/10.1016/j.msea.2005.08.011>.
- [25] Y. Fan, G. Wu, C. Zhai, Influence of cerium on the microstructure, mechanical properties and corrosion resistance of magnesium alloy, *Mater. Sci. Eng. A* 433 (2006) 208–215, <http://dx.doi.org/10.1016/j.msea.2006.06.109>.
- [26] J. Gui, T.M. Devine, Influence of lithium on the corrosion of aluminum, *Scr. Metall.* 21 (1987) 853–857, [http://dx.doi.org/10.1016/0036-9748\(87\)90336-X](http://dx.doi.org/10.1016/0036-9748(87)90336-X).
- [27] J.P. Moran, E.A.J. Starke, G.E. Stoner, G.L.J. Cahen, *Corrosion* (1986) (n.d.).
- [28] M.C. Bloom, W.A. Fraser, M. Krulfeld, Corrosion of steel in concentrated lithium hydroxide solution at 316C, *Corrosion* 18 (1962) 401–405, <http://dx.doi.org/10.5006/0010-9312-18.11.401>.
- [29] M.C. Bloom, M. Krulfeld, W.A. Fraser, Some effects of alkalis on corrosion of mild steel in steam generating systems, *Corrosion* 19 (1963) 327–330, <http://dx.doi.org/10.5006/0010-9312-19.9.327>.
- [30] A. Yamamoto, S. Hiromoto, Effect of inorganic salts, amino acids and proteins on the degradation of pure magnesium in vitro, *Mater. Sci. Eng. C* 29 (2009) 1559–1568, <http://dx.doi.org/10.1016/j.msec.2008.12.015>.
- [31] C. Liu, Y. Xin, X. Tian, P.K. Chu, Degradation susceptibility of surgical magnesium alloy in artificial biological fluid containing albumin, *J. Mater. Res.* 22 (2007) 1806–1814, <http://dx.doi.org/10.1557/jmr.2007.0241>.
- [32] W.R. Zhou, Y.F. Zheng, M.A. Leeftang, J. Zhou, Mechanical property, biocorrosion and in vitro biocompatibility evaluations of Mg–Li–(Al)–(RE) alloys for future cardiovascular stent application, *Acta Biomater.* 9 (2013) 8488–8498, <http://dx.doi.org/10.1016/j.actbio.2013.01.032>.